THE INFLUENCE OF STACKING SEQUENCE ON THE STRENGTH OF BONDED CFRP JOINTS

by

Kays Clement Kairouz, M.Sc.

February 1991

A thesis submitted for the degree of Doctor of
Philosophy of the University of London and for
the Diploma of Membership of the Imperial College

Department of Aeronautics
Imperial College of Science, Technology and Medicine
London, SW7 2BY

To my parents

"I bless you, Father, Lord of heaven
and of earth, for hiding these things
from the learned and the clever and
revealing them to mere children."

(Mt. 11:25)

ABSTRACT

The influence of stacking sequence on the mechanisms of failure and strength of bonded carbon fibre-reinforced plastic joints is investigated. Emphasis is placed on identifying the initiation and modes of failure and on the correlation of the performance of a joint with numerical prediction.

An introduction to composite materials, adhesively bonded joints and the objectives of the current project are given in Chapter 1. A basis for the present study is provided in Chapter 2 by reviewing some of the open literature in this field.

In Chapter 3 theoretical aspects relating to the analysis of composite joints are presented. Formulae and illustrations are given for some of the key effective mechanical properties of the adherends which affect the performance of a single lap joint. The continuum method of Hart-Smith is revised and modified to account for the effect of Poisson's ratio in bending. The limitations of the bending stiffness parameter are discussed. An outline of the geometrically nonlinear finite element analysis used is given together with failure criteria for the adhesive and adherends.

The various experimental techniques used are addressed in Chapter 4. The rationale for selecting the lay-ups and stacking sequences is given. After discussing surface pretreatment of the adherends, the problematic area of adhesive voids and how it was overcome is presented. Emphasis is placed on drying the adhesive and adherends prior to bonding. To control the bondline thickness, shims are used under an appropriate pressure. Moiré interferometry is discussed briefly and expressions relating deformations and strains are given. The importance of fractographic analysis in the understanding of the modes of failure is outlined.

The performance of joints with six-ply, eight-ply, sixteen-ply, cross-ply and other miscellaneous lay-ups are given in Chapters 5–9 respectively. Detailed descriptions of the mechanisms of failure are given, supported by fractographic and numerical analyses. A comparison has been made between Hart-Smith's and linear and nonlinear finite element analyses. Good agreement has been obtained between

moiré and numerically predicted strains. It has been shown that joint failure may be predicted using geometrically nonlinear finite element analysis.

In Chapter 10, a simple joint ranking factor, which ranks joint strength relative to stacking sequence changes, is proposed. This factor encompasses the different effects of the adherends' effective mechanical properties.

The conclusions of the current study and recommendations for future work are given in Chapter 11. It is found that a single 0° layer next to the bondline may not necessarily increase joint strength as compared to similarly placed ±45° plies. This is mainly due to the bending moment relief offered by 'soft' ply groups and enhanced resistance to bend-twist coupling effects.

Mechanical testing of the composite (unidirectional) and adhesive were undertaken and the results are reported in Appendix A. The materials' ultimate strengths and strains are used for joint failure prediction. Appendix B provides tensile properties of various laminates. There is some evidence that placing ±45° plies on the laminate's surfaces provides some enhancement to the tensile strength due to the 'padding' effect offered to the load bearing 0° layers. Finally, flexural properties of some laminates are given in Appendix C. An attempt has been made to relate the higher bending strain with laminates having ±45° surface layers to the yielding effect in metallic adherends.

ACKNOWLEDGEMENTS

I would like to thank my supervisor, Mr. F.L. Matthews, for his assistance and advice throughout the course of this project. This work was conducted with the financial support of the Procurement Executive, Ministry of Defence. The author is grateful to the contract monitors, Drs. B.M. Parker and S.M. Bishop of the Royal Aerospace Establishment, Farnborough, for their guidance and encouragement.

Thanks are due to Prof. J. Morton of Virginia Polytechnic Institute and State University, Virginia, U.S.A., for his collaboration on the moiré interferometry experiments. I wish to thank the technical staff of the Department of Aeronautics, especially Messrs. J.P. O'Leary, G. Senior and R. Wilkins.

CONTENTS

1 INTRODUCTION 20

2 LITERATURE SURVEY 22
2.1 Introduction 22
2.2 Advantages and disadvantages of adhesive bonding 23
2.3 Theoretical analysis 25
2.4 Experimental analysis 35
2.5 Surface preparation 38
2.6 Adhesive voids 40
2.7 Effect of stacking sequence 41
2.8 Effect of bondline thickness 42
2.9 Hygrothermal effects 44
2.10 Conclusions 46

3 THEORETICAL CONSIDERATIONS 51
3.1 Introduction 51
3.2 Adherend mechanical properties 51
3.3 Continuum analysis 58
3.3.1 Adherend stress 58
3.3.2 Adhesive peel stress 59
3.4 Finite element analysis 60
3.4.1 Plane stress 63
3.4.2 Plane strain 64
3.4.3 Geometrically nonlinear formulation 65
3.4.4 Adhesive failure criterion 67
3.4.5 Adherend failure criterion 68

4 EXPERIMENTAL METHODS 71
4.1 Introduction 71
4.2 Materials 71
4.3 Lay-ups and stacking sequences 73
4.4 Surface pretreatment of adherends 73
4.5 Adhesive voids 73
4.6 Preparation of bonded joints 74
4.7 Testing of joints 76
4.8 Moiré interferometry 76
4.9 Fractography 78

5 JOINTS WITH SIX-PLY ADHEREND 84
5.1 Introduction 84
5.2 Experimental results 84
5.3 Continuum analysis 85
5.4 Finite element analysis 86
5.5 Discussion 86
5.5.1 Stacking sequence A: $[0/\pm 45]_s$ 87
5.5.2 Stacking sequence B: $[\pm 45/0]_s$ 88
5.6 Conclusions 88

6 JOINTS WITH EIGHT-PLY ADHEREND 101
6.1 Introduction 101
6.2 Experimental results 101
6.3 Continuum analysis 102
6.4 Finite element analysis 102
6.5 Discussion 103
6.5.1 Comparison between Hart-Smith's and finite element analyses 103
6.5.2 Mechanisms of failure 105
6.6 Conclusions 107

7 JOINTS WITH SIXTEEN-PLY ADHEREND 125
7.1 Introduction 125
7.2 Experimental results 125
7.2.1 Moiré interferometry 126
7.3 Continuum analysis 126
7.4 Finite element analysis 126
7.5 Discussion 127
7.5.1 Comparison between moiré and finite element analyses 127
7.5.2 Failure analysis 128
7.5.3 Adhesive toughening phase 131
7.6 Conclusions 131

8 JOINTS WITH CROSS-PLY ADHEREND 160
8.1 Introduction 160
8.2 Experimental results 160
8.3 Continuum analysis 160
8.4 Finite element analysis 161
8.5 Discussion 161
8.5.1 Lay-up $[90/0]_{2s}$ 161
8.6 Conclusions 163

9 OTHER LAY-UPS 178
9.1 Introduction 178
9.2 Experimental results 178
9.3 Continuum analysis 178
9.4 Finite element analysis 179

9.5 Discussion 179
9.5.1 Unidirectional $[0_8]_s$ lay-up 179
9.5.2 Lay-up Q: $[\pm 45/90/0_2/\pm 45/0]_s$ 180
9.6 Conclusions 181

10 DESIGN GUIDELINES 194
10.1 Introduction 194
10.2 Joint ranking factor 194
10.3 Discussion 196
10.3.1 Six-ply adherends 196
10.3.2 Eight-ply adherends 196
10.3.3 Sixteen-ply adherends 196
10.3.4 Cross-ply adherends 197
10.3.5 Other lay-ups 197
10.3.6 Other groupings 197
10.4 Conclusions 198

11 CONCLUSIONS AND RECOMMENDATIONS FOR FUTURE WORK 203
11.1 Conclusions 203
11.1.1 Six-ply adherends 204
11.1.2 Eight-ply adherends 205
11.1.3 Sixteen-ply adherends 206
11.1.4 Cross-ply adherends 206
11.1.5 Other lay-ups 207
11.2 Recommendations for future work 208

APPENDICES

A MECHANICAL PROPERTIES OF THE COMPOSITE AND ADHESIVE 209
A.1 Introduction 209
A.2 Modes of failure 209
A.2.1 Longitudinal tensile failure 209
A.2.2 Transverse tensile failure 210
A.2.3 Longitudinal compression failure 210
A.2.4 Transverse compression failure 211
A.2.5 In-plane shear failure 211
A.3 Unidirectional properties 211
A.4 Adhesive mechanical properties 212

B TENSILE PROPERTIES OF LAMINATES 218
B.1 Introduction 218
B.2 Results and discussion 218

C FLEXURAL PROPERTIES OF LAMINATES 224
C.1 Introduction 224
C.2 Three-point flexure test 224

C.3 Modes of failure 225
C.4 Test results 226

REFERENCES 229

TABLES

Chapter 4

4.1 Lay-ups and stacking sequences used in the experimental programme 79

Chapter 5

5.1 Test results 90
5.2 Adherend mechanical properties and stresses from Hart-Smith's analysis 90

Chapter 6

6.1 Test results 108
6.2 Adherend mechanical properties and stresses from Hart-Smith's analysis 109
6.3 Comparison between Hart-Smith's and finite element analyses results (25 mm overlap) 110

Chapter 7

7.1 Test results 132
7.2 Adherend mechanical properties and stresses from Hart-Smith's analysis 132

Chapter 8

8.1 Test results 165
8.2 Adherend mechanical properties and stresses from Hart-Smith's analysis 165

Chapter 9

9.1 Test results 182
9.2 Adherend mechanical properties and stresses from Hart-Smith's analysis 182

Chapter 10

10.1 Joint ranking factors 199
10.2 JRF with other groupings 201

Appendix A

A.1 Mechanical properties of XAS/914C composite 213
A.2 Mechanical properties of Redux 308A adhesive 213

Appendix B

B.1 Tensile strength of laminates 220
B.2 Mechanical properties of laminates 220

Appendix C

C.1 Flexural properties of six-ply adherends 227
C.2 Flexural properties of eight-ply adherends 227

Chapter 2

2.1 Adhesively bonded joint types and their relative uses [1]..... 47
2.2 Typical variations of shear and peel stresses in a single lap joint [5]..... 48
2.3 Schematic explanation of the shearing in the adhesive [8]: (a) Unloaded lap joint. (b) Loaded joint with inextensible adherends. (c) Joint with elastic adherends... 48
2.4 Schematic explanation of the bending of the adherends and of the resulting tearing stresses at the ends of the overlap [8]: (a) Lap joint before deformation. (b) Eccentricity of loading near the overlap. (c) Bending moment near the overlap. (d) Final deformation of the joint..... 49
2.5 Failure of single lap bonded joints (brittle and yielding adherends) [1]..... 49
2.6 Variation of peak induced adhesive stress with thickness of adhesive at ends of overlap [58]..... 50

Chapter 3

3.1 The lateral contractions resulting from membrane Poisson's effects..... 69
3.2 The effect of bending Poisson's ratio on adherend curvatures..... 69
3.3 The effect of mutual bend-twist coupling on torsional deformation..... 70
3.4 Typical load-displacement curve for a single lap joint loaded to failure..... 70

Chapter 4

4.1 SEM showing: (a) Laminate surface texture as moulded. (b) Laminate surface texture after sand blasting. (c) Fibre damage due to sand blasting. (d) Adhesive voids..... 80
4.2 A fractured joint with high void content adhesive layer..... 80
4.3 The bonding arrangement and the resulting specimen configuration. Dimensions are given in millimetres (not to scale)..... 81
4.4 Variations in bondline thickness due to peel-ply impression..... 82
4.5 Increase of adhesive layer thickness at end of lap due to rounding of adherend edge as a result of sand blasting..... 82
4.6 Steps to produce specimen grating by replication process and four-beam optical arrangement [79]..... 83

Chapter 5

5.1 The bonded specimens after fracture. (a) Stacking sequence A: $[0/\pm 45]_s$. (b) Stacking sequence B: $[\pm 45/0]_s$..... 91
5.2 Geometry and finite element model of six-ply adherend joint. Dimensions are given in millimetres (not to scale)..... 92
5.3 Out-of-plane displacement of the adherend centreline using linear analysis. Stacking sequence A: $[0/\pm 45]_s$ at 505.7 N/mm^2 applied stress..... 93

5.4 Out-of plane displacements of the adherend centrelines using nonlinear analysis. The applied stresses for stacking sequences A and B are 505.7 N/mm^2 and 652.1 N/mm^2 respectively. 93

5.5 Adherend longitudinal direct strain (ϵ_{xx}) distribution along the y-axis at the end of the lap using nonlinear analysis. The applied stresses for stacking sequences A and B are 505.7 N/mm^2 and 652.1 N/mm^2 respectively. 94

5.6 Adherend longitudinal direct strain (ϵ_{xx}) distribution along the y-axis at the fillet tip using nonlinear analysis. The applied stresses for stacking sequences A and B are 505.7 N/mm^2 and 652.1 N/mm^2 respectively. 94

5.7 Longitudinal direct strain (ϵ_{xx}) distribution along the centreline of the 0° ply next to the bondline. Stacking sequence A: $[0/\pm45]_s$ at 505.7 N/mm^2 applied stress... 95

5.8 Longitudinal direct stress (σ_{xx}) distribution along the centreline of the 0° ply next to the bondline. Stacking sequence A: $[0/\pm45]_s$ at 505.7 N/mm^2 applied stress... 95

5.9 Transverse direct strain (ϵ_{yy}) distribution along the centreline of the 0° ply next to the bondline. Stacking sequence A: $[0/\pm45]_s$ at 505.7 N/mm^2 applied stress... 96

5.10 Transverse direct stress (σ_{yy}) distribution along the centreline of the 0° ply next to the bondline. Stacking sequence A: $[0/\pm45]_s$ at 505.7 N/mm^2 applied stress... 96

5.11 Shear strain (γ_{xy}) distribution along the centreline of the 0° ply next to the bondline. Stacking sequence A: $[0/\pm45]_s$ at 505.7 N/mm^2 applied stress..... 97

5.12 Shear stress (τ_{xy}) distribution along the centreline of the 0° ply next to the bondline. Stacking sequence A: $[0/\pm45]_s$ at 505.7 N/mm^2 applied stress..... 97

5.13 Longitudinal and transverse direct and shear strain (ϵ_{xx}, ϵ_{yy} and γ_{xy} respectively) distributions along the centreline of the adhesive layer using nonlinear analysis. Stacking sequence A: $[0/\pm45]_s$ at 505.7 N/mm^2 applied stress..... 98

5.14 Longitudinal and transverse direct and shear stress (σ_{xx}, σ_{yy} and τ_{xy} respectively) distributions along the centreline of the adhesive layer using nonlinear analysis. Stacking sequence A: $[0/\pm45]_s$ at 505.7 N/mm^2 applied stress..... 98

5.15 Longitudinal and transverse direct and shear strain (ϵ_{xx}, ϵ_{yy} and γ_{xy} respectively) distributions along the centreline of the +45° layer next to the bondline using nonlinear analysis. Stacking sequence B: $[\pm45/0]_s$ at 652.1 N/mm^2 applied stress. 99

5.16 Longitudinal and transverse direct and shear stress (σ_{xx}, σ_{yy} and τ_{xy} respectively) distributions along the centreline of the +45° layer next to the bondline using nonlinear analysis. Stacking sequence B: $[\pm45/0]_s$ at 652.1 N/mm^2 applied stress. 99

5.17. Longitudinal and transverse direct and shear strain (ϵ_{xx}, ϵ_{yy} and γ_{xy} respectively) distributions along the centreline of the adhesive layer using nonlinear analysis. Stacking sequence B: $[\pm45\ /0]_s$ at 652.1 N/mm^2 applied stress..... 100

5.18 Longitudinal and transverse direct and shear stress (σ_{xx}, σ_{yy} and τ_{xy} respectively) distributions along the centreline of the adhesive layer using nonlinear analysis. Stacking sequence B: $[\pm45\ /0]_s$ at 652.1 N/mm^2 applied stress..... 100

Chapter 6

6.1 The bonded specimens with stacking sequences D–F after fracture. (a) 25 mm overlap. (b) 12.5 mm overlap..... 111

6.2 Finite element discretisation, boundary conditions and deformed shapes due to applied mean failure stress (25 mm overlap). Displacements in the y-direction are magnified twenty times..... 112

6.3 Geometry and finite element model of eight-ply adherend joint. Dimensions are given in millimetres (not to scale)..... 113

6.4 Adherend longitudinal direct stress (σ_{xx}) distribution along the y-axis at the fillet tip using nonlinear finite element analysis. The applied stresses for stacking sequences D, E and F are 508.7 N/mm^2, 571.0 N/mm^2 and 535.8 N/mm^2 respectively..... 114

6.5 Adherend longitudinal direct stress (σ_{xx}) distribution along the y-axis using Hart-Smith's analysis..... 114
6.6 Adherend longitudinal direct strain (ϵ_{xx}) distribution along the y-axis at the end of the lap. The applied stresses for stacking sequences D, E and F are 508.7 N/mm^2, 571.0 N/mm^2 and 535.8 N/mm^2 respectively..... 115
6.7 Adherend longitudinal direct strain (ϵ_{xx}) distribution along the y-axis at the fillet tip. The applied stresses for stacking sequences D, E and F are 508.7 N/mm^2, 571.0 N/mm^2 and 535.8 N/mm^2 respectively..... 115
6.8 Longitudinal direct strain (ϵ_{xx}) distribution along the centreline of the +45° layer next to the bondline. Stacking sequence D: $[\pm 45/0_2]_s$ at 508.7 N/mm^2 applied stress..... 116
6.9 Transverse direct and shear strain (ϵ_{yy} and γ_{xy} respectively) distributions along the centreline of the +45° layer next to the bondline. Stacking sequence D: $[\pm 45/0_2]_s$ at 508.7 N/mm^2 applied stress..... 116
6.10 Longitudinal direct strain (ϵ_{xx}) distribution along the centreline of the 0° layer next to the bondline. Stacking sequence E: $[0/\pm 45/0]_s$ at 571.0 N/mm^2 applied stress..... 117
6.11 Transverse direct and shear strain (ϵ_{yy} and γ_{xy} respectively) distributions along the centreline of the 0° layer next to the bondline. Stacking sequence E: $[0/\pm 45/0]_s$ at 571.0 N/mm^2 applied stress..... 117
6.12 Longitudinal direct strain (ϵ_{xx}) distribution along the centreline of the 0° layer next to the bondline. Stacking sequence F: $[0_2/\pm 45]_s$ at 535.8 N/mm^2 applied stress..... 118
6.13 Transverse direct and shear strain (ϵ_{yy} and γ_{xy} respectively) distributions along the centreline of the 0° layer next to the bondline. Stacking sequence F: $[0_2/\pm 45]_s$ at 535.8 N/mm^2 applied stress..... 118
6.14 Two-dimensional view of joint fracture (stacking sequence D: $[\pm 45/0_2]_s$)..... 119
6.15 Failure initiation and progression (stacking sequence D: $[\pm 45/0_2]_s$)..... 119
6.16 The fractured surfaces of stacking sequence D: $[\pm 45/0_2]_s$, 25 mm overlap. Only the first three plies are shown. For clarity, the adhesive fillet is not drawn..... 120
6.17 SEM, taken from stacking sequence D: $[\pm 45/0_2]_s$, 25 mm overlap, showing (refer to Figs. 6.15 and 6.16): (a) View arrow A—fractured adhesive fillet. Slow 'ductile' (section A'–A'') and fast 'brittle' (section A–A') failures are shown. (b) An enlarged view of the adhesive fillet 'ductile' failure band—flaky fracture. (c) Slow 'ductile' shear failure in the +45° layers and adhesive. Note the adhesive shear cusps. (d) Shear cracks in the −45° layer. (e) Fibre fracture and pull-out. (f) Fibre bending (in discrete locations). T—tensile fracture; C—compressive fracture; N/A—neutral axis..... 121
6.18 Two-dimensional view of joint fracture. (a) Stacking sequence E: $[0/\pm 45/0]_s$. (b) Stacking sequence F: $[0_2/\pm 45]_s$..... 122
6.19 Failure initiation and progression (stacking sequences E: $[0/\pm 45/0]_s$ and F: $[0_2/\pm 45]_s$..... 122
6.20 The fractured surfaces of stacking sequences E: $[0/\pm 45/0]_s$ and F: $[0_2/\pm 45]_s$, 25 mm overlap. Only the first ply is shown. The adhesive fillet is drawn in dashed lines. 123
6.21 SEM, taken from stacking sequence F: $[0_2/\pm 45]_s$, 25 mm overlap, showing (refer to Figs. 6.19 and 6.20): (a) View arrow A. Note the tensile fracture of surface fibres. (b) Enlarged view of adhesive fillet fracture taken from section A–A''. (c) Typical tensile fracture of a single fibre taken from section A'–A''. (d) View arrow B. (e) 'Dynamic' fracture at section B–B'. Note fibre bending and twisting. (f) Fibre pull-out at section B–C..... 124

Chapter 7

7.1 The bonded specimens with stacking sequences K–N after fracture..... 133

7.2 U displacement field for stacking sequence L: $[0/\pm45/0_2/\pm45/0]_s$ with increasing load from top to bottom. 134

7.3 V displacement field for stacking sequence L: $[0/\pm45/0_2/\pm45/0]_s$ with increasing load from top to bottom. 135

7.4 U displacement field at end of lap. (a) Stacking sequence K: $[\pm45/0_3/\pm45/0]_s$ at 169.0 N/mm^2 applied stress. (b) Stacking sequence L: $[0/\pm45/0_2/\pm45/0]_s$ at 189.5 N/mm^2 applied stress. 136

7.5 U displacement field at centre of lap. (a) Stacking sequence K: $[\pm45/0_3/\pm45/0]_s$ at 169.0 N/mm^2 applied stress. (b) Stacking sequence L: $[0/\pm45/0_2/\pm45/0]_s$ at 189.5 N/mm^2 applied stress. 137

7.6 V displacement field at centre of lap. (a) Stacking sequence K: $[\pm45/0_3/\pm45/0]_s$ at 169.0 N/mm^2 applied stress. (b) Stacking sequence L: $[0/\pm45/0_2/\pm45/0]_s$ at 189.5 N/mm^2 applied stress. 138

7.7 Geometry and finite element model of sixteen-ply adherend joint. Dimensions are given in millimetres (not to scale). 139

7.8 Finite element models without adhesive fillet—post fillet fracture analysis. The cracked (reduced stiffness) elements are shaded. (a) Stacking sequence K: $[\pm45/0_3/\pm45/0]_s$. The cracked elements simulate shear fracture of the $\pm45°$ layers next to the bondline at end of lap. (b) Stacking sequence L: $[0/\pm45/0_2/\pm45/0]_s$. The cracked element simulates tensile fracture of half the thickness of the $0°$ ply next to the bondline at end of lap. 140

7.9 Adherend longitudinal direct strain distribution along y-axis at fillet tip. (a) Stacking sequence K: $[\pm45/0_3/\pm45/0]_s$ at 169.0 N/mm^2 applied stress. (b) Stacking sequence L: $[0/\pm45/0_2/\pm45/0]_s$ at 189.5 N/mm^2 applied stress. 141

7.10 Adherend longitudinal direct stress distribution along y-axis at fillet tip. (a) Stacking sequence K: $[\pm45/0_3/\pm45/0]_s$ at 169.0 N/mm^2 applied stress. (b) Stacking sequence L: $[0/\pm45/0_2/\pm45/0]_s$ at 189.5 N/mm^2 applied stress. 142

7.11 Variation of adherend longitudinal direct strain with applied stress at the centre of the first ply next to fillet tip. (a) Stacking sequence K: $[\pm45/0_3/\pm45/0]_s$. (b) Stacking sequence L: $[0/\pm45/0_2/\pm45/0]_s$. 143

7.12 Contours of longitudinal direct strain ϵ_{xx} at end of lap. (a) Stacking sequence K: $[\pm45/0_3/\pm45/0]_s$ at 169.0 N/mm^2 applied stress. (b) Stacking sequence L: $[0/\pm45/0_2/\pm45/0]_s$ at 189.5 N/mm^2 applied stress. 144

7.13 Contours of transverse direct strain ϵ_{yy} at end of lap. (a) Stacking sequence K: $[\pm45/0_3/\pm45/0]_s$ at 169.0 N/mm^2 applied stress. (b) Stacking sequence L: $[0/\pm45/0_2/\pm45/0]_s$ at 189.5 N/mm^2 applied stress. 145

7.14 Contours of shear strain γ_{xy} at end of lap. (a) Stacking sequence K: $[\pm45/0_3/\pm45/0]_s$ at 169.0 N/mm^2 applied stress. (b) Stacking sequence L: $[0/\pm45/0_2/\pm45/0]_s$ at 189.5 N/mm^2 applied stress. 146

7.15 Contours of von Mises stress σ_M in fillet. Stacking sequence K: $[\pm45/0_3/\pm45/0]_s$ at 362.5 N/mm^2 applied stress. 147

7.16 Contours of longitudinal direct strain ϵ_{xx} at end of lap. Stacking sequence K: $[\pm45/0_3/\pm45/0]_s$ at 362.5 N/mm^2 applied stress. (a) Before fillet fracture. (b) After fillet fracture. (c) After shear fracture of $\pm45°$ plies. 147

7.17 Contours of transverse direct strain ϵ_{yy} at end of lap. Stacking sequence K: $[\pm45/0_3/\pm45/0]_s$ at 362.5 N/mm^2 applied stress. (a) Before fillet fracture. (b) After fillet fracture. (c) After shear fracture of $\pm45°$ plies. 149

7.18 Contours of shear strain γ_{xy} at end of lap. Stacking sequence K: $[\pm45/0_3/\pm45/0]_s$ at 362.5 N/mm^2 applied stress. (a) Before fillet fracture. (b) After fillet fracture. (c) After shear fracture of $\pm45°$ plies. 150

7.19 Contours of von Mises stress σ_M in fillet. Stacking sequence L: $[0/\pm45/0_2/\pm45/0]_s$ at 354.2 N/mm^2 applied stress. 152

7.20 Contours of longitudinal direct strain ϵ_{xx} at end of lap. Stacking sequence L: $[0/\pm 45/0_2/\pm 45/0]_s$ at 354.2 N/mm^2 applied stress. (a) Before fillet fracture. (b) After fillet fracture. (c) After tensile fracture of 0° ply..... 152

7.21 Contours of transverse direct strain ϵ_{yy} at end of lap. Stacking sequence L: $[0/\pm 45/0_2/\pm 45/0]_s$ at 354.2 N/mm^2 applied stress. (a) Before fillet fracture. (b) After fillet fracture. (c) After tensile fracture of 0° ply..... 154

7.22 Contours of shear strain γ_{xy} at end of lap. Stacking sequence L: $[0/\pm 45/0_2/\pm 45/0]_s$ at 354.2 N/mm^2 applied stress. (a) Before fillet fracture. (b) After fillet fracture. (c) After tensile fracture of 0° ply..... 155

7.23 Two-dimensional view of joint failure mode. (a) Stacking sequence K. (b) Stacking sequences L–N..... 157

7.24 SEM, taken from stacking sequence K: $[\pm 45/0_3/\pm 45/0]_s$, showing (refer to Fig. 7.23(a) for arrow direction): (a) View arrow A—two fracture modes of adhesive fillet: X–X' and X'–X''. (b) View arrow B—adhesive 'ductile' (flaky) failure. (c) View arrow C—two fillet cracks meeting along X'. (d) Fracture of −45° fibres along +45° line at ultimate failure..... 158

7.25 SEM, taken from stacking sequence L: $[0/\pm 45/0_2/\pm 45/0]_s$, showing (refer to Fig. 7.23(b) for arrow direction): (a) View arrow A—adhesive fillet brittle fracture. (b) View arrow A—fibre and associated adhesive (at the bondline level) brittle fracture. (c) View arrow A—fibre tensile fracture. (d) & (e)View arrow B—the step-like fracture of surface fibres. (f) View arrow C—intralaminar shear fracture of 0° surface ply..... 158

7.26 SEM, taken from stacking sequence M: $[0_2/\pm 45/0/\pm 45/0]_s$, showing (refer to Fig. 7.23(b) for arrow direction): (a) View arrow D—adhesive brittle fracture at the bondline level. (b) View arrow E—high concentration of toughening phase particles..... 159

Chapter 8

8.1 The bonded specimens with cross-ply adherends after fracture..... 166

8.2 Joint geometry and finite element model for the $[90/0]_{2s}$ lay-up. Dimensions are given in millimetres (not to scale). The cracked elements are shaded..... 167

8.3 Contours of von Mises stress σ_M in the fillet. Lay-up $[90/0]_{2s}$ at 237.8 N/mm^2 applied stress. (a) Before 90° ply crack. (b) After 90° ply crack..... 168

8.4 Contours of longitudinal directstrain ϵ_{xx} at end of lap. Lay-up $[90/0]_{2s}$ at 237.8 N/mm^2 applied stress. (a) Before 90° ply crack. (b) After 90° ply crack. 169

8.5 Contours of transverse direct strain ϵ_{yy} at end of lap. Lay-up $[90/0]_{2s}$ at 237.8 N/mm^2 applied stress. (a) Before 90° ply crack. (b) After 90° ply crack..... 170

8.6 Contours of shear strain γ_{xy} at end of lap. Lay-up $[90/0]_{2s}$ at 237.8 N/mm^2 applied stress. (a) Before 90° ply crack. (b) After 90° ply crack..... 171

8.7 Variation of longitudinal and transverse direct and shear stresses (σ_{xx}, σ_{yy} and τ_{xy} respectively) along the centreline of the 90° ply next to the bondline. Lay-up $[90/0]_{2s}$ at 237.8 N/mm^2 applied stress..... 172

8.8 Variation of longitudinal and transverse direct and shear stresses (σ_{xx}, σ_{yy} and τ_{xy} respectively) along the centreline of the outermost 0° ply. Lay-up $[90/0]_{2s}$ at 237.8 N/mm^2 applied stress..... 172

8.9 Variation of longitudinal and transverse direct and shear stresses (σ_{xx}, σ_{yy} and τ_{xy} respectively) along the centreline of the adhesive layer. Lay-up $[90/0]_{2s}$ at 237.8 N/mm^2 applied stress..... 173

8.10 Adherend longitudinal direct stress (σ_{xx}) distribution along the y-axis at the fillet tip. Lay-up $[90/0]_{2s}$ at 237.8 N/mm^2 applied stress..... 173

8.11 Two-dimensional view of joint failure mode for adherends with 90° surface ply... 174

8.12 Initiation and progression of failure at fillet tip..... 174

8.13 Three-dimensional view of the fractured surfaces of cross-ply adherends with 90° surface layer. Only the first two plies are shown. 175

8.14 SEM, taken from lay-up $[90/0]_{2s}$, showing (refer to Fig. 8.11 for arrow direction): (a) View arrow *A*—matrix tensile fracture. (b) View arrow *B*—fibre transverse tensile fracture. (c) View arrow *C*—shear cusps on 90° ply surface. Note the transverse cracking in 90° ply and impressions of 0° fibres. (d) View arrow *D*—shear cusps on 0° ply surface. (e) & (f) View arrow *E*—transverse microcracks in 90° ply of about one fibre diameter spacing. (g) & (h) View arrow *F*—shear cusps on 0° ply surface. (i) View arrow *G*—fractured adhesive fillet. (j) View arrow *H*—'brittle' fillet fracture. (k) View arrow *I*—fibre transverse tensile fracture. (l) View arrow *J*—adhesive layer 'brittle' fracture. 176

Chapter 9

9.1 The bonded specimens after fracture. 183

9.2 Contours of von Mises stress σ_M in the fillet. Unidirectional $[0_8]_s$ lay-up at 482.7 N/mm^2 applied stress. 184

9.3 Contours of longitudinal direct strain ϵ_{xx} at end of lap. Unidirectional $[0_8]_s$ lay-up at 482.7 N/mm^2 applied stress. 184

9.4 Contours of transverse direct strain ϵ_{yy} at end of lap. Unidirectional $[0_8]_s$ lay-up at 482.7 N/mm^2 applied stress. 185

9.5 Contours of shear strain γ_{xy} at end of lap. Unidirectional $[0_8]_s$ lay-up at 482.7 N/mm^2 applied stress. 185

9.6 Longitudinal direct stress (σ_{xx}) distribution along the centreline of the 0° ply next to the bondline. Unidirectional $[0_8]_s$ lay-up at 482.7 N/mm^2 applied stress. 186

9.7 Transverse direct and shear stress (σ_{yy} and τ_{xy} respectively) distributions along the centreline of the 0° ply next to the bondline. Unidirectional $[0_8]_s$ lay-up at 482.7 N/mm^2 applied stress. 186

9.8 Contours of von Mises stress σ_M in the fillet. Lay-up Q: $[\pm 45/90/0_2/\pm 45/0]_s$ at 282.8 N/mm^2 applied stress. 187

9.9 Contours of longitudinal direct strain ϵ_{xx} at end of lap. Lay-up Q: $[\pm 45/90/0_2/\pm 45/0]_s$ at 282.8 N/mm^2 applied stress 187

9.10 Contours of transverse direct strain ϵ_{yy} at end of lap. Lay-up Q: $[\pm 45/90/0_2/\pm 45/0]_s$ at 282.8 N/mm^2 applied stress 188

9.11 Contours of shear strain γ_{xy} at end of lap. Lay-up Q: $[\pm 45/90/0_2/\pm 45/0]_s$ at 282.8 N/mm^2 applied stress. 188

9.12 Longitudinal direct stress (σ_{xx}) distribution along the centreline of the +45° ply next to the bondline. Lay-up Q: $[\pm 45/90/0_2/\pm 45/0]_s$ at 282.8 N/mm^2 applied stress 189

9.13 Transverse direct and shear stress (σ_{yy} and τ_{xy} respectively) distributions along the centreline of the +45° ply next to the bondline. Lay-up Q: $[\pm 45/90/0_2/\pm 45/0]_s$ at 282.8 N/mm^2 applied stress. 189

9.14 Two-dimensional view of joint failure with lay-ups O: $[\pm 45/90/0/\pm 45/0]_s$ and Q: $[\pm 45/90/0_2/\pm 45/0]_s$ 190

9.15 Three-dimensional view of the fractured surfaces with lay-ups O: $[\pm 45/90/0/\pm 45/0]_s$ and Q: $[\pm 45/90/0_2/\pm 45/0]_s$. Only the first four plies are shown. For clarity, the adhesive fillet is not drawn. 191

9.16 SEM, taken from lay-up Q: $[\pm 45/90/0_2/\pm 45/0]_s$, showing (refer to Fig. 9.14 for arrow direction): (a) View arrow *A*—the fractured fillet. (b) View arrow *B*—'brittle' adhesive fracture. (c) View arrow *C*—'ductile' adhesive fracture. (d) View arrow *D*—resin cusps due to interlaminar shear on a −45° layer's surface. (e) View arrow *E*—a through-thickness view of a sheared −45° ply. (f) View arrow *E*—an enlarged view showing resin cusps and constituent debonding due to intralaminar shear. (g) View arrow *F*—matrix cracking as seen on the surface of

a 90° ply. (h) & (i) View arrow *G*—transverse cracking in a 90° ply. Note the constituent debonding and fibre transverse tensile failure. (j) View arrow *H*—fillet fracture. (k) View arrow *I*—fillet fracture. (l) View arrow *J*—resin shear cusps on 0° fibres 192

Appendix A

A.1 Longitudinal tensile stress-strain curve for XAS/914C 214
A.2 Transverse tensile stress-strain curve for XAS/914C 214
A.3 Longitudinal compression stress-strain curve for XAS/914C 215
A.4 Transverse compression stress-strain curve for XAS/914C 215
A.5 Shear stress-strain curve for XAS/914C 216
A.6 Longitudinal tensile stress-strain curve for $[(\pm 45)_4]_s$ XAS/914C laminate 216
A.7 Tensile stress-strain curve for Redux 308A [69] 217
A.8 Shear stress-strain curve for Redux 308A [70] 217

Appendix B

B.1 The specimens after tensile fracture (only the test section is shown) 221
B.2 Stress-strain curve for stacking sequence *A*: $[0/\pm 45]_s$ 222
B.3 Stress-strain curve for stacking sequence *B*: $[\pm 45/0]_s$ 222
B.4 Stress-strain curve for stacking sequence *D*: $[\pm 45/0_2]_s$ 223
B.5 Stress-strain curve for stacking sequence *F*: $[0_2/\pm 45]_s$ 223

Appendix C

C.1 Stress-strain curves for six-ply laminates in bending 228
C.2 Stress-strain curves for eight-ply laminates in bending 228

$\mathbf{A}$	In-plane stiffness matrix (N/mm)
$\mathbf{a}$	Displacement vector (mm)
$\mathbf{a}$	In-plane compliance matrix (mm/N)
$\mathbf{B}$	Coupled in-plane and flexural stiffness matrix (N)
$\mathbf{B}_0$	Linear strain shape function
$\mathbf{B}_L$	Large displacement strain shape function
$\bar{\mathbf{B}}^{\mathrm{T}}$	Transposed strain shape function
b	Width of laminate (mm)
c	Half length of overlap (mm)
C_v	Coefficient of variation (%)
$\mathbf{D}$	Flexural stiffness matrix (Nmm)
$\mathbf{D}$	Elasticity matrix (N/mm^2)
D	Flexural rigidity of adherend (Nmm)
$\mathbf{d}$	Flexural compliance matrix (1/Nmm)
E	Adhesive tensile elastic modulus (N/mm^2)
E_1	Longitudinal elastic modulus (N/mm^2)
E_2	Transverse elastic modulus (N/mm^2)
E_b	Effective bending (out-of-plane) elastic modulus of adherend (N/mm^2)
E_m	Effective membrane (in-plane) elastic modulus of adherend (N/mm^2)
$\mathbf{f}$	Force vector (N)
f	Frequency (lines/mm)
G	Adhesive shear modulus (N/mm^2)
G_{12}	In-plane shear modulus (N/mm^2)
I_p	Second moment of area (mm^4)
$\mathbf{K}_0$	Linear (or small displacement) stiffness matrix (N/mm)
$\mathbf{K}_L$	Large displacement (or initial displacement) stiffness matrix (N/mm)
$\mathbf{K}_T$	Tangential (or instantaneous) stiffness matrix (N/mm)
$\mathbf{K}_\sigma$	Geometric stiffness (or initial stress) matrix (N/mm)
k	Eccentricity factor
k_b	Non-dimensionalised bending stiffness parameter for composite adherends
l	Length of overlap (mm)
$\mathbf{M}$	Column matrix of bending moment intensities acting in the xz- and yz-planes and twisting moment intensity acting about x- and y-axes respectively (Nmm)
m	Coefficient of mutual bend-twist coupling
$\mathbf{N}$	Column matrix of direct load intensities and shear load intensity referred to (x, y) coordinates (N)
N_x	Fringe order in the x-direction
N_y	Fringe order in the y-direction

n	Number of plies in a laminate
P	Load (N)
$\mathbf{Q}$	Stiffness matrix (N/mm)
$\bar{\mathbf{Q}}_p$	Transformed reduced stiffness matrix (N/mm)
S_{ij}	Material compliance terms (mm/N)
$\mathbf{T}$	Transformation matrix
t	Thickness of laminate (mm)
t_p	Thickness of pth ply (mm)
U	Longitudinal in-plane displacement (mm)
V	Transverse in-plane displacement (mm)
w	Width of specimen (mm)
z_p	Distance between laminate's reference plane and mid-plane of pth ply (mm)
γ_{xy}	Shear strain (%)
δ	Deflection (mm)
$\boldsymbol{\epsilon}$	Column matrix of mid-plane direct strains and shear strain referred to (x, y) coordinates
ϵ	Strain vector
$\boldsymbol{\epsilon}_0$	Linear strain vector
ϵ_b	Bending strain (%)
ϵ_{xx}	Longitudinal direct strain (%)
ϵ_{yy}	Transverse direct strain (%)
η	Thickness of adhesive layer (mm)
θ	Angle between the reference and material axes systems (°)
$\boldsymbol{\kappa}$	Column matrix of curvature components (mm^{-1})
ν	Adhesive Poisson's ratio
ν_{12}	Major Poisson's ratio
ν_{21}	Minor Poisson's ratio
ν_b	Bending Poisson's ratio
ν_m	Membrane Poisson's ratio
$\boldsymbol{\sigma}$	Stress vector (N/mm^2)
$\boldsymbol{\sigma}_0$	Linear stress vector (N/mm^2)
σ_1	Maximum direct stress (N/mm^2)
σ_2	Minimum direct stress (N/mm^2)
σ_{av}	Adherend average stress (N/mm^2)
σ_b	Adherend bending stress (N/mm^2)
σ_M	von Mises stress (N/mm^2)
σ_{max}	Adherend maximum stress (N/mm^2)
σ_p	Adhesive peel stress (N/mm^2)
σ_{xx}	Longitudinal direct stress (N/mm^2)
σ_Y	Adhesive uniaxial tensile yield stress (N/mm^2)
σ_{yy}	Transverse direct stress (N/mm^2)
τ_{xy}	Shear stress (N/mm^2)
$\Psi(\text{a})$	Nonlinear discrete equation operator

Subscripts

$1, 2, 3$	Material axes system
i, j	Integers signifying position in row and column respectively of an element in a matrix

p	Ply identification number
x, y, z	Reference axes system

ABBREVIATIONS

AJR	Actual joint rank
ASTM	American Society for Testing and Materials
CFRP	Carbon fibre-reinforced plastic
CR	Contractor report
CRAG	Composites Research Advisory Group
GRP	Glass-reinforced plastic
HSA	Hart-Smith's analysis
JRF	Joint ranking factor
LFEA	Linear finite element analysis
NASA	National Aeronautics and Space Administration
NLFEA	Nonlinear finite element analysis
OUP	Oxford University Press
PJR	Predicted joint rank
PTFE	Poly-Tetra-Fluoro-Ethylene
RAE	Royal Aerospace Establishment
RH	Relative humidity
SEM	Scanning electron micrograph
STP	Special technical publication
TM	Technical memorandum
TN	Technical note
TR	Technical report
UPS	Ultraviolet photoelectron spectroscopy
XPS	X-ray photoelectron spectroscopy

Chapter 1

INTRODUCTION

Fibres of various types are stronger along their lengths than the same material in bulk form. This is due to the small cross-sectional dimensions of the fibres, thus minimising the inherent presence of molecular imperfections, flaws and dislocations. The most common man-made fibres used for engineering applications are glass, carbon, Kevlar and boron. The reinforcing fibre in fibrous composites should desirably have the following properties: (a) high modulus of elasticity to give efficient reinforcement, (b) high ultimate strength, (c) low variation of strength between individual fibres, (d) stability and retention of strength during handling and fabrication and (e) uniform fibre geometry.

Unless bound together to form a structural element capable of withstanding loads, fibres by themselves are useless in engineering applications. The binding material is called the matrix. The matrix is required to: (a) bind the fibres together, (b) transfer the loads to the fibres, (c) stop, to some extent, a crack from propagating straight through a mass of fibres, (d) protect the fibres surfaces from damage during handling and in service and (e) be chemically and thermally compatible with the fibres. The most widely used matrices for fibrous composites are the organic 'super polymer' materials, commonly called plastics. Hence the term fibre-reinforced plastics (FRP).

Laminated fibrous composites involve fibrous composites and lamination techniques. Layers of fibre-reinforced material are built up with the fibre direction in each layer oriented in different directions to give the desired different stiffness and strength.

Due to their high specific stiffness and strength, fibre-reinforced plastics are ideal for aircraft and spacecraft structures. However, the successful use of these materials relies significantly upon adhesive bonding for joining structural components.

Adhesive bonding is the preferred and natural method of joining organic composite structures. The adhesive itself is often chemically similar to the resin matrix surrounding the fibres. Many advantages are gained by using adhesive bonding including weight savings, avoiding cut fibres, as obtained with mechanical fastening, and damping and sealing properties. However, the durability of adhesive joints and the relatively low tensile strength of adhesives are two main areas of concern.

Analytical and numerical methods can be of a limited use in the analysis of composite joints. This is mainly due to the layered nature of composites. Although many workers have attempted the analysis of adhesive joints, a detailed account of the mechanisms of failure in composite adhesive joints appears not to exist.

The design of single lap joints is based on specifying a suitable l/t ratio (where l is the overlap length and t is the adherend thickness) to resist a given load. This l/t ratio is selected to minimise the damaging effects of bending. However, with the use of fibre-reinforced plastics, the bending stiffness for a given lay-up may be changed independently of the in-plane stiffness by changing the stacking sequence of the plies. It may therefore be possible to decrease the optimum l/t ratio for a given lay-up by selecting a suitable stacking sequence, with the associated benefits of reduced weight penalty for a given joint.

In aerospace structures there is a preference to place $\pm 45°$ plies on the surface of the laminate as this is better for fatigue and impact performance. Hence, a study of the performance of joints with both $\pm 45°$ and $0°$ surface plies is required. The aim of the present project is to produce a basic understanding of the effect of stacking sequence on the mechanisms of failure and strength of bonded CFRP joints.

Chapter 2

LITERATURE SURVEY

2.1 INTRODUCTION

"The use of adhesive bonding in aircraft structures dates back to the dawn of aviation history. Wooden structures contained glued scarf joints in the primary members, wing spars were often constructed from laminated strips of wood to improve the mechanical properties, and plywood skins and shear webs contained considerable glue in themselves and transferred their loads to the primary structural members entirely through bonded joints. In the infancy of the development of airframes, mechanical fasteners were used only at areas of relatively high load intensity (for which the glued joints were not considered strong enough) and to provide manufacturing breaks to facilitate storage and repair. One is tempted to suggest that our grandfathers' understanding of the respective uses of adhesive bonding and mechanical fastening in aircraft structures seems to have been lost with the passage of time" [1].

Joining metallic structures is a well developed technology involving riveting, bolting, welding, glueing, brazing, soldering and combinations thereof. However, for thermosetting polymer matrix fibre-reinforced composites only adhesive bonding and mechanical fasteners (bolts and rivets) can be utilised. Inherently, adhesive bonding is preferred because of the continuous connection, whereas in drilling the holes for the bolts or rivets, fibres are cut, the joining is at discrete points, and large stress concentrations occur around each hole drilled [2]. Typical examples of adhesively bonded joints and their relative uses are given in Fig. 2.1.

Sneddon [3] published a literature survey on theoretical and experimental investigations into the distribution of stress in adhesive joints in 1961. In 1973,

Mitra [4] reviewed analytical approaches to the determination of stress distribution in bonded joints with particular emphasis devoted to those containing carbon fibre-reinforced plastic adherends. In 1982, Matthews *et al.* [5] published a review of the strength of joints in fibre-reinforced plastics. They subdivided theoretical work into classical and finite element methods (linear and nonlinear analyses). General principles and design guidelines are also presented. A more recent publication by Adams and Wake [6] coverd several aspects of structural adhesive joints.

The present review provides a history and background to the current state-of-the-art in adhesively bonded joints. It is not all inclusive, but provides a basis for the current study.

2.2 ADVANTAGES AND DISADVANTAGES OF ADHESIVE BONDING

The following benefits and limitations of adhesive bonding are quoted from Shields [7]. Depending on the adhesives used, joint design, methods of application, and the intended function of the final assembly, adhesive bonding can offer one or more of the following advantages:

1. The ability to join a variety of materials, which may differ in composition, coefficients of expansion, elastic moduli, and thickness (thin sheets and foils may be joined where other fastening methods would cause distortion or destruction).
2. The elimination of irregular surface contours caused by protruding fasteners such as screws and rivets, with a consequent improvement in the appearance of the finished assembly.
3. The fabrication of complex shapes where other means of fastening are not practicable.
4. The more uniform distribution of stress over the entire bonded area with minimization of stress concentrations, such as those that occur with small contact areas associated with bolts, rivets or spot welds—often thinner materials can be used without loss of strength thus saving weight and cost; for example, the bonding of honeycomb core to thin metal skins.

5. The high damping capacity of adhesive bonds and the elongation properties of many adhesives which allow stresses to be absorbed, distributed, or transferred, thus improving fatigue resistance and giving good vibration damping and flexibility properties.
6. Weight reduction and, since no holes are required for mechanical fasteners, the maintenance of the integrity of structural members.
7. The ability to join heat-sensitive materials prone to destruction by brazing or welding (surface blemishes resulting from the pressure and heat of spot-welding are also avoided thus reducing finishing requirements).
8. Good sealing and insulation properties since bonded joints are sealed against moisture and chemicals; adhesive layers can act as insulators against electricity, heat, or sound, and also reduce or prevent galvanic corrosion between dissimilar materials.
9. The realisation of important cost savings in manufacturing and assembly by reduced material requirements, weight savings, elimination of other operations (such as drilling, screw or nut driving, and finishing), simplified assembly procedures, the replacement of several mechanical fasteners with a single bond, and the joining of several components at the same time.

Adhesive bonding has its limitations also; although current developments in the technology promise to minimise many of these. Among the disadvantages of bonding which have proved restrictive are: (a) the dependence of joint durability on processing conditions, (b) the need for special joint design to avoid cleavage failure and (c) the limited resistance of adhesives to extreme service conditions, especially heat. Thermosetting polyimides and modified epoxies are capable of long term service at 250°C, above which material degradation ensues. Inorganic materials, such as silicates, will function as adhesives up to 1500°C but are brittle, prone to thermal and mechanical shock, and have limited adhesion to metals. The following are a number of additional limitations on the use of adhesives for particular applications:

1. Residual stresses in bonded joints can present problems; these stresses arise where high curing temperatures are involved and are a consequence of the different thermal expansion of the adhesive and the component surfaces.

2. Optimum bond strength is usually not realised instantaneously as it is with welding or mechanical fastening.
3. Many thermosetting adhesives have low peel strength and thermoplastic adhesives tend to creep under sustained loading.
4. The permanence of adhesive bonds in severe environments is frequently unknown: heat, cold, chemical agents, radiation, and bio-deterioration can cause degradation of the adhesive, while incompatible adherend materials may well constitute a corrosion hazard.
5. Inflammability and toxicity are features of many solvent-based adhesives and these add to the assembly hazards.
6. Bonded structures are not easily dismantled for repair or salvage.
7. Rigorous process control with sample joint testing is often needed to maintain reliable joints of uniform quality in production processes; non-destructive testing methods for the assessment of bond quality are not yet entirely satisfactory.

In addition to these disadvantages the bonding process brings with it a number of complicated requirements, which may include: (a) special stages for the preparation of components prior to joining and for adhesive application and (b) the provision of special environmental conditions, often including prolonged periods of curing under maintained heat and pressure. The requirement for special bonding jigs and equipment can also prove a severe financial disincentive, sometimes completley negating any cost savings. Nonetheless, in spite of the difficulties inherent in its use, the financial benefits of adhesive bonding have been realised in many types of production assembly.

2.3 THEORETICAL ANALYSIS

The simplest type of joint is the lap joint in which two sheets overlap and are fixed together by a layer of adhesive between them. Loading in the plane of the sheets produces varying shearing and tearing stresses in the adhesive as well as on the bonded faces and in the material of the sheets. The joint may fail either in the adhesive, or on an interface, or even in the joined members according to the

highest stresses developing in each of these parts and to the strength of adhesive, adhesion and adherends.

The stress distribution is not uniform along a lap joint (see Fig. 2.2) and the peak stress may be several times higher than the mean stress. The mean stress is the load divided by the bonded area. The peak stress, and its ratio to the mean stress (stress concentration), are dependent on the geometrical proportions and the elastic constants of the materials of the joint. The reasons for stress concentration at ends of overlap, as given by de Bruyne and Houwink [8], are:

a) *Differential straining of adherends.* In order to explain differential straining of joined members, a comparison is made between a joint with infinitely stiff non-deformable members and one with extensible members—see Fig. 2.3. It is assumed that there is no bending of the adherends. The adhesive layer thickness is exaggerated for demonstration purposes. The non-deformable adherends (Fig. 2.3(b)) will move as solid blocks and the adhesive will be subjected to shear strain and deform so as to accommodate the displacement e of the adherends, which will be the same throughout the joint. Each adherend is subjected to the full load P just before the joint and transmits it gradually to the other adherend through the adhesive. Thus the stress of adherend I will be highest at A and gradually diminishes towards B where it will be zero. On the contrary, the stress of adherend II will be highest at B and diminishes to zero at A. This variation of stress is unimportant as long as adherends I and II behave as if completely rigid. If the adherends are extensible (Fig. 2.3(c)), and obey the laws of elasticity, they will develop strains proportional to the existing stresses. e_2 is considerably larger than e_1, resulting in higher stress in the adhesive at each end of the overlap.

b) *Bending of adherends due to eccentricity of loading.* The adherends of a single lap joint are offset and the line of pull joining the points of application of the loads P will be oblique and passes through the midpoint of the joint—see Fig. 2.4. Just before the begining of the overlap, the line of pull will be along the inner face of each member, provided of course that the length of each member beyond the joint is considerably longer than the overlap. The eccentric loading of each member will give rise to a bending moment

$M = P \times s/2$ which will tend to pull the adherends apart. Under this moment the adherends, if long enough, bend and the joint distorts. The deformation reduces the tearing stresses because, when thus deformed, the line of pull is nearer to the central axis of each adherend and therefore the bending moment is reduced. The stresses developing in this way are tensile and normal to the interface, and are called *tearing* or *peeling* stresses. These stresses are confined to the areas adjoining the ends of the overlap and may considerably reduce the strength of a lap joint.

The single lap joint is a statically indeterminate structure. It is not possible to analyse thoroughly the structure based on the equations of static equilibrium alone. It is necessary to use the requirements of static equilibrium as well as the requirements of geometry or continuity. It is possible to solve statically indeterminate structures using methods from classical structural mechanics or numerical methods.

Early methods of analysis include those of Volkersen [9], Goland and Reissner [10] and de Bruyne [11]. Volkersen's analysis (known as 'shear lag') is concerned only with the stresses arising from the differential straining in lap joints and does not examine the tearing stresses resulting from the bending of the adherends. The bonded members are assumed to be in pure tension and shear stresses are examined in the adhesive layer only, the maximum being found at each end of the overlap. The adhesive layer is assumed of uniform thickness and its ends are plane and normal to the direction of application of load. The shear stress does not reduce to zero at the adhesive layer free ends.

Goland and Reissner presented an analysis of the shear and normal stress distributions throughout the adhesive of a single lap joint. All materials were assumed to behave elastically. The stress distribution across the adhesive film was assumed to be constant and the adhesive was assumed to be subjected to a condition of plane strain in the plane of the joint. The stress distribution was determined in the adherends just outside the bonded area. This provided a description of the loads being applied to the edge of the joint. The stress distribution was obtained using the theory of small bending for thin cylindrically-bent plates. The two special conditions applied to the bonded area are: (a) the adhesive layer

was assumed to be infinitely thin and relatively inflexible so it could be considered as having no effect on the stress distribution in the adjoining adherends or (b) the adhesive was assumed to have an effect on the bonded members.

In the second case the adherends are treated like cylindrically-bent plates separated by a system of infinitesimal elastic coil-springs. This analysis lead to a differential equation similar to that for the deflection of a beam on an elastic foundation. The importance of this paper lies in its approach to the problem of bending in the single lap joint and the evaluation of the high normal stresses which lead to the peeling type of failure. The major objection to the analysis is the assumption that the adhesive behaves elastically. If this is not a valid assumption for the adhesive the stress distribution will change very rapidly as the material creeps or behaves inelastically.

In his paper de Bruyne introduced the concept of expressing the lap shear strength of adhesives as a function of the square root of adherend thickness-to-length of overlap ratio. The rationale was to find a simple relationship between the strength of a lap joint and its geometry. The value of this technique was shown by presenting the lap shear strength of Redux-bonded steel, clad aluminium alloy and aluminium metal joints, for various combinations of adherend thickness and length of overlap. With this method all of the joint strengths were expressed on a single graph, with all the points on a single curve.

Cornell [12] presented a variation and extension of Goland and Reissner's method [10] for determining the stresses in bonded lap joints by assuming that the two lap joint plates act like simple beams and the more elastic adhesive layer is an infinite number of shear and tension springs. Differential equations were set up which described the transfer of the load in one beam through the springs to the other beam. From the solution of these differential equations a fairly complete analysis of the stresses in the lap joint was obtained. The spring-beam analogy method was applied to a particular type of lap joint and an analysis of the stresses at the discontinuity, stress distributions and the effects of variables on these stresses were presented.

Commencing 1970, a number of publications dealt with the study of single lap joints using experimental, analytical and computational methods. Cherry and

Harrison [13] proposed that by tapering the ends of the adherends it is possible to manufacture a lap joint for which the shear stress in the adhesive layer is uniform throughout the joint, i.e. there are no shear stress concentrations in the adhesive and the maximum load carrying capacity of the adhesive is developed. Wooley and Carver [14] presented stress concentrations as functions of dimensionless, geometric and material parameters. For a given applied stress σ, the maximum shearing stress concentration τ_{max}/σ and tearing stress concentration σ_{max}/σ are plotted as functions of l/t and η/t for different values of E/E_a, where l is the lap length, η is the adhesive thickness, t is the adherend thickness and E and E_a are the moduli of elasticity for the adherend and adhesive respectively. The authors suggested the use of those curves for the design of bonded joints.

The work of Hart-Smith [15] on single lap joints in 1973 is notable. He analysed the influence of a variety of factors on the strength of adhesively bonded single lap joints. The classical approach of Goland and Reissner is improved and extended. The following factors are included in the analysis: (a) adhesive plasticity, (b) stiffness imbalance between the adherends and (c) the influence of laminated composite adherends.

The failure of single lap bonded joints with brittle and yielding adherends are depicted in Fig. 2.5. Hart-Smith predicted three distinct and characteristic failure modes. The first is that of failure of the adherend just outside the joint due to the in-plane stresses resulting from the combination of direct load stresses and bending stresses caused by the eccentricity in the load path. The second mode is the failure of the adhesive layer in shear. While prior elastic studies have concentrated on this mode and much single lap joint design practice is so oriented, the inclusion of adhesive plasticity in the analysis has demonstrated that this potential failure mode is extremely rare in structural practice.

The third failure mode may be manifested in either of two forms and is associated with the adhesive peel stresses. With adherends which are too thick to yield in bending under the eccentric load path, the observed failure in the third mode is that of the adhesive peel stress. With laminated composite adherends, on the other hand, the interlaminar tensile strength is so much less than the peel strength of good structural adhesives that the failure occurs within the continuous laminate at the end(s) of the joint.

From the present author's experience, this last statement is not universally applicable. The through-thickness tensile strength of composite adherends is of comparable value to the tensile strength of structural adhesives. It is the ultimate through-thickness tensile strain of composite adherends which is much less than the ultimate tensile strain of structural adhesives. Further, the statement implies a peel type of failure initiation at the end of the overlap. This contradicts observations with composite single lap joints where an in-plane type of fracture can occur first.

Adherend thermal mismatch is discussed only qualitatively but the effects of adherend stiffness imbalance on the joint strength are characterised quantitatively by Hart-Smith. In his iterative solution of the mathematical equations, account is taken of the significant bending moment relief associated with structural (elastic) deformations under load. The standard half-inch lap shear test is criticised because the failure observed is only infrequently associated with failure of the adhesive in shear.

Barker and Hatt [16] used a two-dimensional linear elastic finite element analysis to evaluate the behaviour of an adhesive joint bonding an advanced composite to a metallic substrate. The analysis of a single lap joint and smoothly tapered joint for different adhesive thicknesses and materials is presented. A special feature of this analysis is the modeling of the adhesive layer with a joint element which behaves as a combined shear and tension spring whose stiffness properties vary with thickness.

Adams and Peppiatt [17] found that Poisson's ratio strains in the adherends of a simple adhesive lap joint induce transverse (across the width) stresses both in the adhesive and in the adherends. Two simultaneous second-order partial differential equations were set up to describe the normal stresses along and across an adherend, and were solved both by an approximate analytical method and a finite difference technique. The two solutions agreed closely. They stated that the transverse adhesive shear stress has a maximum value for joints between metals of about one-third the maximum longitudinal shear stress, and this occurs at the corners of the lap, thus making the corners the most highly stressed parts of the adhesive.

Also Adams and Peppiatt [18] investigated analytically, by the finite element method, joints with either square edges or spew fillets and compared the results with the theoretical solutions of previous authors. The effect of the spew fillet is shown physically by a silicone rubber model. The finite element analysis has shown that if the metallic adherend is assumed to have a small chamfer on its corner due to the etching process, good agreement between the experimental strength ratios and the predicted maximum stress ratios of single and double lap joints is obtained.

In 1974 Hart-Smith [19] analysed single lap, double lap, scarf and stepped lap joints. His analysis of single lap joints was based on earlier work [15]. He concluded that for thin adherends, the bond shear strength is usually so far in excess of the adherend strength that joint design is easily accomplished. For somewhat thicker sections, the adherend strength increases more rapidly than the bond shear strength, indicating that lap joint efficiency may be limited. For still thicker sections, particularly with fibre composites, peel stress failures dominate and stress concentration relief techniques are needed to make lap joints effective. For still thicker sections yet, scarf or stepped lap joints are needed.

Chang and Muki [20] modelled the adherends by two parallel, infinite strips of equal constant thickness, bonded along a common finite line. The bond is assumed to be infinitesimally thin and the bondline tractions and displacements are taken to be continuous from one adherend to the other. The two-dimensional stress and displacement fields are determined within the scope of the linear elasticity theory of plane strain in this model of an adhesive lap joint, which is subjected to tension-shear type loading. The analysis allowed the prediction of joint strength after cracks have initiated at the lap ends.

In 1975 Oplinger [21] stated that, for organic matrix composites with relatively low transverse moduli, the use of the more sophisticated closed-form analyses allowing for thickness normal and out-of-plane shear deformations is generally advisable. He suggested that investigations which allow for nonlinear response in adhesive joints should be extended to give greater attention to adherend nonlinearity which is likely to be as important in organic matrix adherends as in typical adhesives. Applying fracture mechanics to composite adherend joints is recommended. Such work is needed to provide a clearer picture of factors controlling

joint damage tolerance. Fracture mechanics studies of composite joints should allow for the possibility of predicting failures in plies adjacent to the adhesive as well as in the adhesive itself.

A number of papers have been published by Renton and Vinson commencing in 1975 [22–25]. They undertook analytical and experimental programmes of study concentrating on those parameters considered to be the most influential on the static and fatigue life of an adhesive single lap joint. The selected parameters for study were: overlap length, adhesive thickness, orientation of the laminae of the laminated adherends (particularly the plies immediately adjacent to the adhesive), and the effect on the fatigue life of whether or not the mean value of the fatigue load causes maximum stresses above or below the shear proportional limit of the adhesive material. Their static tests conclusions were: (a) the strongest bonded joint is one of large overlap (0.6 inches was the maximum overlap tested!), with all 0° adherends of equal extensional stiffness, (b) the ultimate joint static strength increases with increased lap length, until the adherends become critical and (c) adhesive thickness had a minimal influence on the joint strength.

Dootson and Grant [26] compared theoretical (simple shear lag analysis (e.g. [9]) and generalised Goland and Reissner analysis [10] for joints with adhesives having either linear or nonlinear elastic behaviour) and experimental results on composite/metallic bonded joints. From the theoretical results, it is concluded that a large degree of nonlinearity is a desirable feature of adhesive behaviour to alleviate stress concentrations in the adhesive layer. From the experimental results, it is found that many modes of failure can occur and further work is required before an overall joint failure criterion can be fully defined.

Srinivas [27] analysed single lap, flush and double lap joints using a refined elastic theory which accounts for transverse shear deformation and transverse normal stress—which have been neglected by previous workers. His numerical investigations showed that the maximum peel and shear stresses in the bond can be reduced by: (a) using a combination of flexible and stiff bonds, (b) using stiffer plates and (c) tapering the plates.

Allman [28] published his theory for elastic stresses in adhesive bonded lap joints in 1976. He produced an analysis where the adherends have been modelled

to account for bending, shear and normal stresses. He has set the adhesive shear stress to zero at the overlap ends and allowed a linear variation of the peel stress across the adhesive thickness. His adhesive shear stress is constant throughout the thickness. The approach provides a unified treatment for a wide range of material elastic properties and ensures exact satisfaction of all conditions of stress equilibrium in the joint, including the stress free surface condition at the ends of the adhesive layer.

Thamm [29] studied the stress distribution in lap joints with partially thinned (i.e. tapered) adherends. He concluded that sharpening of the adherends of overlapped adhesive joints yields a substantial increase in strength only when the sharpening is complete; that is the adherends are sharpened as far as possible to a knife edge. Partial sharpening to about half the original thickness is practically valueless from the strength viewpoint.

Bond thickness effects upon stresses in single lap adhesive joints have been investigated analytically by Ojalvo and Eidinoff [30]. Their conclusion are: (a) the variation of shear stress through the bond thickness may be significant, (b) the main difference in stresses obtained between theories which include and those which neglect bond thickness occur at the edges of the joint where the stresses are highest, (c) the shear and peel stress distributions may vary significantly between theories which include and those which ignore the effect of bond thickness, (d) the inclusion of bond thickness effects increases the predicted maximum shear stresses and reduces the predicted peel stresses and (e) the effect of bond thickness is more pronounced when joints with short overlaps, thick adherends and stiff adhesives are analysed.

Cooper and Sawyer [31] showed, using finite element (linear and nonlinear), Goland and Reissner and photoelastic analyses, that for a single lap joint the influence of the geometric nonlinear behaviour of the joint has a sizeable influence on the stresses in the adhesive. The results indicated that the Goland-Reissner solution is sufficiently accurate to be used in qualitative prediction of the effect of parametric variables on the shear and peel stresses along the centre of the adhesive bondline. The adhesive stress distribution obtained with a finite element analysis showed that the assumption of constant shear and peel stress through the adhesive

thickness used in the Goland-Reissner solution is valid over the interior of the lap region but deteriorates in the vicinity of the free edge reentrant corner where a two-dimensional elastic analysis predicts singular stresses. The stress distribution in the ASTM D1002-72 lap joint configuration showed that this test specimen is inadequate for determining the shear strength of adhesives even in a qualitative sense.

Interfacial stresses and strength of lap joints have been analysed by Chan and Sun [32] using a high order finite element (linear elasticity and small deflection theory). They claimed that beyond a certain point the increase in the overlap length can only move farther apart the zones of the peel stress without altering the size and magnitude. From the present author's experience, this is a direct consequence of not allowing for geometric nonlinearity. Their results indicate that the magnitude of the shear stress in the middle portion of the overlap decreases as the overlap length increases and would vanish entirely if the overlap length is sufficiently large. Also, the peel stress zone tends to become narrow and the peak stresses become higher as the value of the adhesive-to-adherend thickness ratio decreases.

Pickett and Hollaway [33] analysed single, double and tubular lap joints using classical and finite element theories to predict elastic adhesive stresses. The generality for dissimilar adherends is included in the analyses. The governing differential equations obtained when using the classical approach necessitated a numerical solution and a procedure which uses the finite difference method is described. The various classical and finite element solutions have shown a reasonable agreement for case studies representing the jointing configurations under investigation.

The present author in an earlier study [34] used two laminated composite plate elements of opposite ply stacking sequence to resemble the effect of a bonded single lap joint. The plane in which the tensile load is applied does not correspond to the mid-plane of the laminated plates used. The objective was to simplify the modelling of such joints. In 1988, Roy and Reddy [35] published their work on finite element analysis of adhesively bonded composite joints with moisture diffusion and delayed failure. They emphasised the importance of modelling the adhesive in a bonded joint as a viscoelastic material. Also, at high stress levels, nonlinear viscoelastic effects can produce creep strains that are significantly larger than the linear viscoelastic predictions and such effects, therefore, should be accounted for.

2.4 EXPERIMENTAL ANALYSIS

Most studies have been conducted on large models of a joint; then using the principle of similarity, it is assumed that the results obtained in the model will also be true in an actual joint. Cornell [12] used brittle lacquer and photoelastic stress analysis techniques to determine experimentally the stress distribution in a lap-type joint consisting of a thin tab strip brazed to a thicker base bar. The brittle lacquer technique was used to determine the effects of adherend thickness, braze thickness and braze modulus on the maximum principal stress in the base bar. The specimens investigated were two to four times their normal size. The photoelastic study was carried out on a composite model consisting of two different plastics with a modulus of elasticity ratio of 2 to 1. The models were four times the normal size. It was generally found that the brittle lacquer and photoelastic studies agreed with the results obtained analytically.

In 1954, Mylonas [36] carried out photoelastic analysis on lap and butt joints. Models were made using a mixture of resins, cast between 0.5 inch-square Bakelite bars reinforced with stainless steel studdings. The shape of the adhesive layer edge was controlled by either machine shaping it or using soluble salt forms that could be dissolved away from the model after the resin had cured. The adhesive in the model was a block of resin 0.5 by 0.5 inch square and of varying lengths. Mylonas points out that this square adhesive gives rise to a complex three-dimentional stress distribution in the model, while in an actual joint it is one of plane strain.

The purpose of the investigation was to study the effect of the adhesive layer edge on the stress distribution at the end of the joint. Tests were conducted first to determine whether the length of the overlap had any effect on the stress distribution. It was concluded that as long as the ratio of the overlap length to thickness of the adhesive layer was larger than 3, the length of the overlap had no effect. This is in sharp contrast to what is generally accepted for actual joints.

It was found that for curved adhesive layer edges the stress varied from tension to compression along the edge with an isotropic point in the centre. The radius of the adhesive layer edge was varied. It was concluded that for small radii the joint was most likely to fail cohesively in the adhesive and for large radii the joint would fail along the adherend-adhesive interface.

For models with straight adhesive layer edges it was found that the maximum stress concentration in the adhesive was greatest for a 90° angle of inclination between the adhesive layer edge and the adherend and that the stress concentration decreased as the angle decreased.

Mylonas has shown that the geometry of the adhesive layer edge has a strong effect on the stress distribution in the joint. The only questions concerning the study are whether these large 0.5 inch-square blocks of resin behave the same as a much thinner adhesive film and whether these models are similar to an adhesive joint.

Demarkles [37] investigated the stress distribution in models of riveted and bonded lap-type joints made from foam rubber. The deformations in the models were exaggerated due to the low modulus of the rubber material and it was possible to determine the deformations experimentally. Models of bonded joints were made by bonding together two sheets of foam rubber using a latex adhesive. The adhesive used had the same mechanical properties as the foam rubber. The model then was analogous to a joint in which the adhesive and adherends had the same properties and the adhesive was infinitely thin. The same model could probably have been obtained by simply cutting the entire joint from a single piece of foam rubber.

Deformation measurements were made on the joint by photographing the displacements of a reference grid painted on the specimen using black shellac. Shear stress and normal stress distributions were determined from the deformations. These distribution curves are actually the stress distribution in the adherends, and not in the adhesive. In these models there is essentially no adhesive present and the models do not really simulate a lap joint, but rather an offset in a solid piece of material.

An attempt was also made to determine the stress distribution in an actual joint by placing a photogrid with a 0.254 mm spacing on a Redux-bonded magnesium lap joint. The photogrid was applied in the area of the ends of the overlap. The joints were loaded to failure. The deformations in the joint were too small to be indicated by any change in the photogrid.

An analysis of a lap joint was presented that was similar to Volkersen's analysis of a supported lap joint without bending. A comparison was made of the shear stress distribution along the lap predicted by the analysis and that obtained from the rubber models. The theoretical analysis predicted higher stresses than the models.

Adams *et al.* [38] constructed models of adhesive joints in which hard rubber has been used as the adherends and relatively soft foam rubber as the adhesive. Various types of lap joint have been studied and the model results compared with theory. In general, the correlation between model and theory was very close. Two types of joint configuration that remove the stress concentration from the ends of the lap by profiling the adhesive layer have been shown. The stress distribution for a scarf joint has also been presented. The existence of strains across a lap joint due to Poisson's ratio has been demonstrated. Adams and Peppiatt [18] demonstrated physically the effect of adhesive spew fillet by a silicon rubber model. It was shown that the highest stresses exist at the the adherend corner within the spew.

Tuttle *et al.* [39] presented a technique which allowed the measurement of the in-plane longitudinal direct strains within an adhesively bonded joint. Single lap joints were fabricated using titanium Ti-6-4 adherends and FM-300 structural adhesive. Specimens were fabricated both with and without embedded strain gauges (in the adhesive layer). Each specimen was subjected to a tensile test to failure at room temperature. The embedded strain gauges did not affect ultimate strengths, although ultimate strains may have been. Repeatable longitudinal direct strains were measured within the joint at stress levels up to 90% of the ultimate strength. The results compared well with a finite element analysis of the single lap joint.

Post *et al.* [40] measured displacement fields in a thick adherend lap joint by high sensitivity moiré interferometry. Contour maps of in-plane U (longitudinal) and V (through-thickness) displacements were obtained across adhesive and adherend surfaces. Loads ranged from a modest load to a near-failure load. Quantitative results were given for displacements and strains in the adhesive and along the adhesive/adherend boundary lines. The results showed nearly constant shear strain in the adhesive, nonlinear strains as a function of load or average shear stress, and viscoelastic or time-dependent response. Longitudinal direct strains in

the adhesive were nearly two orders of magnitude less than the shear strains. They concluded that, with its subwavelength displacement resolution and high spatial resolution, moiré interferometry is especially well suited for deformation studies of adhesive joints.

2.5 SURFACE PREPARATION

Fibre-reinforced plastics have low surface energies [41]. An energetic surface will make a liquid spread on it, while a surface of low energy will let it remain as a discrete drop. Sufficient surface energy is needed in order to cause spreading of an adhesive and thus intimate molecular contact between it and the substrate. Poor wetting may be due to contamination, which can be removed by a suitable surface treatment. Surface energies may be examined experimentally by observing the contact angle between liquids of various surface tensions and the substrate. Zero contact angle corresponds to complete wetting. X-ray photoelectron spectroscopy (XPS) is used to examine surfaces and contaminants.

Epoxy and polyester resin-based composites do not strongly adsorb water, form oxides or corrode in moist environments. In addition, they are polar which makes them receptive to adhesive bonding. This combination of properties results in surface treatments being required which simply remove contaminants such as oils, mould lubricants or general dirt. There are two main techniques used to achieve this: (a) abrasion and solvent cleaning and (b) the tear ply method. Abrasive paper, wire brush or grit blasting are used for abrasion. This not only removes contamination but also a surface film. Abrasion increases the apparent surface energy. It also provides surface roughness enabling the adhesive to 'key' into the surface. Surface rugosity can affect the kinetics of wetting by the adhesive and it has been shown that the rate of spreading on a very rough surface is much greater than on a polished surface. It has also been shown that random roughness, as distinct from the more uniform surface achieved by polishing, can increase the strength of a joint, probably by changing the stress distribution at the interface.

The tear ply method involves the laying-up before autoclaving of one ply of fabric, such as nylon or equivalent, on the laminate surface to be bonded. Just prior to bonding the tear ply is removed and a fresh, 'clean' and bondable surface is exposed. Of the two techniques abrasion gives a better result.

Stone [42] studied the effect of the degree of abrasion of carbon fibre composite surfaces on strengths of adhesive bonded joints. He concluded the following: (a) incomplete abrasion of CFC surfaces can give large reductions in joint strengths with some adhesives, (b) low strengths given by lightly abraded surfaces are probably due to PTFE residues from release cloths used for moulding and (c) close control of grit blasting conditions, allied to thorough inspection, is required to ensure complete abrasion without exposure of carbon fibres.

Hart-Smith [43] discussed several aspects of surface preparation techniques. Grit blasting is claimed to produce the strongest bonded joint. He criticised the use of uncoated (with release agent) tear plies as the tear ply is bonded so tenaciously that it tends to delaminate below the surface (thereby damaging the laminate) and the tear ply itself often breaks, so that a razor blade must be used to restart the stripping. Even with peel plies coated with 'nontransferring' release agent, the removal of the peel ply is not an adequate surface preparation. The initial surface contains a replicate of the weave in the peel ply so that the surface consists of a gridwork of local hills surrounding little valleys. If those roughnesses are not sanded off, a small air bubble collects in each of those valleys and, having no escape path, prevents the adhesive from contacting as much as 30 or 40 percent of the total bond area. This may be the reason why grit blasting is superior to even the best of the peel plies. It is recommended to use distilled water to remove any residual dust particles from the surface rather than contaminating it with a solvent wipe.

He stated that the ideal means of verifying the adequacy of surface preparation is to spray on a primer having the same wetting characteristics as the water-break test (water forms a thin continuous coating and 'wets' the entire area of a properly prepared composite surface while it collects in discrete 'beads' and is repelled by an improperly or unprepared surface). If the primer wets the entire surface, it would be baked on or air-dried to protect the part until the next operation. If the primer showed contamination, it could be removed chemically before it hardened and the surface recleaned.

Parker and Waghorne [44] described the effects of surface contamination and various abrasive pretreatments on the properties of adhesive-bonded CFRP joints.

They concluded that before bonding, the composite must be given a surface pre-treatment that is adequate to remove virtually all traces of release agent.

According to Hart-Smith *et al.* [45] satisfactory surface treatments can easily be verified by the simple water-break test. They also stated that the art of grit blasting should be mastered because it both creates the best surface preparation and can be used for repair as well as original manufacture.

Parker [46] studied the effect of priming carbon fibre-reinforced composite before bonding. In general, the use of a primer had very little effect on the strength of bonded joints. Parker [47] discussed methods of testing surfaces of carbon fibre composites for bondability. Non-destructive techniques (water-break test and ultraviolet photoelectron spectroscopy (UPS)) and coupon testing (single lap joint, floating roller peel and Boeing wedge tests) were used. The water-break test is found to be simple but not very discriminating and cannot be used for water soluble contaminants. UPS shows contamination clearly but has yet to be correlated with the effect of contamination on bond strength. The three coupon tests correlated between themselves.

2.6 ADHESIVE VOIDS

Adhesive voids can be formed during bonding at elevated temperature by water vapour emitted from the composite, the adhesive or both. Voids in the fillets may promote cracking by acting as stress raisers. Autoclaving single lap joints, as opposed to press-curing, prevents cracking by reducing the void content [48]. Sage and Tiu [49] concluded that voids can be reduced by drying the composite for at least one hour at the bond cure temperature and drying the adhesive at 50°C for 30 minutes, prior to bonding. The voids can be eliminated entirely by bonding under isostatic pressure above the saturated water vapour pressure at the cure temperature.

The effect of voids in adhesive joints with CFRP adherends has also been studied by Allen [50]. He gave three possible sources of adhesive voids: (a) water which had been adsorbed (or absorbed) by the plastic, (b) air which had been entrapped in pores or surface irregularities in the surface of the plastic and (c) volatile organic material released from within the plastic as a result of the procedure used in curing the adhesive.

Hart-Smith [1], however, reported that in most cases adhesive bonds are much more tolerant to flaws than is generally recognised. He claimed that the critical location in a bonded joint is usually at one end of the overlap and flaws tend not to occur there; they form more often in the interior, where air bubbles can be trapped. The interior of the joint is usually lightly loaded anyway and, even neglecting that, local flaws were found to have no effect on the strength of bonded joints until they became so large as to shift the critical location away from the edge of the joint to a location adjacent to the flaw. When this happened, the load redistribution was so great that a substantial loss of strength occured.

From the current author's experience, adhesive voids can seriously affect the performance of a joint. Measures to dry the adhesive and adherends prior to bonding are of vital importance for an optimum joint.

2.7 EFFECT OF STACKING SEQUENCE

The performance of a joint between adherends made from unidirectional prepreg depends, for a given lay-up, on the stacking sequence, since changing the latter changes the bending stiffness without altering the extensional stiffness. In 1969, Dallas [51] measured the strengths of composite adhesive bonded joints, riveted joints and joints containing both rivets and bonds. The fibre orientation of the adherends was found to be a significant variable. Althof [52] reported that the lap shear strength of unidirectional laminates is greater than that of multidirectional ones since the interlaminar shear strength decreases as the angle between the fibre orientation and direction of loading increases.

Renton and Vinson [23] found that ply orientation overall, or of the ply immediately adjacent to the adhesive had a minor influence on the static joint strength (0.6 inches was the longest overlap tested). This is not surprising with the short overlaps used. Yuceoglu and Updike [53] studied stress concentrations in bonded multi-layer stiffening strips and base plates. They found that the stacking sequence and the stiffness ratios of the base plate-to-stiffeners may change drastically the interlayer stress concentrations. Matthews and Tester [54] investigated the effect of changing the stacking sequence in $0°/\pm 45°$ lay-up carbon fibre-reinforced plastic adherends, on the joint strength of bonded single lap joints. It was found that stacking sequence influence strength.

Cushman *et al.* [55] reported that placing a softer ply group at the joint interface (±45° vs. 0°) resulted in a more uniform shear strain along the joint interface, thus increasing double lap joint strength. Similar results have been obtained from the present work on single lap joints in that having ±45° surface plies offers a more uniform strain distribution at the end of the lap and contributes, in certain cases, to improved joint strength. Static tests on double butt strap joints conducted by Martin and Sage [56] resulted in 'soft' joints (±45° plies are put on the outer surfaces to reduce shear stress concentration) being 3.5% stronger than 'hard' joints (0° plies are put on the outer surfaces to reduce peel stress concentration).

The effect of variation of laminate stacking sequence adjacent to the bondline upon adherend and adhesive stresses was evaluated using finite element analysis by Grant and Lewington [57]. They concluded that variation of stacking sequence, local to the bondline, appears to have little influence upon local adherend stresses of a double lap joint. The lowest stresses occured with 0° layers next to the bondline. The adhesive stresses were all higher than the local adherend stresses. This contradicts the results from the current work in that stacking sequence changes have a significant effect on local adherend stresses. The reason for this contradiction may be attributed to the bending effects in single lap joints.

Clearly, the question of the influence of stacking sequence on the performance of a bonded joint, or indeed on other areas such as impact and fatigue, is open to debate. The present work is aimed at providing a more fundamental understanding of the underlying mechanisms of failure with different adherend stacking sequences. To this end, experimental and analytical techniques have been employed.

2.8 EFFECT OF BONDLINE THICKNESS

According to Hart-Smith [58] the best adhesive bonds have a thickness ranging from 0.12 to 0.25 mm. The most frequent bond flaw in the highly stressed areas is not even recognised as such, because the bond shows up as perfect on all ultrasonic inspections. This flaw is the pinch-off at the joint edge that results in an ultra-thin layer of adhesive right where both analysis and test indicate that a bondline thicker than nominal would be preferred. Fig. 2.6 depicts the loss in strength, with

respect to a uniform adhesive bond, due to pinch-off at the edge and indicates how much additional strength could be attained by deliberately thickening the adhesive slightly in that area.

The effect of bondline thickness on joint strength with glass reinforced plastic (GRP) adherends has been investigated by Bowditch and Stannard [59]. It has been shown that for a bondline thickness of up to 0.1 mm, no adverse effects were noted. However, beyond this, the reduction in joint strength is rapid. Very thin bondlines appear to give rise to joints which are marginally less strong than those with rather thicker bondlines. It may be that these very thin bondlines are small compared with the thickness necessary with these adhesives, involving a rubbery phase, for optimum performance. Any increase in bondline thickness beyond about 0.1 mm was associated with a progressive reduction in joint strength and this may be attributable to a combination of factors.

Firstly, the inability of the acrylic adhesive used to cure through great thicknesses inevitably leads to weaker bondlines and, indeed, to cohesively weaker films. In addition to this, thicker bondlines are also associated with lower shear strain rates on debonding and greater peeling or cleavage forces with the particular test specimen geometry and debonding methods that were employed. Both these factors contribute to lower apparent joint strengths. When the joints were broken, it was noticed that failure was always cohesive within the GRP until a bondline thickness of 0.2 mm was reached, at which point an element of adhesive failure became apparent. Bondline thicknesses greater than 0.2 mm led to 100% adhesive failure. With standard joints, there are two conflicting mechanisms operating simultaneously. On the one hand, stress concentrations are reduced as the bondline gets thicker but, on the other hand, increasing bondline thickness is inevitably associated with a loss in performance due to incomplete cure.

Parker [60 and 61] found that for some adhesives, unaged joint strength decreased with increasing bondline thickness; for other adhesives thick bondlines were accompanied by high void contents.

2.9 HYGROTHERMAL EFFECTS

It is known that the exposure of adhesively bonded joints to hot-humid environment can seriously reduce their durability. Several workers have attempted to assess hygrothermal effects either qualitatively or quantitatively. Weitsman [62] analysed the bonding stresses at the interface between an adhesive layer and a composite adherend when the exposed edges of the adhesive absorb moisture or when the joint is subjected to an elevated temperature. The analysis is based upon variational principles. It is claimed that the results provide a satisfactory explanation to the debonding phenomena that are observed at the centre of the adhesive joint as well as near the exposed edges. It is shown that the maximum interlaminar tensile stress can occur at either of the above sites and that the exact location of the maximum stress depends on the geometry of the joint and on the progress of moisture diffusion.

Stone [63] studied the effect of temperature and duration of cure on the heat distortion temperature, joint strength and durability of some structural adhesives bonded to aluminium. He concluded that considerable variation can be made to adhesive cure cycles with the aim of reducing thermal mismatch stress and strain, while maintaining joint strengths.

Hart-Smith [58] presented a computer program that permits a step-by-step (along the bondline) variation of adhesive properties, thus allowing systematic assessments of environmental effects, particularly due to the absorption of moisture that plasticises many adhesives. A comparison of the strengths of metal-metal and metal-CFRP adhesive bonded joints at various test temperatures was made by Stone [64]. His main conclusion is that metal-CFRP joints are weaker than mechanically similar metal-metal joints, particularly at low temperature. This is due to the combined effects of differential contraction of adherends in metal-CFRP joints and the relatively low transverse tensile strength of CFRP.

Myhre *et al.* [65] studied moisture problems in advanced composite structural repair. They concluded the following: (a) pre-bond moisture, either in the repair environment or absorbed into the damaged laminate, is degrading to the durability of many adhesives, (b) moisture resistant composites and adhesives are available and their selection, where possible, will do much to alleviate moisture problems and

(c) an estimate can be made of a laminate's moisture condition by the controlled drying and effluent moisture monitoring procedure.

The effect of moisture in the surface of carbon fibre-reinforced composite laminates on the strength of CFRP-CFRP joints bonded with hot-cured structural adhesives, for laminates exposed to high humidity and for laminates stored for up to two years in a freezer, has been studied by Parker [66]. She found that there was some evidence that laminates post-cured and stored with the release cloth in place gave better joints than those which were stripped of release cloth before post-cure. She recommended that if a CFRP laminate which is to be bonded has to be stored, it should, if possible, be stored in a dry atmosphere without removing the resin-impregnated release cloth until immediately before bonding. Otherwise the laminate should be dried at an appropriate temperature before bonding.

Parker [60] examined the effect of extended hot-humid exposure of adhesive bonded carbon fibre composite joints with 175°C cured matrix. Joints bonded with five epoxy adhesives were exposed to 50°C/96% RH (relative humidity) for up to three years. Changes in joint shear strength were measured at a range of temperatures and the proportions of different modes of failure estimated.

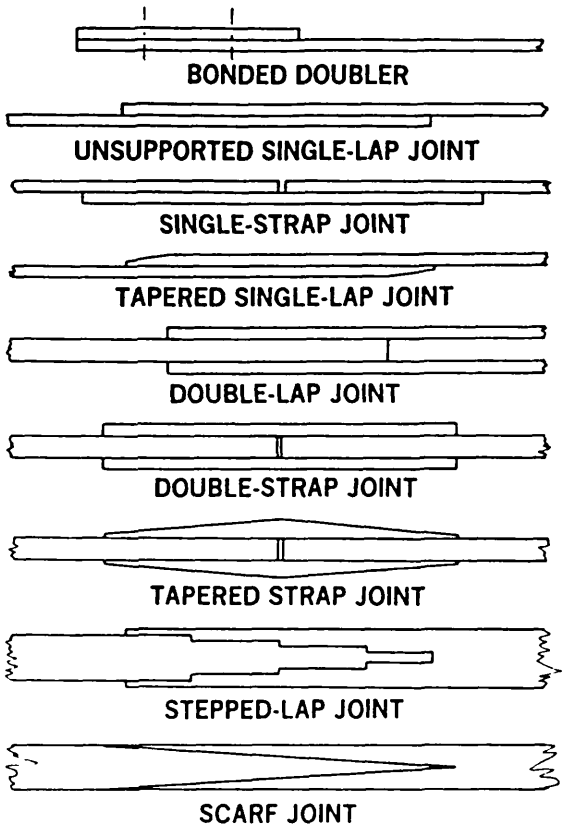
In general, joint strengths were reduced by exposure to high humidity, those of 120°C adhesives being affected more than those of 175°C cured adhesives. At low joint water uptakes, composite properties seemed to control changes in joint strength, but at high contents adhesive properties were dominant.

Proportions of modes of failure (in adhesive, in composite and at the interface) were different for each adhesive. While the 120°C cured adhesives only showed some interfacial failure, this seemed to be associated with the time of drying of the composite before exposure, and the proportion of interfacial failure did not increase with exposure time.

Parker [61] also investigated the effect of extended hot-humid exposure of adhesive bonded carbon fibre composite (120°C cured matrix) joints. All joint strengths were reduced, the reduction depending on the adhesive, test temperature and exposure time.

2.10 CONCLUSIONS

1. Adhesive bonding is the preferred method of joining organic composite structures.
2. Geometric nonlinearity is of paramount importance in the analysis of single lap joints.
3. The design of bonded joints in laminated composite materials should be aimed at minimising interlaminar shear and through-thickness tensile stresses.
4. Proper surface preparation is vital for a reliable bond.
5. Adhesive voids need to be minimised by drying the adhesive and laminate prior to bonding.
6. Further work is needed on the influence of laminate surface plies and stacking sequence on joint strength.
7. A controlled bondline thickness is an important factor in joint design.
8. Hygrothermal effects can reduce joint strengths.



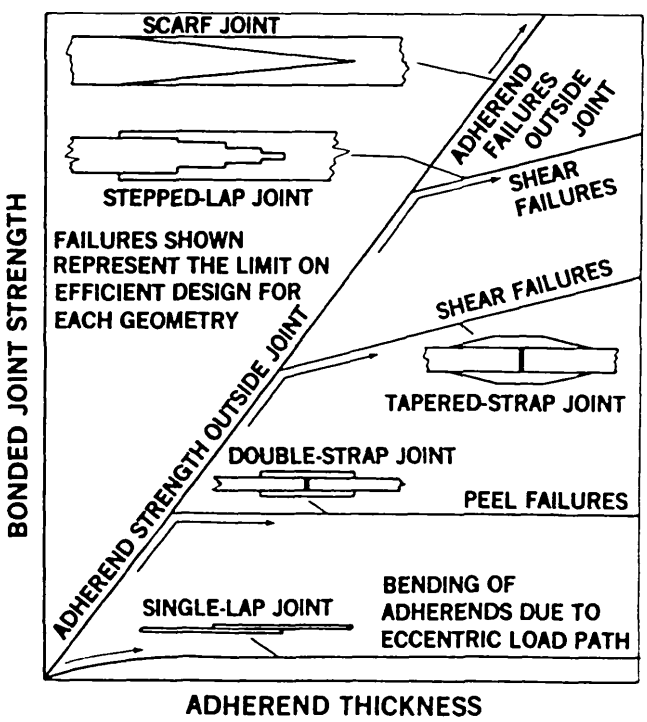


Fig. 2.1. Adhesively bonded joint types and their relative uses [1].

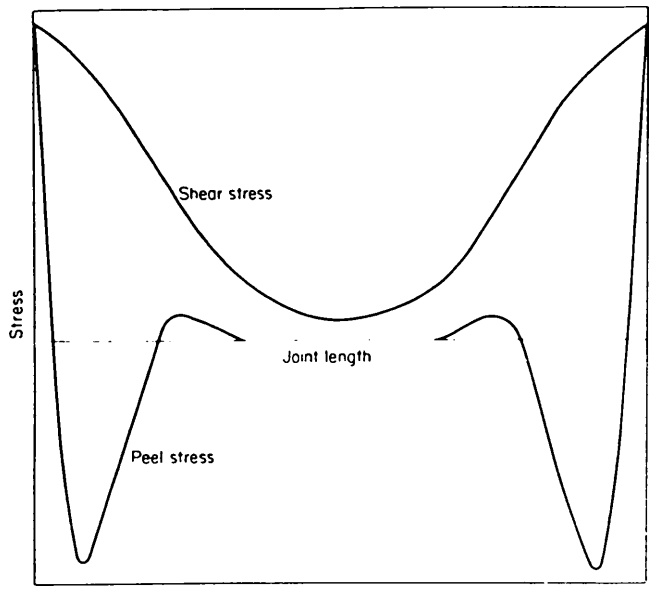


Fig. 2.2. Typical variations of shear and peel stresses in a single lap joint [5].

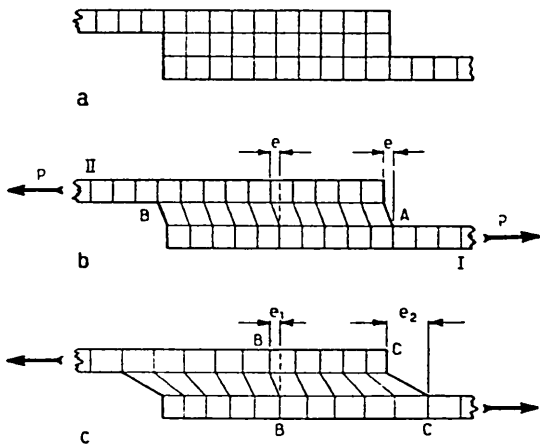


Fig. 2.3. Schematic explanation of the shearing in the adhesive [8]:
(a) Unloaded lap joint.
(b) Loaded joint with inextensible adherends.
(c) Joint with elastic adherends.

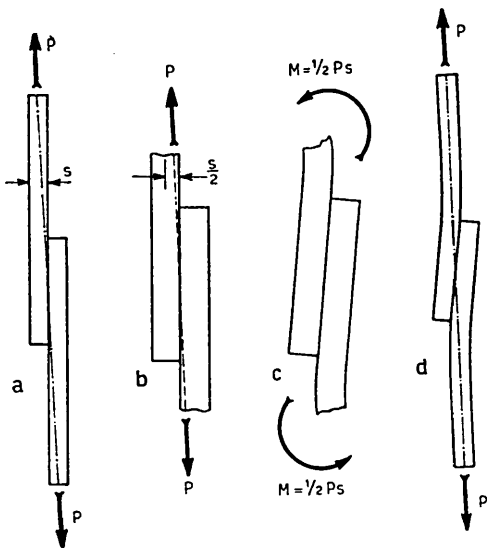


Fig. 2.4. Schematic explanation of the bending of the adherends and of the resulting tearing stresses at the ends of the overlap [8]:
(a) Lap joint before deformation.
(b) Eccentricity of loading near the overlap.
(c) Bending moment near the overlap.
(d) Final deformation of the joint.

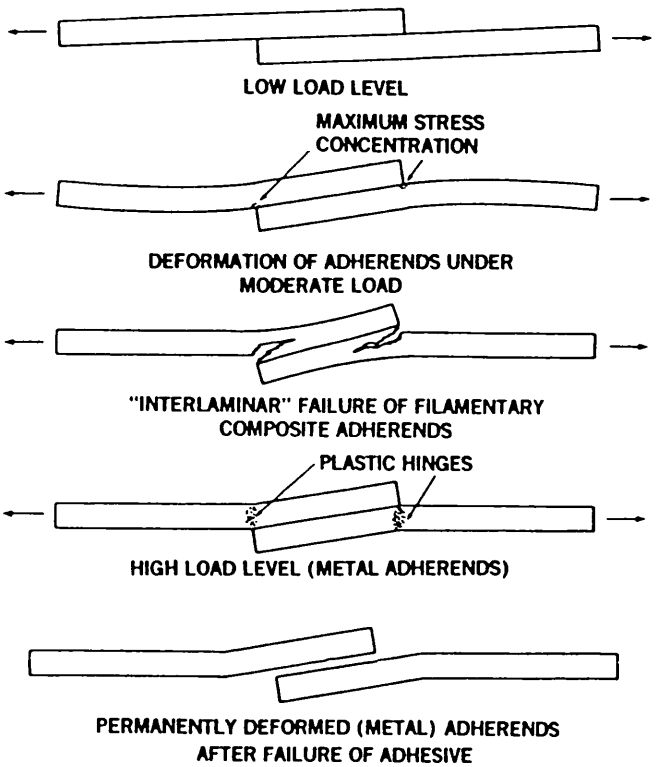


Fig. 2.5. Failure of single lap bonded joints (brittle and yielding adherends) [1].

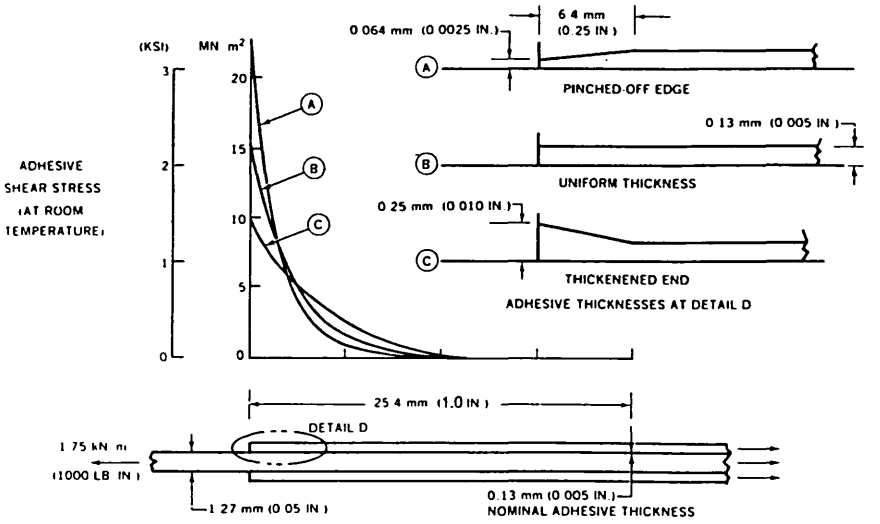


Fig. 2.6. Variation of peak induced adhesive stress with thickness of adhesive at ends of overlap [58].

Chapter 3

THEORETICAL CONSIDERATIONS

3.1 INTRODUCTION

The interaction of various adherend mechanical properties on the performance of a joint is discussed. The continuum method of Hart-Smith is given with a modified expression for k_b (non-dimensionalised bending stiffness parameter for composite adherends) to take into account the influence of bending Poisson's ratio ν_b. The governing equations for the geometrically nonlinear finite element analysis are presented together with failure criteria for the adhesive and composite.

3.2 ADHEREND MECHANICAL PROPERTIES

The complete three-dimensional strain-stress system of relationships for a homogeneous solid is as follows

$$\begin{Bmatrix} \epsilon_x \\ \epsilon_y \\ \epsilon_z \\ \gamma_{xz} \\ \gamma_{yz} \\ \gamma_{xy} \end{Bmatrix} = \begin{bmatrix} S_{11} & S_{12} & S_{13} & S_{14} & S_{15} & S_{16} \\ S_{12} & S_{22} & S_{23} & S_{24} & S_{25} & S_{26} \\ S_{13} & S_{23} & S_{33} & S_{34} & S_{35} & S_{36} \\ S_{14} & S_{24} & S_{34} & S_{44} & S_{45} & S_{46} \\ S_{15} & S_{25} & S_{35} & S_{45} & S_{55} & S_{56} \\ S_{16} & S_{26} & S_{36} & S_{46} & S_{56} & S_{66} \end{bmatrix} \begin{Bmatrix} \sigma_x \\ \sigma_y \\ \sigma_z \\ \tau_{xz} \\ \tau_{yz} \\ \tau_{xy} \end{Bmatrix}, \tag{3.1}$$

where ϵ_x, ϵ_y and ϵ_z are direct strains and γ_{xz}, γ_{yz} and γ_{xy} are shear strains referred to (x, y, z) coordinates. σ_x, σ_y and σ_z are direct stresses and τ_{xz}, τ_{yz} and τ_{xy} are shear stresses referred to the same coordinates system. S_{ij} = material compliance terms (i and j indicate position in row and column respectively in complete matrix of compliances). In standard theory of plates it is assumed that the stress σ_z in the z-direction (through the plate's thickness) is zero. Thus the terms of the

third column of the matrix of compliances make no contribution to the strains. Additionally, there will be no coupling between in-plane strains ϵ_x, ϵ_y and γ_{xy} and out-of-plane direct strain ϵ_z and out-of-plane shear stresses τ_{xz} and τ_{yz}. Also, ϵ_z is not coupled to τ_{xy}. Consequently, Eq. (3.1) reduces to

$$\begin{Bmatrix} \epsilon_x \\ \epsilon_y \\ \epsilon_z \\ \gamma_{xz} \\ \gamma_{yz} \\ \gamma_{xy} \end{Bmatrix} = \begin{bmatrix} S_{11} & S_{12} & S_{13} & 0 & 0 & S_{16} \\ S_{12} & S_{22} & S_{23} & 0 & 0 & S_{26} \\ S_{13} & S_{23} & S_{33} & 0 & 0 & 0 \\ 0 & 0 & 0 & S_{44} & S_{45} & 0 \\ 0 & 0 & 0 & S_{45} & S_{55} & 0 \\ S_{16} & S_{26} & 0 & 0 & 0 & S_{66} \end{bmatrix} \begin{Bmatrix} \sigma_x \\ \sigma_y \\ 0 \\ \tau_{xz} \\ \tau_{yz} \\ \tau_{xy} \end{Bmatrix}. \tag{3.2}$$

Eq. (3.2) is most conveniently written in terms of the following two smaller symmetric matrices

$$\begin{Bmatrix} \epsilon_x \\ \epsilon_y \\ \gamma_{xy} \end{Bmatrix} = \begin{bmatrix} S_{11} & S_{12} & S_{16} \\ S_{12} & S_{22} & S_{26} \\ S_{16} & S_{26} & S_{66} \end{bmatrix} \begin{Bmatrix} \sigma_x \\ \sigma_y \\ \tau_{xy} \end{Bmatrix} \tag{3.3}$$

and

$$\begin{Bmatrix} \gamma_{xz} \\ \gamma_{yz} \end{Bmatrix} = \begin{bmatrix} S_{44} & S_{45} \\ S_{45} & S_{55} \end{bmatrix} \begin{Bmatrix} \tau_{xz} \\ \tau_{yz} \end{Bmatrix}, \tag{3.4}$$

together with an equation for ϵ_z which is not required. In the principal axes of orthotropy (1, 2) of a single layer the terms S_{16} and S_{26} become zero since, in the direction of axes of orthotropy, coupling between in-plane shear and direct stresses is eliminated. Thus,

$$\begin{Bmatrix} \epsilon_1 \\ \epsilon_2 \\ \gamma_{12} \end{Bmatrix} = \begin{bmatrix} S_{11} & S_{12} & 0 \\ S_{12} & S_{22} & 0 \\ 0 & 0 & S_{66} \end{bmatrix} \begin{Bmatrix} \sigma_1 \\ \sigma_2 \\ \tau_{12} \end{Bmatrix}. \tag{3.5}$$

In order to calculate layer stresses from layer strains, the compliance matrix **S** of Eq. (3.5) must be inverted to become the stiffness matrix **Q** giving

$$\begin{Bmatrix} \sigma_1 \\ \sigma_2 \\ \tau_{12} \end{Bmatrix} = \begin{bmatrix} Q_{11} & Q_{12} & 0 \\ Q_{12} & Q_{22} & 0 \\ 0 & 0 & Q_{66} \end{bmatrix} \begin{Bmatrix} \epsilon_1 \\ \epsilon_2 \\ \gamma_{12} \end{Bmatrix}, \tag{3.6}$$

in which the terms Q_{ij} are given by

$$Q_{11} = \frac{E_1}{1 - \nu_{12}\nu_{21}}, \qquad Q_{12} = \frac{\nu_{21}E_1}{1 - \nu_{12}\nu_{21}} = \frac{\nu_{12}E_2}{1 - \nu_{12}\nu_{21}},$$

$$Q_{22} = \frac{E_2}{1 - \nu_{12}\nu_{21}} \qquad \text{and} \qquad Q_{66} = G_{12},$$

where E_1 = longitudinal elastic modulus, E_2 = transverse elastic modulus, G_{12} = in-plane shear modulus, ν_{12} = major Poisson's ratio and ν_{21} = minor Poisson's ratio. The stresses and strains referred to the layer coordinates (1, 2) can be related to those for the plate reference axes (x, y) by the standard formulae for the transformation of stress and strain components. Thus,

$$\bar{\mathbf{Q}} = \mathbf{TQ}$$

where $\bar{\mathbf{Q}}$ = transformed reduced stiffness matrix, $\mathbf{T}$ = transformation matrix and $\mathbf{Q}$ = reduced stiffness matrix. In full matrix notation the relationship is as follows:

$$\begin{Bmatrix} \bar{Q}_{11} \\ \bar{Q}_{22} \\ \bar{Q}_{66} \\ \bar{Q}_{12} \\ \bar{Q}_{16} \\ \bar{Q}_{26} \end{Bmatrix} =$$

$$\begin{bmatrix} \cos^4\theta & \sin^4\theta & 2\cos^2\theta\sin^2\theta & 4\cos^2\theta\sin^2\theta \\ \sin^4\theta & \cos^4\theta & 2\cos^2\theta\sin^2\theta & 4\cos^2\theta\sin^2\theta \\ \cos^2\theta\sin^2\theta & \cos^2\theta\sin^2\theta & -2\cos^2\theta\sin^2\theta & (\cos^2\theta-\sin^2\theta)^2 \\ \cos^2\theta\sin^2\theta & \cos^2\theta\sin^2\theta & \cos^4\theta+\sin^4\theta & -4\cos^2\theta\sin^2\theta \\ \cos^3\theta\sin\theta & -\cos\theta\sin^3\theta & \cos\theta\sin^3\theta-\cos^3\theta\sin\theta & 2(\cos\theta\sin^3\theta-\cos^3\theta\sin\theta) \\ \cos\theta\sin^3\theta & -\cos^3\theta\sin\theta & \cos^3\theta\sin\theta-\cos\theta\sin^3\theta & 2(\cos^3\theta\sin\theta-\cos\theta\sin^3\theta) \end{bmatrix}$$

$$\begin{Bmatrix} Q_{11} \\ Q_{22} \\ Q_{12} \\ Q_{66} \end{Bmatrix}$$

where θ = angle between the reference axes system (x, y) and material axes system $(1, 2)$. Thus in reference axes system (x, y) the stress-strain relationship is as follows

$$\begin{Bmatrix} \sigma_x \\ \sigma_y \\ \tau_{xy} \end{Bmatrix} = \begin{bmatrix} \bar{Q}_{11} & \bar{Q}_{12} & \bar{Q}_{16} \\ \bar{Q}_{12} & \bar{Q}_{22} & \bar{Q}_{26} \\ \bar{Q}_{16} & \bar{Q}_{26} & \bar{Q}_{66} \end{bmatrix} \begin{Bmatrix} \epsilon_x \\ \epsilon_y \\ \gamma_{xy} \end{Bmatrix}. \tag{3.7}$$

In a laminate consisting of n plies, the in-plane and flexural deformations relationships for the laminate can be written as follows

$$\begin{Bmatrix} \mathbf{N} \\ \mathbf{M} \end{Bmatrix} = \begin{bmatrix} \mathbf{A} & \mathbf{B} \\ \mathbf{B} & \mathbf{D} \end{bmatrix} \begin{Bmatrix} \boldsymbol{\epsilon} \\ \boldsymbol{\kappa} \end{Bmatrix}, \tag{3.8}$$

where $\mathbf{N}$ = column matrix of direct load intensities and shear load intensity referred to (x, y) coordinates, $\mathbf{M}$ = column matrix of bending moment intensities

acting in the xz- and yz-planes and twisting moment intensity acting about x- and y-axes respectively, $\mathbf{A}$ = in-plane stiffness matrix, $\mathbf{B}$ = coupled in-plane and flexural stiffness matrix, $\mathbf{D}$ = flexural stiffness matrix, $\boldsymbol{\epsilon}$ = column matrix of mid-plate direct strains and shear strain referred to (x, y) coordinates and $\boldsymbol{\kappa}$ = column matrix of curvature components of plate. The plate stiffnesses $\mathbf{A}$, $\mathbf{B}$ and $\mathbf{D}$ are given by

$$\mathbf{A} = \sum_{p=1}^{n} t_p \bar{\mathbf{Q}}_p \tag{3.9}$$

$$\mathbf{B} = -\sum_{p=1}^{n} t_p z_p \bar{\mathbf{Q}}_p \tag{3.10}$$

$$\mathbf{D} = \sum_{p=1}^{n} (t_p z_p^2 + I_p) \bar{\mathbf{Q}}_p \tag{3.11}$$

where t_p = thickness of pth ply, z_p = distance between laminate's reference plane and mid-plane of pth ply, I_p = second moment of area per unit width of pth ply about its mid-plane $(= t_p^3/12)$ and suffix p is ply identification number. The thickness of the individual layers are small enough that I_p can be neglected and therefore $\mathbf{D}$ is usually reduced to

$$\mathbf{D} = \sum_{p=1}^{n} t_p z_p^2 \bar{\mathbf{Q}}_p. \tag{3.12}$$

From Eq. (3.10) it can be seen that for balanced (symmetric) laminates $\mathbf{B}$ is zero and Eq. (3.8) reduces to two uncoupled equations

$$\mathbf{N} = \mathbf{A}\boldsymbol{\epsilon} \quad \text{and} \quad \mathbf{M} = \mathbf{D}\boldsymbol{\kappa} \tag{3.13}$$

or

$$\begin{Bmatrix} N_x \\ N_y \\ N_{xy} \end{Bmatrix} = \begin{bmatrix} A_{11} & A_{12} & A_{13} \\ A_{12} & A_{22} & A_{23} \\ A_{13} & A_{23} & A_{33} \end{bmatrix} \begin{Bmatrix} \epsilon_x \\ \epsilon_y \\ \gamma_{xy} \end{Bmatrix} \tag{3.14}$$

and

$$\begin{Bmatrix} M_x \\ M_y \\ M_{xy} \end{Bmatrix} = \begin{bmatrix} D_{11} & D_{12} & D_{13} \\ D_{12} & D_{22} & D_{23} \\ D_{13} & D_{23} & D_{33} \end{bmatrix} \begin{Bmatrix} \kappa_x \\ \kappa_y \\ \kappa_{xy} \end{Bmatrix} \tag{3.15}$$

All the adherends tested in the present programme possessed in-plane orthotropy, i.e. the A_{13} and A_{23} terms of the laminate in-plane stiffness matrix are

zero. This means that in-plane (normal) forces will result in only normal deformation with no shear deformation—no shear coupling. When the D_{13} and D_{23} terms of the laminate flexural stiffness matrix $\mathbf{D}$ are non-zero the laminate does not possess bending orthotropy. Thus, bending loads will result in bending and twisting deformations. Only unidirectional and cross-ply laminates of the adherends tested possess bending orthotropy.

By standard matrix inversion

$$\boldsymbol{\epsilon} = \mathbf{aN} \quad \text{and} \quad \boldsymbol{\kappa} = \mathbf{dM} \tag{3.16}$$

where $\mathbf{a}$ = in-plane compliance matrix and $\mathbf{d}$ = flexural compliance matrix. In full matrix notation the relationships are as follows

$$\begin{Bmatrix} \epsilon_x \\ \epsilon_y \\ \gamma_{xy} \end{Bmatrix} = \begin{bmatrix} a_{11} & a_{12} & a_{13} \\ a_{12} & a_{22} & a_{23} \\ a_{13} & a_{23} & a_{33} \end{bmatrix} \begin{Bmatrix} N_x \\ N_y \\ N_{xy} \end{Bmatrix} \tag{3.17}$$

and

$$\begin{Bmatrix} \kappa_x \\ \kappa_y \\ \kappa_{xy} \end{Bmatrix} = \begin{bmatrix} d_{11} & d_{12} & d_{13} \\ d_{12} & d_{22} & d_{23} \\ d_{13} & d_{23} & d_{33} \end{bmatrix} \begin{Bmatrix} M_x \\ M_y \\ M_{xy} \end{Bmatrix}. \tag{3.18}$$

It is useful to know the effective engineering elastic constants of a laminate for any particular stacking sequence. Consider the only non-zero force acting on a laminate, of width b and thickness t, to be P in the x-direction. The direct load intensity per unit width in the x-direction is given by

$$N_x = \frac{P}{b}$$

and the corresponding stress is

$$\sigma_x = \frac{P}{bt} = \frac{N_x}{t}.$$

From the extensional compliance matrix (Eq. (3.17)),

$$\epsilon_x = a_{11} N_x = a_{11} \sigma_x t$$

$$\frac{\sigma_x}{\epsilon_x} = \frac{1}{t a_{11}}$$

and by definition of the elastic modulus

$$E_m = \frac{\sigma_x}{\epsilon_x}$$

$$E_m = \frac{1}{t a_{11}}. \tag{3.19}$$

E_m is the effective membrane (in-plane) elastic modulus of the adherends in the direction of applied load. Also, from the extensional compliance matrix,

$$\epsilon_y = a_{12} N_x$$

and by definition of Poisson's ratio

$$\nu_m = -\frac{\epsilon_y}{\epsilon_x} = -\frac{a_{12} N_x}{a_{11} N_x}$$

$$\nu_m = -\frac{a_{12}}{a_{11}}. \tag{3.20}$$

ν_m is the effective membrane Poisson's ratio (associated with E_m). Fig. 3.1 shows the lateral contractions in a joint resulting from membrane Poisson's effects.

From the Engineer's Theory of Bending of a homogeneous isotropic beam,

$$\frac{M}{I} = E\kappa$$

where M = applied bending moment, I = second moment of area about the neutral axis, E = modulus of elasticity and κ = curvature of the neutral axis. Thus,

$$\frac{M}{\kappa} = EI = E\frac{bt^3}{12}.$$

This relationship is used to define the effective engineering constants corresponding to an applied bending moment M acting about the y-axis. The moment per unit width about the y-axis is given by

$$M_x = \frac{M}{b}.$$

From the bending compliance matrix (Eq. (3.18)),

$$\kappa_x = d_{11} M_x = d_{11}\frac{M}{b}$$

$$\frac{M}{\kappa_x} = \frac{b}{d_{11}}$$

and by definition,

$$\frac{M}{\kappa_x} = E_b I_x = E_b\frac{bt^3}{12}$$

$$E_b\frac{bt^3}{12} = \frac{b}{d_{11}}$$

$$E_b = \frac{12}{t^3}\frac{1}{d_{11}}. \tag{3.21}$$

E_b is the effective bending (out-of-plane) elastic modulus of the adherends corresponding to the bending moment M_x. Also, from the bending compliance matrix,

$$\kappa_y = d_{12} M_x$$

and by definition of Poisson's ratio

$$\nu_b = -\frac{\kappa_y}{\kappa_x} = -\frac{d_{12} M_x}{d_{11} M_x}$$

$$\nu_b = -\frac{d_{12}}{d_{11}}. \tag{3.22}$$

ν_b is the effective bending Poisson's ratio of the adherends (associated with E_b). Fig. 3.2 shows the effect of bending Poisson's ratio on the adherend curvatures. This effect is responsible for longitudinal splitting, clearly demonstrated when testing a single lap joint with unidirectional adherends. The beneficial effect of ν_b is to stiffen the laminate in bending due to the anti-clastic curvature (transverse bending).

From the bending compliance matrix,

$$\kappa_{xy} = d_{13} M_x$$

and by definition, the coefficient of mutual bend-twist coupling is

$$m = \frac{\kappa_{xy}}{\kappa_x} = \frac{d_{13} M_x}{d_{11} M_x}$$

$$m = \frac{d_{13}}{d_{11}}. \tag{3.23}$$

The effect of mutual bend-twist coupling on torsional deformation of a joint is depicted in Fig. 3.3. The twisting curvatures κ_{xy} cancel each other at the lap region but the net effect is a shear system set-up in the joint [67].

It is clear from Figs. 3.1 and 3.3 that failure is likely to initiate at a joint corner. However, with adherends possessing mutual bend-twist coupling, one corner at a lap end is favoured over the other. This is because the corner under through-thickness tension is a more likely failure initiation site than the corner under through-thickness compression—see Fig. 3.3.

3.3 CONTINUUM ANALYSIS

Hart-Smith [15] undertook extensive work on single lap joints and considered the effect of stacking sequence. Design charts resulted from his analysis. His analytical solution is used here to calculate critical adherend and adhesive stresses, in preference to other theories mentioned in Chapter 2, due to the above reasons. The mean experimental failure stresses are used as input to his equations given below. The adhesive shear stress is not usually critical in composite bonded single lap joints. Although several simplifying assumptions are made in his analysis, it helps to a certain degree to explain the present results.

A Fortran computer programme was written to compute the effective mechanical properties of the adherends needed for this analysis [68]. The material properties of the composite and adhesive are given in Appendix A. All the results are based on nominal specimen dimensions.

3.3.1 Adherend stress

The adherend maximum direct stress adjacent to the bondline at the end of the overlap, due to axial load and bending moment, is the most critical with thin adherends and short overlaps—less than $50t$.

The average stress is given by

$$\sigma_{av} = \frac{P}{t}, \tag{3.24}$$

where P = experimental mean load at failure per unit joint width and t = thickness of adherend.

The bending stress at the laminate surface fibres is given by

$$\sigma_b = 3k\sigma_{av}\left(1 + \frac{\eta}{t}\right), \tag{3.25}$$

where η = thickness of adhesive layer, k = eccentricity factor = $\left[1 + \xi c + \frac{\xi^2 c^2}{6}\right]^{-1}$, c = half length of overlap, $\xi = \sqrt{P/D}$ and D = flexural rigidity of adherends. According to Hart-Smith, D is given by

$$D = \frac{E_b t^3}{12(1-\nu_m^2)}. \tag{3.26}$$

In his calculation of the flexural rigidity, Hart-Smith did not consider the effect of the variation of bending Poisson's ratio ν_b. He used, for a given stacking sequence, the bending elastic modulus with the membrane Poisson's ratio—which does not change with stacking sequence. The differences between ν_m and ν_b vary considerably depending on the stacking sequence. The effect of ν_b should, therefore, be included in the analysis. Thus the corrected flexural rigidity, which is used in the present analysis, is given by

$$D = \frac{E_b t^3}{12\left(1-\nu_b^2\right)}. \tag{3.27}$$

The adherend maximum direct stress is given by

$$\sigma_{max} = \sigma_{av} + \sigma_b. \tag{3.28}$$

3.3.2 Adhesive peel stress

The adhesive peel stress is also important as it introduces through-thickness tensile stress in the composite. The peel stress is given by Hart-Smith as

$$\sigma_p = k\sigma_{av}\left(1+\frac{\eta}{t}\right)\left[\frac{3E\left(1+\nu_m^2\right)t}{2k_b E_m \eta}\right]^{1/2}, \tag{3.29}$$

where E = adhesive tensile elastic modulus and k_b = non-dimensionalised bending stiffness parameter for composite adherends (the ratio of the actual flexural rigidity of the laminate to that assuming isotropic rigidity). Hart-Smith defines the bending stiffness parameter as

$$\begin{aligned} k_b &= \frac{\frac{E_b t^3}{12(1-\nu_m^2)}}{\frac{E_m t^3}{12(1-\nu_m^2)}} \\ &= \frac{E_b}{E_m} \\ &= \frac{\frac{12}{d_{11}t^3}}{\frac{1}{a_{11}t}} \\ &= \frac{12a_{11}}{d_{11}t^2}. \end{aligned} \tag{3.30}$$

However, taking into consideration the effect of bending Poisson's ratio gives the modified expression for the bending stiffness parameter (used in the current analysis) as

$$
\begin{aligned}
k_b &= \frac{\frac{E_b t^3}{12(1-\nu_b^2)}}{\frac{E_m t^3}{12(1-\nu_m^2)}} \\
&= \frac{\frac{12}{d_{11}t^3}\frac{t^3}{12\left\{1-\left(-\frac{d_{12}}{d_{11}}\right)^2\right\}}}{\frac{1}{a_{11}t}\frac{t^3}{12\left\{1-\left(-\frac{a_{12}}{a_{11}}\right)^2\right\}}} \\
&= \frac{12d_{11}\left(a_{11}^2-a_{12}^2\right)}{t^2 a_{11}\left(d_{11}^2-d_{12}^2\right)}.
\end{aligned} \tag{3.31}
$$

The definition of k_b does not, of course, address directly the influence of laminate surface plies as it is based on 'smeared' mechanical properties of the laminate. Its use should, therefore, be restricted to laminates having the same surface ply orientation for a given set of stacking sequences. This is because of the change of the mechanisms of failure with the change of surface plies. Further, the behaviour of a single lap bonded joint is three-dimensional. k_b does not cater, for example, for the effect of twisting of the laminate when bent due to the offset of the load path. It is therefore important to be aware of the limitations of this parameter.

3.4 FINITE ELEMENT ANALYSIS

In linear elastic analysis, small displacements and strains are assumed with a linear form of strain-displacement relationship. This means that the geometry of the elements remains basically unchanged during the loading process. However, it is known that for an accurate determination of stress distributions in single lap joints a geometrically nonlinear analysis has to be used [15 and 31]. This is because of the reduction in the bending moment at the end of the overlap region due to the deformation of the adherends as loading increases. Thus, the geometry of the elements has to be updated as loading progresses, otherwise an overestimation of stresses would result due to the geometrically unrelieved bending moment at the end of the overlap region. In such a case, the updated Lagrangian description of motion may be used with large displacements but small strains.

Also, linear elastic analysis implies a linear form of material stress-strain relationship. Composite materials exhibit material nonlinearity in longitudinal and through-thickness tension and in shear, with the latter nonlinearity being the most severe. Hence, it is important to take into account this effect, especially if the adherends have $\pm 45°$ surface plies.

Ductile adhesives, as opposed to brittle adhesives used for high temperature applications, have a nonlinear stress-strain relationship in tension and in shear [69 and 70]. Usually, large shear strains—about 30%—are attained before failure in a typical adhesive shear test, e.g. napkin ring shear test. Adhesives in composite single lap joints are more likely to fail, if at all, in transverse tension (peel) rather than in shear, although failure is usually within the adherends. Hence, the adhesive shear stress-strain relationship may remain largely linear until failure, i.e. no plasticity due to shear loading. However, plasticity may occur due to transverse tension loading. It is interesting to note that this situation is reversed for a double lap joint. Iterative processes are used to approximate the material nonlinear stress-strain curve. Again, ignoring material nonlinearities would increase the predicted value of peak stresses in the joint.

A linear analysis is always a necessary precursor to a nonlinear one but, bearing in mind the above remarks on its limitations, can often also produce useful information. Clearly there is also a saving on computing time and memory requirements.

Initially, the finite element package ICB-FINEL [71] (Apollo Domain workstation version) was used. The obvious advantage was the availability of this software on a workstation resulting in minimal computing cost. However, this advantage is undermined by the limited memory available when running large models. Eight-noded membrane plate elements (QM08) were used for each ply and for the adhesive. Each ply contained one element through its thickness. Two elements were used through the adhesive thickness. The adhesive fillet was not modelled. Work undertaken with this package served to optimise mesh grading and produce some of the early linear analysis results. An attempt was also made to use Mindlin eight-noded laminated plate elements with large displacement analysis. However, several 'bugs' were found with this routine. An attempt to resolve

these problems proved to be time consuming. The geometrically nonlinear analysis with this package was abandoned due to the above reason.

Abaqus [72] is a finite element computer programme which is mainly known for its nonlinear capabilities. This software is installed on the College's VAX 8600 computer. All the finite element analysis results reported have been obtained using the Abaqus system except where otherwise indicated. The models included 45° angle fillets. Mesh grading has been used to concentrate elements at critical regions. Typical element aspect ratio at critical regions is between 1 and 5, while aspect ratios exceeding 100 are used well away from the end of the overlap. Details of elements used are given in appropriate Chapters. Composite and adhesive mechanical properties used in the analyses are given in Appendix A. A linear form of material stress-strain relationship is assumed.

The first 25 mm from either end of the model is suppressed from moving in the out-of-plane direction. This is not so much to resemble the effect of the grips of the testing machine, but it is found necessary, for the type of elements used, to obtain satisfactory overall joint deformation.

Mean experimental stress at joint failure has been applied to the finite element models by imposing the equivalent in-plane displacement. This method of stress application is more 'realistic' than applying nodal forces, for each layer, at the adherend end. This is because the stress in each layer is dependent, of course, on its stiffness. The equivalent in-plane displacement has been established by incrementing (say 0.1 mm increment) an arbitrary applied displacement (say 2 mm) and calculating the equivalent applied stress for each displacement increment. The applied stress is calculated by adding the nodal reactions at an adherend end and dividing by the cross-sectional area of the model adherend. The model has a unit width (1 mm). A stress-displacement curve is then plotted. The equivalent displacement to the experimental mean stress at failure (joint strength) can easily be read from the stress-displacement curve.

Numerical simulation of joint failure has been undertaken. For this purpose, cracked (reduced stiffness) elements have been used. The mechanical properties of the cracked elements are 1% of their original values. It should be noted that the reduced stiffness elements are not used to simulate what happens at a crack

tip—which would require special elements—but merely to assess local stress/strain redistribution with a view to examining failure sequence. Further improvement can also be effected by modelling the resin rich interface between the plies.

3.4.1 Plane stress

Abaqus plane stress elements are used in the case of comparison between finite element analysis and moiré interferometry results (Chapter 7). The elements used are:

1. CPS8R: eight-noded, isoparametric, reduced integration (to save on computing cost), quadrilateral membrane plate element.
2. CPS6: six-noded, isoparametric, triangular membrane plate element.

The moiré grid is applied to a surface where σ_{zz} is zero—specimen edge. Shear components in the z-direction must also be zero,

$$\tau_{zx} = \tau_{zy} = 0. \tag{3.32}$$

Under these conditions the stress equations of equilibrium in Cartesian coordinates reduce to:

$$\frac{\partial \sigma_{xx}}{\partial x} + \frac{\partial \tau_{xy}}{\partial y} + X = 0 \tag{3.33}$$

$$\frac{\partial \tau_{xy}}{\partial x} + \frac{\partial \sigma_{yy}}{\partial y} + Y = 0 \tag{3.34}$$

where X and Y are body forces in the x and y directions. The following stress and strain relationships then apply:

$$\epsilon_{xx} = \frac{1}{E}\left(\sigma_{xx} - \nu\sigma_{yy}\right), \qquad \epsilon_{yy} = \frac{1}{E}\left(\sigma_{xy} - \nu\sigma_{xx}\right)$$

$$\sigma_{xx} = \frac{E}{(1-\nu^2)}\left(\epsilon_{xx} + \nu\epsilon_{yy}\right), \qquad \sigma_{yy} = \frac{E}{(1-\nu^2)}\left(\epsilon_{yy} + \nu\epsilon_{xx}\right)$$

$$\tau_{xy} = G\gamma_{xy} = \frac{E}{2(1+\nu)}\gamma_{xy}.$$

3.4.2 Plane strain

A state of plane strain is assumed to exist at the centreline plane of the specimen which the two-dimensional finite element model is meant to represent. In this case, the Abaqus plane strain elements used are:

1. CPE8R: eight-noded, isoparametric, reduced integration, quadrilateral membrane plate element.
2. CPE4R: four-noded, isoparametric, reduced integration, quadrilateral membrane plate element.
3. CPE6: six-noded, isoparametric, triangular membrane plate element.
4. CPE3: three-noded, isoparametric, triangular membrane plate element.

Plane strain problems are defined as those in which the strains in the z-direction are zero. Thus

$$\epsilon_{zz} = \gamma_{yz} = \gamma_{zx} = 0. \tag{3.35}$$

Also, from the basic assumptions of plane elastic problems,

$$\tau_{zy} = \tau_{zx} = 0.$$

The equations of stress equilibrium in this case again reduce to:

$$\frac{\partial \sigma_{xx}}{\partial x} + \frac{\partial \tau_{xy}}{\partial y} + X = 0 \tag{3.36}$$

$$\frac{\partial \tau_{xy}}{\partial x} + \frac{\partial \sigma_{yy}}{\partial y} + Y = 0 \tag{3.37}$$

The stress-strain relations are then as follows:

$$\epsilon_{xx} = \frac{(1-\nu^2)}{E}\left(\sigma_{xx} - \frac{\nu}{(1-\nu)}\sigma_{yy}\right), \qquad \epsilon_{yy} = \frac{(1-\nu^2)}{E}\left(\sigma_{yy} - \frac{\nu}{(1-\nu)}\sigma_{xx}\right)$$

$$\sigma_{xx} = \frac{E(1-\nu)}{(1+\nu)(1-2\nu)}\left(\epsilon_{xx} + \frac{\nu}{(1-\nu)}\epsilon_{yy}\right)$$

$$\sigma_{yy} = \frac{E(1-\nu)}{(1+\nu)(1-2\nu)}\left(\epsilon_{yy} + \frac{\nu}{(1-\nu)}\epsilon_{xx}\right)$$

$$\tau_{xy} = G\gamma_{xy}.$$

It should be noted that the plane strain equations can be derived simply from the plane stress equations by replacing

$$\nu \quad \text{by} \quad \frac{\nu}{(1-\nu)} \quad \text{and} \quad E \quad \text{by} \quad \frac{E}{(1-\nu^2)}.$$

3.4.3 Geometrically nonlinear formulation

Fig. 3.4 shows a typical load-displacement curve for a single lap joint in tension. The initial nonlinear part of the curve is due to joint rotation. In modelling this part small load increments are required with the necessary iterations for each load increment. The geometry of the model is updated with each load increment. As the load increases the joint 'stabilises' with the corresponding linear part of the load-displacement curve. Clearly at this stage larger load increments may be applied with the problem being reduced to a linear one. An outline of the nonlinear solution procedure is given below. For a fuller treatment of the geometrically nonlinear analysis the reader is referred to reference [73].

For equilibrium between internal and external forces, it is possible to obtain the equilibrium equations using the virtual work principle. Thus,

$$\Psi(\mathbf{a}) = \int_V \bar{\mathbf{B}}^{\mathrm{T}} \boldsymbol{\sigma} \, dV - \mathbf{f} = 0 \tag{3.38}$$

where Ψ = the sum of external and internal forces being a function of global displacement $\mathbf{a}$, $\bar{\mathbf{B}}^{\mathrm{T}}$ = transposed strain shape function, $\boldsymbol{\sigma}$ = stress vector, $\mathbf{f}$ = force vector and V = volume. $\bar{\mathbf{B}}$ is defined from strain definition as

$$d\boldsymbol{\epsilon} = \bar{\mathbf{B}} \, d\mathbf{a} \tag{3.39}$$

where $\boldsymbol{\epsilon}$ = strain vector and $\mathbf{a}$ = displacement vector.

For large displacements, the strains depend nonlinearly on displacement, and the matrix $\bar{\mathbf{B}}$ is dependent on $\mathbf{a}$. Thus,

$$\bar{\mathbf{B}} = \mathbf{B}_0 + \mathbf{B}_L(\mathbf{a}) \tag{3.40}$$

in which $\mathbf{B}_0$ = linear strain shape function and $\mathbf{B}_L$ = large displacement strain shape function (a function of $\mathbf{a}$) . If strains are reasonably small the general elastic relation can still be written as

$$\boldsymbol{\sigma} = \mathbf{D}(\boldsymbol{\epsilon} - \boldsymbol{\epsilon}_0) + \boldsymbol{\sigma}_0 \tag{3.41}$$

where $\mathbf{D}$ = elasticity matrix (stress-strain relationship), $\boldsymbol{\epsilon}_0$ = linear strain vector and $\boldsymbol{\sigma}_0$ = linear stress vector.

The solution of Eq. (3.38) is approached iteratively. Using the Newton-Raphson method a relation between da and $d\Psi$ is required. Thus, taking appropriate variations of Eq. (3.38) with respect to da gives

$$d\Psi = \int_V d\bar{\mathbf{B}}^T \boldsymbol{\sigma}\, dV + \int_V \bar{\mathbf{B}}^T\, d\boldsymbol{\sigma}\, dV = \mathbf{K}_T\, da \tag{3.42}$$

where $\mathbf{K}_T$ = tangential (or instantaneous) stiffness matrix. Using Eqs. (3.41) and (3.39) gives

$$d\boldsymbol{\sigma} = \mathbf{D}\, d\boldsymbol{\epsilon} = \mathbf{D}\bar{\mathbf{B}}\, da$$

and if Eq. (3.40) is valid

$$d\bar{\mathbf{B}} = d\mathbf{B}_L$$

Therefore

$$d\Psi = \int_V d\mathbf{B}_L^T \boldsymbol{\sigma}\, dV + \bar{\mathbf{K}}\, da \tag{3.43}$$

where

$$\bar{\mathbf{K}} = \int_V \bar{\mathbf{B}}^T \mathbf{D} \bar{\mathbf{B}}\, dV = \mathbf{K}_0 + \mathbf{K}_L, \tag{3.44}$$

$\mathbf{K}_0$ = linear (or small displacement) stiffness matrix and $\mathbf{K}_L$ = large displacement (or initial displacement) stiffness matrix and contains only terms which are linear and quadratic in **a**. $\mathbf{K}_0$ and $\mathbf{K}_L$ are given by

$$\mathbf{K}_0 = \int_V \mathbf{B}_0^T \mathbf{D} \mathbf{B}_0\, dV$$

$$\mathbf{K}_L = \int_V (\mathbf{B}_0^T \mathbf{D} \mathbf{B}_L + \mathbf{B}_L^T \mathbf{D} \mathbf{B}_L + \mathbf{B}_L^T \mathbf{D} \mathbf{B}_0)\, dV$$

The first term of Eq. (3.43) can generally be written as

$$\int_V d\mathbf{B}_L^T \boldsymbol{\sigma}\, dV \equiv \mathbf{K}_\sigma\, da \tag{3.45}$$

where $\mathbf{K}_\sigma$ = geometric stiffness (or initial stress) matrix. Thus

$$d\Psi = (\mathbf{K}_0 + \mathbf{K}_\sigma + \mathbf{K}_L)\, da = \mathbf{K}_T\, da \tag{3.46}$$

Thus the iterative solution procedure is as follows:

a) Determine the linear elastic solution as a first approximation to $\mathbf{a}^0$.

b) Ψ^0 is found using Eq. (3.38) with appropriate definition of $\bar{\mathbf{B}}$ and stresses as given by Eq. (3.41).

c) Matrix $\mathbf{K}_T^0$ is established.

d) Correction is computed as

$$\Delta \mathbf{a}^0 = -(\mathbf{K}_T^0)^{-1} \Psi^0$$

Processes (b), (c) and (d) are repeated until Ψ^n becomes sufficiently small. Superscripts ^{0} and ^{n} indicate the first and nth iteration respectively for each load increment.

3.4.4 Adhesive failure criterion

Three failure criteria for isotropic materials are available on the Abaqus finite element system, viz. maximum principal stress, Tresca and von Mises. For the adhesive fillet, subjected to a complex stress system, the von Mises failure criterion will be used. The maximum principal stress failure criterion is suitable for brittle materials and there is considerable experimental evidence that this criterion should not be applied for ductile materials [74]. Of the two criteria suitable for ductile materials (Tresca and von Mises), the von Mises criterion is preferred. This is because it has received considerable verification in practice and is widely regarded as the most reliable basis for design [74].

The von Mises theory states that failure occurs when the maximum shear strain energy component in the complex stress system is equal to that at the yield point in the tensile test. It should be noted that the absolute values of adhesive uniaxial compressive and tensile yield stresses are asumed to be the same. Thus in terms of principal stresses σ_1 and σ_2 (i.e. the maximum and minimum direct stresses),

$$\frac{1}{2}\left\{(\sigma_1 - \sigma_2)^2 + \sigma_1^2 + \sigma_2^2\right\} = \sigma_Y^2 \tag{3.47}$$

where σ_Y = adhesive uniaxial tensile yield stress,

$$\sigma_1 = \frac{\sigma_x + \sigma_y}{2} + \frac{1}{2}\sqrt{(\sigma_x - \sigma_y)^2 + 4\tau_{xy}^2} \tag{3.48}$$

$$\sigma_2 = \frac{\sigma_x + \sigma_y}{2} - \frac{1}{2}\sqrt{(\sigma_x - \sigma_y)^2 + 4\tau_{xy}^2} \tag{3.49}$$

σ_x, σ_y and τ_{xy} are direct stresses and shear stress respectively in the x, y coordinate system. Substituting for σ_1 and σ_2 into Eq. (3.47) yields the von Mises stress as:

$$\sigma_M = \sqrt{\sigma_x^2 + \sigma_y^2 - \sigma_x\sigma_y + 3\tau_{xy}^2}. \tag{3.50}$$

Adhesive failure is assumed to occur when σ_M exceeds σ_Y.

3.4.5 Adherend failure criterion

Several failure criteria exist for composite materials. The more well known ones are: (a) maximum stress, (b) maximum strain, (c) Tsai-Hill, (d) Tsai-Wu and (e) Hoffman. Reference [75] outlines 18 failure criteria used for composite materials. No interactive failure criterion is available on the Abaqus system. This restricts the choice to limit criteria. Of the maximum stress and maximum strain criteria, the latter has been selected as strain contours can easily be plotted for the whole of the laminate cross-section by strain averaging. Stresses, on the other hand, can not be averaged at a nodal point common to two plies of different material properties as they 'jump' from ply to ply according to its stiffness.

Failure is assumed to occur if any strain in the adherend material axes system $(1, 2)$ exceeds the respective ultimate failure strain. Thus,

$$\begin{aligned} \epsilon_{1t} < X_{\epsilon t}, \qquad & |\epsilon_{1c}| < |X_{\epsilon c}| \\ \epsilon_{2t} < Y_{\epsilon t}, \qquad & |\epsilon_{2c}| < |Y_{\epsilon c}| \\ & |\gamma_{12}| < S_\epsilon \end{aligned} \tag{3.51}$$

where ϵ_{1t} and ϵ_{1c} are longitudinal direct tensile and compressive strains respectively, ϵ_{2t} and ϵ_{2c} are transverse direct tensile and compressive strains respectively and γ_{12} is the shear strain in the material axes system. $X_{\epsilon t}$, $X_{\epsilon c}$, $Y_{\epsilon t}$, $Y_{\epsilon c}$ and S_ϵ are the corresponding ultimate strains. From Mohr's strain circle [74], for a plane strain condition, the shear strain in the material axes system for the $\pm 45°$ plies is given by

$$\gamma_{12} = \epsilon_{xx}$$

where ϵ_{xx} is the longitudinal direct strain in the reference axes system (x, y).

If any inequality is not satisfied, then it is assumed that the ply has failed by a mechanism associated with $X_{\epsilon t}$, $X_{\epsilon c}$, $Y_{\epsilon t}$, $Y_{\epsilon c}$ or S_ϵ respectively. Note that there is no interaction between the modes of failure. This is not strictly one failure criterion but five sub-criteria.

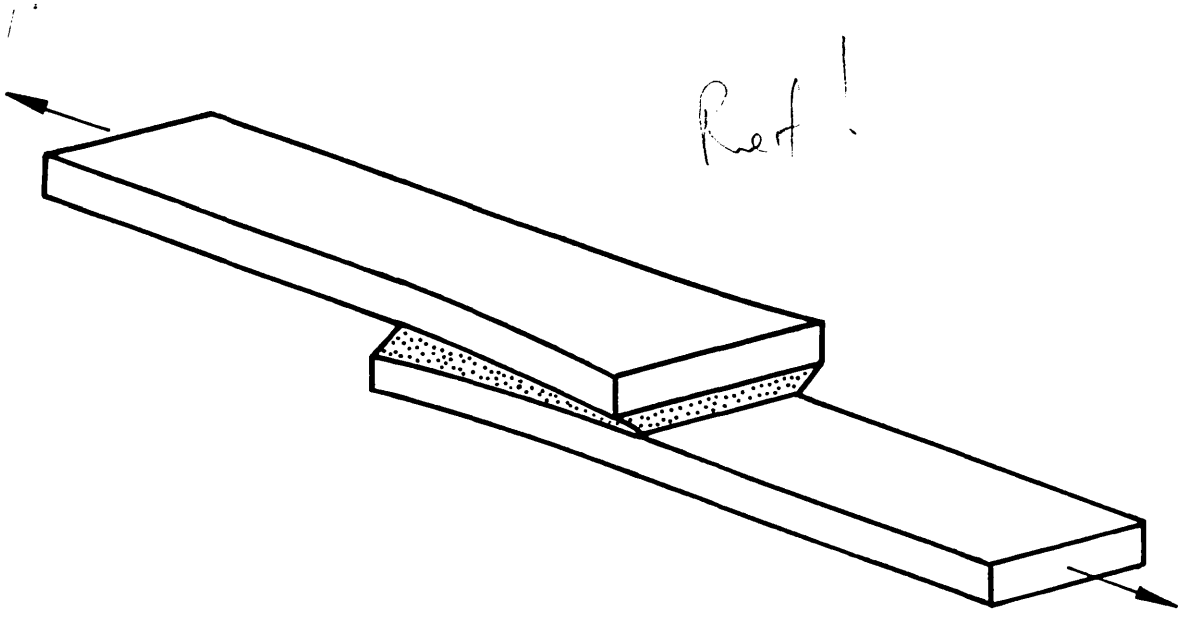


Fig. 3.1. The lateral contractions resulting from membrane Poisson's effects.

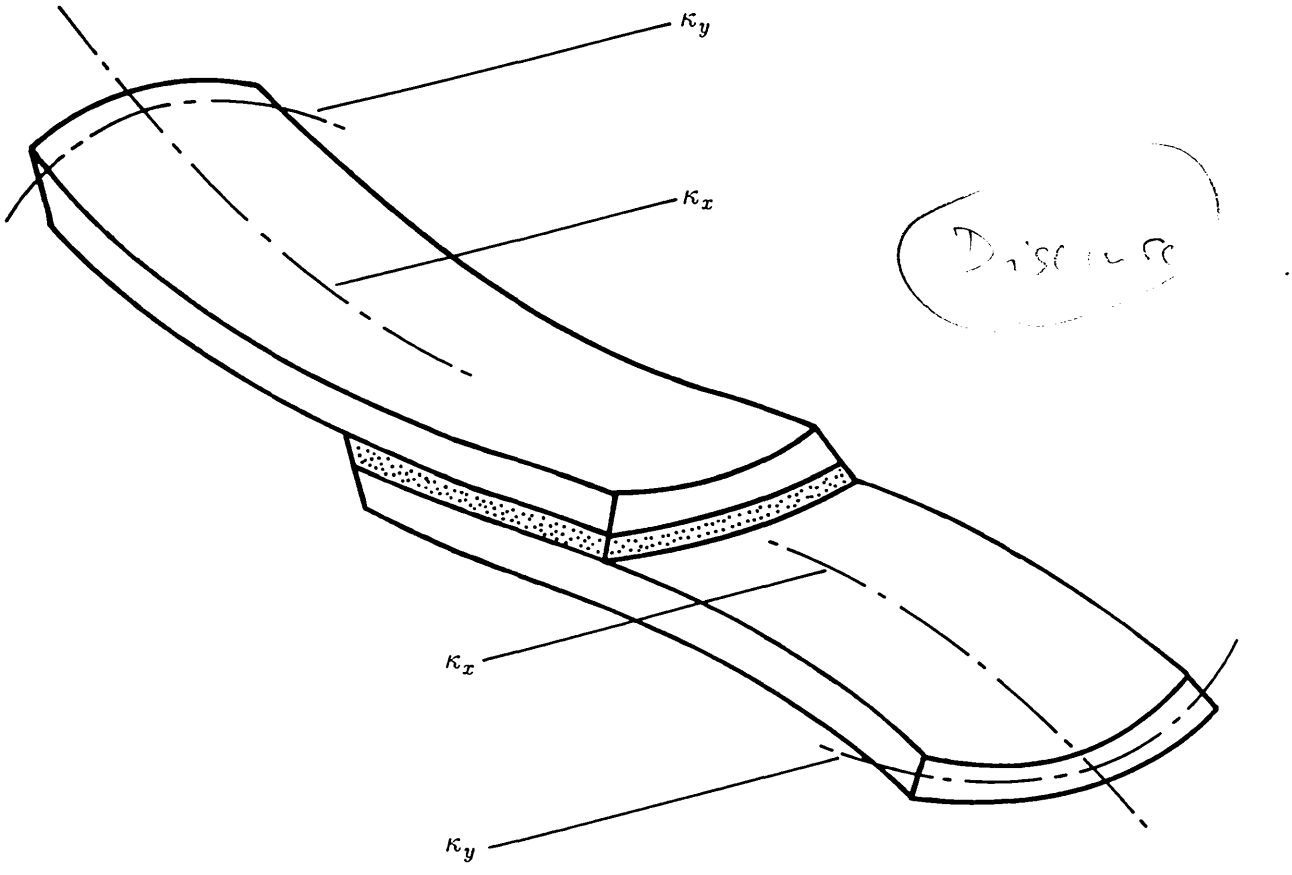


Fig. 3.2. The effect of bending Poisson's ratio on adherend curvatures.

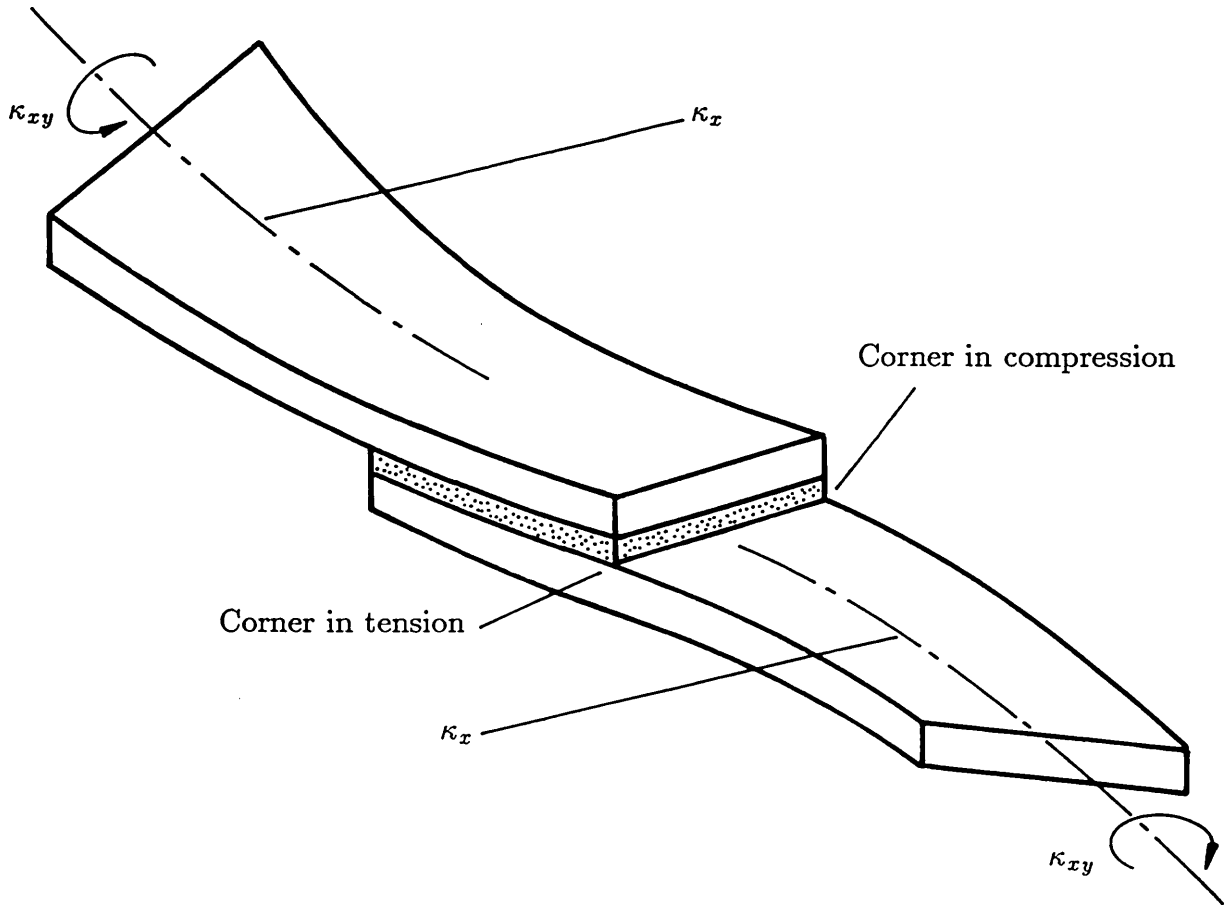


Fig. 3.3. The effect of mutual bend-twist coupling on torsional deformation.

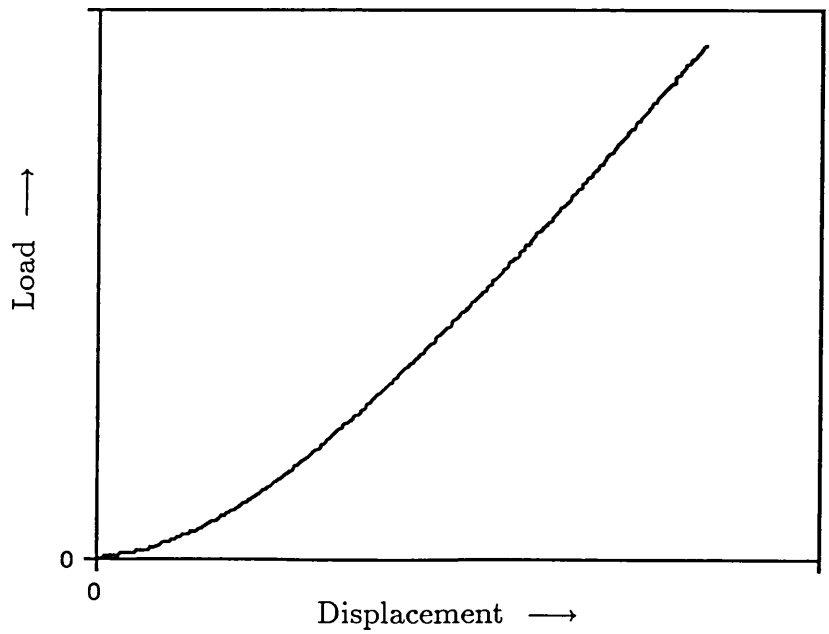


Fig. 3.4. Typical load-displacement curve for a single lap joint loaded to failure.

Chapter 4

EXPERIMENTAL METHODS

4.1 INTRODUCTION

Differences in prepreg batches, curing and post-curing cycles and fibre volume fractions—to name just a few—could result in the same composite material having different mechanical properties. This would subsequently affect the results of any experimental study. Variability in surface preparation and bonding, e.g. incomplete curing of the adhesive, also influence the quality of the bonded specimens. It is therefore vital to maintain consistency in specimen preparation and testing procedures.

4.2 MATERIALS

The adherends were made from Courtaulds Grafil XAS carbon fibres preimpregnated with Ciba-Geigy 914 epoxy resin. This composite exhibits very high strength retention between -60 and $+180°C$ operational temperatures [76]. Curing of the laminates (against PTFE-coated glass cloth) was carried out in the Department of Aeronautics autoclave facility. The following curing cycle was used:

a) Apply vacuum (22–26 in Hg (74–88 kN/m^2)).

b) Heat to 120°C.

c) Apply pressure to 60 lbf/in^2 (414 kN/m^2). Vacuum was vented at 20 lbf/in^2 (138 kN/m^2).

d) Heat to 175°C.

e) Dwell for one hour.

f) Cool to 60°C before pressure removal and laminate ejection.

The whole cycle took about $3\frac{1}{4}$ hours. It should be noted that the curing pressure used ($414\,kN/m^2$) was less than that recommended by the manufacturer ($700\,kN/m^2$). The lower pressure used had been shown to improve laminate quality. The resulting laminates had a nominal ply thickness of 0.125 mm and nominal fibre volume fraction of 0.60. Post-curing of the laminates (after the removal of the glass release cloth) was carried out in an air-circulating oven at 190°C for four hours. Post-curing is required to obtain the optimum high temperature performance of the composite. Ultrasonic C-scanning was used to check the panels for quality.

The adhesive used for joining the adherends was Ciba-Geigy Redux 308A. The adhesive is supplied in the form of a lightweight flexible film. It is free from solvents and contains minimal volatile constituents [77]. It has a strong self-filleting action with controlled flow characteristics to reduce the risk of local joint starvation. The operating temperature of the adhesive is up to approximately 120°C. The adhesive contains ballotini—glass beads of 0.076 mm diameter—to give a uniform bondline thickness. It should be noted that this method of maintaining a uniform bondline thickness is superior to the use of a carrier—nylon mesh—which reduces the mechanical properties of the adhesive. Also, in fatigue loading the nylon mesh acts as a crack initiator.

The recommended curing temperature of the adhesive is 150°C (measured at the bondline) for one hour at a pressure of 25–50 lbf/in^2 ($170–350\,kN/m^2$). This procedure will produce bonds with well balanced properties and is particularly recommended when high peel strength is required. In cases where some sacrifice in the peel strength is acceptable, slightly higher shear strength can be obtained by curing the adhesive for one hour at 170°C with the above stated pressure. A nominal tolerance of ±5°C on the curing temperature is permissible.

The mechanical properties of the composite and adhesive were measured and are listed in Appendix A.

4.3 LAY-UPS AND STACKING SEQUENCES

The adherend lay-ups and stacking sequences tested are given in Table 4.1. Code letters were used for the more complex lay-ups. In selecting the lay-ups/stacking sequences particular attention was paid to the relative position of the $\pm 45°$ layers and to the 'blocking' of the 0° plies. It can be seen that the emphasis of the study is on the $0°/\pm 45°$ lay-up. This lay-up is typical in aerospace vehicle skins. Cross-ply ($0°/90°$), $0°/\pm 45°/90°$ and unidirectional lay-ups are included to further the understanding of the underlying mechanisms of failure.

4.4 SURFACE PRETREATMENT OF ADHERENDS

Prior to bonding it is necessary to remove the release agent 'skin' on the laminate [44]. Dry sand blasting was used to remove this contamination. The particle size was between 45 and 85 microns and the blasting pressure was 276 kPa. Fig. 4.1(a) and (b) shows laminate surface texture before and after sand blasting respectively. Fibre damage due to sand blasting is depicted in Fig. 4.1(c). Following sand blasting the adherends were thoroughly washed in cold running water whilst rubbing with a soft brush. The laminates were then dried as described below.

4.5 ADHESIVE VOIDS

Any moisture in the adhesive or composite will evaporate during the bonding cycle causing voids in the adhesive layer and fillet region. Fig. 4.1(d) is a plan view on a fractured adhesive joint with high void content. High void content in the adhesive layer leads to cohesive/adhesive failure as shown in Fig. 4.2. It is essential, therefore, to dry the adhesive and adherends prior to bonding as noted by Sage and Tiu [49]. The adhesive was dried in a vacuum oven for half an hour at 50°C, immediately before use. It was checked with the adhesive manufacturer that this process does not initiate polymer cross-linking [78]. The adherends were dried in an air-circulating oven for one hour at 150°C, or better still at 160°C to allow for temperature fluctuations during the curing cycle of the adhesive—the adhesive curing temperature being 150°C. It is recommended to carry out the composite drying process even if the laminates are considered to be 'nominally' dry.

It is recognised that the above drying procedure, whilst serving its purpose to dry the laminates quickly, is too severe if the laminates are fully saturated and require heating for a prolonged period of time at elevated temperature [66]. Thus, to avoid possible degradation of the resin matrix properties and fibre/matrix bond due to the drying procedure used, it is suggested that a more gentle drying process be adopted in this case. This can be in the form of heating the laminates at 40–50°C for a period of several months. However, this treatment causes 'physical ageing' (chemical change) [61].

4.6 PREPARATION OF BONDED JOINTS

The bonding was done in a jig to give 12.5 or 25 mm overlaps. The adherend panels were machined with locating slots at the ends of the overlap region, which fitted over pins on a baseplate to give the required overlap—see Fig. 4.3. Silicon rubber sheets were sandwiched between the jig and the laminates for uniform pressure distribution.

It should be noted that the adherends, for a given stacking sequence, were manufactured in pairs with opposite stacking sequence, enabling the surfaces against the autoclave table to be used for bonding and hence ensure joint symmetry about the adhesive layer. The autoclave table surface of a laminate is usually flatter than the pressure plate surface, and thus allows a more uniform joint to be produced.

The adhesive was cured at 150°C for one hour. There is no restriction by the adhesive manufacturer on the heating-up or cooling-down rates. The temperature was monitored by a thermocouple placed at the bondline. The manufacturer's recommended bonding pressure is between 170 and 350 kN/m^2. However, problems encountered with getting a consistent bondline thickness led to using 0.1 mm steel shims at the bondline under an appropriate pressure. The shims were held in position by high temperature adhesive tape. It should also be noted that the use of the heavy duty heated press for bonding crushed the 0.076 mm glass beads in the adhesive used to control the bondline thickness, and hence pressing against steel shims gave a better result. This was because the press did not allow the regulation of the relatively low pressure required for bonding.

Excess adhesive squeezed out of the adhesive layer forming spew fillets at the lap ends. It should be noted that the adhesive film was cut to exactly the size of the bond area. The formation of adhesive fillets could have been easily avoided by the use of silicon rubber as dams at the lap ends. However, it was decided, at an early stage of the programme, to keep the adhesive fillet to resemble typical joints produced in industry despite the variations and inconsistency which may result.

The lap region of the bonded panels was examined using ultrasonic C-scanning and X-ray radiography to check joint integrity. However, only limited information resulted from the use of the above techniques, e.g. a widthwise taper in the adhesive layer may be detected using C-scanning.

Strips (25 mm wide) were cut from each laminate and bonded using Ciba-Geigy Araldite 2001 two-part epoxy adhesive (cured for 15 hours at room temperature) across the end of each adherend panel to form end tabs for the specimens when the bonded panels were finally cut. End tabs were used to avoid distortion of the specimen when inserted in the machine jaws. The end tab size was found adequate to resist the applied shear loading and to avoid slippage in the machine jaws. The end tabs were kept well away from the lap region to avoid any diffusion of stresses from the ends into the lap region. Four 25 mm wide and 275 or 287.5 mm long specimens, corresponding to 25 mm and 12.5 mm overlaps respectively, were cut from the bonded plates using a diamond tipped saw of maximum particle size of 353 microns. Saw marks on the edges of the specimens were removed by hand abrasion with 320 grade wet/dry emery paper.

The adhesive layer thickness was measured using a microscope with a micrometer stage for incident light. The adhesive layer varied in thickness from peel-ply impression as shown in Fig. 4.4 so an average of several readings over the entire overlap was taken. The adhesive layer at the very end of the lap region was thicker than its nominal thickness due to the rounding of the adherend end as a result of sand blasting—see Fig. 4.5. The dimensions of each specimen were measured and recorded.

All the laminates and bonded joints were stored dry in a vacuum oven at 35°C throughout manufacture and until testing.

4.7 TESTING OF JOINTS

For each lay-up, four specimens were tested in a Zwick computer-controlled, screw driven, tensile testing machine at a loading rate of 2 mm/min. A set square was used to align the specimen in the testing machine. All joint failures were within the adherends, i.e. no cohesive or adhesive failures. Test results are based on actual specimen dimensions (stress is load divided by the cross-sectional area of adherend).

Crack arrestment (stopping the test as soon as a crack initiates) has been successful in some cases. This technique has been used to monitor crack initiation in the adhesive fillet which usually occurs before ultimate joint failure.

4.8 MOIRÉ INTERFEROMETRY

Moiré interferometry is an optical method that produces whole-field contour maps of in-plane displacement components, U and V. Sensitivity is in the subwavelength range, 0.417 μm per fringe order. In addition to high sensitivity, the method is characterised by high contrast interference fringes and high spatial resolution. While it is similar in many ways to classical and holographic interferometry, which are techniques primarily useful for out-of-plane displacement measurements, W, moiré interferometry provides the important in-plane displacements. The displacements are related directly to strains.

A high frequency crossed-line diffraction grating is replicated on the specimen surface using a special mould, as illustrated in Fig. 4.6. The result is a thin—0.025 mm—reflective phase grating firmly adhered to the specimen, which deforms together with the specimen surface. The initial frequency of the specimen grating, before loads are applied, is $f/2$, where f is 2400 lines/mm. Sensitivity, or displacement per fringe order, is the reciprocal of f.

The specimen grating is observed in an optical arrangement illustrated schematically in Fig. 4.6. Two beams of coherent light from C' and D' intersect at an angle of 2α in the horizontal plane and form a virtual reference grating with its grating lines perpendicular to the x-direction. Beams from A' and B' intersect at 2α in a vertical plane and form a virtual reference grating with lines perpendicular

to the y-direction. The frequency reference grating is $f = (2\sin\alpha)/\lambda$, where λ is the wavelength of the light. Each reference grating interacts with the similarly oriented lines of the specimen grating to form the interference patterns recorded in the camera. The patterns are contour maps of displacements governed by the relationships:

$$U = \frac{1}{f} N_x \tag{4.1}$$

$$V = \frac{1}{f} N_y \tag{4.2}$$

where U and V are in-plane x and y components of displacement at any point; N_x and N_y are the fringe orders at that point in the corresponding fringe patterns, i.e., the patterns formed using grating lines perpendicular to the x- and y-directions respectively.

Strains can be calculated from the displacement fields by the small strain relations:

$$\epsilon_x = \frac{\partial U}{\partial x} = \frac{1}{f}\left(\frac{\partial N_x}{\partial x}\right) \approx \frac{1}{f}\left(\frac{\Delta N_x}{\Delta x}\right) \tag{4.3}$$

$$\epsilon_y = \frac{\partial V}{\partial y} = \frac{1}{f}\left(\frac{\partial N_y}{\partial y}\right) \approx \frac{1}{f}\left(\frac{\Delta N_y}{\Delta y}\right) \tag{4.4}$$

$$\gamma_{xy} = \frac{\partial U}{\partial y} + \frac{\partial V}{\partial x} = \frac{1}{f}\left(\frac{\partial N_x}{\partial y} + \frac{\partial N_y}{\partial x}\right) \approx \frac{1}{f}\left(\frac{\Delta N_x}{\Delta y} + \frac{\Delta N_y}{\Delta x}\right) \tag{4.5}$$

where ϵ_x and ϵ_y are normal strains in the x- and y-directions respectively and γ_{xy} is shear strain. In the finite-increment form, the increments are good approximations of the differentials when Δx and Δy are small compared to dimensions of the specimen and small compared to the widths of zones of high strain gradients.

A detailed description of the technique is given by Post [79]. Some examples of the application of moiré interferometry to composite materials are given in references [80–83]. In the current work, moiré interferometry has been used to determine the longitudinal direct strain distributions in some adherends at the end of the overlap region with different stacking sequences. This work has been undertaken at the Department of Engineering Science and Mechanics, Virginia Polytechnic Institute and State University, Blacksburg, Virginia, U.S.A., with the collaboration of Prof. J. Morton. Moiré strains are compared with the predicted strains from geometrically nonlinear finite element analyses. The results are reported in Chapter 7.

4.9 FRACTOGRAPHY

The purpose of fractography is to acquire a detailed understanding of the fracture of bonded CFRP joints. The modes of fracture and sequence of failure are analysed. This leads to the prediction of the initial cause of failure of bonded joints. Fractured joint surfaces are mounted on specimen stubs using silver loaded epoxy adhesive, coated with gold by sputtering and examined in a JEOL JSM-T220A scanning electron microscope of 5 nm resolution. An extensive fractographic analysis of composite materials has been undertaken by Purslow [84–86]. A more recent worker in this field is Greenhalgh [87].

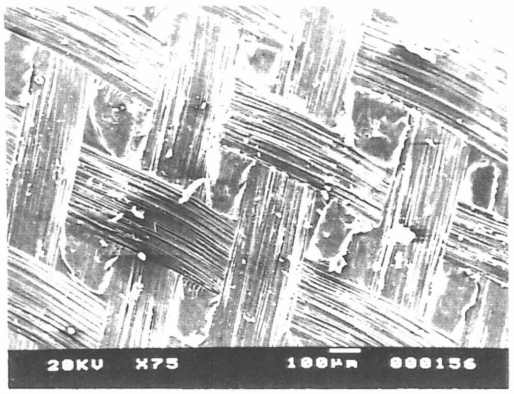
Table 4.1. Lay-ups and stacking sequences used in the experimental programme.

Lay-up/stacking sequence	l/t
A: $[0/\pm 45]_s$	33.3
B: $[\pm 45/0]_s$	33.3
D: $[\pm 45/0_2]_s$	25.0
E: $[0/\pm 45/0]_s$	25.0
F: $[0_2/\pm 45]_s$	25.0
K: $[\pm 45/0_3/\pm 45/0]_s$	12.5
L: $[0/\pm 45/0_2/\pm 45/0]_s$	12.5
M: $[0_2/\pm 45/0/\pm 45/0]_s$	12.5
N: $[0_3/(\pm 45)_2/0]_s$	12.5
$[0/90]_{3s}$	16.7
$[90/0]_{3s}$	16.7
$[0/90]_{2s}$	25.0
$[90/0]_{2s}$	25.0
$[0/90]_s$	50.0
$[90/0]_s$	50.0
O: $[\pm 45/90/0/\pm 45/0]_s$	14.3
P: $[0/90/(\pm 45)_2/0]_s$	14.3
Q: $[\pm 45/90/0_2/\pm 45/0]_s$	12.5
R: $[0_2/90/(\pm 45)_2/0]_s$	12.5
$[0_4]_s$	25.0
$[0_8]_s$	12.5

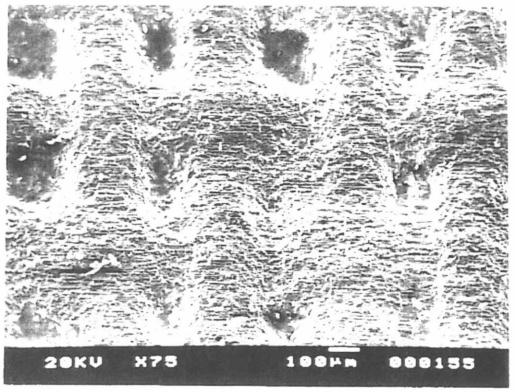
l/t— ratio of overlap length to thickness of adherend.

All overlap lengths are 25 mm.

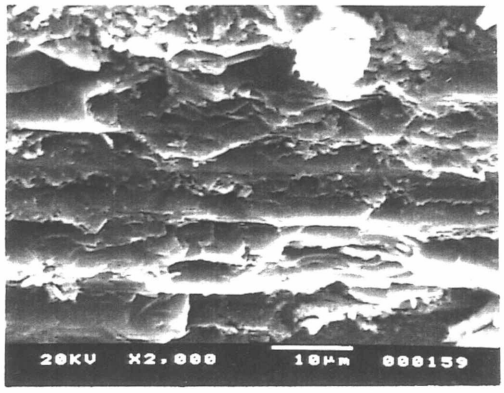
Laminates D, E and F are also tested with 12.5 mm overlap ($l/t = 12.5$).



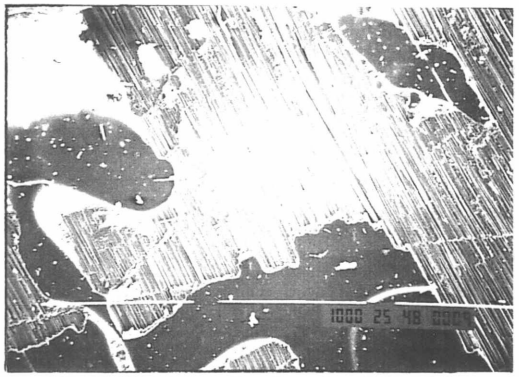
(a)



(b)



(c)



(d)

Fig. 4.1. SEM showing:
(a) Laminate surface texture as moulded.
(b) Laminate surface texture after sand blasting.
(c) Fibre damage due to sand blasting.
(d) Adhesive voids.

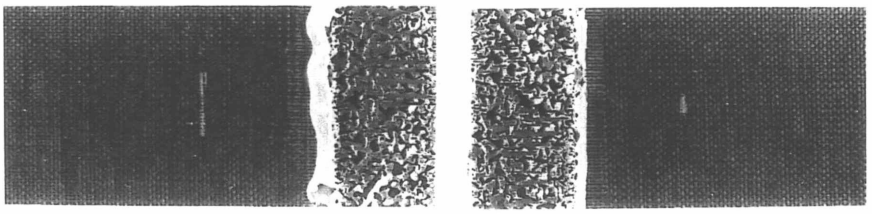


Fig. 4.2. A fractured joint with high void content adhesive layer.

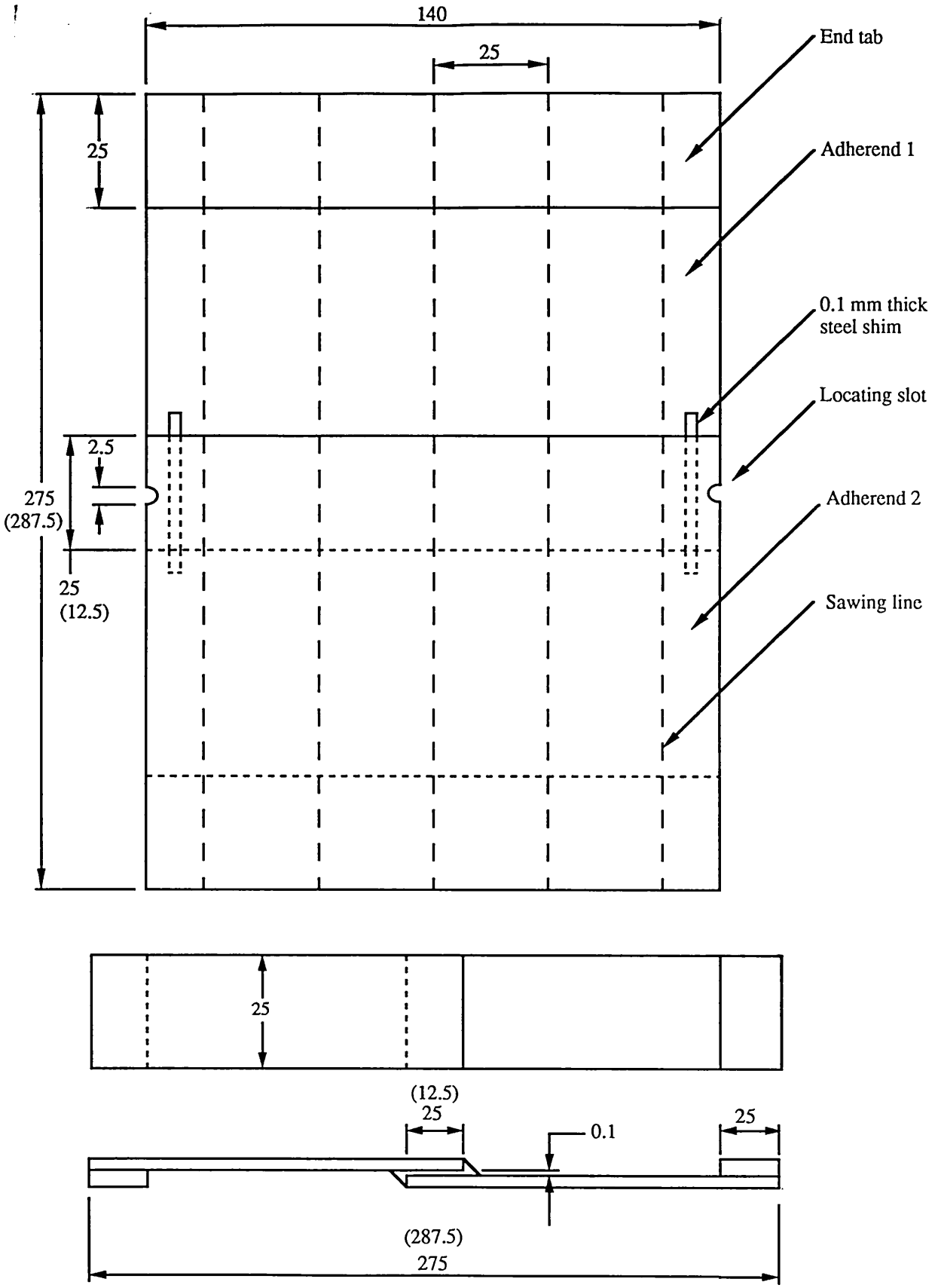


Fig. 4.3. The bonding arrangement and the resulting specimen configuration. Dimensions are given in millimetres (not to scale).

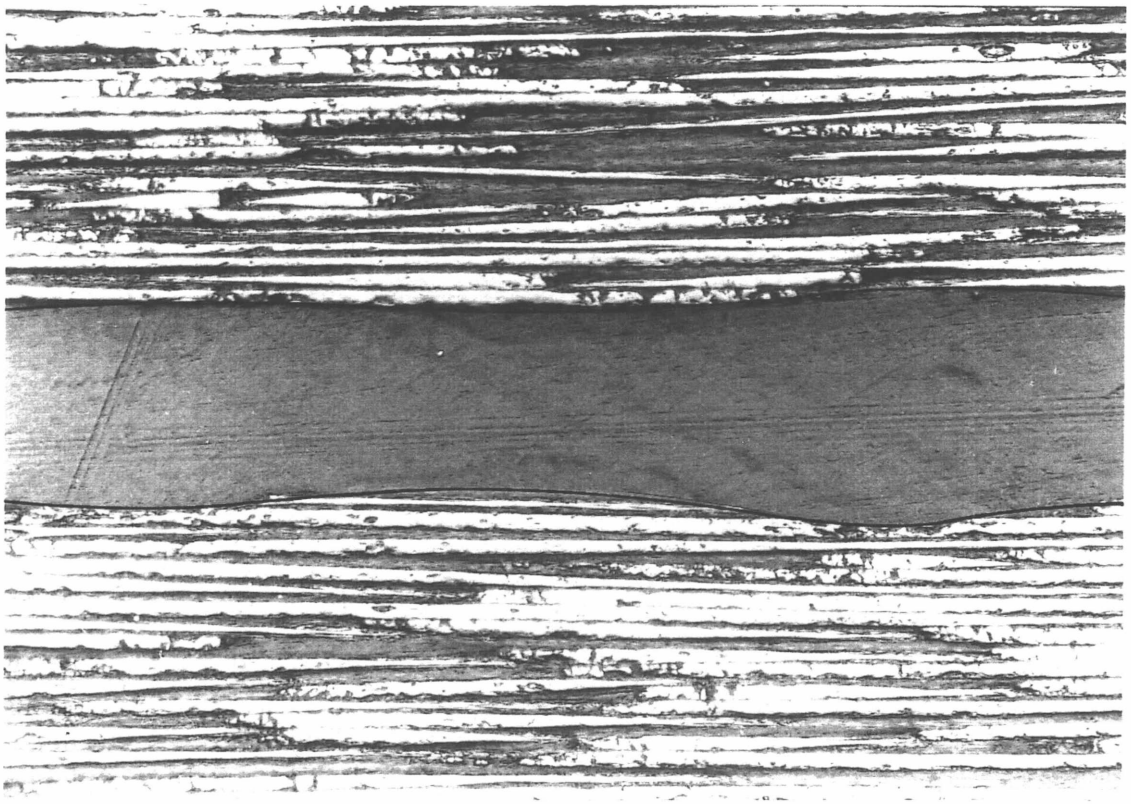


Fig. 4.4. Variations in bondline thickness due to peel-ply impression.

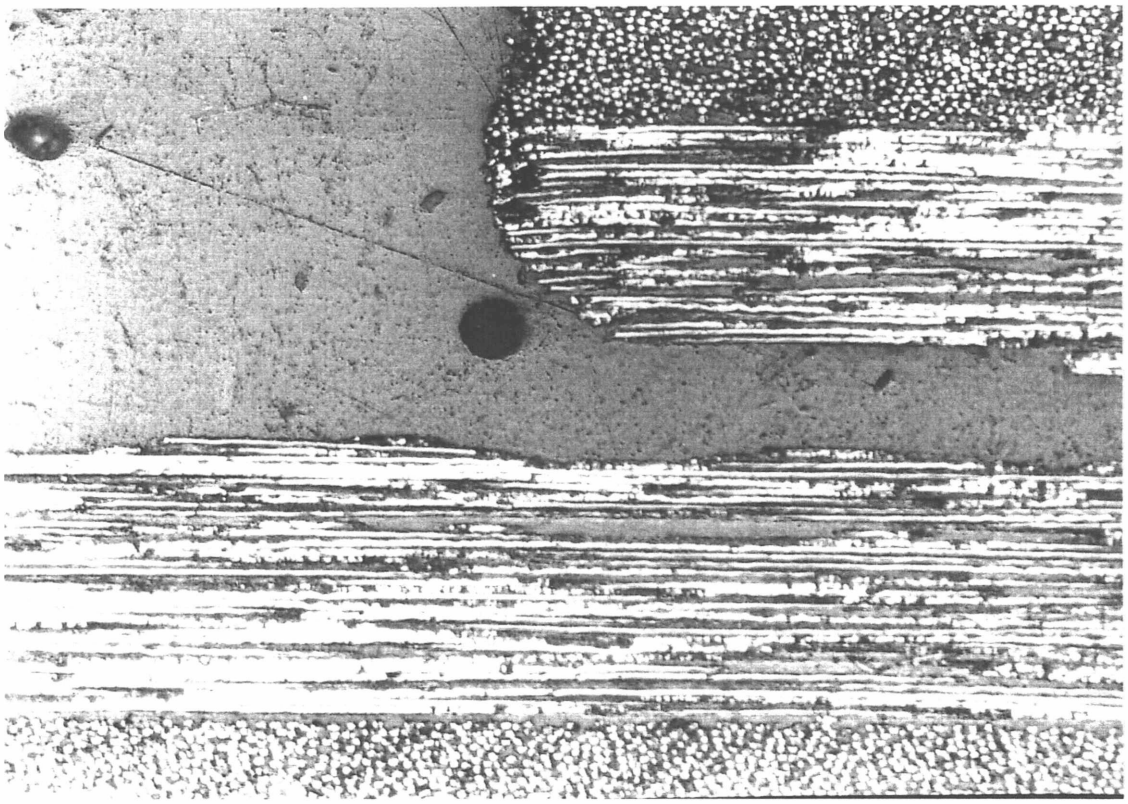


Fig. 4.5. Increase of adhesive layer thickness at end of lap due to rounding of adherend edge as a result of sand blasting.

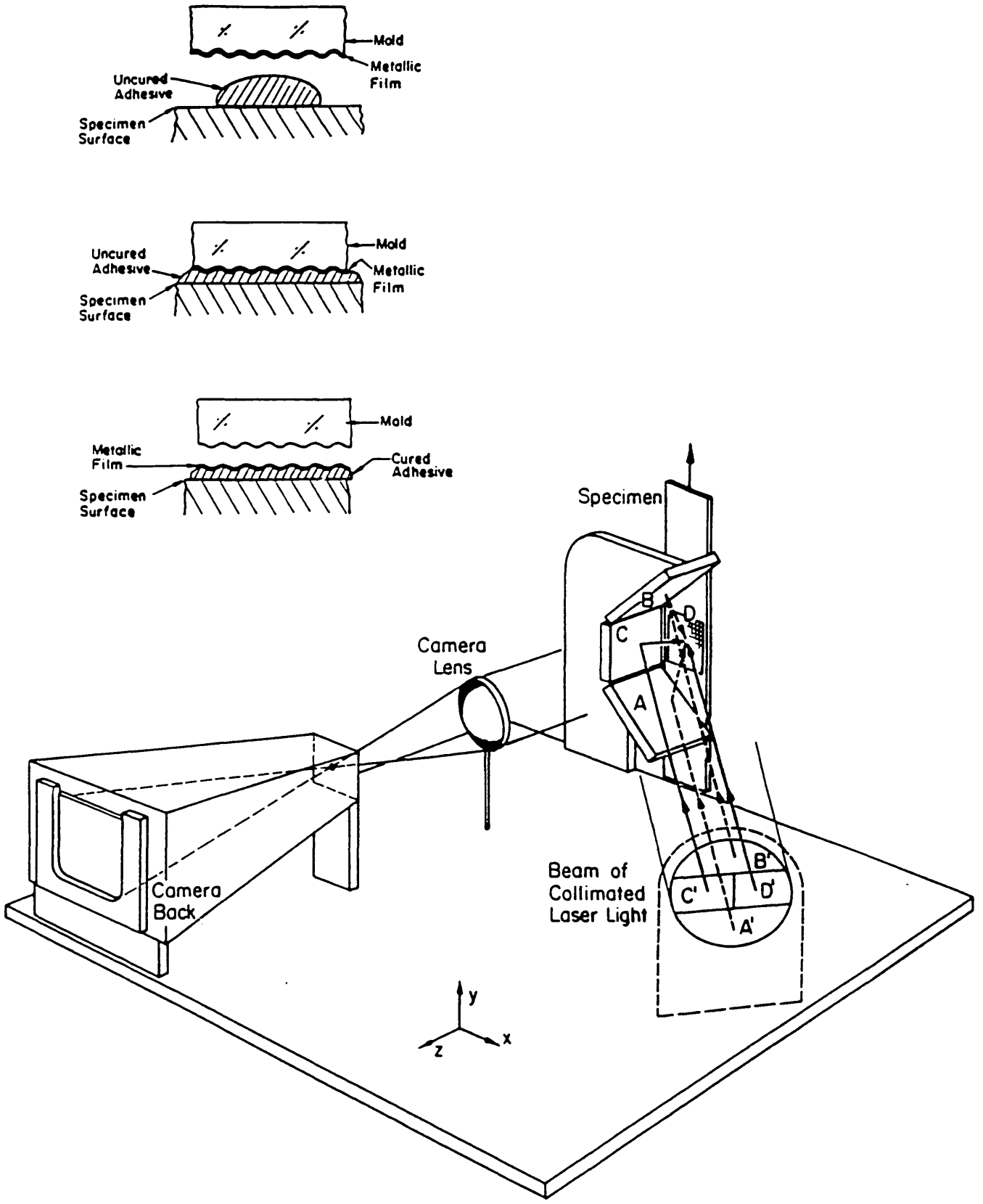


Fig. 4.6. Steps to produce specimen grating by replication process and four-beam optical arrangement [79].

Chapter 5

JOINTS WITH SIX-PLY ADHERENDS



5.1 INTRODUCTION

The performance is presented of joints with six-ply adherends with the following stacking sequences:

A: $[0/\pm 45]_s$.

B: $[\pm 45/0]_s$.

The l/t ratio used is 33.3. The bending stiffness parameter k_b and the predicted stresses using Hart-Smith's analysis are evaluated. A comparison is made between linear and nonlinear finite element analyses. Joint strains and stresses predicted by a nonlinear finite element analysis are compared to the material ultimate strains and stresses.

5.2 EXPERIMENTAL RESULTS

The experimental results are given in Table 5.1. The results indicate that joints with stacking sequence B are stronger than those with stacking sequence A. Fig. 5.1 shows failure of the joints outside the overlap region. It should be noted that with thin adherends, the adhesive fillet tends to spread over the adherend and the neat 45° fillet angle associated with thicker adherends is not formed.

5.3 CONTINUUM ANALYSIS

Table 5.2 shows adherend mechanical properties and stresses from Hart-Smith's analysis. As mentioned in Chapter 3, the bending stiffness parameter k_b is best compared for adherends having the same surface plies for a given set of stacking sequences. Thus k_b does not act, in this case, as a joint ranking factor. The same argument applies to the flexural rigidity parameter D. The higher value of the effective bending Poisson's ratio of stacking sequence B can only act to increase the stiffness of the laminate in bending due to the anti-clastic curvature.

The coefficient of mutual bend-twist coupling is not incorporated in Hart-Smith's analysis. However, this mechanical property affects the performance of a joint and its value is affected by stacking sequence changes. The coefficient of mutual bend-twist coupling of stacking sequence B is 40% lower than that of stacking sequence A. Clearly the reduced twisting of stacking sequence B will result in lower shear stresses set-up in a joint with stacking sequence B than those occuring in a joint with stacking sequence A. A joint ranking factor will be proposed in Chapter 10 which encompasses the above mechanical properties of the adherends.

The adherend bending stress for stacking sequence B is lower than that for stacking sequence A due to the reduced eccentricity factor k as a result of the lower flexural rigidity of stacking sequence B. The maximum adherend stress next to the bondline at the end of the overlap, compared to the strength of the surface plies, is either under predicted for stacking sequence A (782.4 N/mm^2) or over predicted for stacking sequence B (829.5 N/mm^2). The ultimate tensile strength of a 0° ply is 1540 N/mm^2 and that of ±45° plies is 230 N/mm^2. The maximum peel stress in the adhesive layer for stacking sequences A and B (70.8 N/mm^2 and 66.0 N/mm^2 respectively) approaches the tensile strength of the adhesive (68 N/mm^2). However, no peel type of failure in the adhesive has been observed experimentally. As mentioned in Chapter 3, this poor prediction is mainly due to the 'smeared' mechanical properties of the adherends used in the analysis.

H-S averaged yld ?

5.4 FINITE ELEMENT ANALYSIS

The joint geometry and finite element discretisation are shown in Fig. 5.2. Elements of type CPE8R are used for most of the model with some elements of type CPE6 used at the free surface of the adhesive fillet. Each adherend is modelled using 38 elements along its length and 6 elements through its thickness. The adhesive layer is modelled using 16 elements along its length and two elements through its thickness. An adhesive fillet contained 36 elements. The results of linear and nonlinear analyses are presented in Figs. 5.3–5.18.

5.5 DISCUSSION

The dominant mode of failure with these adherends is that of adherend fracture outside the bonded region. From Table B.1, Appendix B, the tensile strength of stacking sequence B is higher, by about 15%, than that of stacking sequence A. This is due to the 'padding' effect offered by the surface $\pm 45°$ layers to the load bearing $0°$ fibres. Joint strength with stacking sequence B is, however, more than 15% higher than that with stacking sequence A (see Table 5.1) due to factors other than simply tensile strength.

A comparison of stacking sequences A and B in bending is shown in Fig. C.1, Appendix C. Although the bending strength of stacking sequence A is much higher than that of stacking sequence B, the latter stacking sequence allows a higher bending strain at failure. The higher bending strain at failure offered by stacking sequence B allows for a bending moment relief at the end of the overlap. This will consequently result in lower bending stresses at the end of the overlap, though a larger joint rotation may occur than stacking sequence A. This phenomenon is analogous to the yielding effect in metallic adherends.

Large out-of-plane displacement is predicted when a linear analysis is used as shown in Fig. 5.3 for stacking sequence A. Fig. 5.4 compares the nonlinear adherend displacements of the two stacking sequences along their centrelines. The predicted maximum displacements at the end of the overlap region are in the order of a fraction of a millimetre. These displacements have been confirmed experimentally by using dial test indicators. Figs. 5.5 and 5.6 show adherend

longitudinal direct strain distributions at the end of the lap and at the fillet tip positions respectively. Higher longitudinal direct strains are attained at the fillet tip than at the end of the lap. However, usually fillet fracture occurs before adherend failure and strain maxima will shift to the end of lap position prior to ultimate joint failure.

5.5.1 Stacking sequence A: $[0/\pm 45]_s$

Figs. 5.7–5.12 compare linear and nonlinear strains and stresses at the centreline of the 0° ply next to the bondline at the fillet region. From Fig. 5.7, the maximum nonlinear longitudinal direct strain in the 0° ply (just over 1.2%), occuring at the fillet tip, has approached the ultimate longitudinal strain (1.25%) indicating adherend failure as observed experimentally. From Fig. 5.8 the corresponding maximum nonlinear stress (1670 N/mm^2) also indicates 0° ply failure as the ultimate tensile strength of this ply is 1540 N/mm^2. The gross over-estimation of the linear analysis is only but too apparent. Both the nonlinear peel and shear strains and stresses along the centreline of the 0° ply are below their respective ultimate values—see Figs. 5.9–5.12.

The nonlinear longitudinal and transverse direct and shear strain and stress distributions along the centreline of the adhesive layer are shown in Figs. 5.13 and 5.14 respectively. From Fig. 5.13, the maximum longitudinal and transverse direct strains (2.2% and 0.7% respectively) are below the ultimate tensile strain of the adhesive (3.5%). However, the peak shear strain (6.2%) exceeds the ultimate shear strain of the adhesive (4.2%—assuming a linear shear stress-strain relationship). This result indicates that, in this case, the nonlinear shear stress-strain relationship of the adhesive needs to be modelled as no shear type of failure in the adhesive has been observed experimentally. From Fig. 5.14, both the maximum longitudinal direct and shear stresses (80 N/mm^2 and 69 N/mm^2 respectively) have exceeded the ultimate tensile and shear strengths of the adhesive (68 N/mm^2 and 49 N/mm^2 respectively) indicating, again, the need for nonlinear material modelling. The peak transverse direct stress (47 N/mm^2) is below its respective ultimate value.

5.5.2 Stacking sequence B: $[\pm 45/0]_s$

Figs. 5.15 and 5.16 show the nonlinear longitudinal and transverse direct and shear strain and stress distributions respectively along the centreline of the $+45°$ layer next to the bondline at the fillet region. As mentioned in Chapter 3, the longitudinal direct strain in $\pm 45°$ layers is equivalent to the intralaminar shear strain. Thus, from Fig. 5.15, the maximum longitudinal direct strain (2.3%) has exceeded the ultimate linear shear strain of the composite (1.61%) indicating shear fracture as observed experimentally. The peak transverse direct strain (0.3%) is below its respective ultimate value (0.77%).

Figs. 5.17 and 5.18 show the nonlinear longitudinal and transverse direct and shear strain and stress distributions respectively along the centreline of the adhesive layer. Similar arguments to those for stacking sequence A may be made.

5.6 CONCLUSIONS

1. Joints with stacking sequence A are weaker than those with stacking sequence B due to the following reasons:
   a) The bending moment relief offered by the 'soft' surface ply group of stacking sequence B outweighs the benefit of the unidirectional surface layer of stacking sequence A. This phenomenon is analogous to the yielding effect in metallic adherends.
   b) The coefficient of mutual bend-twist coupling and bending Poisson's ratio act together in favour of a stronger joint with stacking sequence B.
   c) The basic tensile strength of stacking sequence A is lower than that of stacking sequence B.
2. The bending stiffness parameter k_b does not act as a joint ranking factor as it does not address directly the influence of laminates' surface plies. The poor prediction of the adherend and adhesive stresses by Hart-Smith's analysis is mainly due to the 'smeared' mechanical properties of the adherends.
3. The geometrically nonlinear finite element analysis predicts joint failure using either maximum strain or maximum stress failure criteria. However, the

nonlinear shear stress-strain relationship of the adhesive needs to be modelled. The linear finite element analysis grossly over-estimates joint strains and stresses.

Table 5.1. Test results.

	Stress at failure (N/mm^2)			
Stacking sequence	Min.	Max.	Mean	C_v (%)
A: $[0/\pm45]_s$	457.5	529.9	505.7	6.5
B: $[\pm45/0]_s$	611.5	730.0	652.1	8.2

C_v—Coefficient of variation

Table 5.2. Adherend mechanical properties and stresses from Hart-Smith's analysis.

Stacking sequence	E_m	E_b	ν_m	ν_b	D	k_b	m	P	σ_{av}	σ_b	σ_{max}	σ_p
A: $[0/\pm45]_s$	61.6	103.8	0.668	0.491	4.8	1.229	−0.240	388.4	517.9	264.5	782.4	70.8
B: $[\pm45/0]_s$	61.6	26.5	0.668	0.654	1.6	0.417	−0.144	514.4	685.9	143.6	829.5	66.0

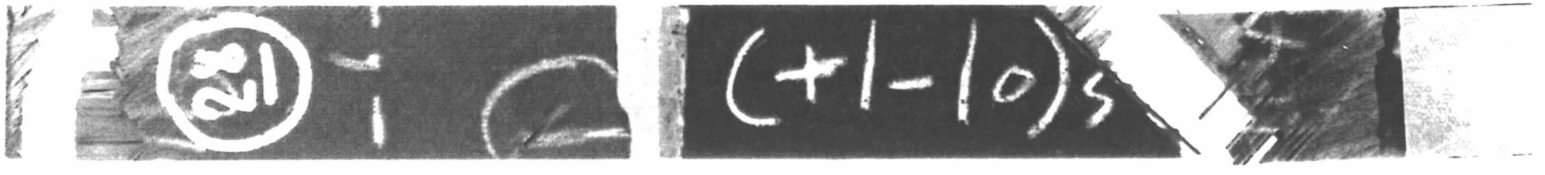
E_m— effective membrane elastic modulus of adherends in direction of applied load ($\times 10^3$ N/mm^2).
E_b— effective bending elastic modulus of adherends corresponding to a bending moment about an in-plane axis normal to the direction of applied load ($\times 10^3$ N/mm^2).
ν_m— effective membrane Poisson's ratio of adherends associated with E_m.
ν_b— effective bending Poisson's ratio of adherends associated with E_b.
D— flexural rigidity of adherends ($\times 10^3$ Nmm).
k_b— bending stiffness parameter.
m— coefficient of mutual bend-twist coupling corresponding to a bending moment about an in-plane axis normal to the direction of applied load.
P— experimental mean load at failure per unit joint width (N/mm).

σ_{av}— adherend average stress.
σ_b— adherend bending stress.
σ_{max}— adherend maximum stress.
σ_p— adhesive peel stress.

All stresses are given in N/mm^2.



(a) Stacking sequence A: $[0/\pm 45]_s$.



(b) Stacking sequence B: $[\pm 45/0]_s$.

Fig. 5.1. The bonded specimens after fracture.

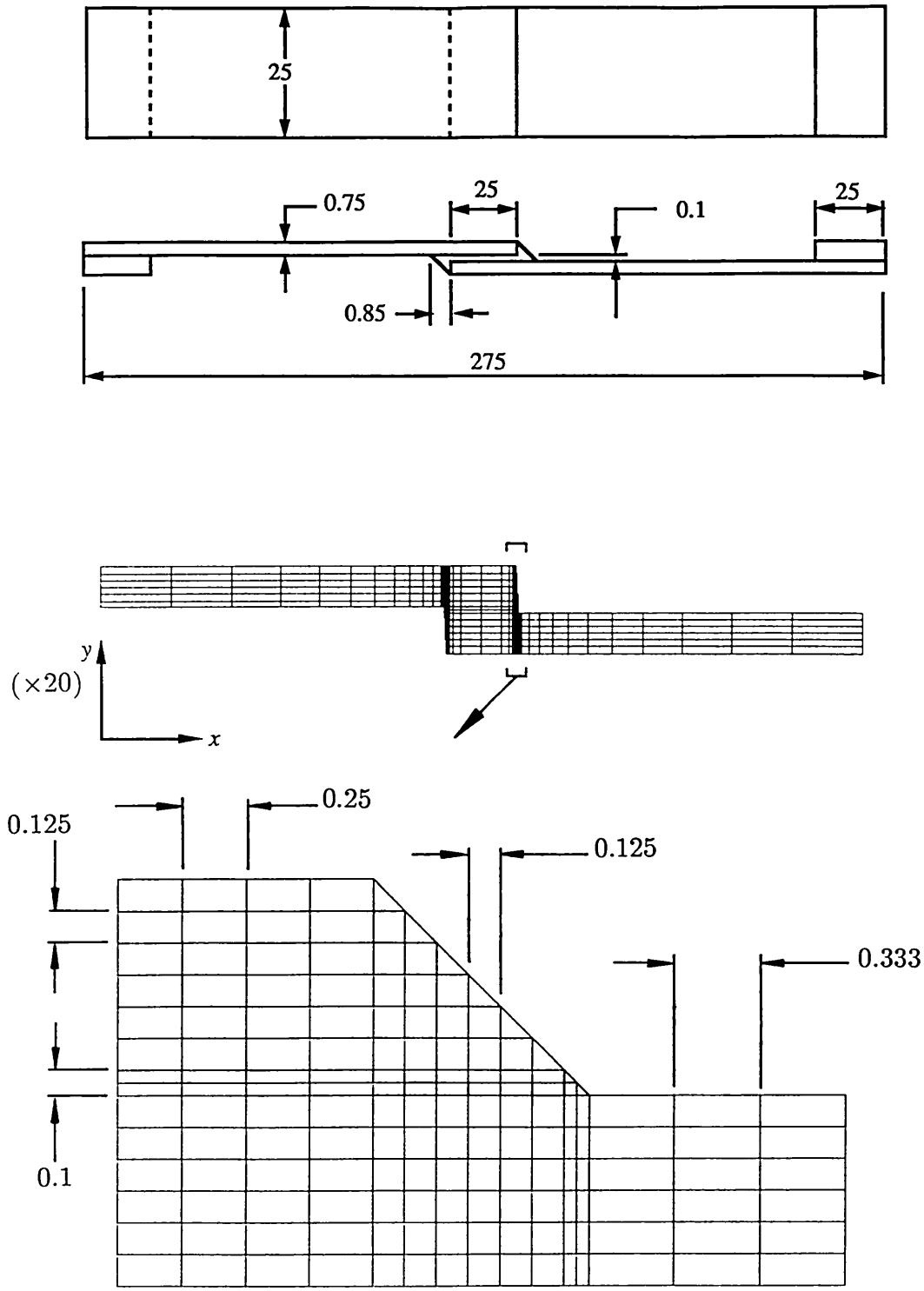


Fig. 5.2. Geometry and finite element model of six-ply adherend joint. Dimensions are given in millimetres (not to scale).

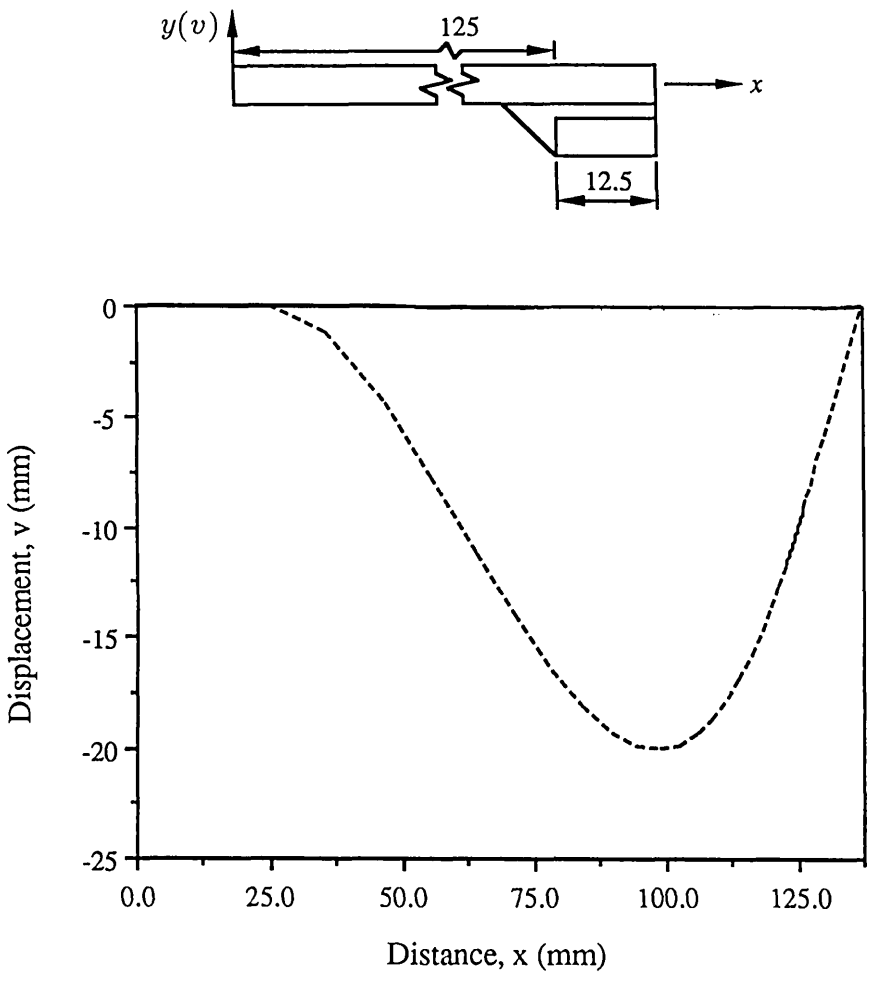


Fig. 5.3. Out-of-plane displacement of the adherend centreline using linear analysis. Stacking sequence A: $[0/\pm 45]_s$ at 505.7 N/mm^2 applied stress.

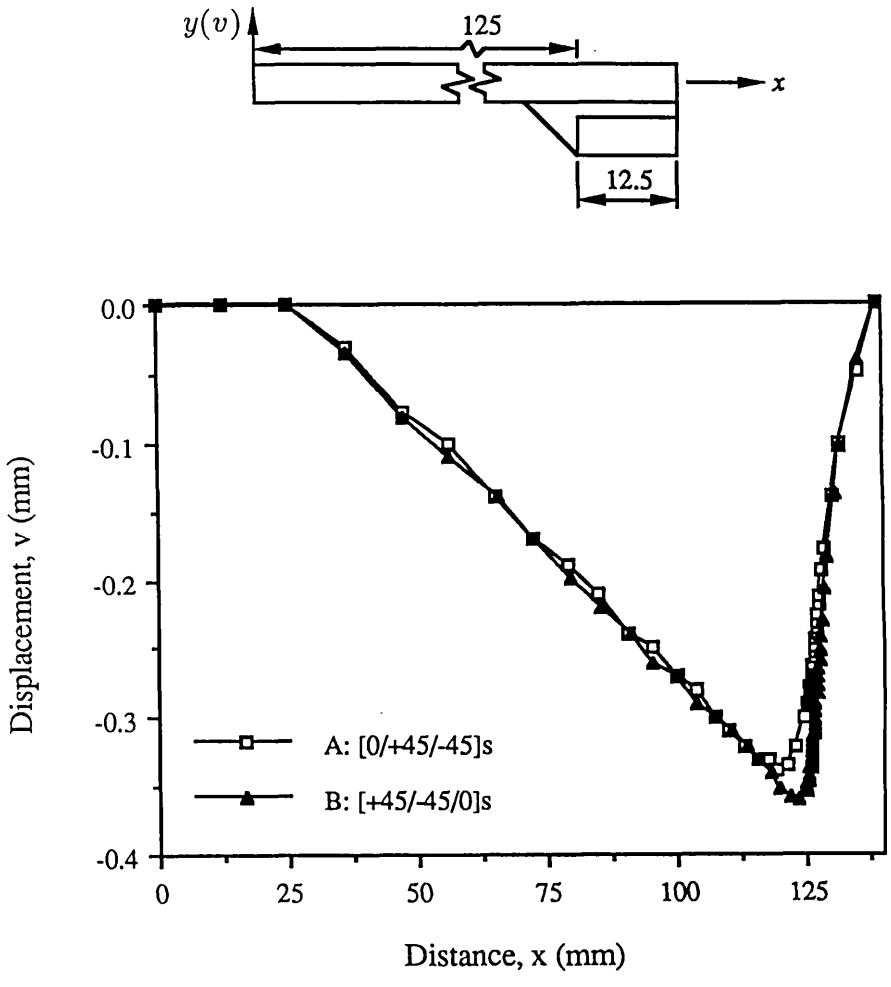


Fig. 5.4. Out-of plane displacements of the adherend centrelines using nonlinear analysis. The applied stresses for stacking sequences A and B are 505.7 N/mm^2 and 652.1 N/mm^2 respectively.

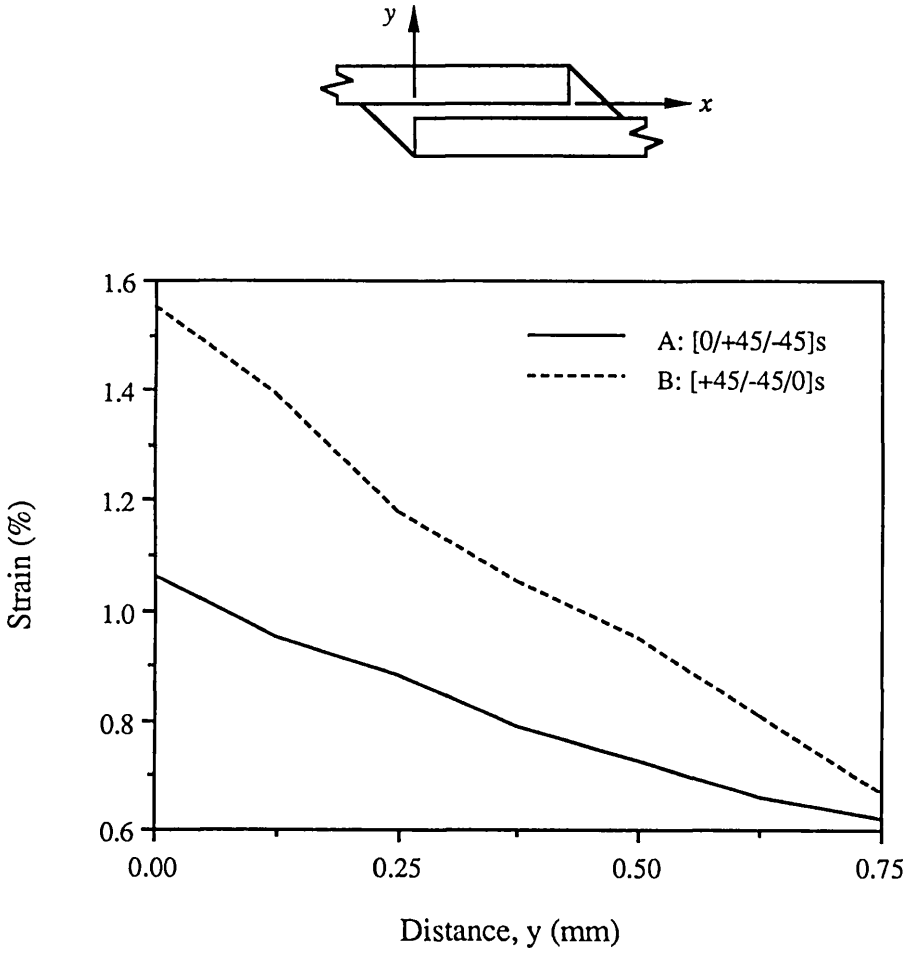


Fig. 5.5. Adherend longitudinal direct strain (ϵ_{xx}) distribution along the y-axis at the end of the lap using nonlinear analysis. The applied stresses for stacking sequences A and B are 505.7 N/mm^2 and 652.1 N/mm^2 respectively.

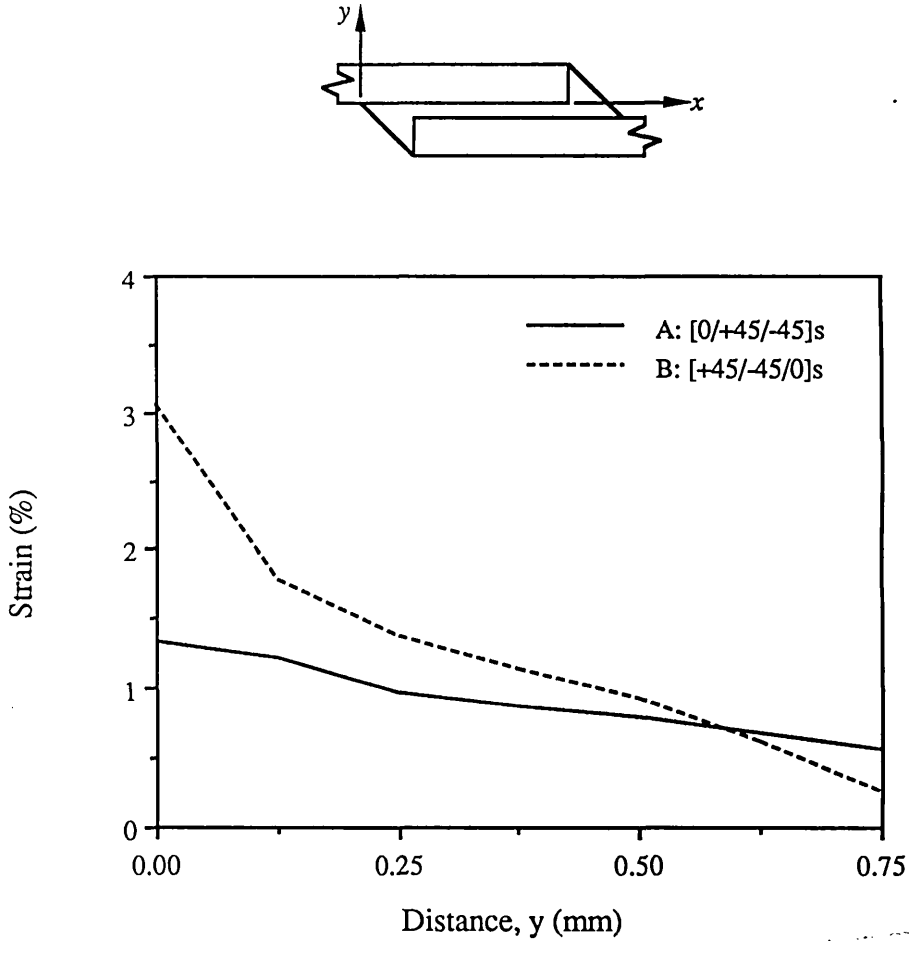


Fig. 5.6. Adherend longitudinal direct strain (ϵ_{xx}) distribution along the y-axis at the fillet tip using nonlinear analysis. The applied stresses for stacking sequences A and B are 505.7 N/mm^2 and 652.1 N/mm^2 respectively.

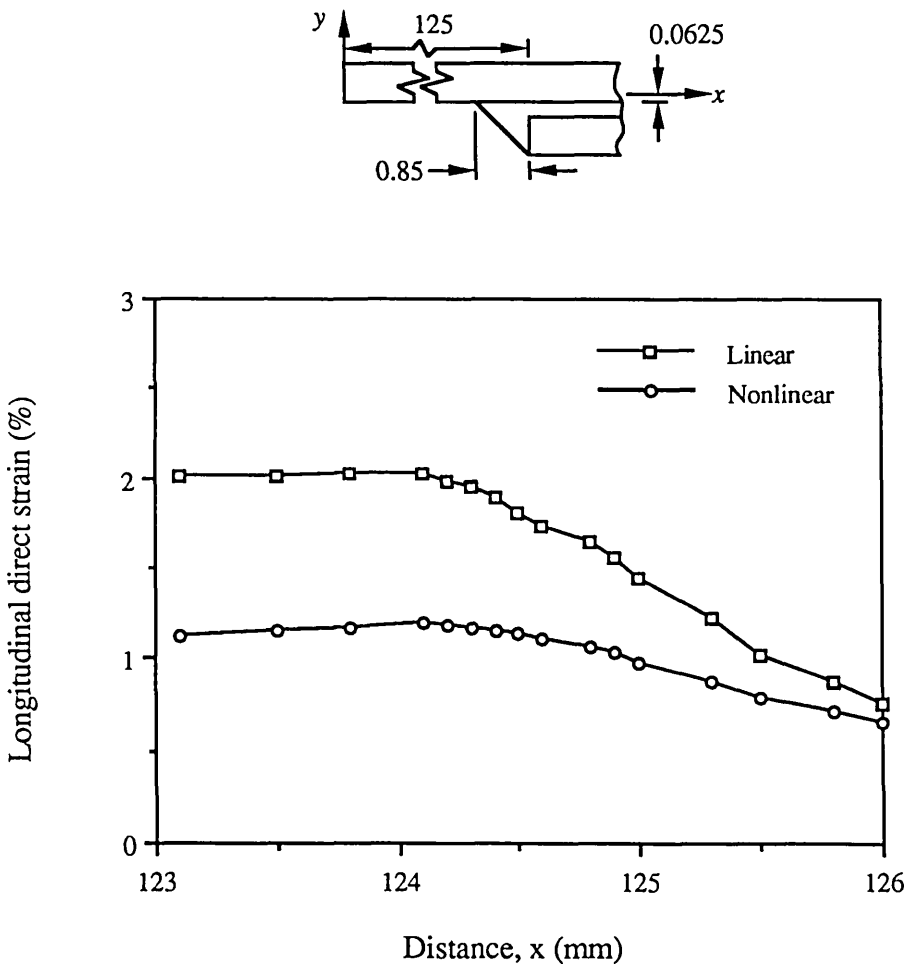


Fig. 5.7. Longitudinal direct strain (ϵ_{xx}) distribution along the centreline of the 0° ply next to the bondline. Stacking sequence A: $[0/\pm 45]_s$ at 505.7 N/mm^2 applied stress.

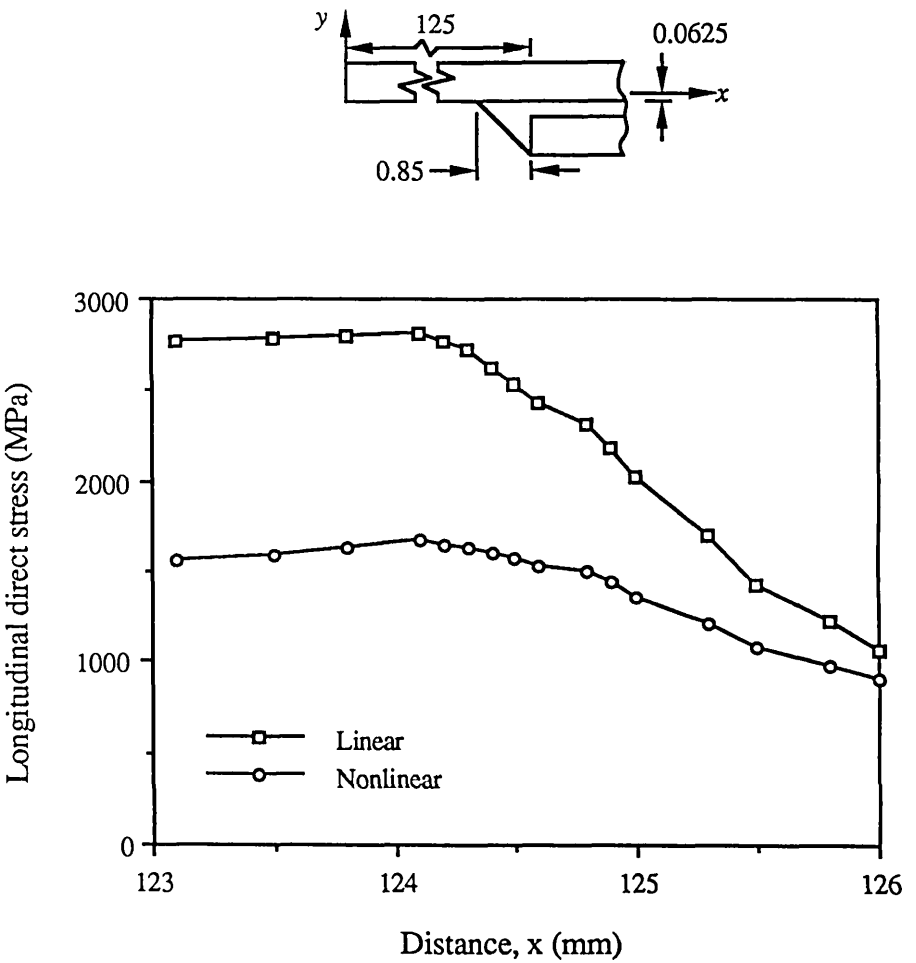


Fig. 5.8. Longitudinal direct stress (σ_{xx}) distribution along the centreline of the 0° ply next to the bondline. Stacking sequence A: $[0/\pm 45]_s$ at 505.7 N/mm^2 applied stress.

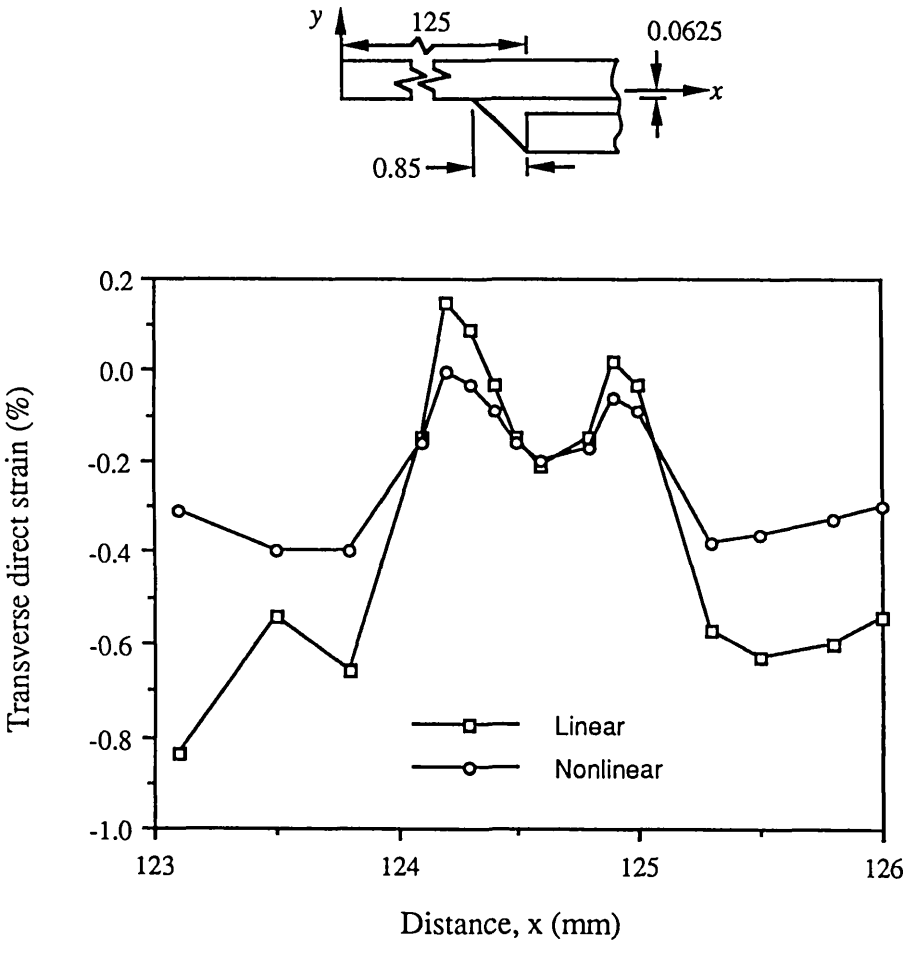


Fig. 5.9. Transverse direct strain (ϵ_{yy}) distribution along the centreline of the 0° ply next to the bondline. Stacking sequence A: $[0/\pm 45]_s$ at 505.7 N/mm^2 applied stress.

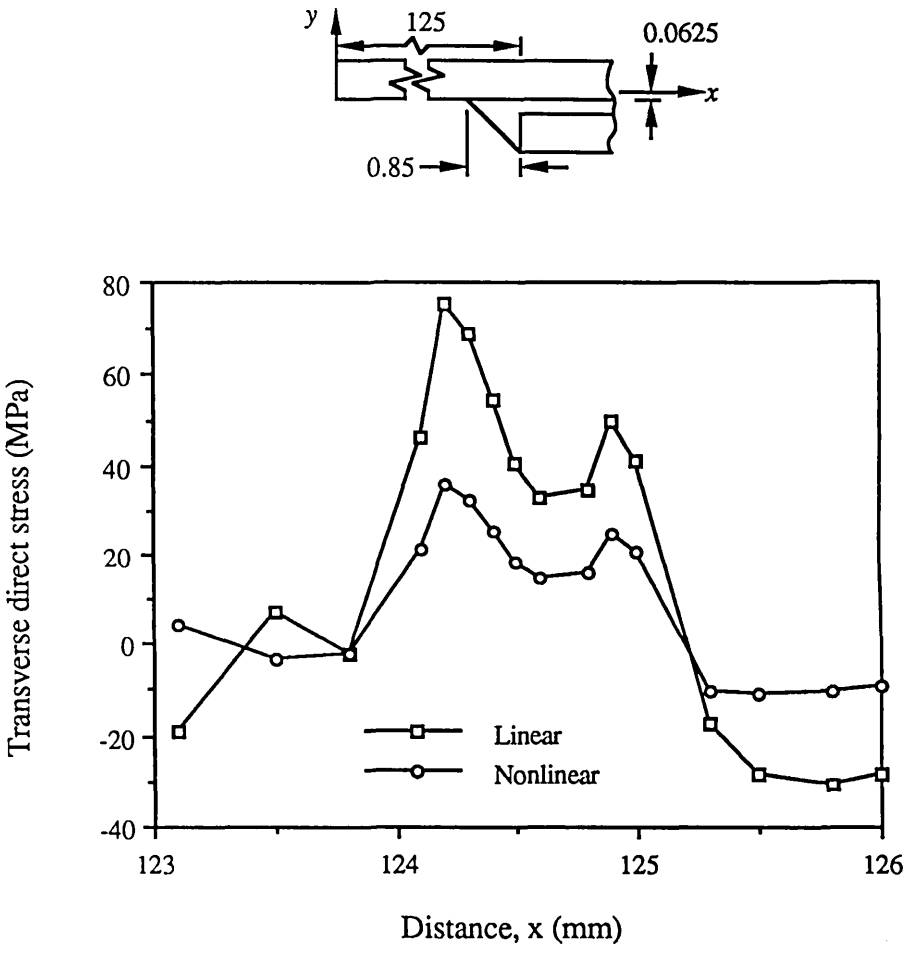


Fig. 5.10. Transverse direct stress (σ_{yy}) distribution along the centreline of the 0° ply next to the bondline. Stacking sequence A: $[0/\pm 45]_s$ at 505.7 N/mm^2 applied stress.

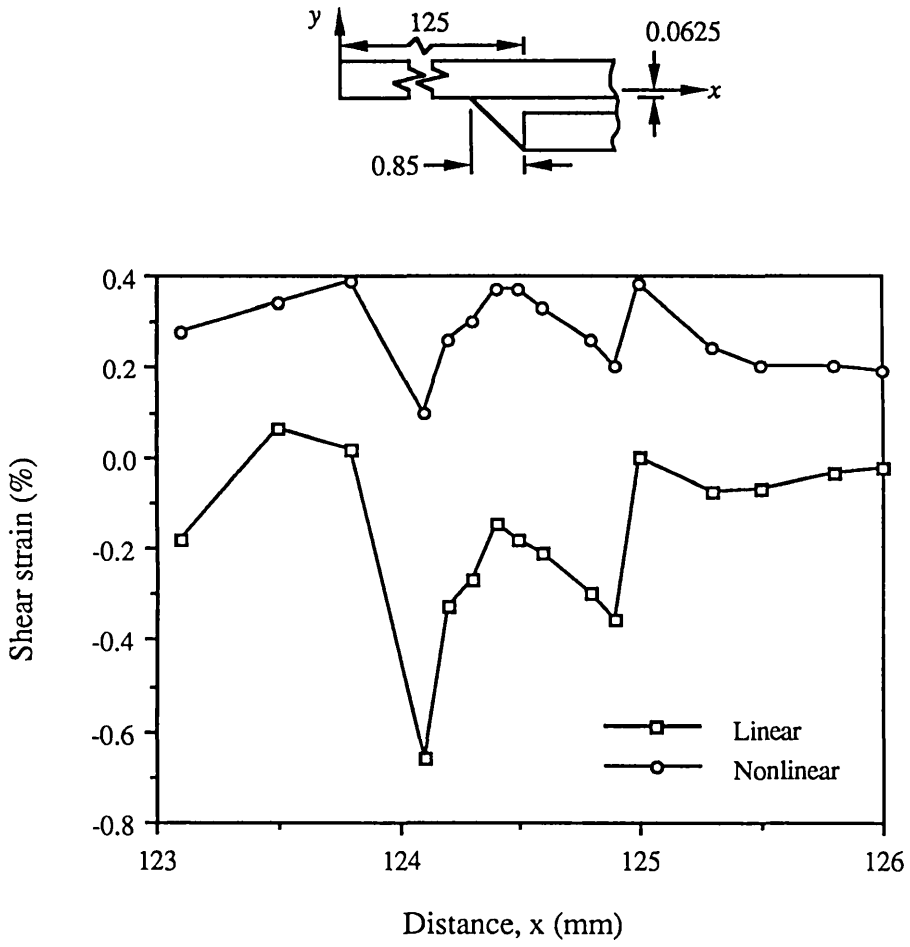


Fig. 5.11. Shear strain (γ_{xy}) distribution along the centreline of the 0° ply next to the bondline. Stacking sequence A: $[0/\pm 45]_s$ at 505.7 N/mm^2 applied stress.

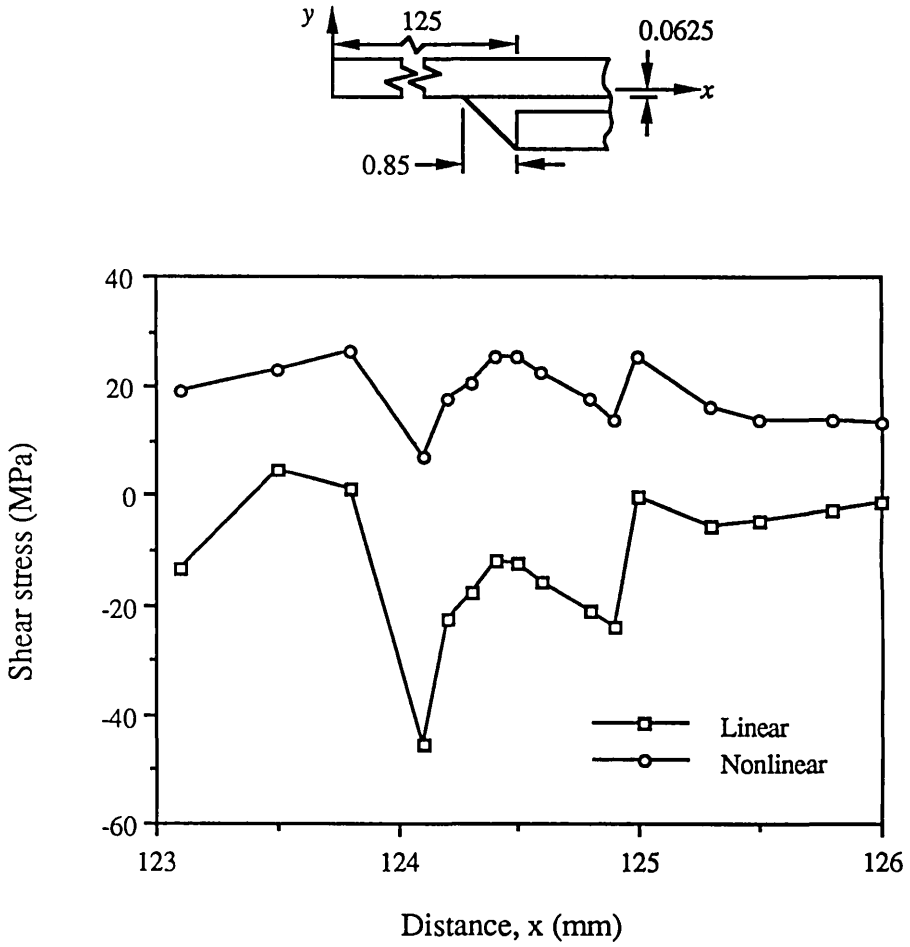


Fig. 5.12. Shear stress (τ_{xy}) distribution along the centreline of the 0° ply next to the bondline. Stacking sequence A: $[0/\pm 45]_s$ at 505.7 N/mm^2 applied stress.

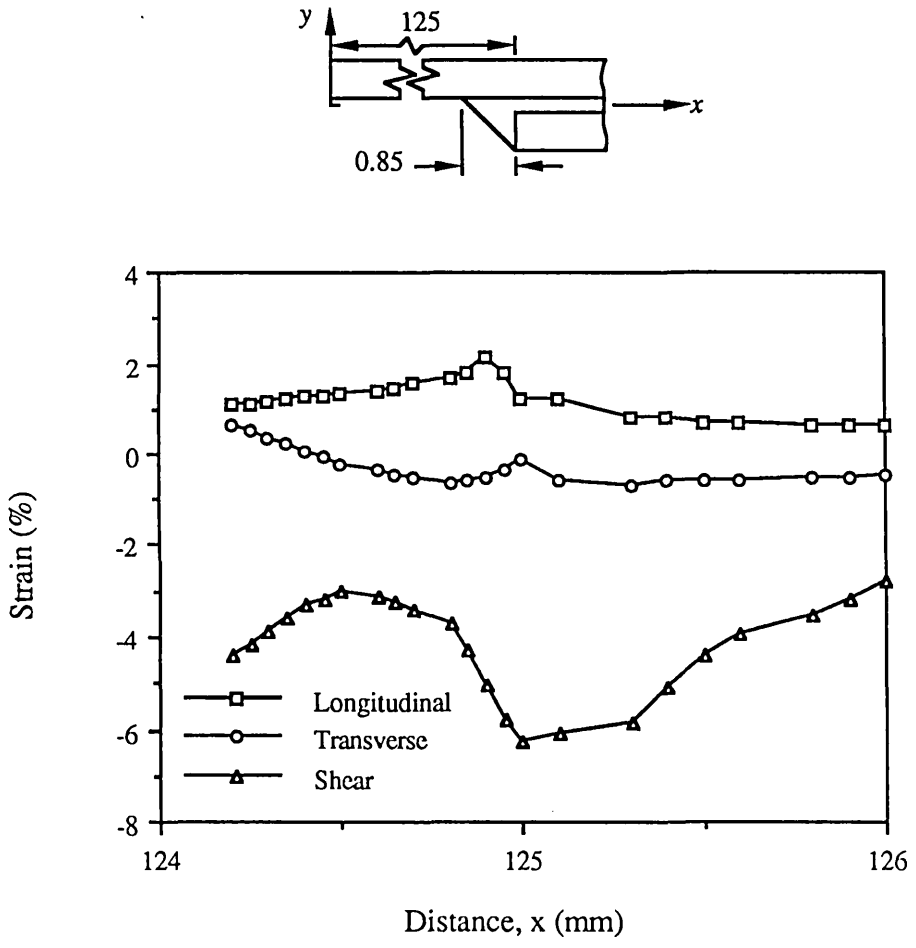


Fig. 5.13. Longitudinal and transverse direct and shear strain (ϵ_{xx}, ϵ_{yy} and γ_{xy} respectively) distributions along the centreline of the adhesive layer using nonlinear analysis. Stacking sequence A: $[0/\pm 45]_s$ at $505.7\,\mathrm{N/mm^2}$ applied stress.

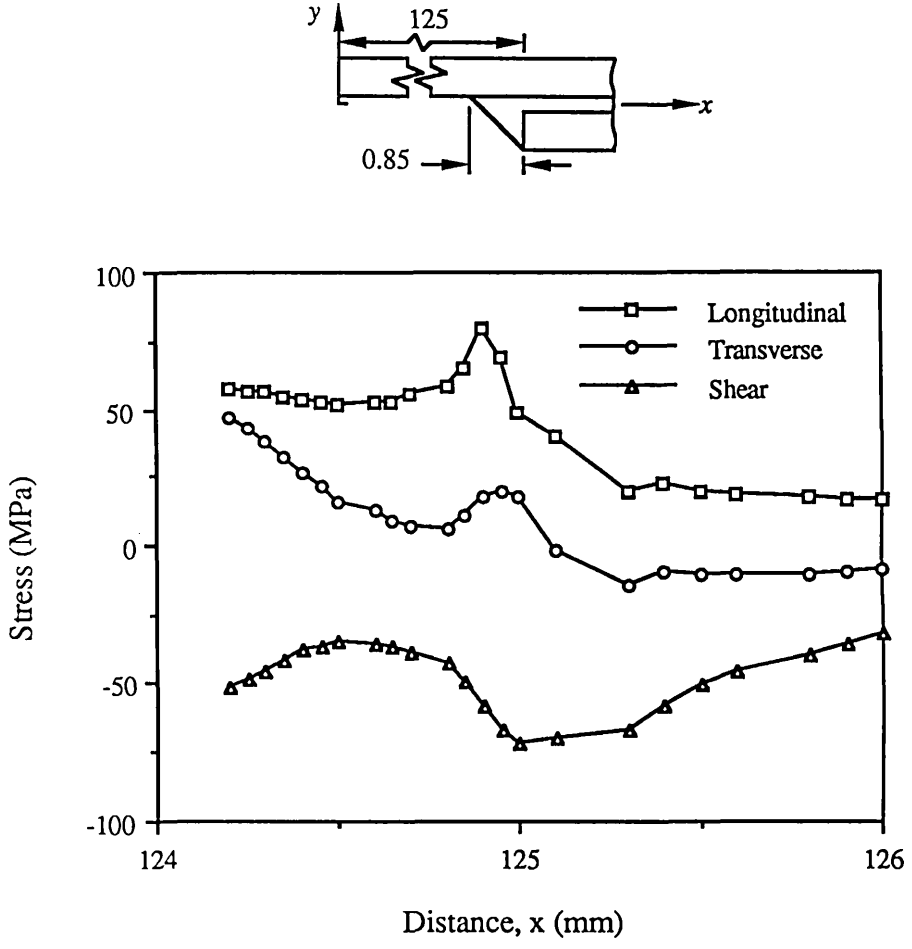


Fig. 5.14. Longitudinal and transverse direct and shear stress (σ_{xx}, σ_{yy} and τ_{xy} respectively) distributions along the centreline of the adhesive layer using nonlinear analysis. Stacking sequence A: $[0/\pm 45]_s$ at $505.7\,\mathrm{N/mm^2}$ applied stress.

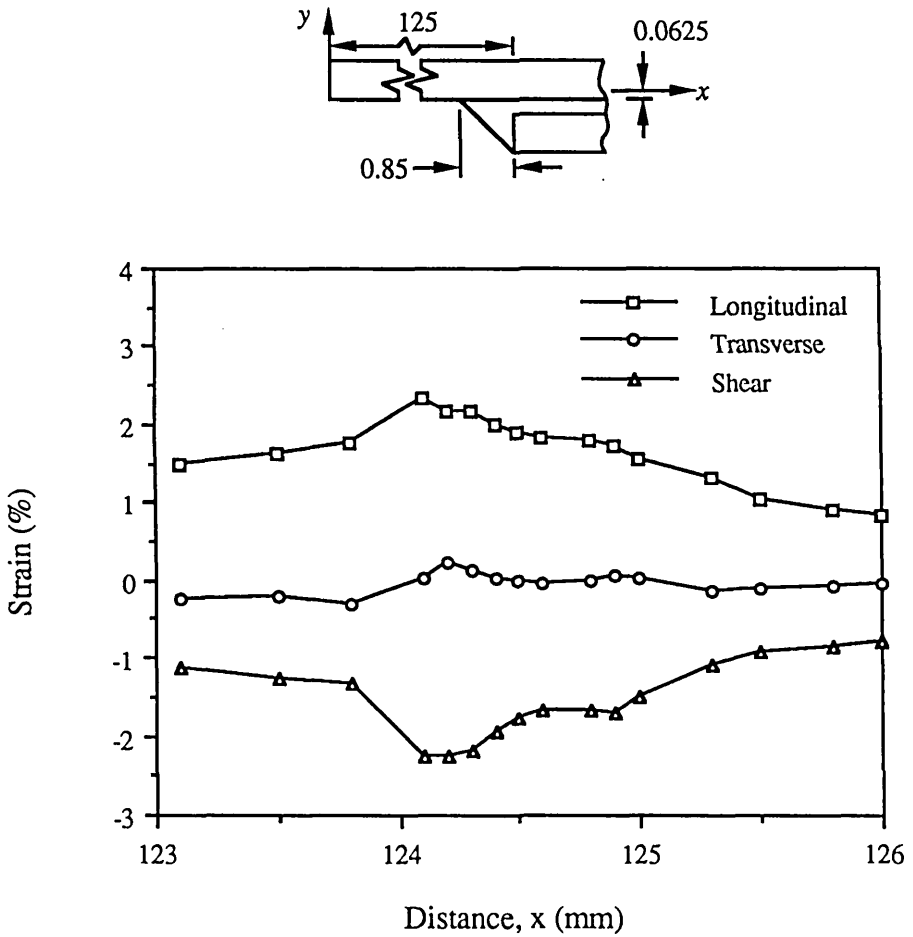


Fig. 5.15. Longitudinal and transverse direct and shear strain (ϵ_{xx}, ϵ_{yy} and γ_{xy} respectively) distributions along the centreline of the +45° layer next to the bondline using nonlinear analysis. Stacking sequence B: $[\pm 45/0]_s$ at 652.1 N/mm^2 applied stress.

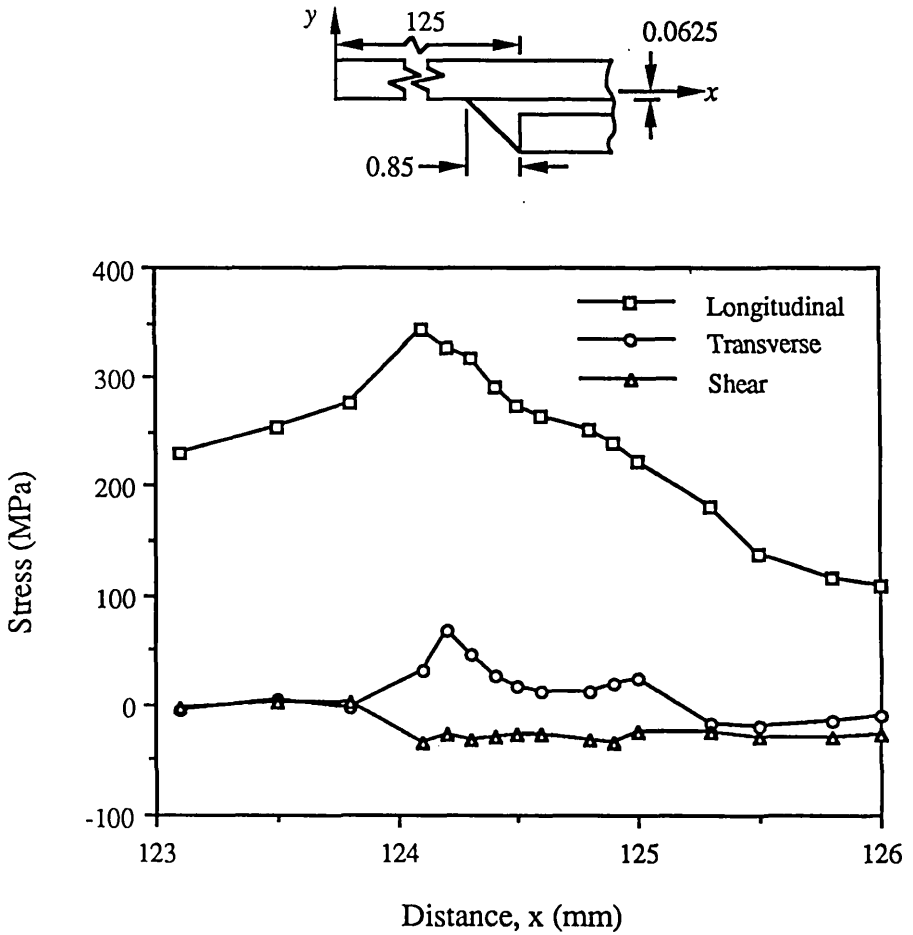


Fig. 5.16. Longitudinal and transverse direct and shear stress (σ_{xx}, σ_{yy} and τ_{xy} respectively) distributions along the centreline of the +45° layer next to the bondline using nonlinear analysis. Stacking sequence B: $[\pm 45/0]_s$ at 652.1 N/mm^2 applied stress.

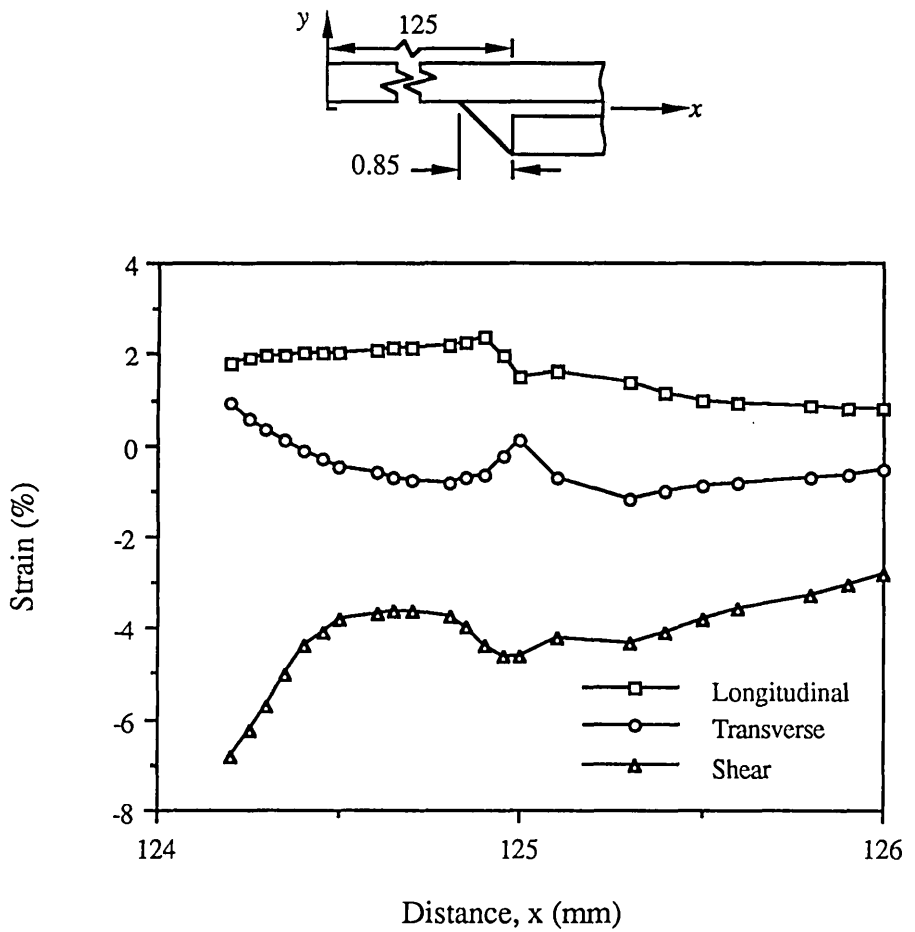


Fig. 5.17. Longitudinal and transverse direct and shear strain (ϵ_{xx}, ϵ_{yy} and γ_{xy} respectively) distributions along the centreline of the adhesive layer using nonlinear analysis. Stacking sequence B: $[\pm 45/0]_s$ at 652.1 N/mm^2 applied stress.

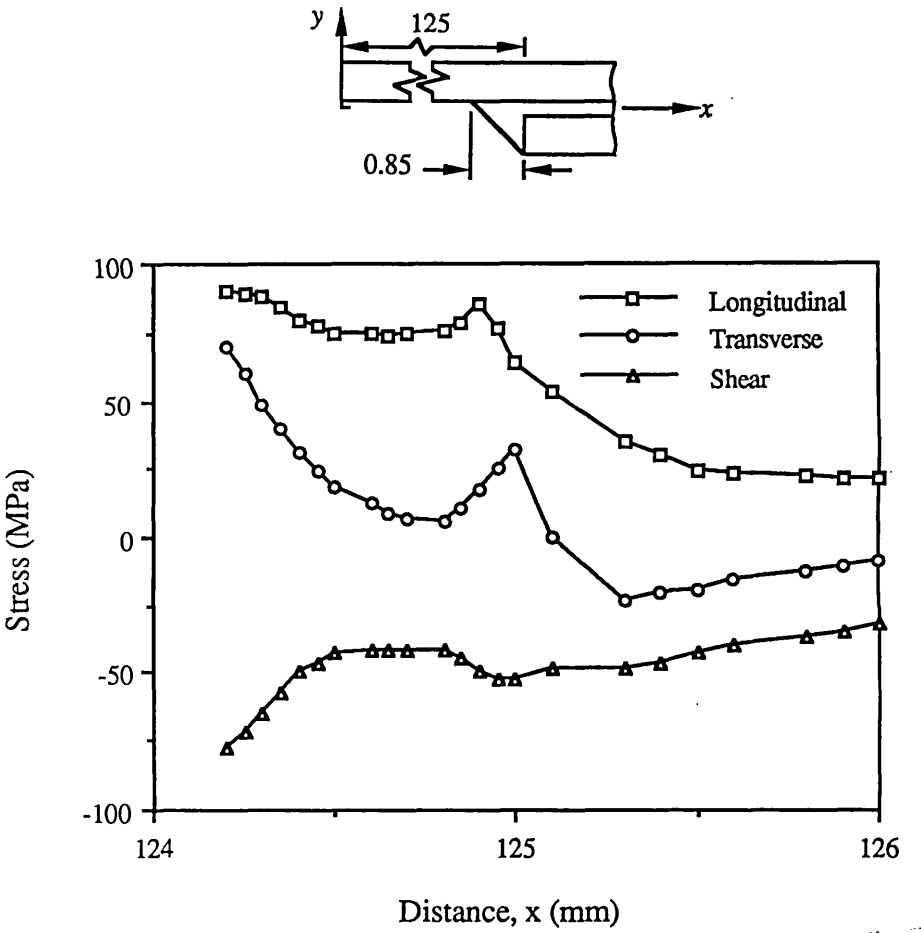


Fig. 5.18. Longitudinal and transverse direct and shear stress (σ_{xx}, σ_{yy} and τ_{xy} respectively) distributions along the centreline of the adhesive layer using nonlinear analysis. Stacking sequence B: $[\pm 45/0]_s$ at 652.1 N/mm^2 applied stress.

Chapter 6

JOINTS WITH EIGHT-PLY ADHEREND S

6.1 INTRODUCTION

The performance is presented of joints with eight-ply adherends with the following stacking sequences:

D: $[\pm 45/0_2]_s$.

E: $[0/\pm 45/0]_s$.

F: $[0_2/\pm 45]_s$.

The l/t ratios used are 25 and 12.5. A comparison is made between Hart-Smith's and linear and geometrically nonlinear finite element analyses. A detailed account of the mechanisms of failure is given. This is supported by numerical and fractographic results.

6.2 EXPERIMENTAL RESULTS

The experimental results are given in Table 6.1. For the 25 mm overlap, the order of the stacking sequence relative to mean joint strength is as follows: E, F and D. For the 12.5 mm overlap, joints with stacking sequences D and E are of equal mean strength followed by joints with stacking sequence F. However, the maximum strength values for the 12.5 mm overlap follow the same order as that for the 25 mm overlap. The fractured joints are shown in Fig. 6.1. All failures are within the adherends, i.e. no cohesive or adhesive failures.

The percentage increases in joint strength, for stacking sequences D, E and F, as the l/t ratio is increased from 12.5 to 25 are 16%, 30% and 24% respectively.

This seems to suggest that the effect of the l/t ratio is influenced by the adherend stacking sequence and by the surface plies. As the l/t ratio is increased, higher joint strengths may be attained with adherends having 0° surface layer than those with ±45° surface plies.

6.3 CONTINUUM ANALYSIS

The adherend mechanical properties and stresses from Hart-Smith's analysis are given in Table 6.2. It can be seen that the flexural rigidity and bending stiffness parameters for stacking sequence F are higher than those for stacking sequence E. However, contrary to expectations, joints with stacking sequence F are weaker than those with stacking sequence E.

Comparing stacking sequences D, E and F, it can be seen that the bending Poisson's ratio decreases while the coefficient of mutual bend-twist coupling increases as the bending stiffness increases. Thus, it is thought that a certain combination of the adherend mechanical properties may determine the strongest joint.

The relative increase in the adherend bending and adhesive peel stresses with the decrease in the overlap length can be seen from Table 6.2(a) and (b). A discussion of the adherend and adhesive stresses obtained using Hart-Smith's analysis will be presented together with comparison to stresses obtained using the finite element method.

6.4 FINITE ELEMENT ANALYSIS

The results of linear finite element analysis, using the FINEL package are shown in Fig. 6.2. It can be seen that as the D_{11} term of the flexural stiffness matrix D is increased, joint deformation is decreased.

Joint geometry (25 mm overlap) and finite element model using the Abaqus system are shown in Fig. 6.3. Elements of type CPE4R are used for most of the model with some elements of type CPE3 used at the free surface of the adhesive fillet. Each layer of the eight-ply adherend is modelled using 48 elements along its length and two elements through its thickness. The adhesive layer is modelled

using 16 elements along its length and two elements through its thickness. An adhesive fillet contained 171 elements. The adherend direct stress distribution, for stacking sequences D, E and F, using nonlinear finite element analysis (Fig. 6.4) is compared to that using Hart-Smith's analysis (Fig. 6.5). The results of nonlinear analysis are presented in Figs. 6.6–6.13.

6.5 DISCUSSION

From Table B.1, Appendix B, the tensile strength of stacking sequence D is higher, by about 15%, than that of stacking sequence F. A comparison of stacking sequences D, E and F in bending is shown in Fig. C.2, Appendix C. Similar arguments to those made in Chapter 5 regarding the tensile and flexural properties of the lamiantes may be made.

The following discussion applies to the 25 mm overlaps but similar arguments may be made for the 12.5 mm overlaps.

6.5.1 Comparison between Hart-Smith's and finite element analyses

A basic assumption in Hart-Smith's work is that the longitudinal direct stress varies linearly through the thickness of the adherend. The finite element analysis however gives ply-by-ply variations. The results are compared in Figs. 6.4 and 6.5. Table 6.3, to which all the comments below relate, shows a comparison between the adherend and adhesive stresses obtained using Hart-Smith's and finite element (Abaqus) analyses for the 25 mm overlap.

Hart-Smith's analysis

Comparing the adherend maximum longitudinal direct stress for stacking sequence D (767 N/mm^2) to the laminate's tensile strength (1031 N/mm^2) does not suggest an adherend failure. If the surface ply strength (230 N/mm^2) is considered, however, the predicted failure stress is over-estimated by approximately a factor of three.

Although the adherend maximum longitudinal direct stresses for stacking sequences E and F (969 N/mm^2 and 938 N/mm^2 respectively), have exceeded the

laminates' tensile strength (901 N/mm^2, assuming stacking sequences E and F have the same strength), indicating possible adherend failure, this is not here an appropriate measure of strength. Of most relevance is the stress in the outermost 0° ply. It is this which resists most of the tensile load, having a tensile strength of 1540 N/mm^2.

There is no significant variation in the adhesive peel stress with stacking sequence changes. This is due to the incorporation of the geometrically nonlinear effect which may not necessarily result in a significantly higher peel stress as the flexibility of the adherends is increased. The tensile strength of the adhesive (68 N/mm^2) has been exceeded, but experiments show no sign of adhesive peel failure.

Linear finite element analysis

Clearly the stresses are grossly over-estimated, exceeding by several times their respective strengths. This is due to not allowing for the bending moment relief as the joint rotates.

The adherend and adhesive stresses predicted for stacking sequence D are by far the most over-estimated of the three stacking sequences. This is to expected as the largest joint rotation occurs with stacking sequence D.

An increase is seen in the adhesive peel stress as the flexibility of the adherends is increased. This may seem reasonable, but in fact it is a direct consequence of not allowing for the bending moment relief.

Nonlinear finite element analysis

Very good agreement is found between the predicted stresses and observed experimental behaviour. The predicted maximum adherend direct stresses have approached their respective ultimate values indicating shear fracture in the +45° ply next to the bondline for stacking sequence D and fibre tensile failure in the 0° layer next to the bondline for stacking sequences E and F.

The predicted adhesive peel stresses are, in all cases, lower than the tensile strength of the adhesive. As stated above, adhesive peel failure has not been

observed experimentally. Again, the lack of variation in the adhesive peel stresses with stacking sequence is due to the bending moment relief brought about by incremental loading with the associated iterations for each load increment.

6.5.2 Mechanisms of failure

The mechanisms of failure of adherends with $\pm 45°$ and $0°$ surface plies are presented. The discussion is supported by results of nonlinear finite element and fractographic analyses.

For all stacking sequences, failure usually initiates by fillet fracture followed by adherend failure. Fillet fracture affects the strain distribution in the adherends. The adherend longitudinal direct strain distribution at the end of the lap and at the fillet tip before fillet fracture are shown in Figs. 6.6 and 6.7 respectively. The shifting of strain maxima to the end of lap position after fillet fracture will be simulated numerically in Chapter 7.

Adherends with $\pm 45°$ surface plies

Fig. 6.14 shows a general two-dimensional view of joint fracture with stacking sequence D. More detailed diagrams of the modes of failure are presented in Figs. 6.15 and 6.16. Failure is initiated by fillet fracture at A (see Figs. 6.15 and 6.17(a)) and proceeds, almost parallel to the adherend edge, towards A'.

From Fig. 6.8, the maximum shear strain in the material axes system γ_{12} in the $+45°$ layer next to the bondline (1.62%) has exceeded the ultimate shear strain (1.61%) indicating intralaminar shear cracking, as observed experimentally. Fig. 6.9 shows the transverse direct and shear strain (in the reference axes system) distributions along the centreline of the $+45°$ layer. It can be seen that the maximum peel strain (0.14%) is well below the ultimate transverse tensile strain (0.77%). Shear cracking in the $+45°$ ply next to the bondline is associated with a 'ductile' adhesive failure as shown in Fig. 6.17(b) and (c).

The distance between one shear crack and the other is between 0.5 and 1 mm in the $+45°$ layer and rather closer in the $-45°$ layer—see Fig. 6.17(d). The $+45°$ layer is less constrained in shear than the $-45°$ layer as the latter layer is bounded

also by a 0° ply and this affects the cracking density in the ±45° plies. The interaction between the +45° and −45° plies governs the progression of the initial shear cracks and the subsequent spreading of the cracks in the +45° layer. This interaction also governs the distance between the shear cracks, which is thought to be caused by a similar process to the cracking seen in 0°/90° cross-ply laminates [88].

Eventually the shear cracks in the +45° and −45° layers interact causing delamination between these layers. Some longitudinal shear cracking within the 0° ply are also observed as shown in Fig. 6.16. Shear cracks spreading in the −45° layer are associated with delamination between the −45° and 0° layers. Final fracture occurs at a region in the −45° layer where fibre tensile, pull-out and bending failures occur—see Figs. 6.16 and 6.17(e) and (f).

Adherends with 0° surface ply

The modes of fracture of joints with stacking sequences E and F are shown in Figs. 6.18–6.20. The initiation of failure at the fillet is the same as described for stacking sequence D—see Figs. 6.19 and 6.21(a) and (b).

From Fig. 6.10 (stacking sequence E), the maximum longitudinal direct strain in the 0° ply next to the bondline (1.17%) has approached the ultimate longitudinal direct strain (1.25%) indicating fibre tensile fracture, as observed experimentally—see Fig. 6.21(c) and (d). Both the maximum peel and shear strains at the centreline of the 0° ply next to the bondline (0.04% and 0.38% respectively) are below their respective ultimate values as seen in Fig. 6.11. Similar results for stacking sequence F are presented in Figs. 6.12 and 6.13. However, the maximum longitudinal direct strain in somewhat under predicted.

As the through-thickness tensile crack in the 0° layer reaches into the ply, a change in crack path occurs. This is caused by the shear strains at the crack tip initiating delamination parallel to the 0° fibres. Delamination is assisted by the presence of peel strains. Figs. 6.20 and 6.21(e) and (f) show the ultimate 'dynamic' nature of failure.

6.6 CONCLUSIONS

1. With all stacking sequences, failure is usually initiated by fillet fracture followed by adherend failure. Fillet fracture initiates at the fillet free surface and propagates, almost parallel to the adherend edge, to the fillet root.
2. For adherends with $\pm 45°$ surface plies, failure proceeds inwards from the surface layer and is manifested by intralaminar and interlaminar shear cracking.
3. For adherends with $0°$ surface layer, failure initiates by fibre tensile fracture followed by delamination within the $0°$ ply.
4. The linear finite element analysis predicts higher stresses than the continuum method of Hart-Smith because it considers the discrete layered nature of the laminate and does not allow for geometric nonlinearity. Laminate failure load may be predicted using nonlinear finite element analysis.

Table 6.1. Test results.

(a) 25 mm overlap.

	Stress at failure (N/mm^2)			
Stacking sequence	Min.	Max.	Mean	C_v (%)
D: $[\pm 45/0_2]_s$	479.6	521.8	508.7	3.9
E: $[0/\pm 45/0]_s$	544.9	619.5	571.0	6.0
F: $[0_2/\pm 45]_s$	512.5	581.2	535.8	6.0

(b) 12.5 mm overlap.

	Stress at failure (N/mm^2)			
Stacking sequence	Min.	Max.	Mean	C_v (%)
D: $[\pm 45/0_2]_s$	422.5	452.2	440.0	3.3
E: $[0/\pm 45/0]_s$	391.1	467.0	440.0	8.1
F: $[0_2/\pm 45]_s$	414.8	456.9	432.7	4.7

C_v—Coefficient of variation

Table 6.2. Adherend mechanical properties and stresses from Hart-Smith's analysis.

(a) 25 mm overlap.

Stacking sequence	E_m	E_b	ν_m	ν_b	D	k_b	m	P	σ_{av}	σ_b	σ_{max}	σ_p
D: $[\pm 45/0_2]_s$	81.0	37.1	0.638	0.672	5.6	0.496	−0.093	527.2	527.2	240.0	767.2	100.4
E: $[0/\pm 45/0]_s$	81.0	91.5	0.638	0.580	11.5	1.009	−0.138	592.0	592.0	377.1	969.1	110.6
F: $[0_2/\pm 45]_s$	81.0	123.8	0.638	0.440	12.8	1.124	−0.165	552.0	552.0	386.0	938.0	107.3

(b) 12.5 mm overlap.

Stacking sequence	E_m	E_b	ν_m	ν_b	D	k_b	m	P	σ_{av}	σ_b	σ_{max}	σ_p
D: $[\pm 45/0_2]_s$	81.0	37.1	0.638	0.672	5.6	0.496	−0.093	460.4	460.4	457.9	918.3	191.8
E: $[0/\pm 45/0]_s$	81.0	91.5	0.638	0.580	11.5	1.009	−0.138	457.2	457.2	601.7	1058.9	176.7
F: $[0_2/\pm 45]_s$	81.0	123.8	0.638	0.440	12.8	1.124	−0.165	458.4	458.4	626.0	1084.4	174.0

E_m— effective membrane elastic modulus of adherends in direction of applied load ($\times 10^3$ N/mm^2).

E_b— effective bending elastic modulus of adherends corresponding to a bending moment about an in-plane axis normal to the direction of applied load ($\times 10^3$ N/mm^2).

ν_m— effective membrane Poisson's ratio of adherends associated with E_m.

ν_b— effective bending Poisson's ratio of adherends associated with E_b.

D— flexural rigidity of adherends ($\times 10^3$ Nmm).

k_b— bending stiffness parameter.

m— coefficient of mutual bend-twist coupling corresponding to a bending moment about an in-plane axis normal to the direction of applied load.

P— experimental mean load at failure per unit joint width (N/mm).

σ_{av}— adherend average stress.

σ_b— adherend bending stress.

σ_{max}— adherend maximum stress.

σ_p— adhesive peel stress.

All stresses are given in N/mm^2.

Table 6.3. Comparison between Hart-Smith's and finite element analyses results (25 mm overlap).

	σ_{max}			σ_p		
Stacking sequence	HSA	LFEA	NLFEA	HSA	LFEA	NLFEA
D: $[\pm 45/0_2]_s$	767	3111	241	100	532	38
E: $[0/\pm 45/0]_s$	969	9701	1654	111	260	40
F: $[0_2/\pm 45]_s$	938	6425	1480	107	185	37

σ_{max}— maximum adherend longitudinal direct stress, occuring adjacent to the bondline at the end of the overlap region, due to direct load and bending moment.

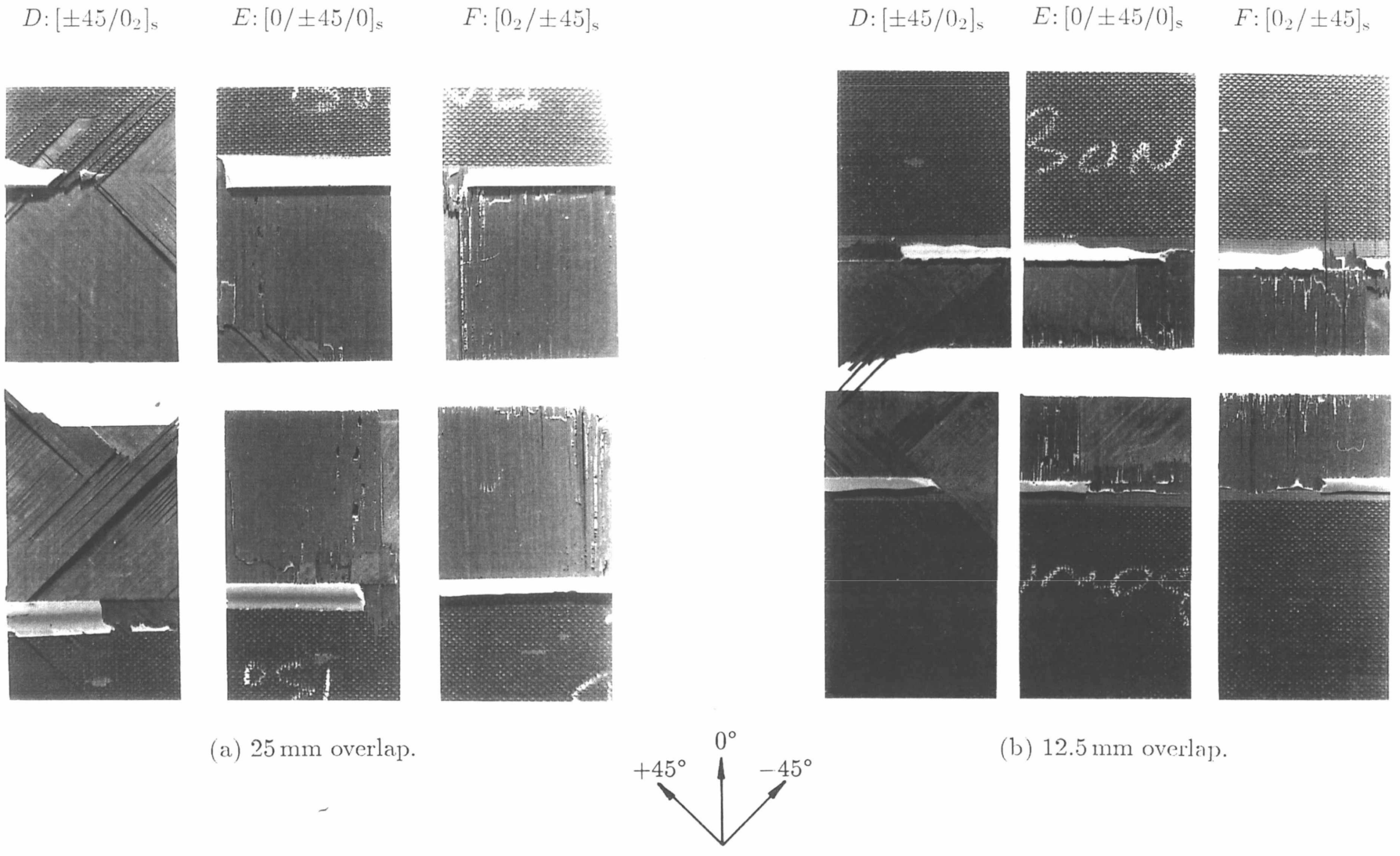
σ_p— peak adhesive peel stress at the end of the overlap region.

HSA— Hart-Smith's Analysis.

LFEA— Linear Finite Element Analysis.

NLFEA— Nonlinear Finite Element Analysis.

All stresses are given in N/mm^2.



(a) 25 mm overlap.

(b) 12.5 mm overlap.

Fig. 6.1. The bonded specimens with stacking sequences D–F after fracture.

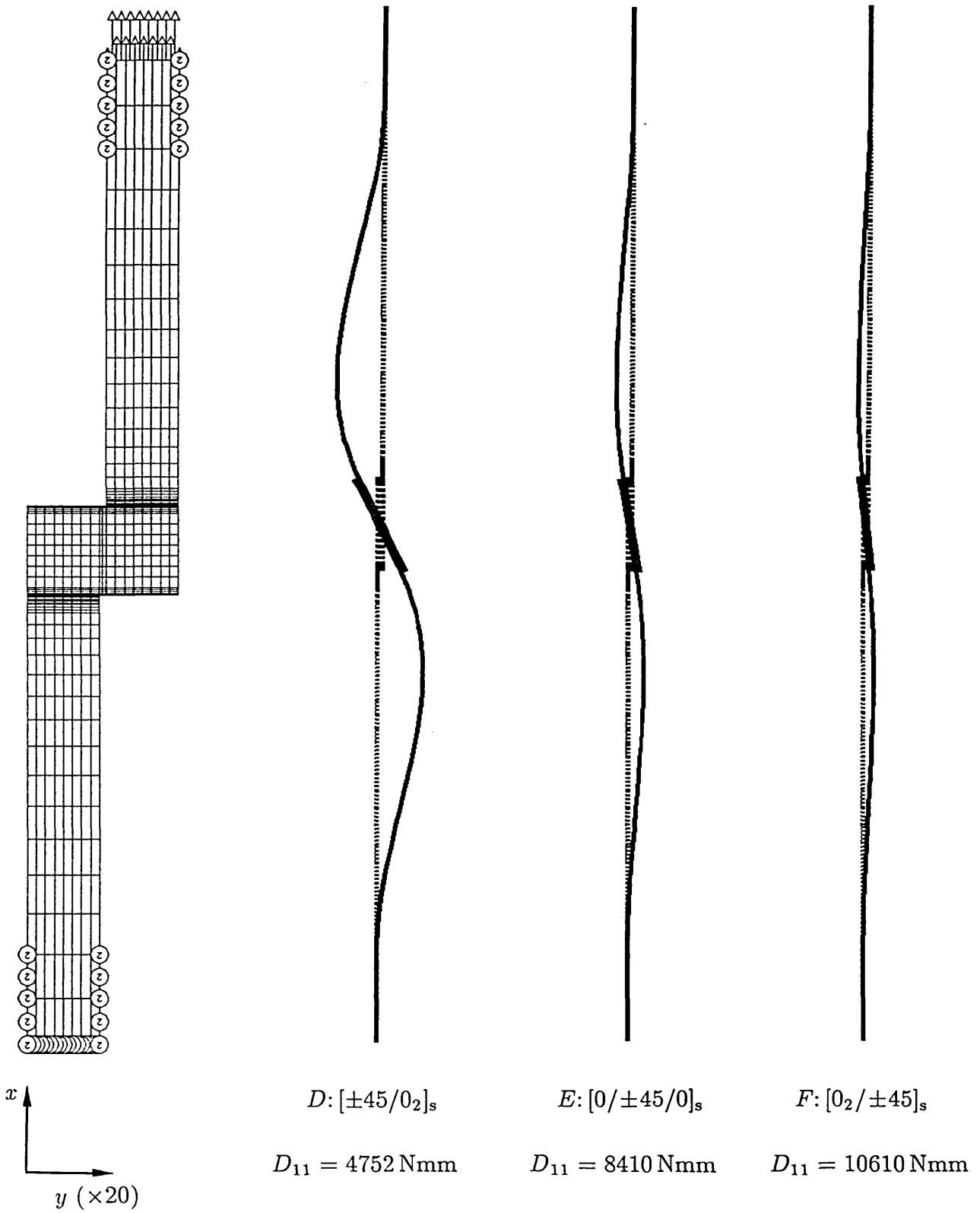


Fig. 6.2. Finite element discretisation, boundary conditions and deformed shapes due to applied mean failure stress (25 mm overlap). Displacements in the y-direction are magnified twenty times.

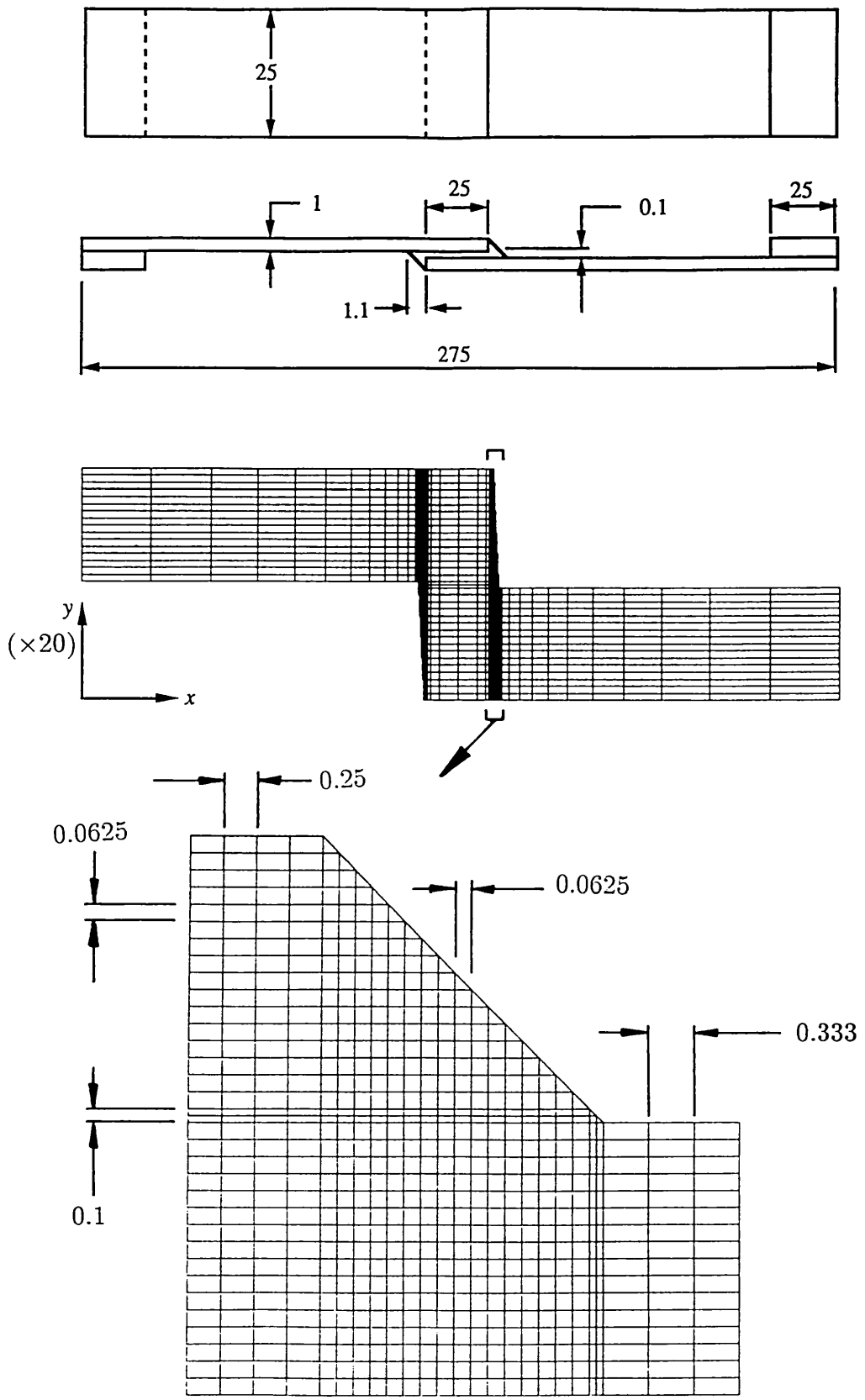


Fig. 6.3. Geometry and finite element model of eight-ply adherend joint. Dimensions are given in millimetres (not to scale).

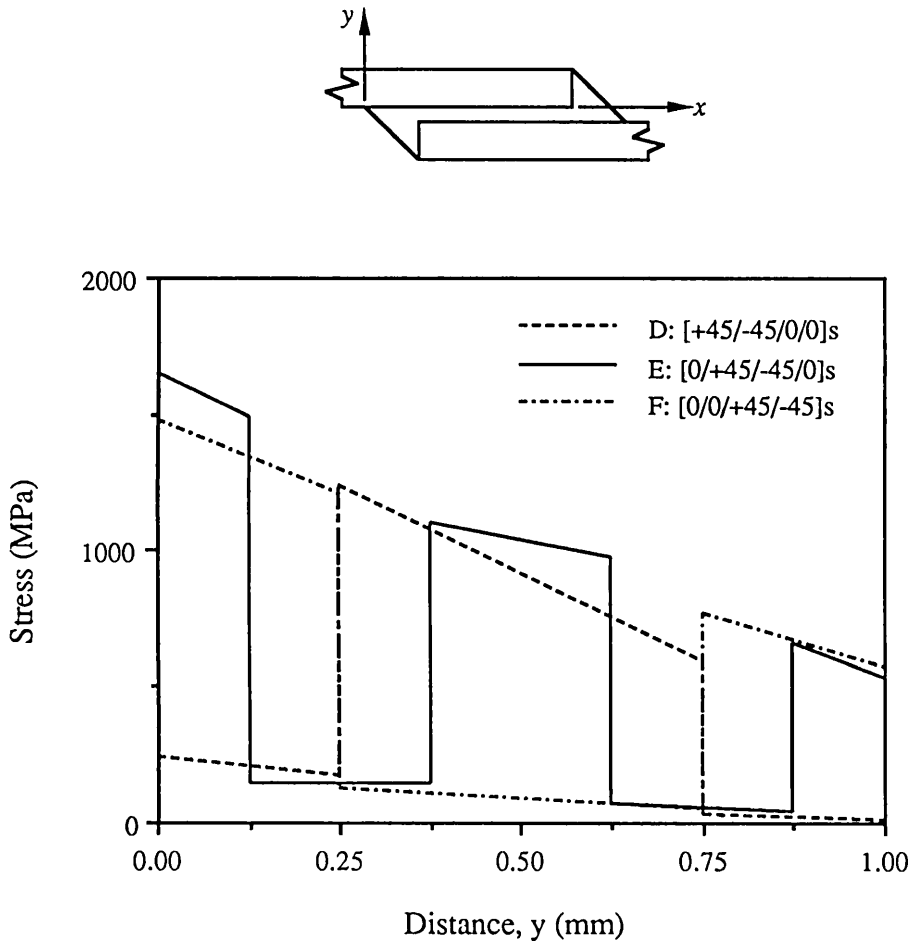


Fig. 6.4. Adherend longitudinal direct stress (σ_{xx}) distribution along the y-axis at the fillet tip using nonlinear finite element analysis. The applied stresses for stacking sequences D, E and F are 508.7 N/mm^2, 571.0 N/mm^2 and 535.8 N/mm^2 respectively.

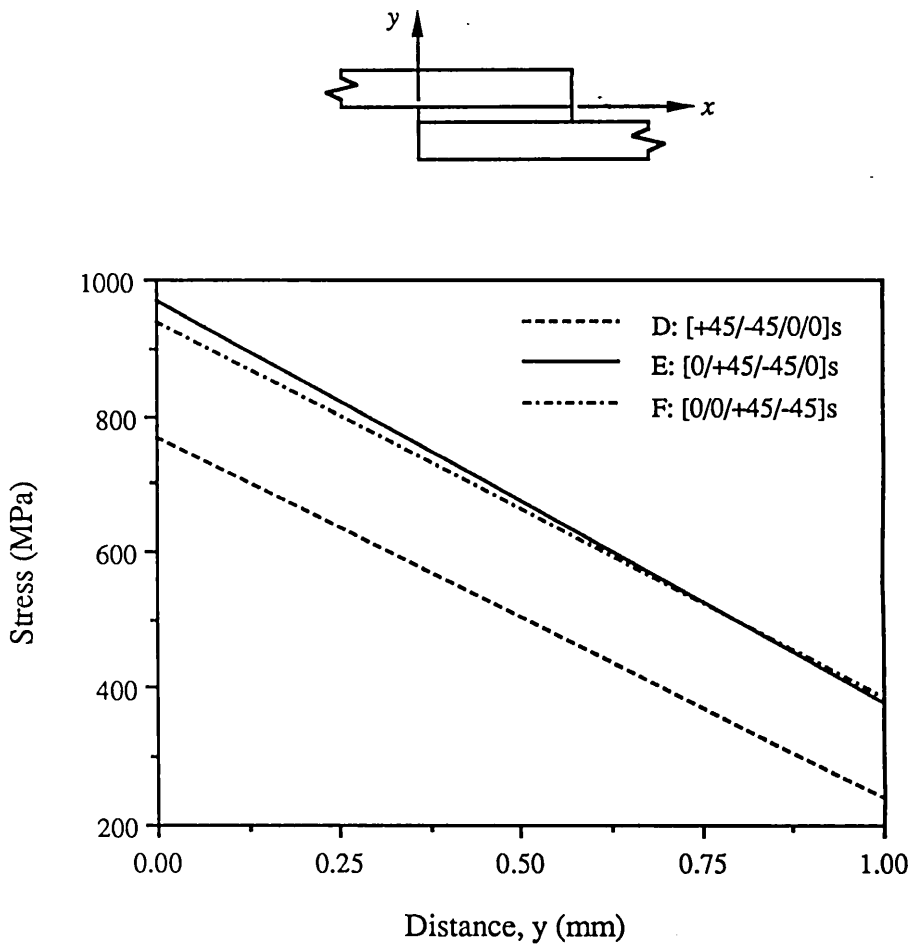


Fig. 6.5. Adherend longitudinal direct stress (σ_{xx}) distribution along the y-axis using Hart-Smith's analysis.

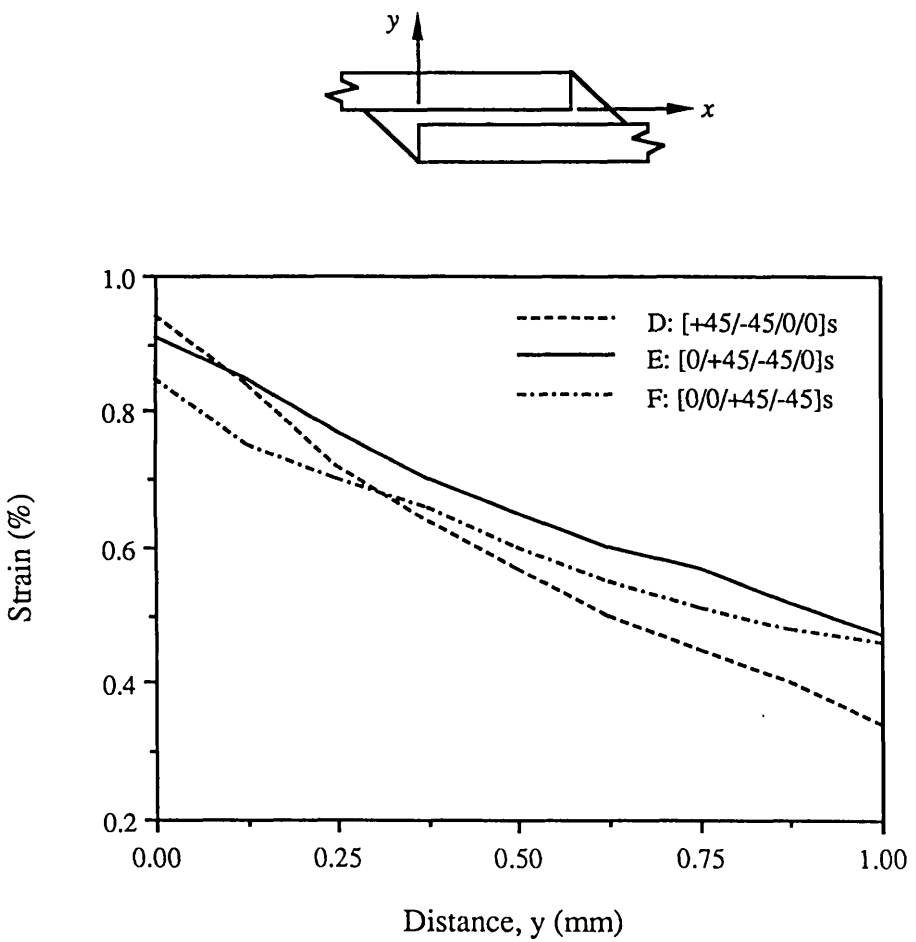


Fig. 6.6. Adherend longitudinal direct strain (ϵ_{xx}) distribution along the y-axis at the end of the lap. The applied stresses for stacking sequences D, E and F are 508.7 N/mm^2, 571.0 N/mm^2 and 535.8 N/mm^2 respectively.

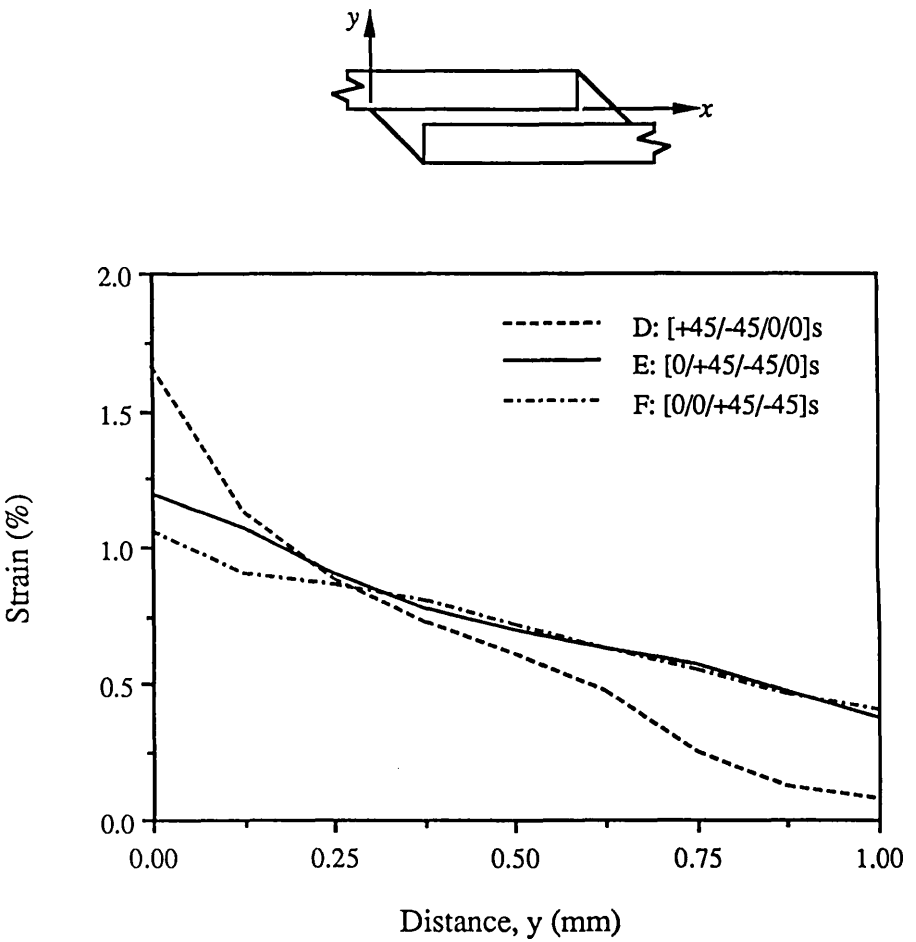


Fig. 6.7. Adherend longitudinal direct strain (ϵ_{xx}) distribution along the y-axis at the fillet tip. The applied stresses for stacking sequences D, E and F are 508.7 N/mm^2, 571.0 N/mm^2 and 535.8 N/mm^2 respectively.

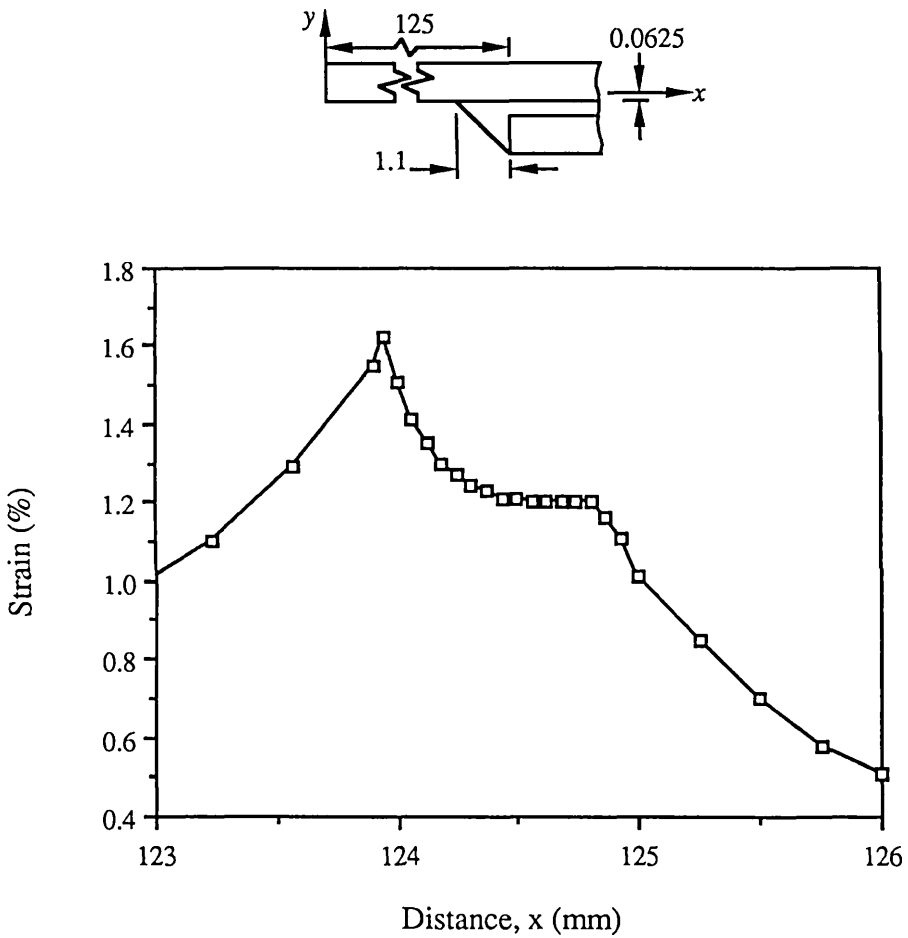


Fig. 6.8. Longitudinal direct strain (ϵ_{xx}) distribution along the centreline of the +45° layer next to the bondline. Stacking sequence D: $[\pm 45/0_2]_s$ at 508.7 N/mm^2 applied stress.

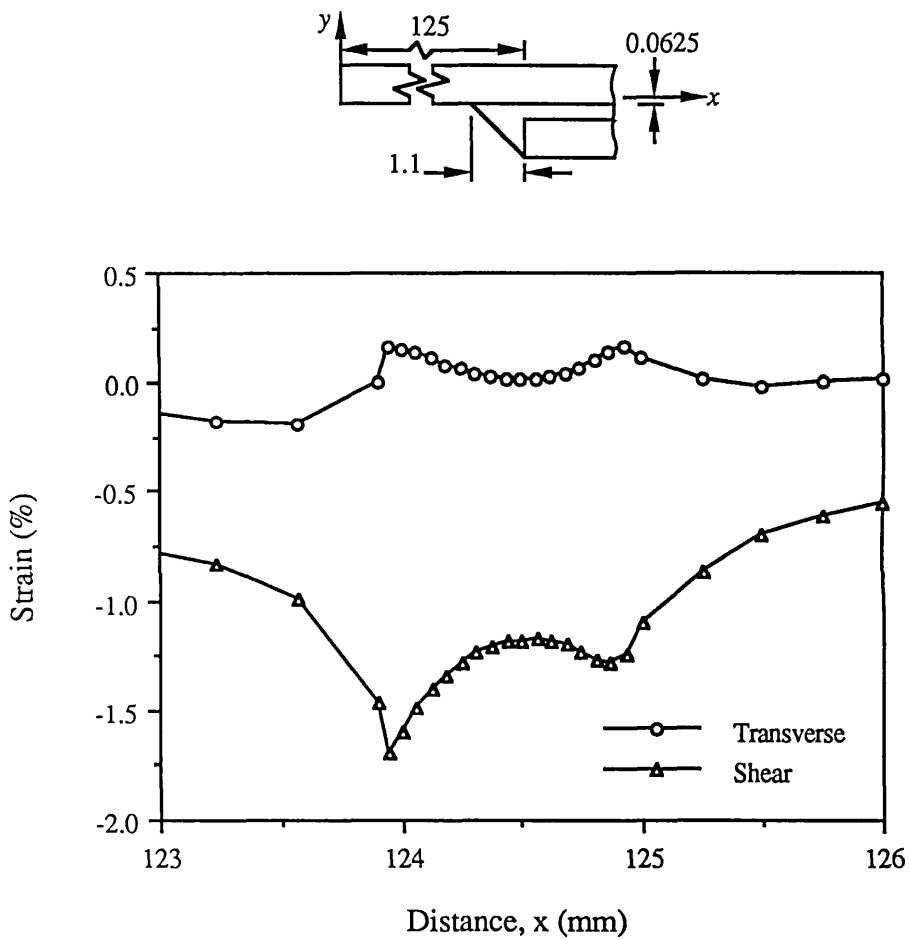


Fig. 6.9. Transverse direct and shear strain (ϵ_{yy} and γ_{xy} respectively) distributions along the centreline of the +45° layer next to the bondline. Stacking sequence D: $[\pm 45/0_2]_s$ at 508.7 N/mm^2 applied stress.

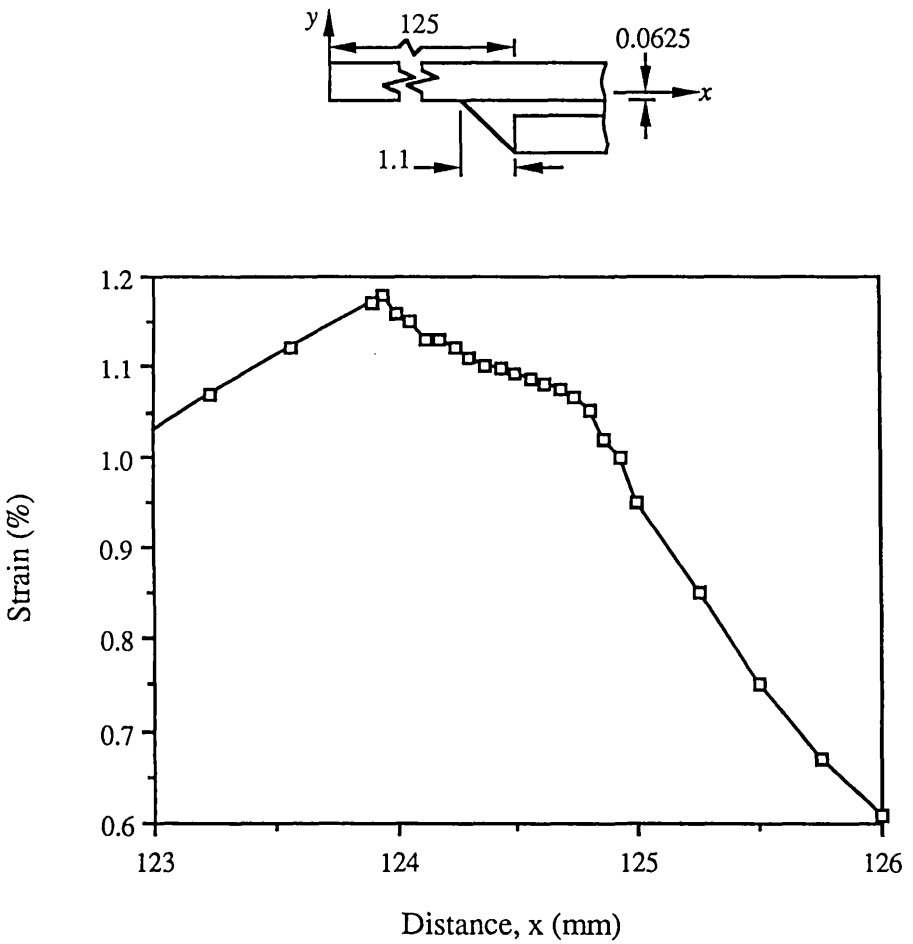


Fig. 6.10. Longitudinal direct strain (ϵ_{xx}) distribution along the centreline of the 0° layer next to the bondline. Stacking sequence E: $[0/\pm 45/0]_s$ at 571.0 N/mm^2 applied stress.

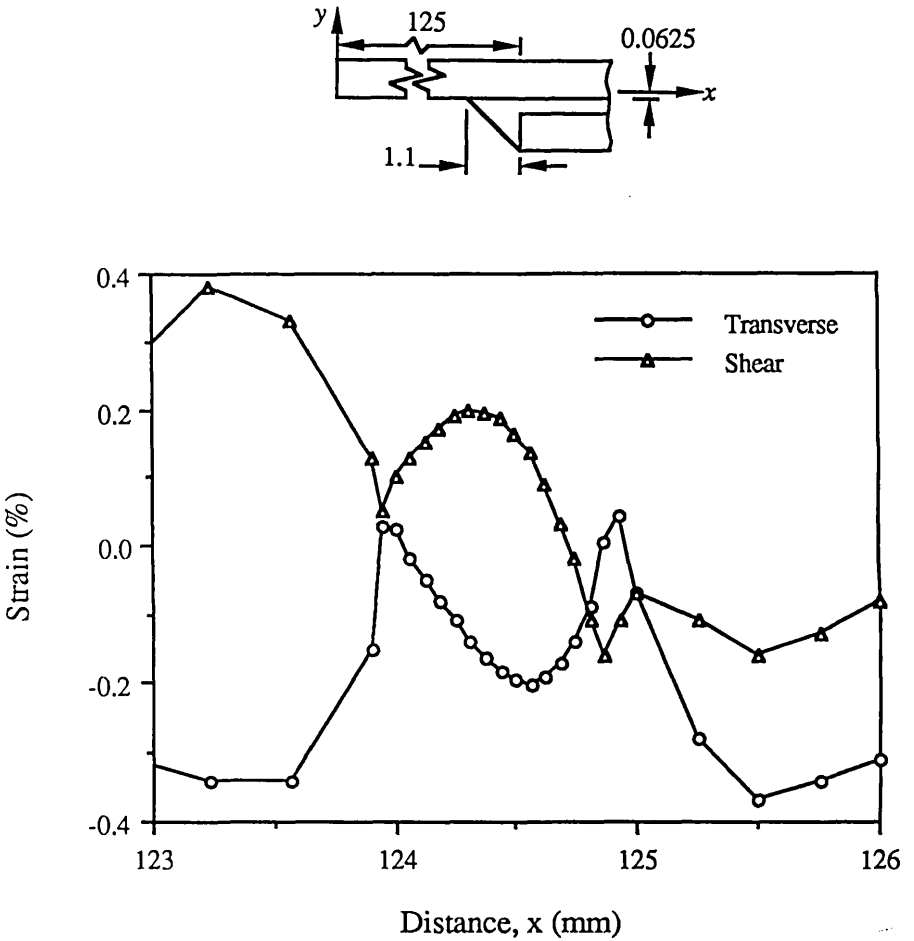


Fig. 6.11. Transverse direct and shear strain (ϵ_{yy} and γ_{xy} respectively) distributions along the centreline of the 0° layer next to the bondline. Stacking sequence E: $[0/\pm 45/0]_s$ at 571.0 N/mm^2 applied stress.

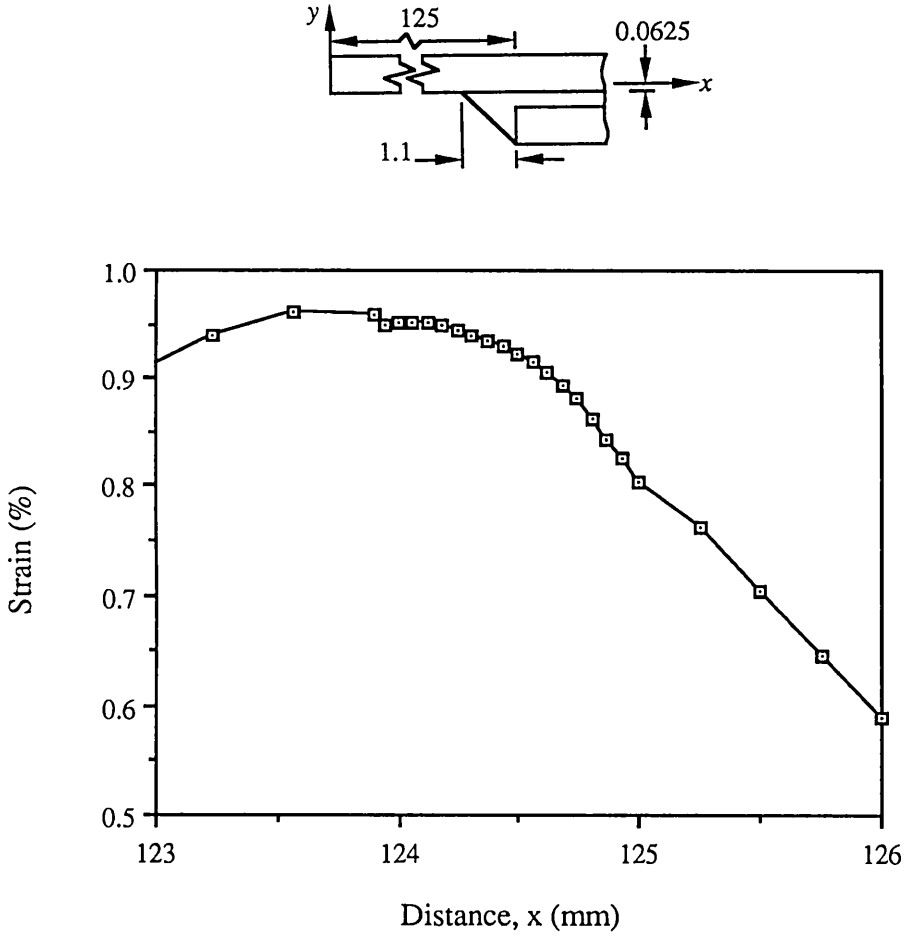


Fig. 6.12. Longitudinal direct strain (ϵ_{xx}) distribution along the centreline of the 0° layer next to the bondline. Stacking sequence F: $[0_2/\pm 45]_s$ at 535.8 N/mm^2 applied stress.

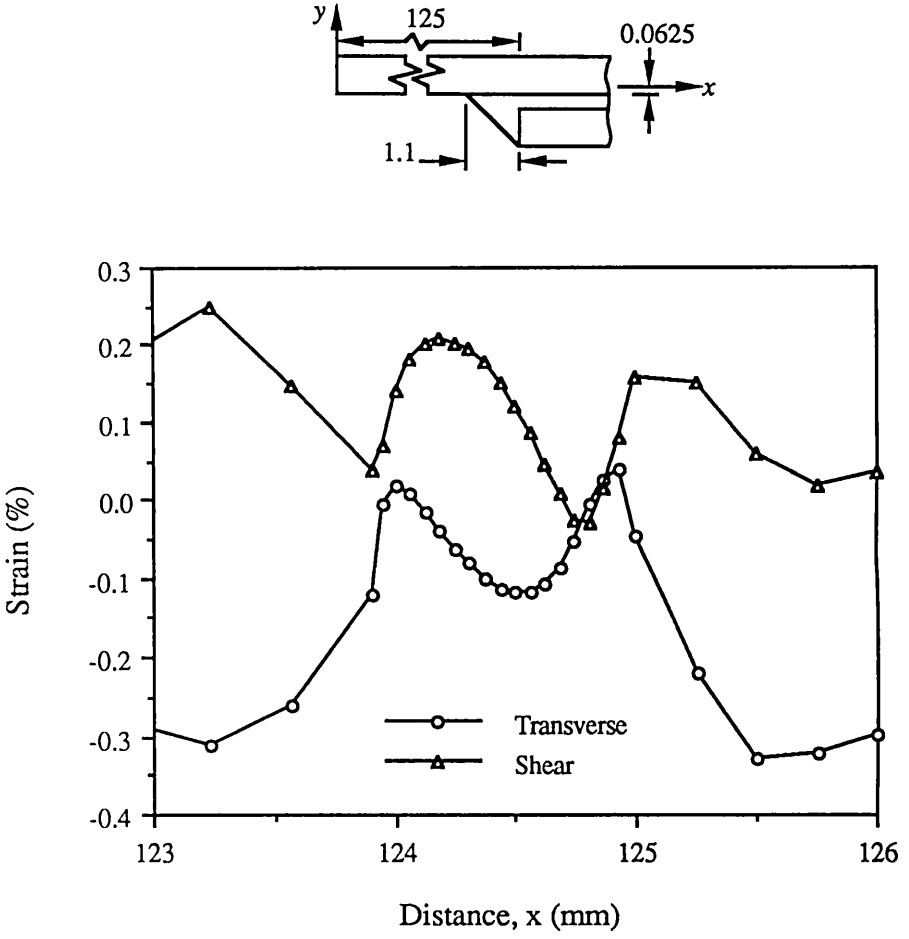


Fig. 6.13. Transverse direct and shear strain (ϵ_{yy} and γ_{xy} respectively) distributions along the centreline of the 0° layer next to the bondline. Stacking sequence F: $[0_2/\pm 45]_s$ at 535.8 N/mm^2 applied stress.

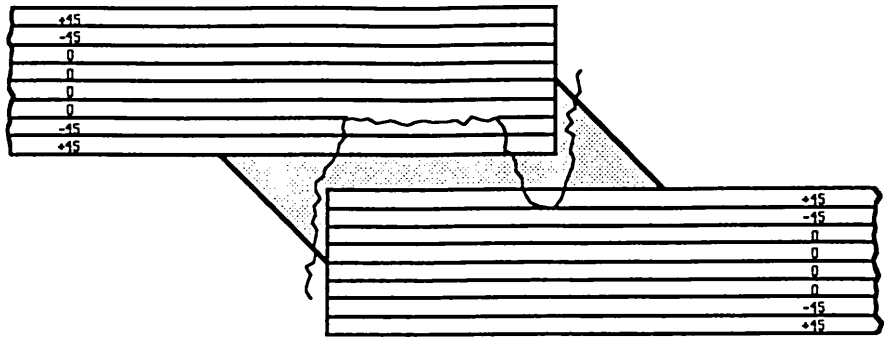


Fig. 6.14. Two-dimensional view of joint fracture (stacking sequence D: $[\pm 45/0_2]_s$).

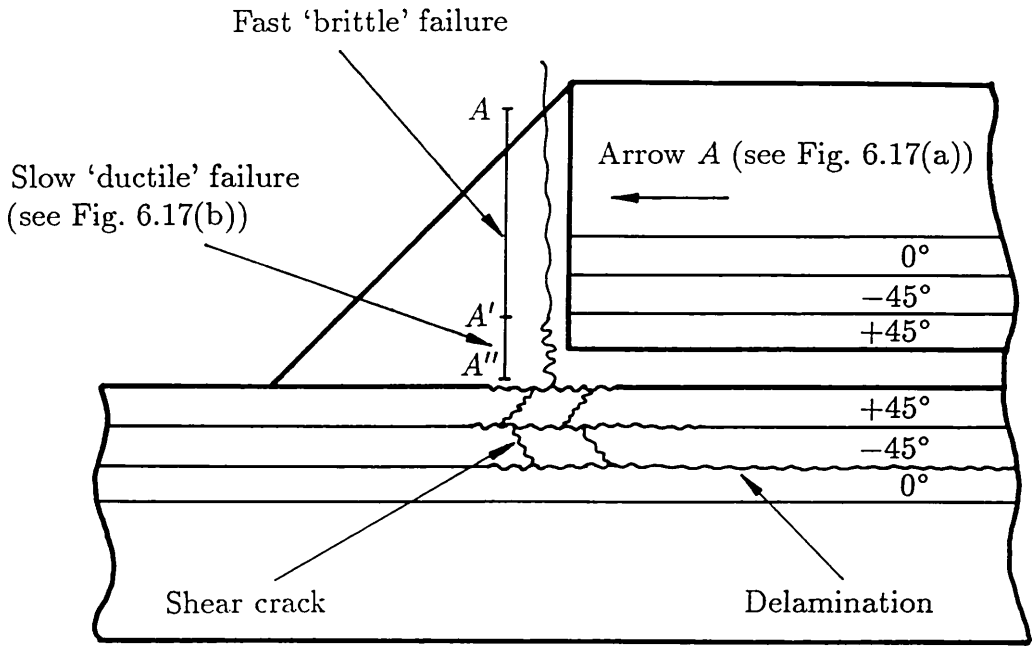


Fig. 6.15. Failure initiation and progression (stacking sequence D: $[\pm 45/0_2]_s$).

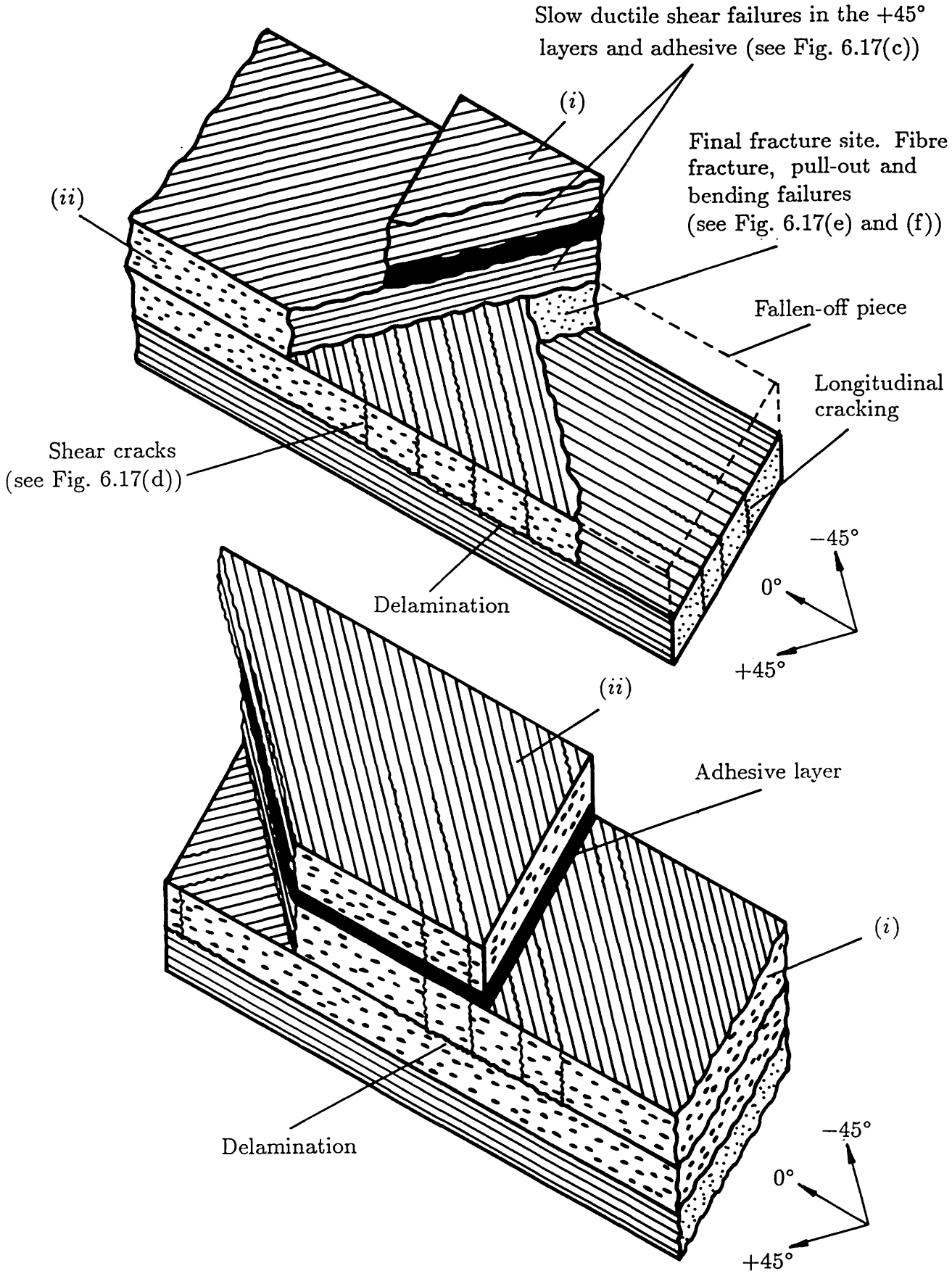


Fig. 6.16. The fractured surfaces of stacking sequence D: $[\pm 45/0_2]_s$, 25 mm overlap. Only the first three plies are shown. For clarity, the adhesive fillet is not drawn.

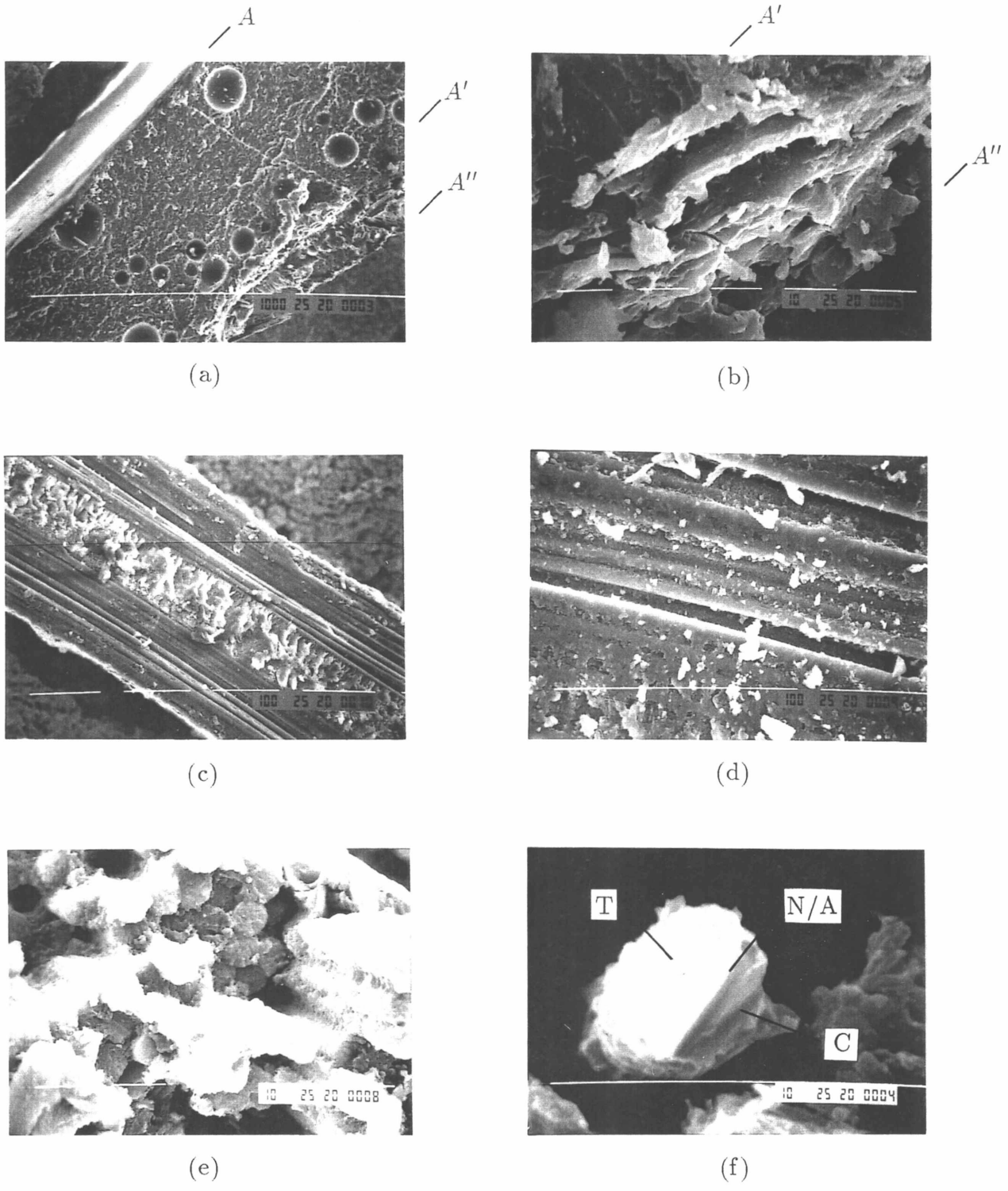


Fig. 6.17. SEM, taken from stacking sequence D: $[\pm 45/0_2]_s$, 25 mm overlap, showing (refer to Figs. 6.15 and 6.16):

(a) View arrow A—fractured adhesive fillet. Slow 'ductile' (section A'–A'') and fast 'brittle' (section A–A') failures are shown.

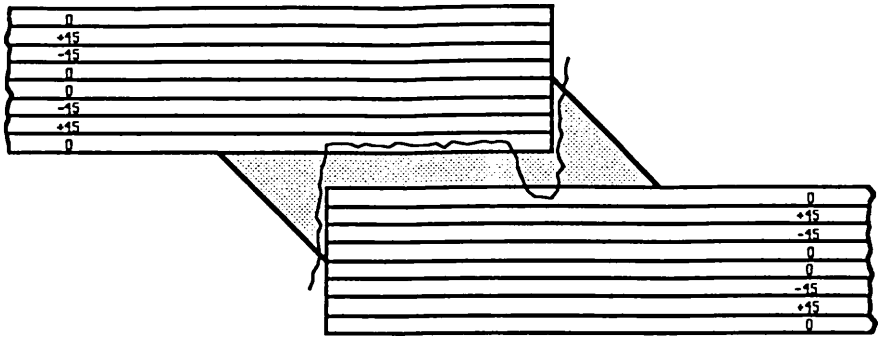
(b) An enlarged view of the adhesive fillet 'ductile' failure band—flaky fracture.

(c) Slow 'ductile' shear failure in the +45° layers and adhesive. Note the adhesive shear cusps.

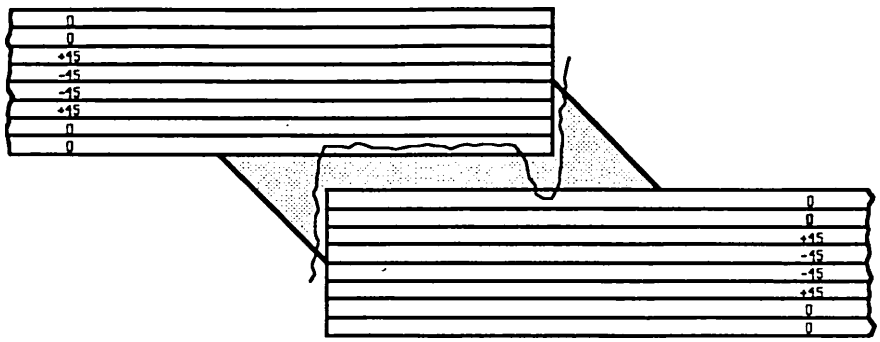
(d) Shear cracks in the −45° layer.

(e) Fibre fracture and pull-out.

(f) Fibre bending (in discrete locations). T—tensile fracture; C—compressive fracture; N/A—neutral axis.



(a) Stacking sequence E: $[0/\pm 45/0]_s$.



(b) Stacking sequence F: $[0_2/\pm 45]_s$.

Fig. 6.18. Two-dimensional view of joint fracture.

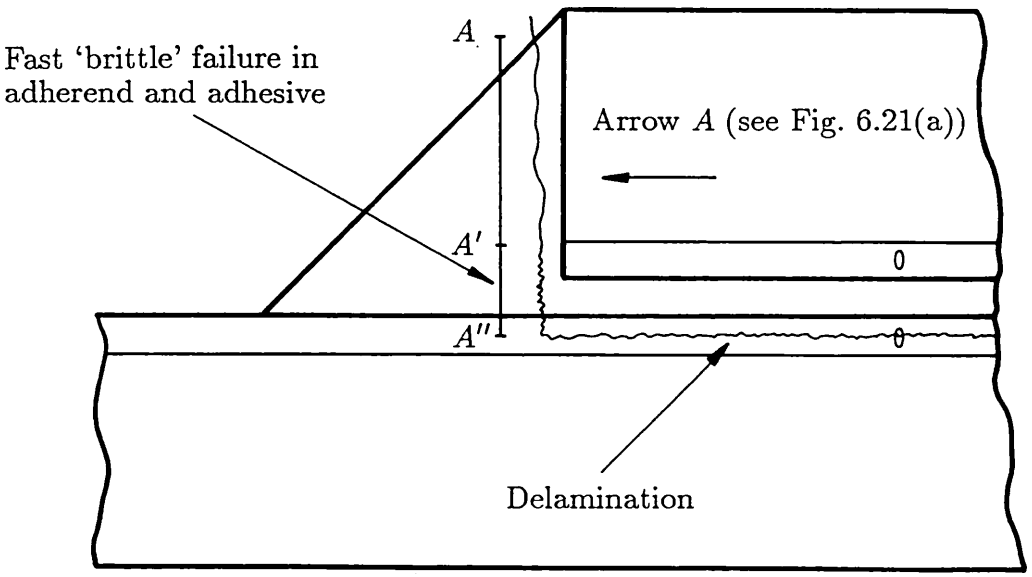


Fig. 6.19. Failure initiation and progression (stacking sequences E: $[0/\pm 45/0]_s$ and F: $[0_2/\pm 45]_s$.

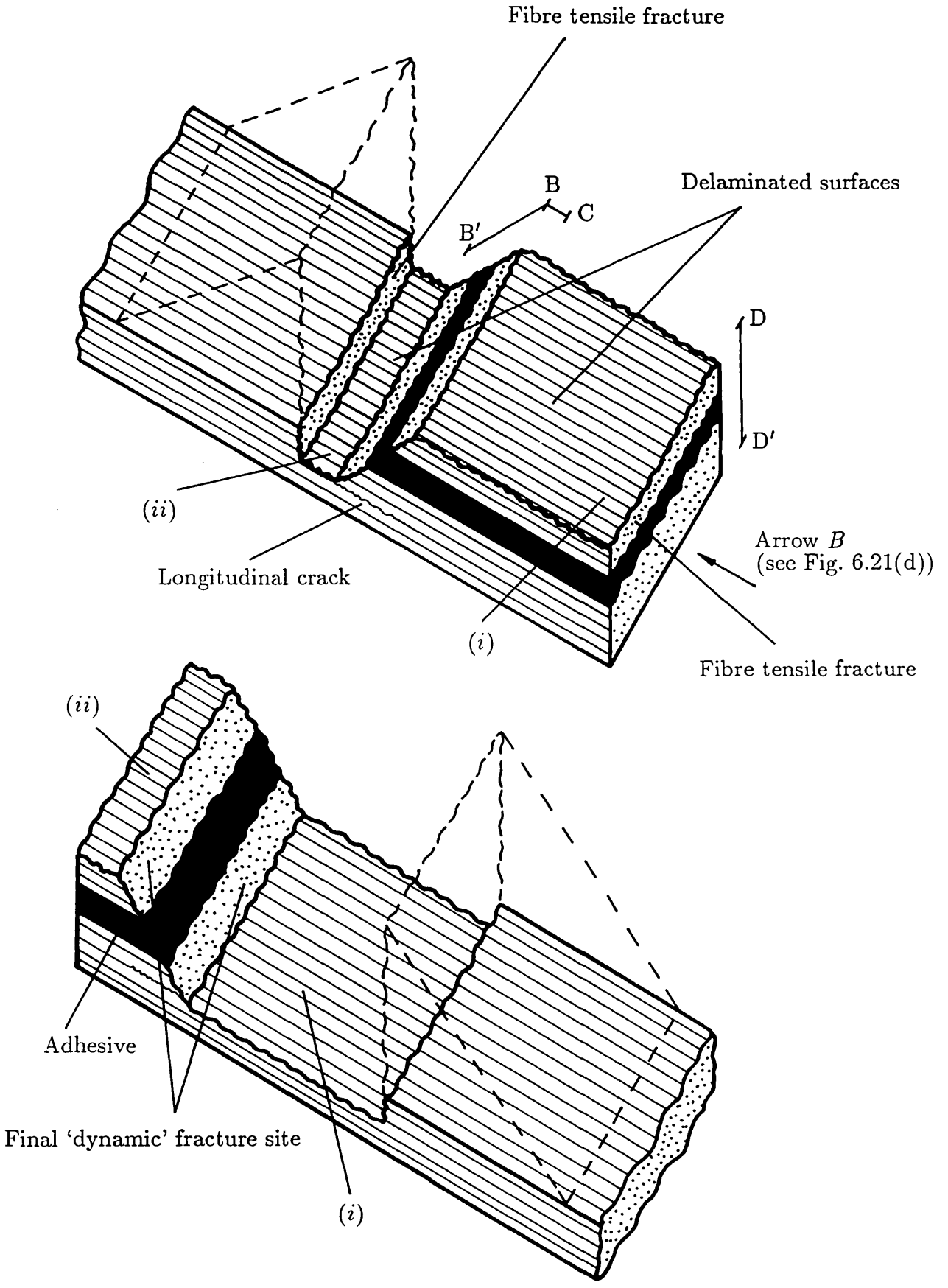
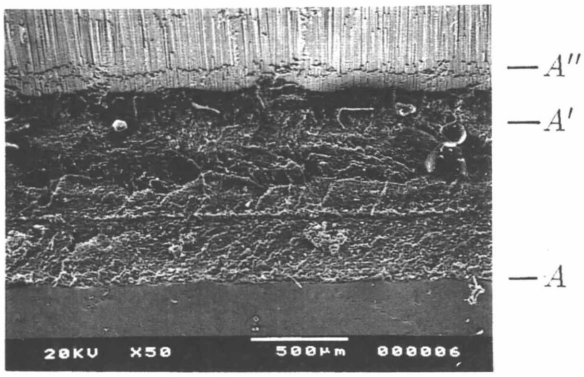


Fig. 6.20. The fractured surfaces of stacking sequences E: $[0/\pm45/0]_s$ and F: $[0_2/\pm45]_s$, 25 mm overlap. Only the first ply is shown. The adhesive fillet is drawn in dashed lines.

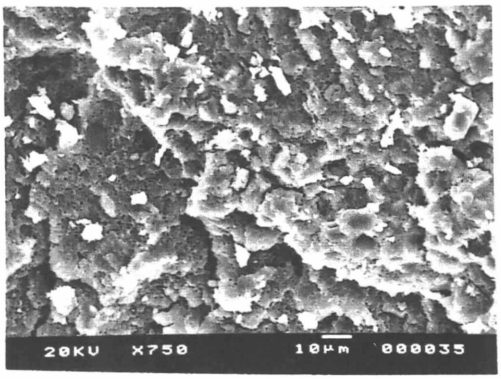


$-A''$

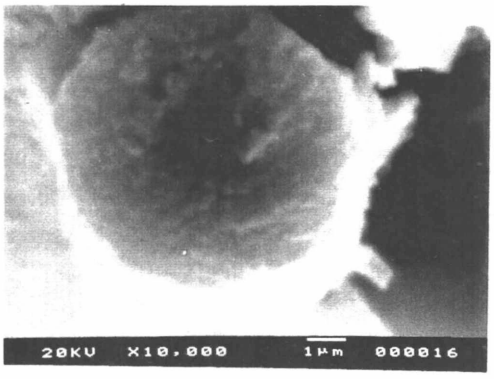
$-A'$

$-A$

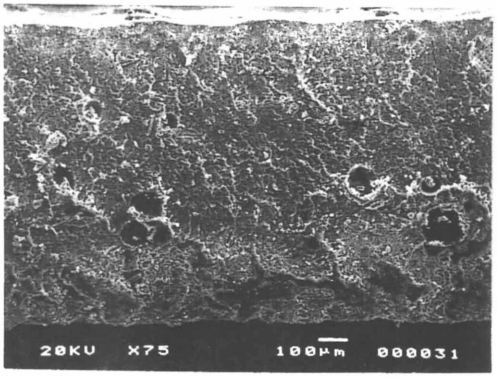
(a)



(b)



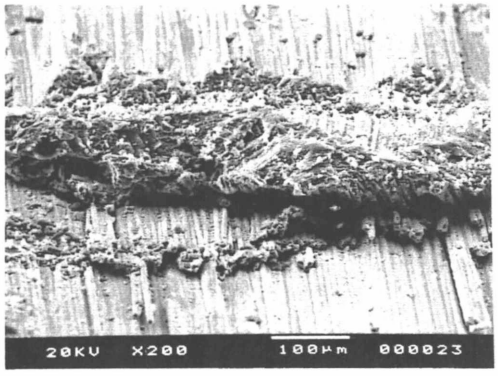
(c)



$-D'$

$-D$

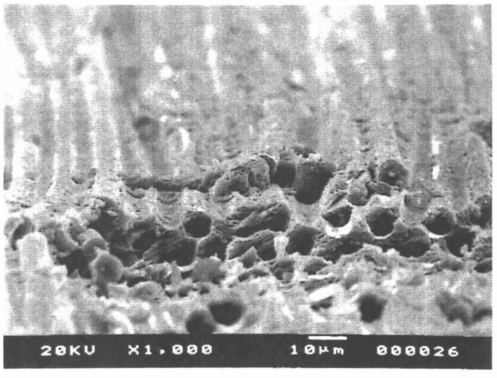
(d)



$-B$

$-B'$

(e)



$-C$

$-B$

(f)

Fig. 6.21. SEM, taken from stacking sequence F: $[0_2/\pm 45]_s$, 25 mm overlap, showing (refer to Figs. 6.19 and 6.20):

(a) View arrow A. Note the tensile fracture of surface fibres.
(b) Enlarged view of adhesive fillet fracture taken from section A–A''.
(c) Typical tensile fracture of a single fibre taken from section A'–A''.
(d) View arrow B.
(e) 'Dynamic' fracture at section B–B'. Note fibre bending and twisting.
(f) Fibre pull-out at section B–C.

Chapter 7

JOINTS WITH SIXTEEN-PLY ADHERENDS

7.1 INTRODUCTION

The performance is presented of joints with sixteen-ply adherends with the following stacking sequences:

K: $[\pm 45/0_3/\pm 45/0]_s$.

L: $[0/\pm 45/0_2/\pm 45/0]_s$.

M: $[0_2/\pm 45/0/\pm 45/0]_s$.

N: $[0_3/(\pm 45)_2/0]_s$.

The l/t ratio used is 12.5. Strains obtained using moiré interferometry are compared to predicted strains using linear and nonlinear finite element analyses. Numerical simulation of the sequence of joint failure has been undertaken. The resulting strain distributions have been correlated to the joint experimental performance.

7.2 EXPERIMENTAL RESULTS

Test results are given in Table 7.1. The order of the stacking sequence relative to joint strength is as follows: N, M, K and L. It is interesting to note that joints with stacking sequence K are stronger that those with stacking sequence L. The fractured joints are shown in Fig. 7.1. The initiation of failure at a joint corner (refer to Chapter 3) can clearly be seen for stacking sequences L, M and N.

7.2.1 Moiré interferometry

Moiré interferometry has been used to determine strain distributions in the joint with all the stacking sequences. However, only limited results are presented in this report. For the full results, the reader is referred to reference [89]. Strains obtained using moiré interferometry will be compared to predicted strains using linear and nonlinear finite element analyses.

Figs. 7.2 and 7.3 show, over the whole lap region, U (longitudinal) and V (transverse) displacement fields respectively for stacking sequence L. The increase in the density of fringes as the load is increased is obvious. Concentration of displacement fringes occurs at the end of the lap regions as seen in Fig. 7.4. Figs. 7.5 and 7.6 show typical U and V displacement fields at the centre of the lap respectively.

7.3 CONTINUUM ANALYSIS

Adherend mechanical properties and stresses from Hart-Smith's analysis are presented in Table 7.2. For stacking sequences L, M and N, joint strength is increased as the flexural rigidity and bending stiffness parameters are increased.

For all stacking sequences, both the adherend bending and adhesive peel stresses are high with the former being higher than the adherend average stress. Similar arguments to those made in Chapters 5 and 6 regarding the adherend mechanical properties and Hart-Smith's stresses may be made.

7.4 FINITE ELEMENT ANALYSIS

The geometry and finite element discretisation for the joint are shown in Fig. 7.7. Only joints with stacking sequences K and L have been analysed which correspond to 'soft' ($\pm 45°$) and 'hard' ($0°$) surface plies respectively. Plane stress elements are used when the finite element analysis results are compared with those of moiré interferometry. Plane strain elements are used in all other cases. Elements of type CPS8R/CPE8R are used for most of the model with some elements of type CPS6/CPE6 used at the free surface of the adhesive fillet. Each layer of the sixteen-ply adherend is modelled using 48 elements along its length and one element through its thickness. The adhesive layer is modelled using 16 elements along

its length and two elements through its thickness. An adhesive fillet contained 171 elements.

Fillet fracture usually preceds adherend failure. Thus, for post fillet fracture analysis, the adhesive fillet has been removed as shown in Fig. 7.8. Cracking of the adherends has been simulated by reducing the stiffness (by 99%) of the appropriate elements—see Fig. 7.8. The results are presented in Figs. 7.9–7.22 (the reference axes system (x, y) is shown in Figs. 7.7 and 7.8). All the results are from nonlinear analysis except where otherwise stated.

7.5 DISCUSSION

The results indicate that there is no advantage in placing a single 0° layer next to the bondline as compared to ±45° plies. Placing more than one longitudinal ply next to the bondline increases the bending stiffness of the laminate significantly so as to increase joint strength.

The mechanisms of failure are the same as those discussed in Chapter 6 for the eight-ply laminates. The only difference is that fillet fracture does not occur almost parallel to the adherend edge but at an angle to it—see Fig. 7.23.

7.5.1 Comparison between moiré and finite element analyses

Strains obtained using moiré interferometry are compared to predicted strains using linear and nonlinear finite element analyses for stacking sequences K and L.

During the loading of the joint to failure, moiré strains have been determined at several load intervals. Fig. 7.9 shows a comparison of the adherend longitudinal direct strain distribution at the fillet tip using moiré interferometry and linear and nonlinear finite element analyses at an intermediate stress level before joint failure. Clearly, the linear analysis over predicts the adherend strains while good agreement between the nonlinear and moiré interferometry analyses has been obtained. The corresponding stress distributions to the strain distributions presented in Fig. 7.9 are given in Fig. 7.10. The variation of the adherend longitudinal direct strain with applied stress is nonlinear as shown in Fig. 7.11.

Contours of longitudinal and transverse direct and shear strains at the end of the lap using nonlinear analysis are shown in Figs. 7.12–7.14 respectively. Fig. 7.12

may be compared directly to the U displacement field shown in Fig. 7.4. It can be seen that $\pm 45°$ surface plies (Fig. 7.12(a)) offer a more uniform strain distribution than a $0°$ surface layer (Fig. 7.12(b)).

7.5.2 Failure analysis

The sequence of joint failure with stacking sequences K and L has been simulated numerically and the resulting strain distributions have been compared to experimental performance. It will be shown that, contrary to numerical prediction, fillet fracture initiates at the fillet free surface and not at the fillet root. This has been established by crack arrestment technique as noted in Chapter 4.

The discussion presented for stacking sequence L applies to stacking sequences M and N.

Stacking sequence K: $[\pm 45/0_3/\pm 45/0]_s$

Fig. 7.15 shows contours of von Mises stress in the adhesive fillet. It can be seen that the von Mises stress at the fillet root ($100\,\mathrm{N/mm^2}$) has exceeded the tensile strength of the adhesive ($68\,\mathrm{N/mm^2}$). This indicates that fillet fracture would initiate at the fillet root and not at the fillet free surface as observed experimentally. This contradiction may be attributed to voids, though minimal, in the adhesive fillet acting as stress raisers and causing premature failure initiation at the fillet free surface. It has been claimed that the mechanical properties of the adhesive fillet are inferior to those of the adhesive layer [31]. The reason given for this behaviour is that, unlike the adhesive layer, the fillet is cured under zero pressure.

Contours of longitudinal and transverse direct and shear strains at the end of the lap before fillet fracture are shown in Figs. 7.16(a), 7.17(a) and 7.18(a) respectively. It can be seen from Fig. 7.16(a) that the maximum intralaminar shear strain in the $+45°$ layer next to the bondline is 1.4% ($\epsilon_{xx} = \gamma_{12}$). Thus, this ply is on the verge of shear cracking, the ultimate shear strain being 1.61%. From Fig. 7.17(a), the maximum transverse direct strain in the adherends is 0.6%. This is below the ultimate transverse direct strain of the adherends (0.77%).

The fracture of the adherends is three-dimensional, but a simplified two-dimensional view is presented in Fig. 7.23(a). Initially, a fillet crack starts at

X'' and proceeds towards X' at the right hand fillet (for the given failure configuration). Cracking of the right hand fillet is followed by cracking of the left hand fillet from X'' to X'.

Figs. 7.16(b), 7.17(b) and 7.18(b) show strain contours at the end of the lap after fillet fracture. From Fig. 7.16(b), the shear strain in the +45° ply next to the bondline at the end of the lap corner has been increased to 2.5%. This value exceeds the ultimate in-plane shear strain indicating shear cracking. Fig. 7.17(b) shows high peel strain (1.1%) in the +45° ply next to the bondline at the lap corner. This peel strain will assist in the delamination of the +45° and −45° layers at the tip of the +45° ply shear cracks.

Shear cracking in +45° layers next to the bondline follows 'ductile' failure of the right hand adhesive fillet at section X'–X—see Fig. 7.24(a) and (b). Shear cracking in the +45° layer spreads to the adjacent −45° layer followed by delamination at the 0°/–45° interface from right to left. Figs. 7.16(c), 7.17(c) and 7.18(c) show strain contours at the end of the lap after the shear fracture of the ±45° layers next to the bondline. From Fig. 7.18(c), the shear strain at the $0°/-45°$ interface is 2%. This value exceeds the ultimate interlaminar shear strain(1.61%) causing a shear type of fracture along the $0°/-45°$ interface. Delamination along the $0°/-45°$ interface is assisted by the high peel strain at this interface (1.5%, from Fig. 7.17(c)).

The crack propagation along the 0°/–45° interface finally meets the left hand fillet crack along X', i.e. from X to X'—see Fig. 7.24(c). At ultimate failure some −45° fibres fracture along a line of the neighbouring +45° fibres as shown in Fig. 7.24(d).

Stacking sequence L: $[0/\pm 45/0_2/\pm 45/0]_s$

Again, the contours of von Mises stress in the fillet (see Fig. 7.19) indicate failure initiation at the fillet root. This contradicts experimental observations of failure initiation at the fillet free surface due to the reasons mentioned above. Figs. 7.20(a), 7.21(a) and 7.22(a) show strain contours at the end of the lap before fillet fracture. From Fig. 7.20(a), the maximum longitudinal direct strain in the 0°

ply next to the bondline is 1.2%, occuring at the end of lap corner. This is just below the ultimate longitudinal strain (1.25%). From Fig. 7.21(a), the maximum peel strain in the adhesive and adherends are below their respective ultimate values. It can be seen from Fig. 7.22(a) that the maximum shear strain in the adhesive and adherends (7% and 2% respectively) have exceeded their respective ultimate linear values (4.28% and 1.61% respectively) indicating the need for nonlinear modelling of the shear stress-strain relationship of the adhesive and adherends.

A two-dimensional view of the mode of joint failure with stacking sequence L is shown in Fig. 7.23(b). It can be seen that the right hand crack has propagated faster than the left hand crack. Thus, the right hand fillet fractures first at the surface, with the crack propagating to the fillet root as seen in Fig. 7.25(a). This is followed by similar fracture of the left hand fillet.

Fillet fracture causes strain concentrations in the surface ply next to the bondline at the end of lap corner. It is seen from Fig. 7.20(b) that the maximum longitudinal direct strain in the 0° ply (1.4%) exceeds its ultimate value causing fibre tensile fracture as observed experimentally in this site—see Fig. 7.25(b) and (c). In addition, from Figs. 7.21(b) and 7.22(b), high peel and shear strains (1.4% and 2% respectively) are present to aid delamination.

Figs. 7.20(c), 7.21(c) and 7.22(c) show strain contours at the end of the lap after tensile fracture of half the thickness of the surface 0° ply. High shear strain concentration at the crack tip (2%, from Fig. 7.22(c)) causes an intralaminar shear fracture within the 0° ply. Delamination within the 0° ply is assisted by the high peel strain at the crack tip (1.6%, from Fig. 7.21(c)).

Intralaminar shear fracture in the 0° layer is followed by further fibre tensile fracture. The process of alternating tensile and shear fractures is repeated several times causing a step-like fracture as depicted in Fig. 7.25(d) and (e). A single ply contains about 15 through-thickness fibres of 8 μm diameter. It is estimated that about 7–8 through-thickness fibres are fractured before a shear crack finally dominates at about mid-way through the first ply. A shear cracked surface is shown in Fig. 7.25(f). The right and left hand shear cracks cross at ultimate failure.

7.5.3 Adhesive toughening phase

Adhesives usually contain rubber particles to enhance their toughness. These particles are about 1 μm in diameter. A micrograph of the adhesive taken at bondline level (Fig. 7.26(a)) shows an 'average' distribution of rubber particles. Note also the 'brittle' fracture mode associated with stacking sequence M—no drawing of particle holes.

A concentration of rubber particles has been observed just above the end of the adhesive layer in the fillet region as shown in Fig. 7.26(b). This may have been caused by a wash-out of the toughening phase. The thickness of this band is about 0.15 mm. It is thought that this concentration of rubber particles can locally reduce the elastic modulus of the adhesive.

7.6 CONCLUSIONS

1. There is no advantage in placing a single 0° layer next to the bondline as compared to ±45° plies (stacking sequences K and L). Placing more than one longitudinal ply next to the bondline increases the bending stiffness of the laminate significantly so as to increase joint strength (stacking sequences M and N).
2. With all stacking sequences, fillet fracture initiates at the fillet free surface and propagates at an angle to the adherend edge to the fillet root.
3. Strains obtained using moiré interferometry agree well with predicted strains using geometrically nonlinear finite element analysis. Hence, material nonlinearity seems to be of little influence.
4. The predicted strains using numerical crack simulation correlate with the sequence of joint failure.

Table 7.1. Test results.

	Stress at failure (N/mm^2)			
Stacking sequence	Min.	Max.	Mean	C_v (%)
K: $[\pm 45/0_3/\pm 45/0]_s$	352.0	389.2	362.5	4.9
L: $[0/\pm 45/0_2/\pm 45/0]_s$	345.9	361.9	354.2	2.2
M: $[0_2/\pm 45/0/\pm 45/0]_s$	413.3	471.2	431.3	6.3
N: $[0_3/(\pm 45)_2/0]_s$	440.8	479.5	461.5	3.4

C_v—Coefficient of variation

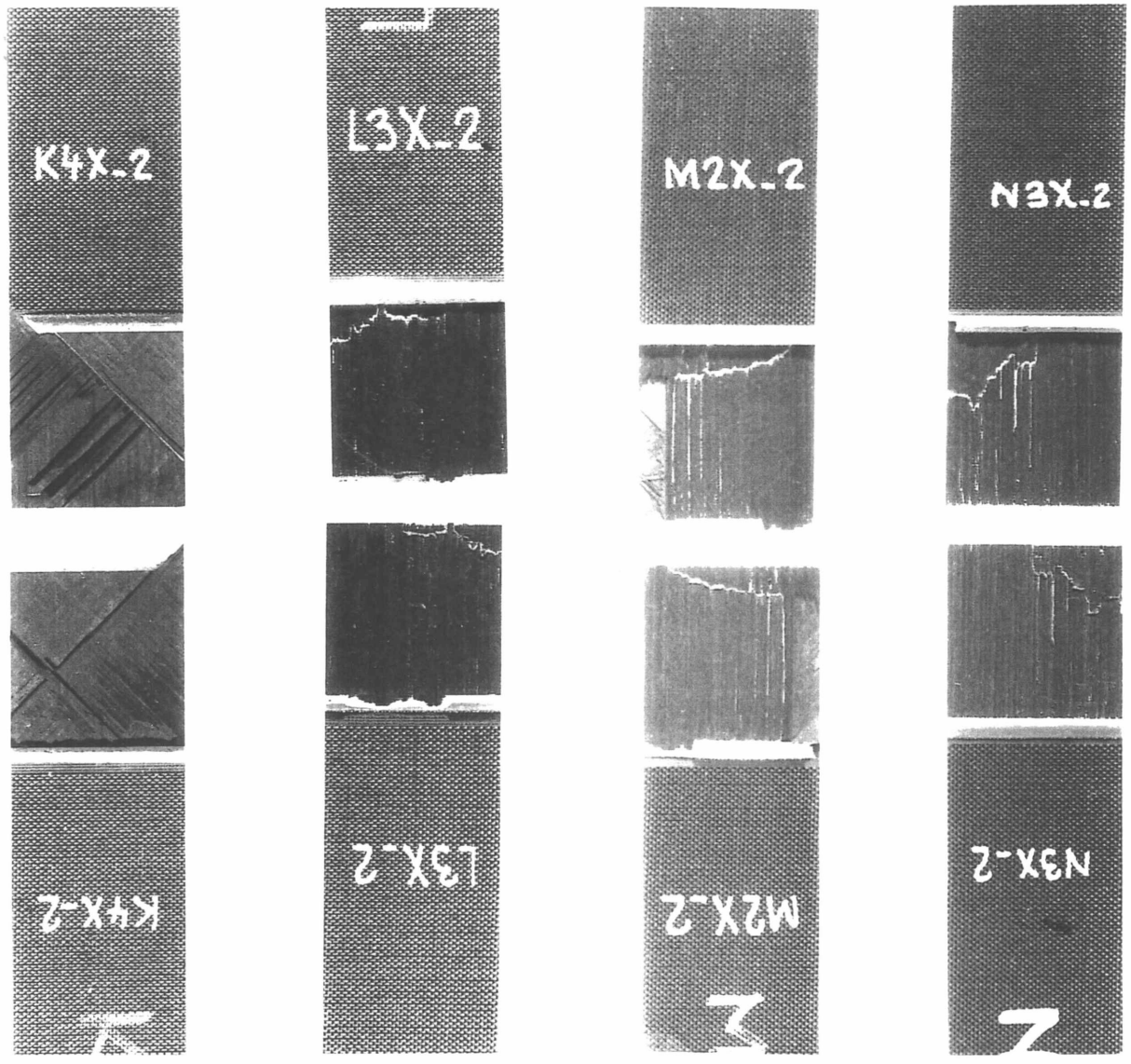
Table 7.2. Adherend mechanical properties and stresses from Hart-Smith's analysis.

Stacking sequence	E_m	E_b	ν_m	ν_b	D	k_b	m	P	σ_{av}	σ_b	σ_{max}	σ_p
K: $[\pm 45/0_3/\pm 45/0]_s$	81.0	66.0	0.638	0.657	77.4	0.850	−0.047	764.4	382.2	481.7	863.9	217.2
L: $[0/\pm 45/0_2/\pm 45/0]_s$	81.0	83.6	0.638	0.626	91.8	1.008	−0.055	740.8	370.4	500.0	870.4	207.6
M: $[0_2/\pm 45/0/\pm 45/0]_s$	81.0	98.5	0.638	0.588	100.4	1.103	−0.065	896.4	448.2	585.0	1033.2	232.1
N: $[0_3/(\pm 45)_2/0]_s$	81.0	110.7	0.638	0.543	104.6	1.149	−0.076	956.8	478.4	619.3	1097.7	240.7

E_m— effective membrane elastic modulus of adherends in direction of applied load ($\times 10^3$ N/mm^2).
E_b— effective bending elastic modulus of adherends corresponding to a bending moment about an in-plane axis normal to the direction of applied load ($\times 10^3$ N/mm^2).
ν_m— effective membrane Poisson's ratio of adherends associated with E_m.
ν_b— effective bending Poisson's ratio of adherends associated with E_b.
D— flexural rigidity of adherends ($\times 10^3$ Nmm).
k_b— bending stiffness parameter.
m— coefficient of mutual bend-twist coupling corresponding to a bending moment about an in-plane axis normal to the direction of applied load.
P— experimental mean load at failure per unit joint width (N/mm).

σ_{av}— adherend average stress.
σ_b— adherend bending stress.
σ_{max}— adherend maximum stress.
σ_p— adhesive peel stress.

All stresses are given in N/mm^2.



K	L	M	N
$[\pm 45/0_3/\pm 45/0]_s$	$[0/\pm 45/0_2/\pm 45/0]_s$	$[0_2/\pm 45/0/\pm 45/0]_s$	$[0_3/(\pm 45)_2/0]_s$

Fig. 7.1. The bonded specimens with stacking sequences K–N after fracture.

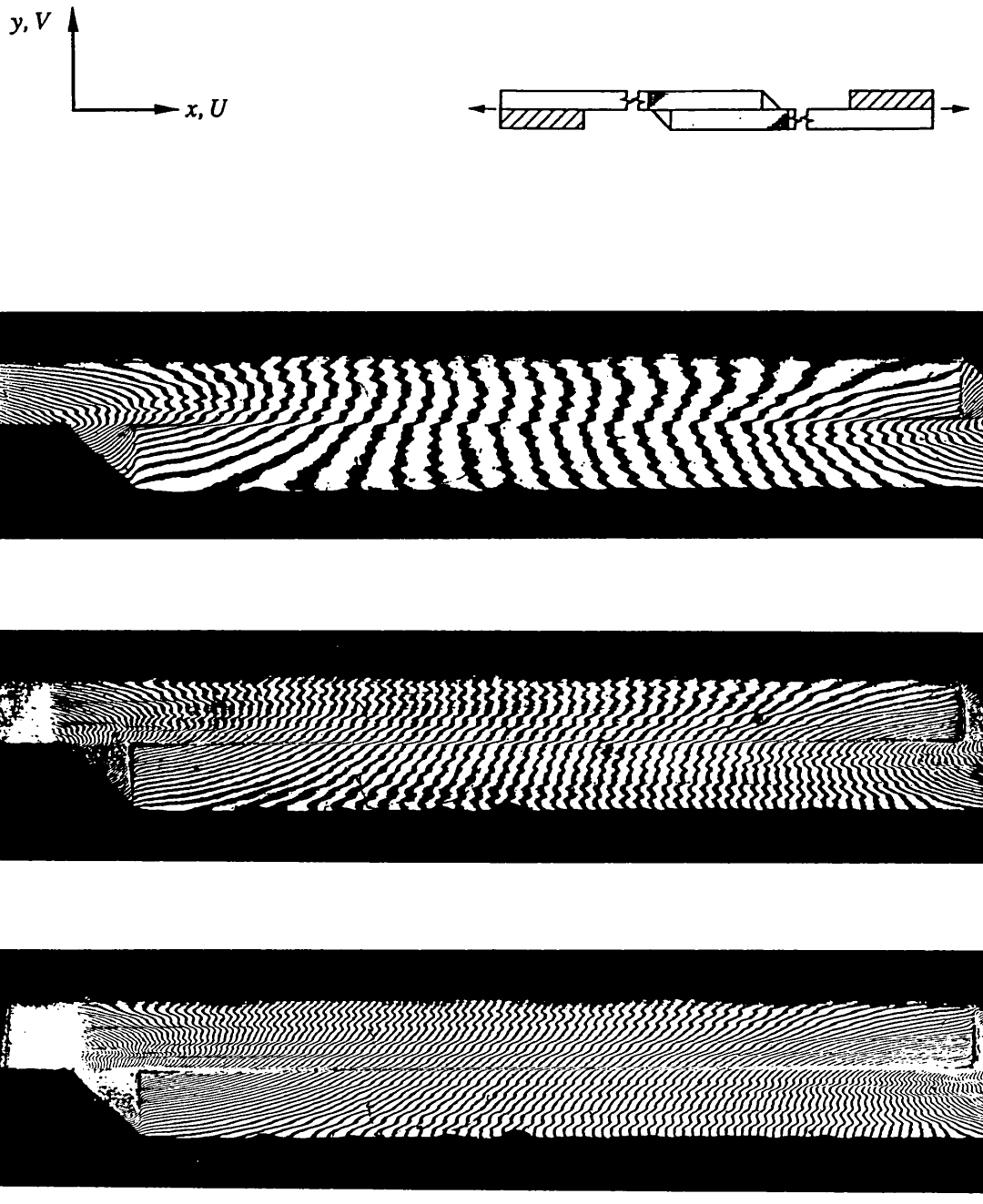


Fig. 7.2. U displacement field for stacking sequence L: $[0/\pm 45/0_2/\pm 45/0]_s$ with increasing load from top to bottom.

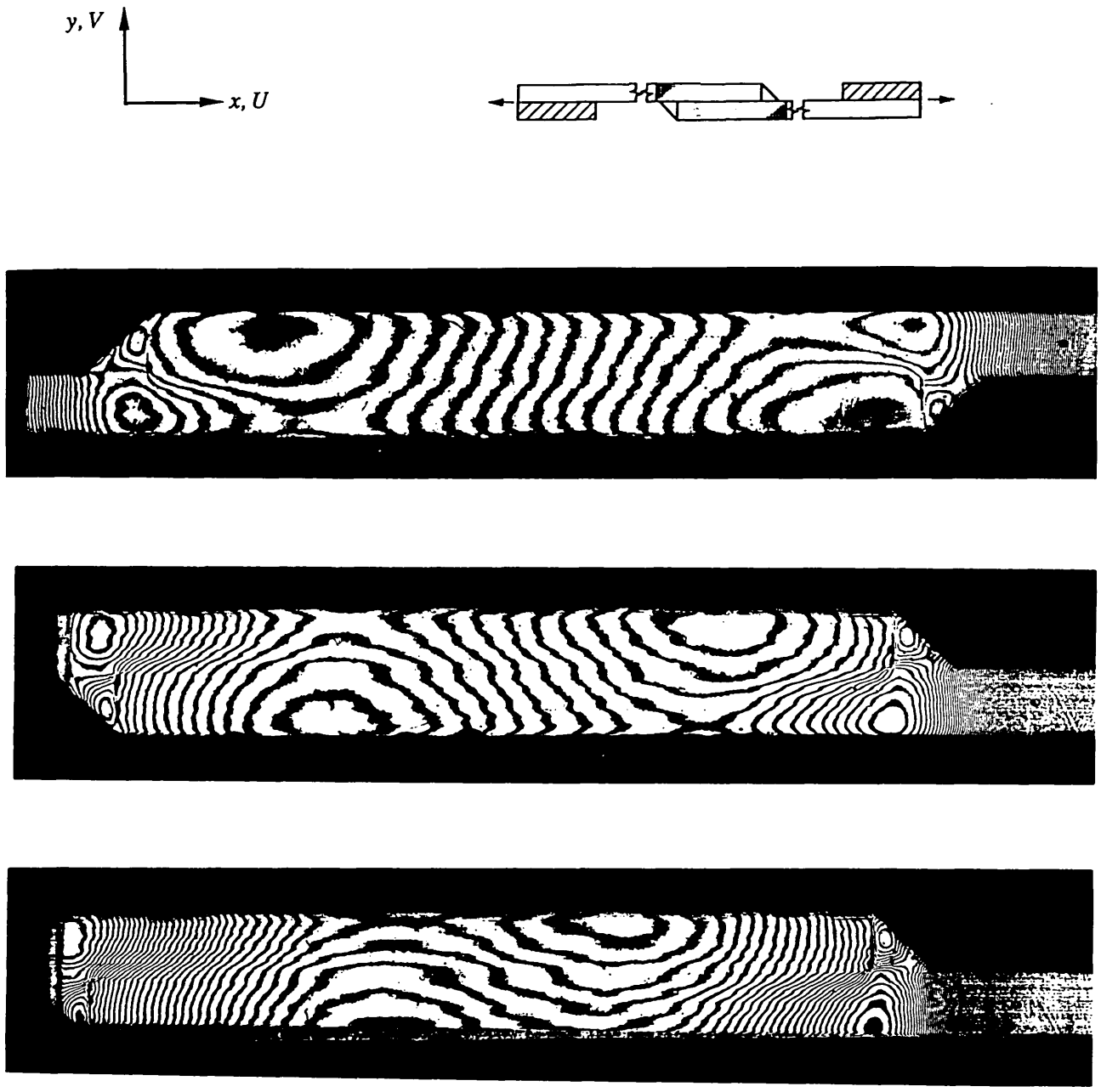
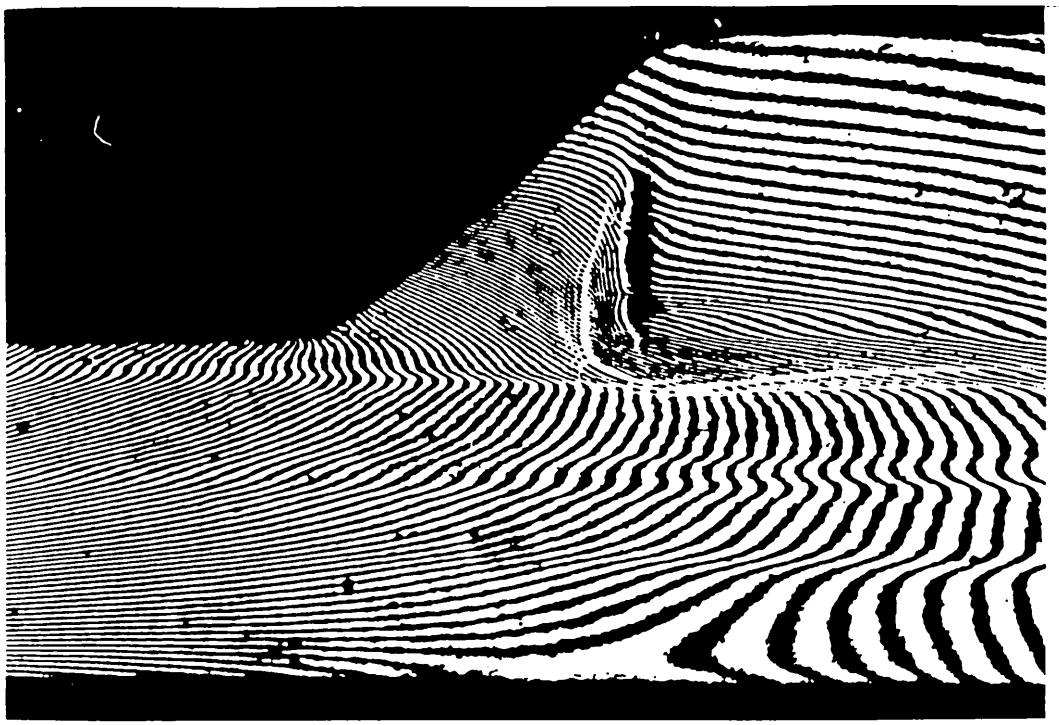
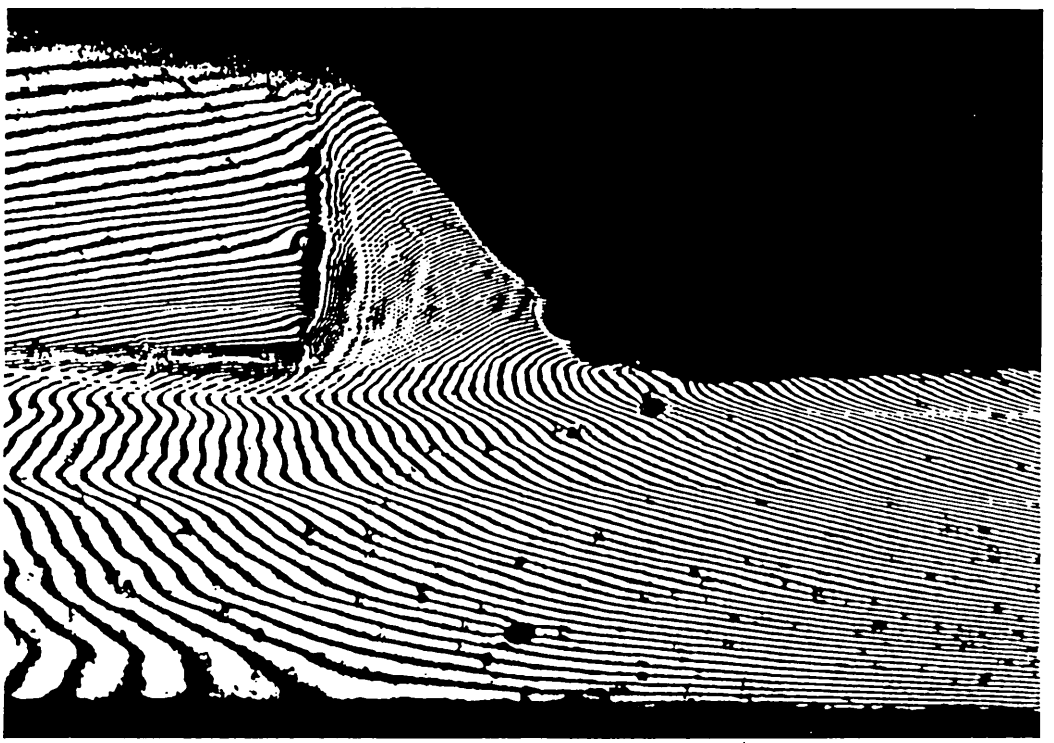


Fig. 7.3. V displacement field for stacking sequence L: $[0/\pm 45/0_2/\pm 45/0]_s$ with increasing load from top to bottom.

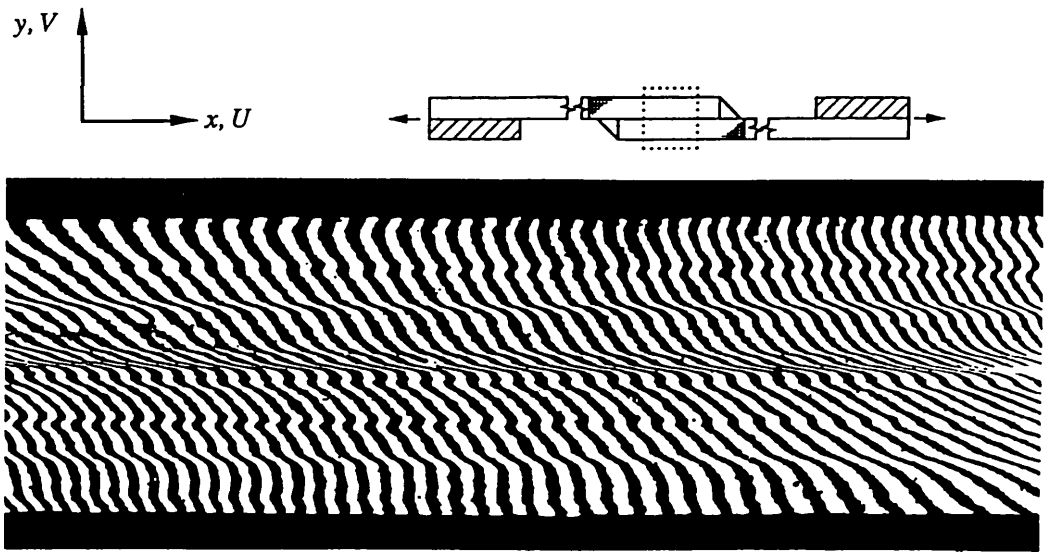


(a) Stacking sequence K: $[\pm 45/0_3/\pm 45/0]_s$ at 169.0 N/mm^2 applied stress.

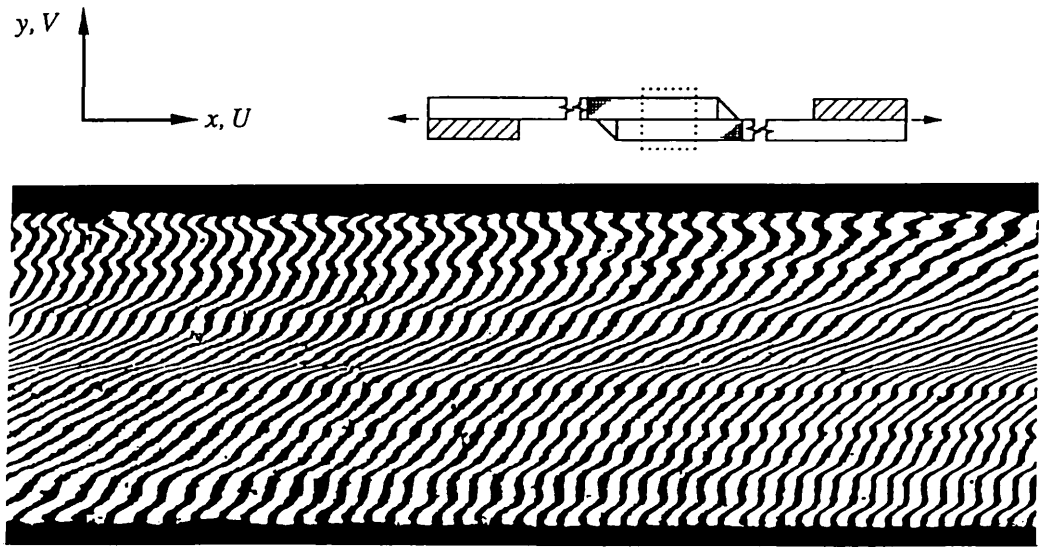


(b) Stacking sequence L: $[0/\pm 45/0_2/\pm 45/0]_s$ at 189.5 N/mm^2 applied stress.

Fig. 7.4. U displacement field at end of lap.

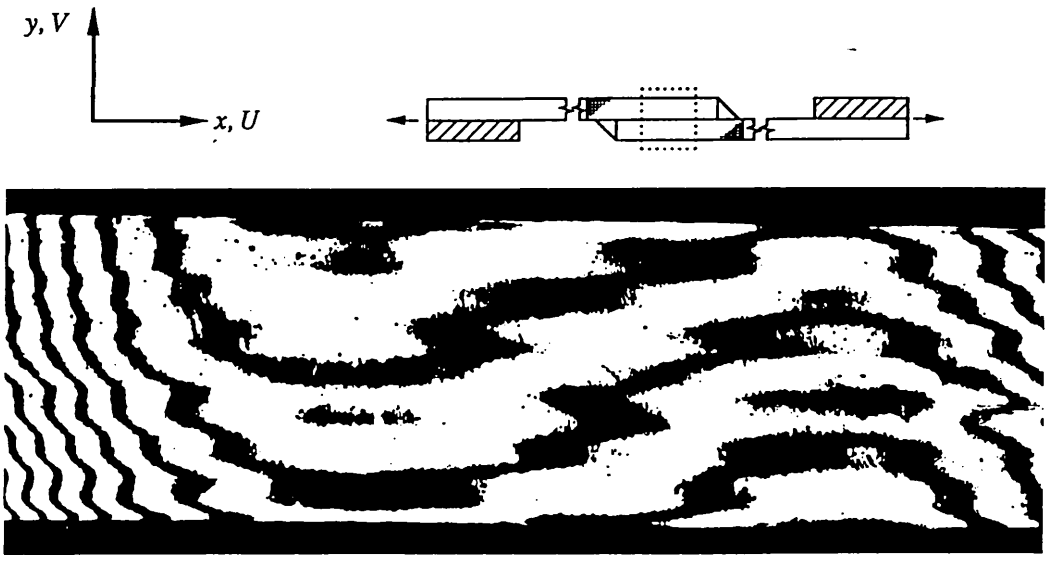


(a) Stacking sequence K: $[\pm 45/0_3/\pm 45/0]_s$ at 169.0 N/mm^2 applied stress.

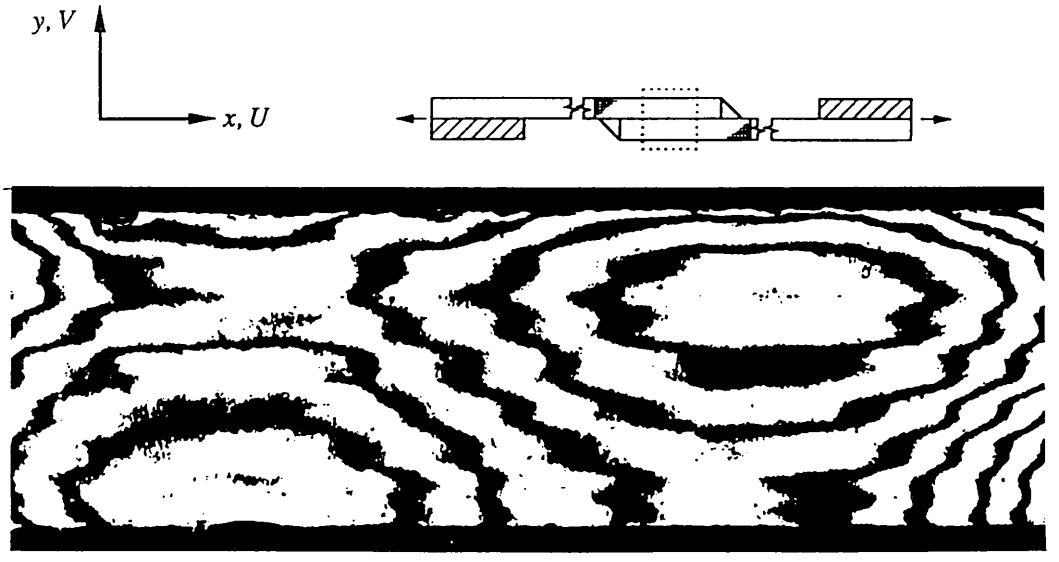


(b) Stacking sequence L: $[0/\pm 45/0_2/\pm 45/0]_s$ at 189.5 N/mm^2 applied stress.

Fig. 7.5. U displacement field at centre of lap. .



(a) Stacking sequence K: $[\pm 45/0_3/\pm 45/0]_s$ at 169.0 N/mm^2 applied stress.



(b) Stacking sequence L: $[0/\pm 45/0_2/\pm 45/0]_s$ at 189.5 N/mm^2 applied stress.

Fig. 7.6. V displacement field at centre of lap.

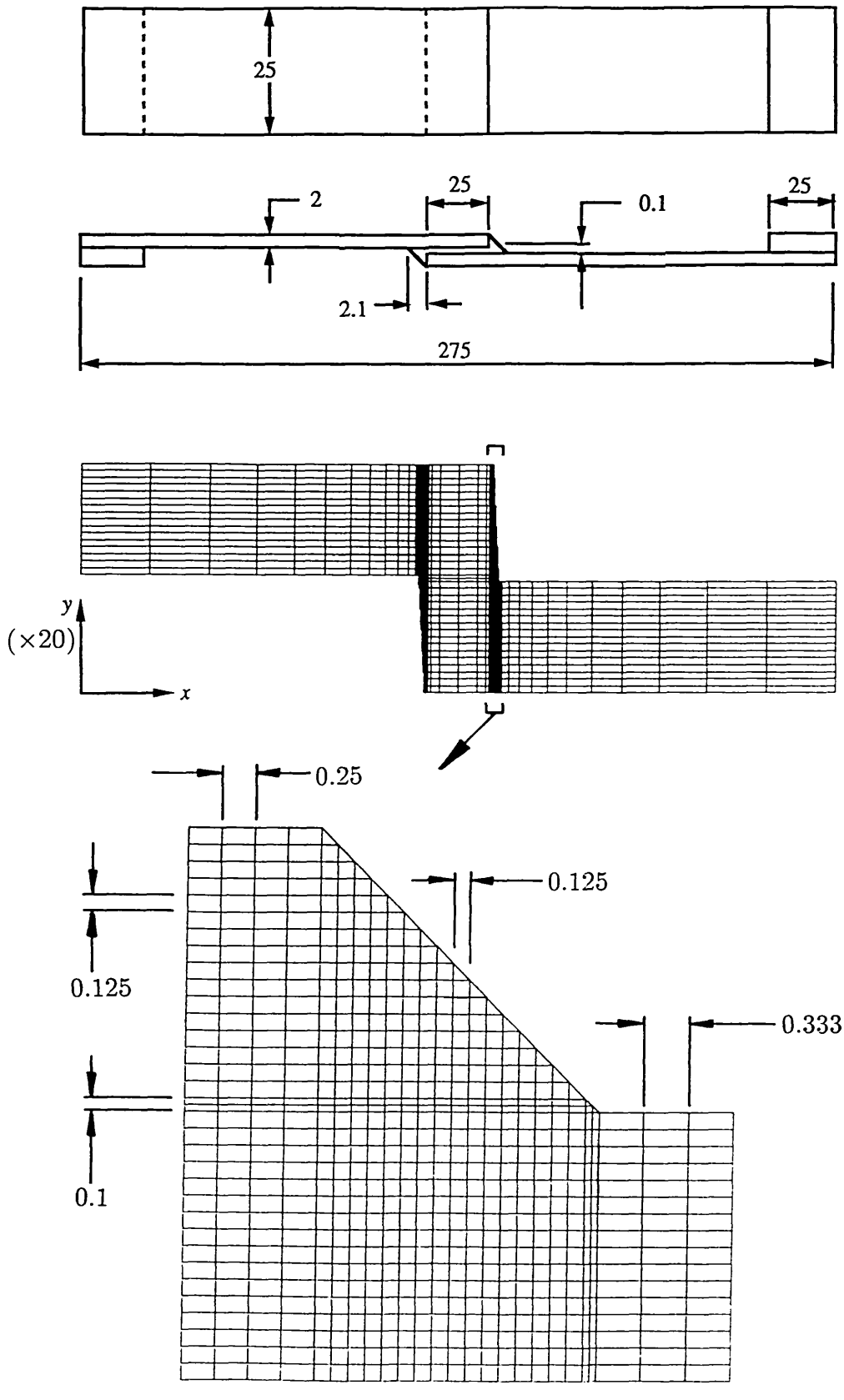
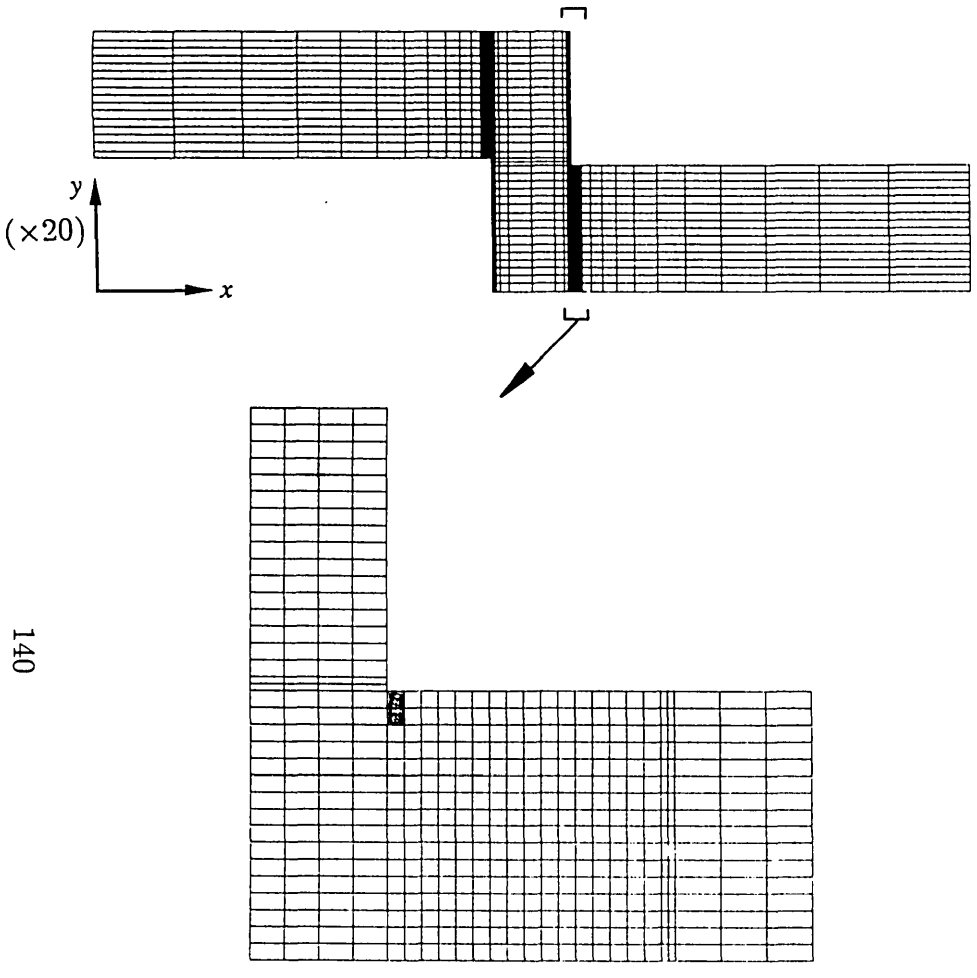
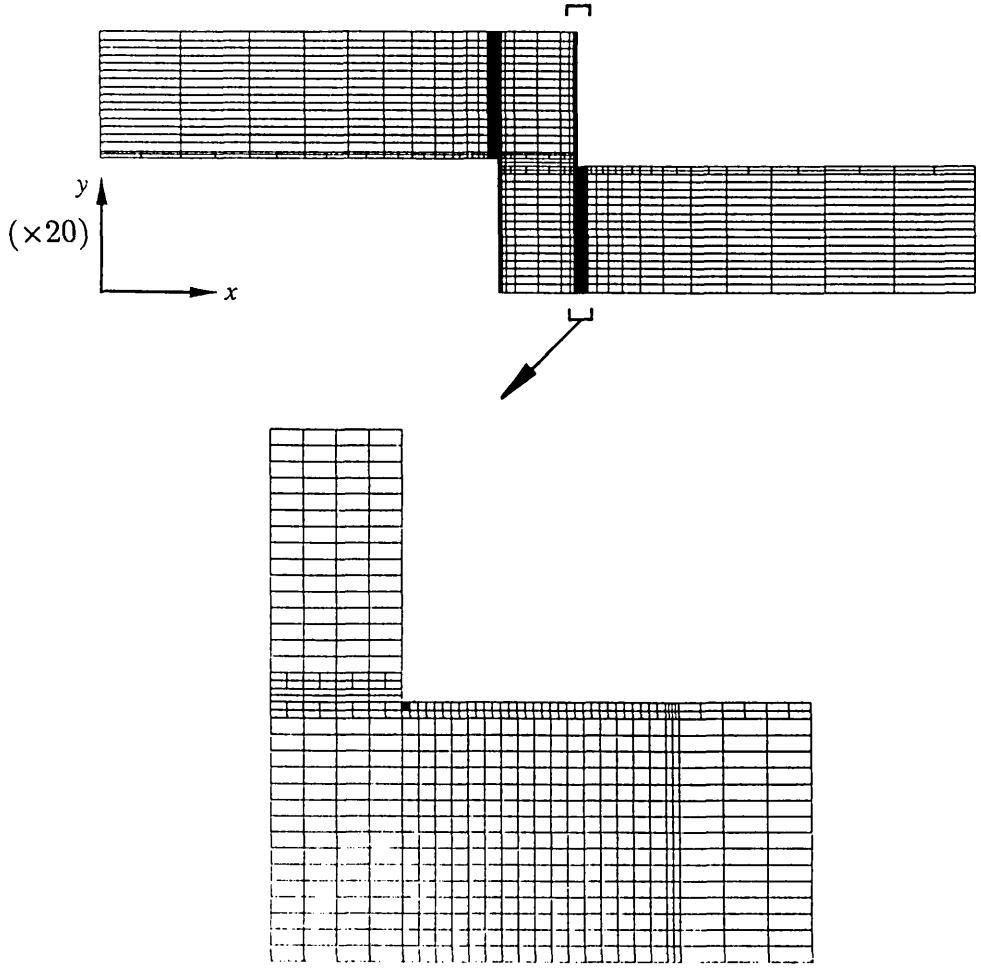


Fig. 7.7. Geometry and finite element model of sixteen-ply adherend joint. Dimensions are given in millimetres (not to scale).

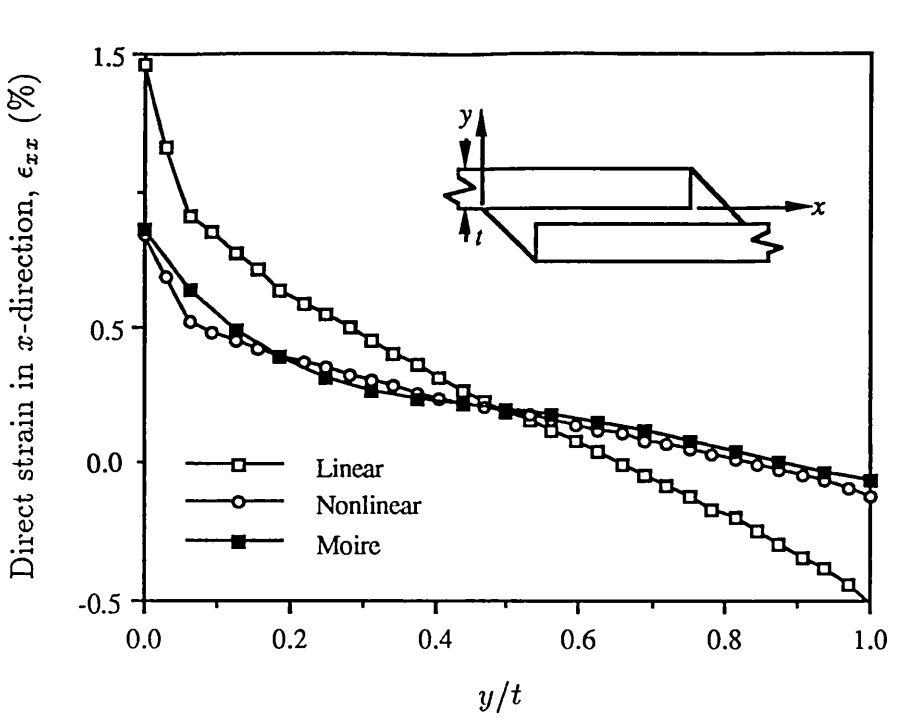


(a) Stacking sequence K: $[\pm 45/0_3/\pm 45/0]_s$. The cracked elements simulate shear fracture of the $\pm 45°$ layers next to the bondline at end of lap.

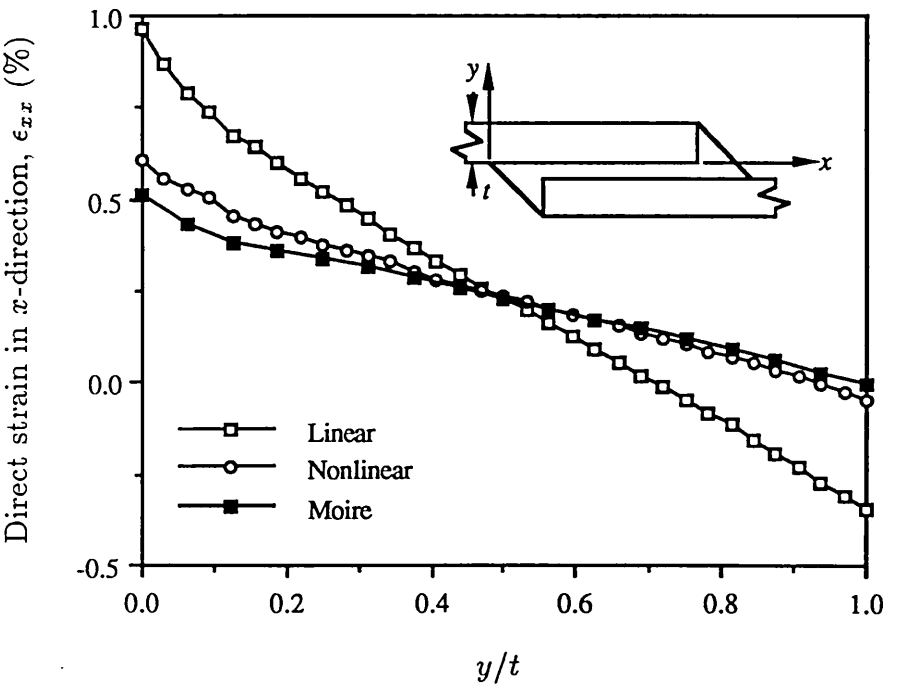


(b) Stacking sequence L: $[0/\pm 45/0_2/\pm 45/0]_s$. The cracked element simulates tensile fracture of half the thickness of the 0° ply next to the bondline at end of lap.

Fig. 7.8. Finite element models without adhesive fillet—post fillet fracture analysis. The cracked (reduced stiffness) elements are shaded.

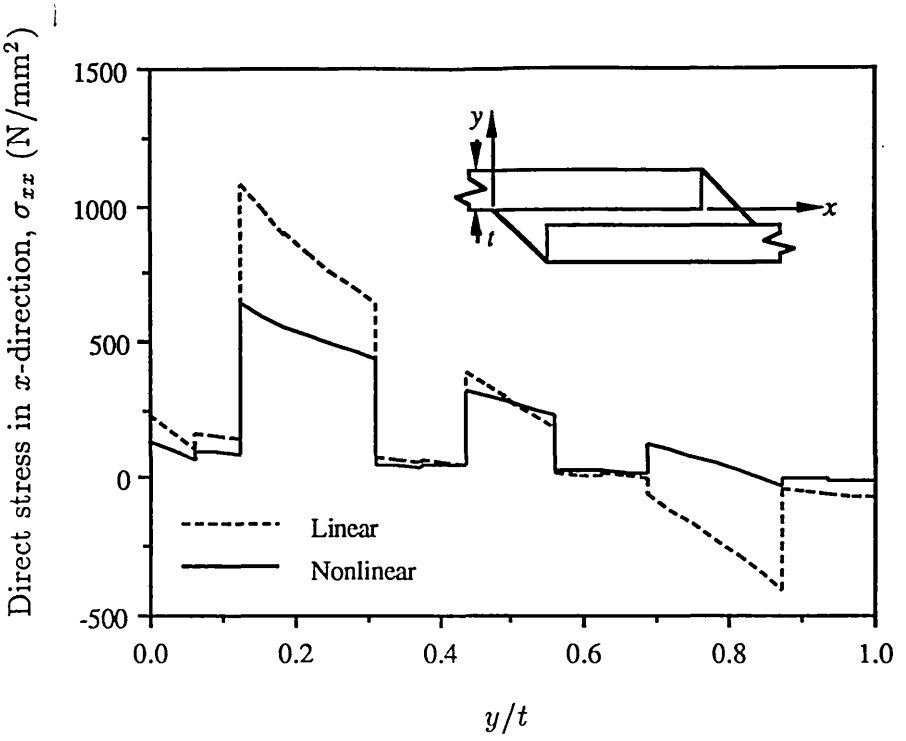


(a) Stacking sequence K: $[\pm 45/0_3/\pm 45/0]_s$ at 169.0 N/mm^2 applied stress.

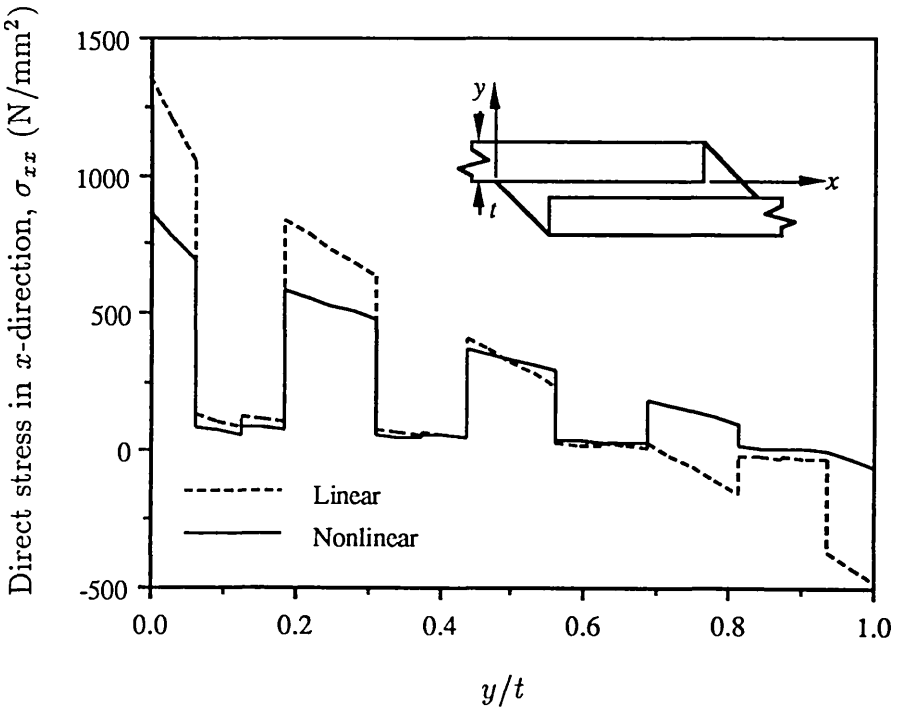


(b) Stacking sequence L: $[0/\pm 45/0_2/\pm 45/0]_s$ at 189.5 N/mm^2 applied stress.

Fig. 7.9. Adherend longitudinal direct strain distribution along y-axis at fillet tip.

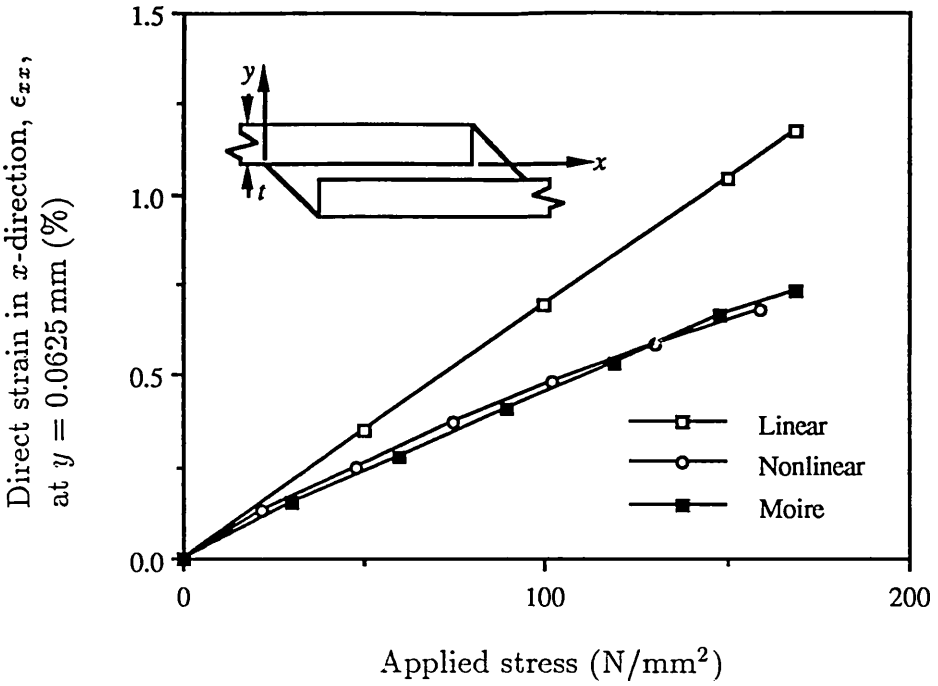


(a) Stacking sequence K: $[\pm 45/0_3/\pm 45/0]_s$ at 169.0 N/mm^2 applied stress.

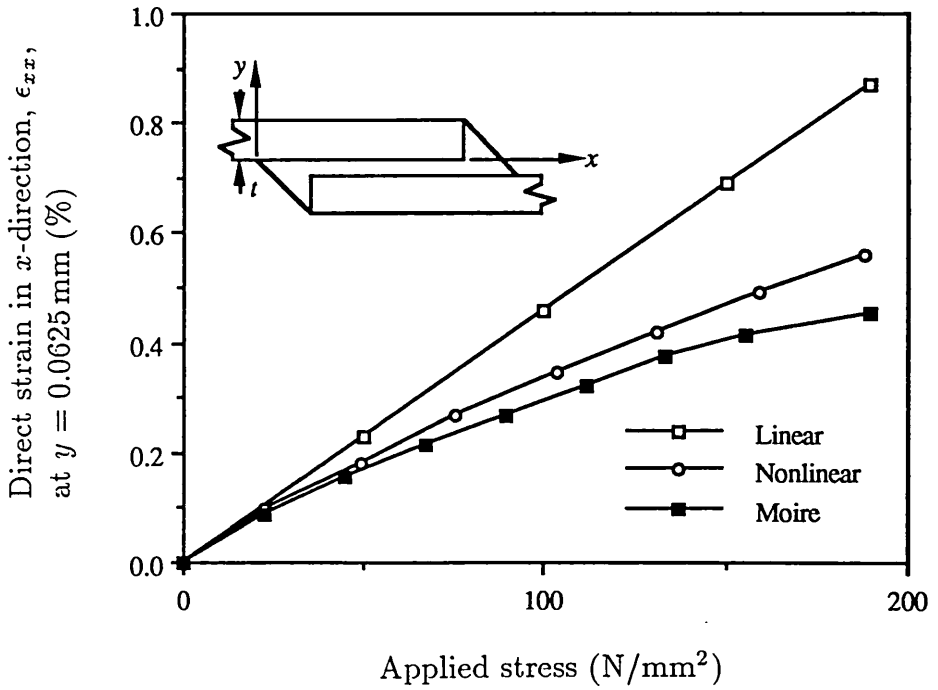


(b) Stacking sequence L: $[0/\pm 45/0_2/\pm 45/0]_s$ at 189.5 N/mm^2 applied stress.

Fig. 7.10. Adherend longitudinal direct stress distribution along y-axis at fillet tip.

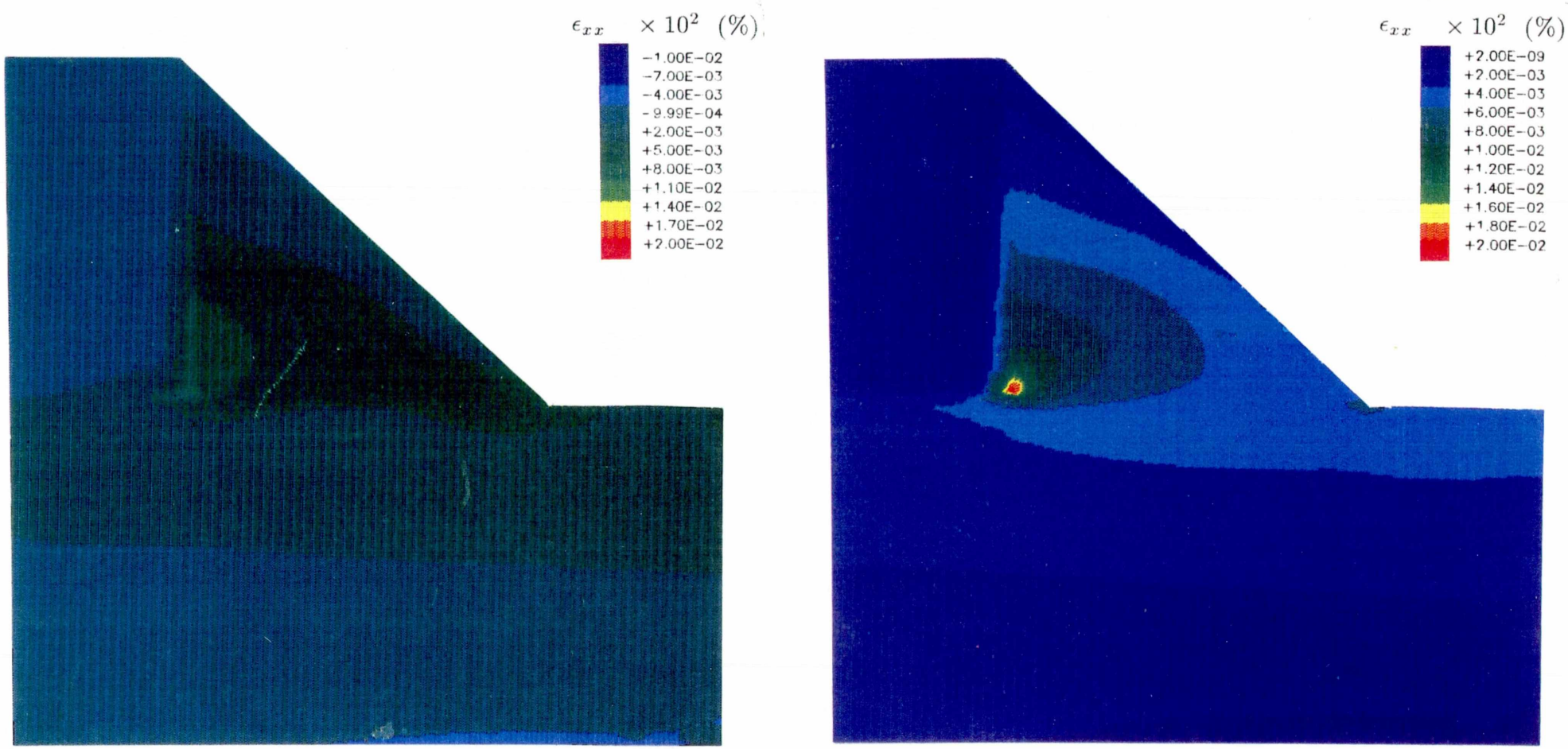


(a) Stacking sequence K: $[\pm 45/0_3/\pm 45/0]_s$.



(b) Stacking sequence L: $[0/\pm 45/0_2/\pm 45/0]_s$.

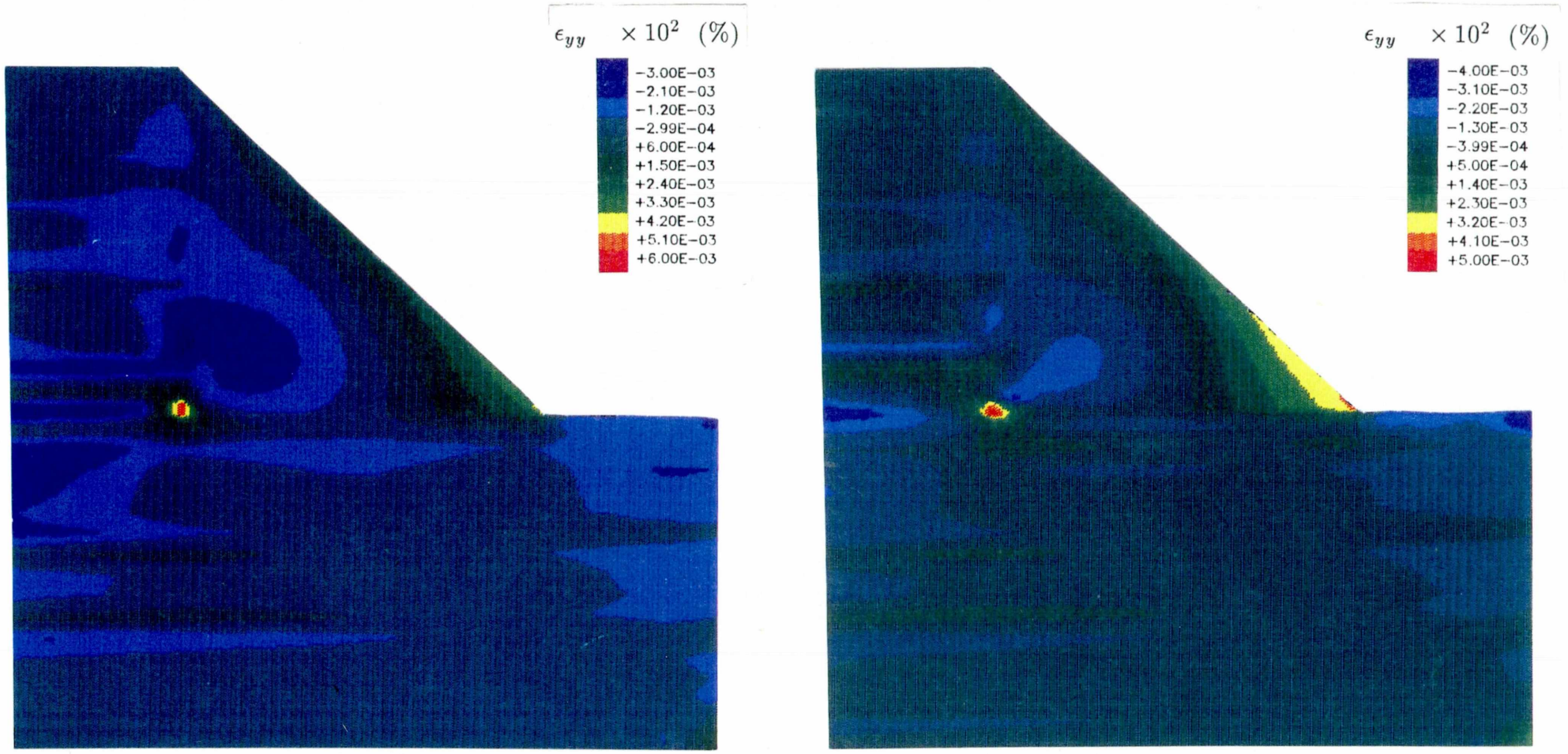
Fig. 7.11. Variation of adherend longitudinal direct strain with applied stress at the centre of the first ply next to fillet tip.



(a) Stacking sequence K: $[\pm 45/0_3/\pm 45/0]_s$ at 169.0 N/mm^2 applied stress.

(b) Stacking sequence L: $[0/\pm 45/0_2/\pm 45/0]_s$ at 189.5 N/mm^2 applied stress.

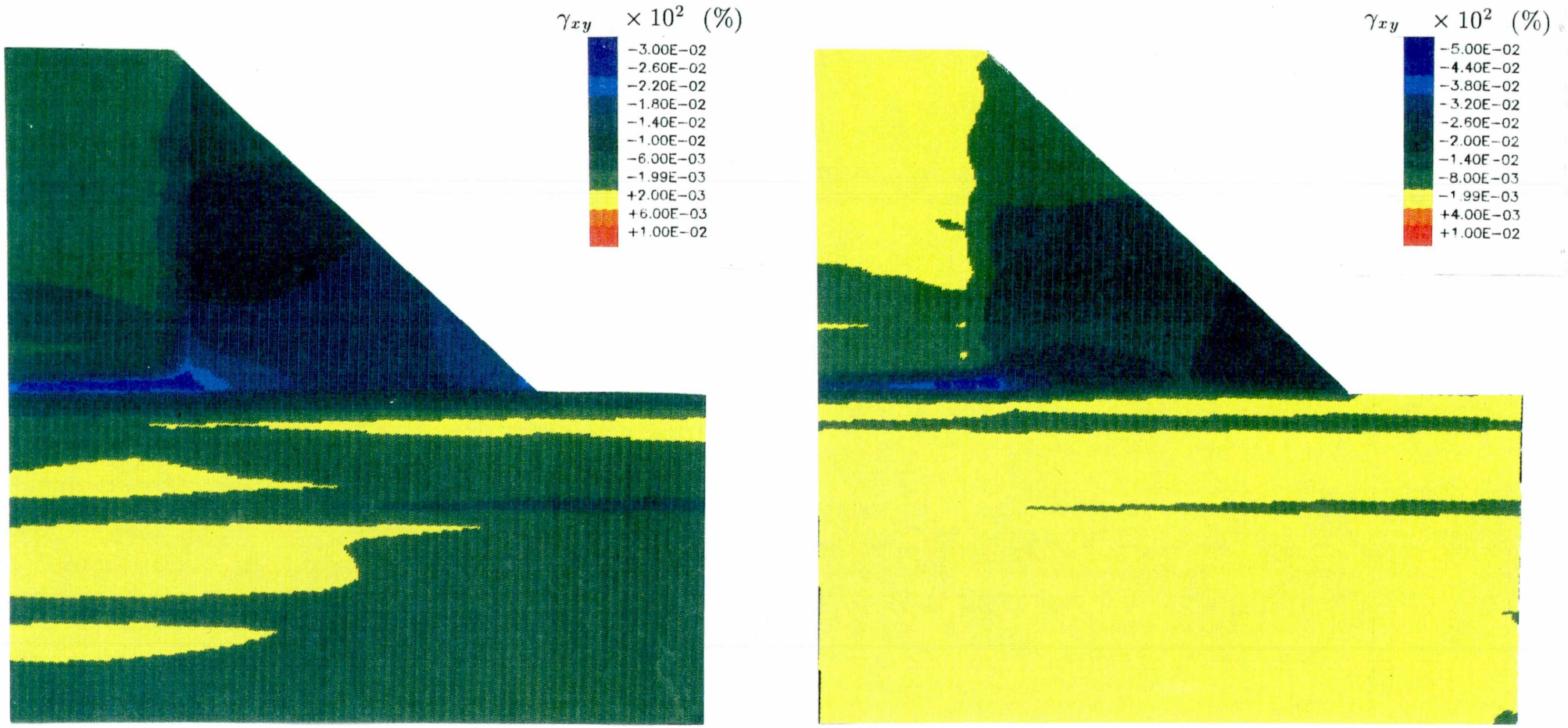
Fig. 7.12. Contours of longitudinal direct strain ϵ_{xx} at end of lap.



(a) Stacking sequence K: $[\pm 45/0_3/\pm 45/0]_s$ at 169.0 N/mm^2 applied stress.

(b) Stacking sequence L: $[0/\pm 45/0_2/\pm 45/0]_s$ at 189.5 N/mm^2 applied stress.

Fig. 7.13. Contours of transverse direct strain ϵ_{yy} at end of lap.



(a) Stacking sequence K: $[\pm 45/0_3/\pm 45/0]_s$ at 169.0 N/mm^2 applied stress.

(b) Stacking sequence L: $[0/\pm 45/0_2/\pm 45/0]_s$ at 189.5 N/mm^2 applied stress.

Fig. 7.14. Contours of shear strain γ_{xy} at end of lap.

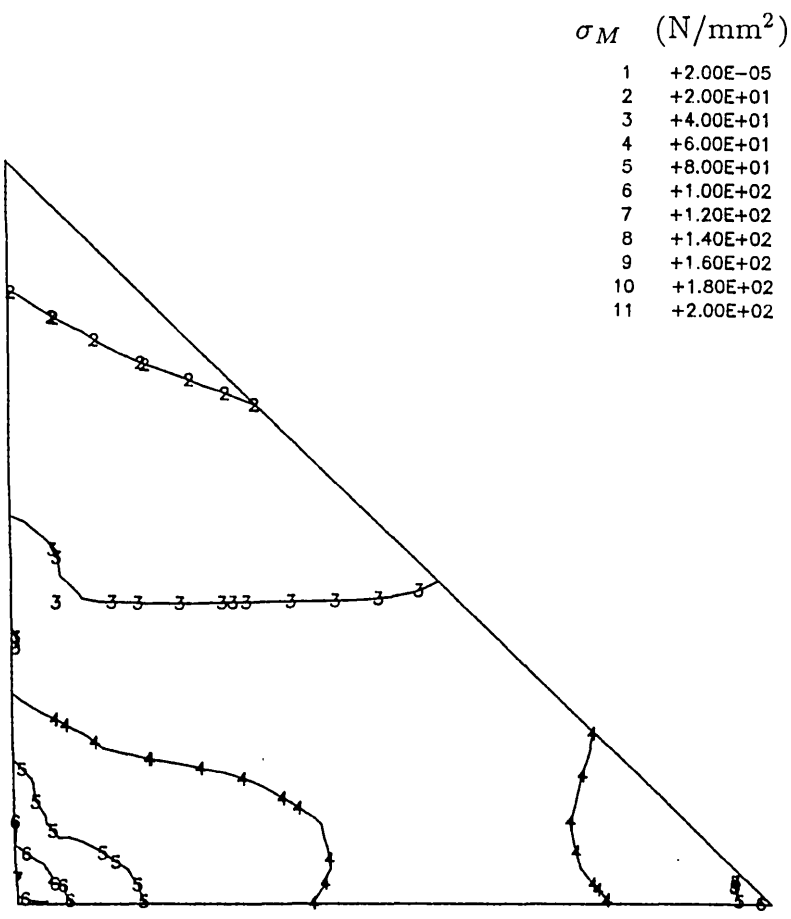
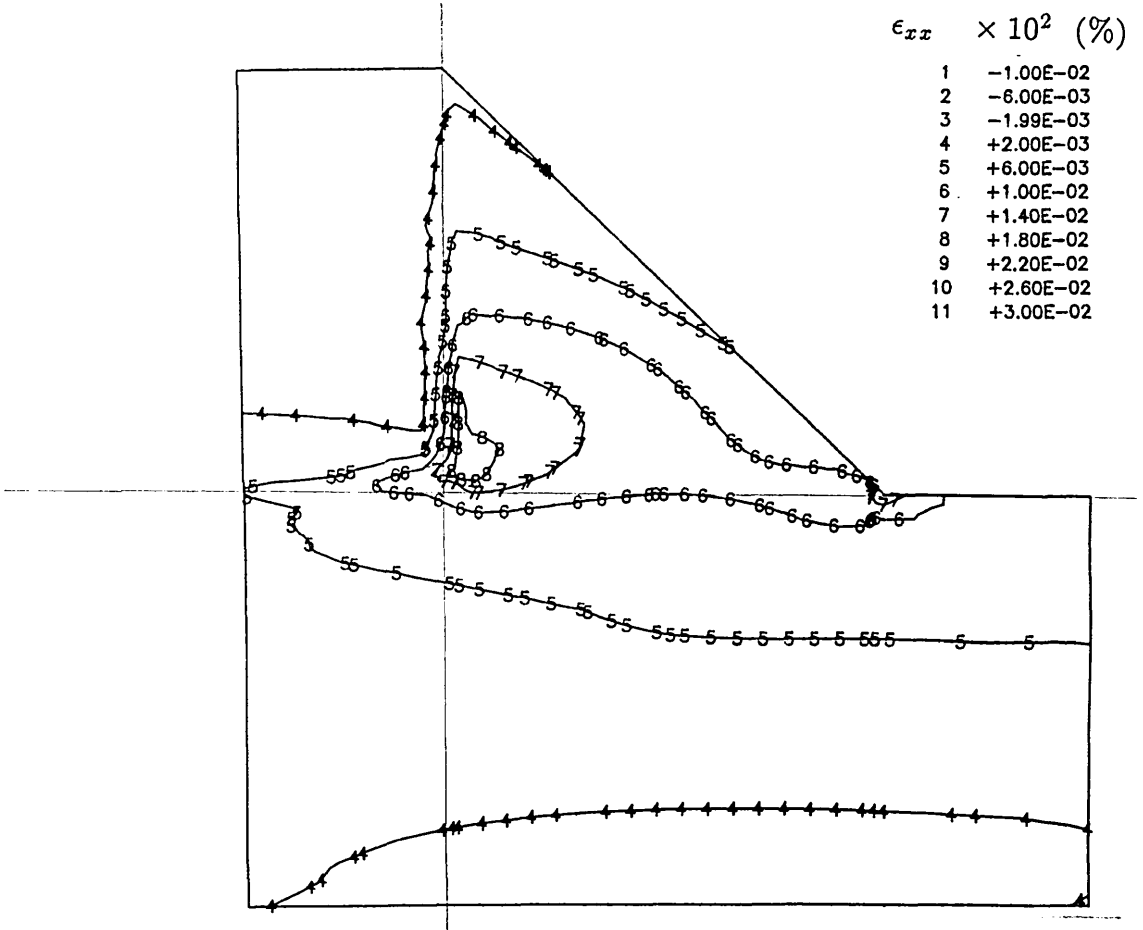
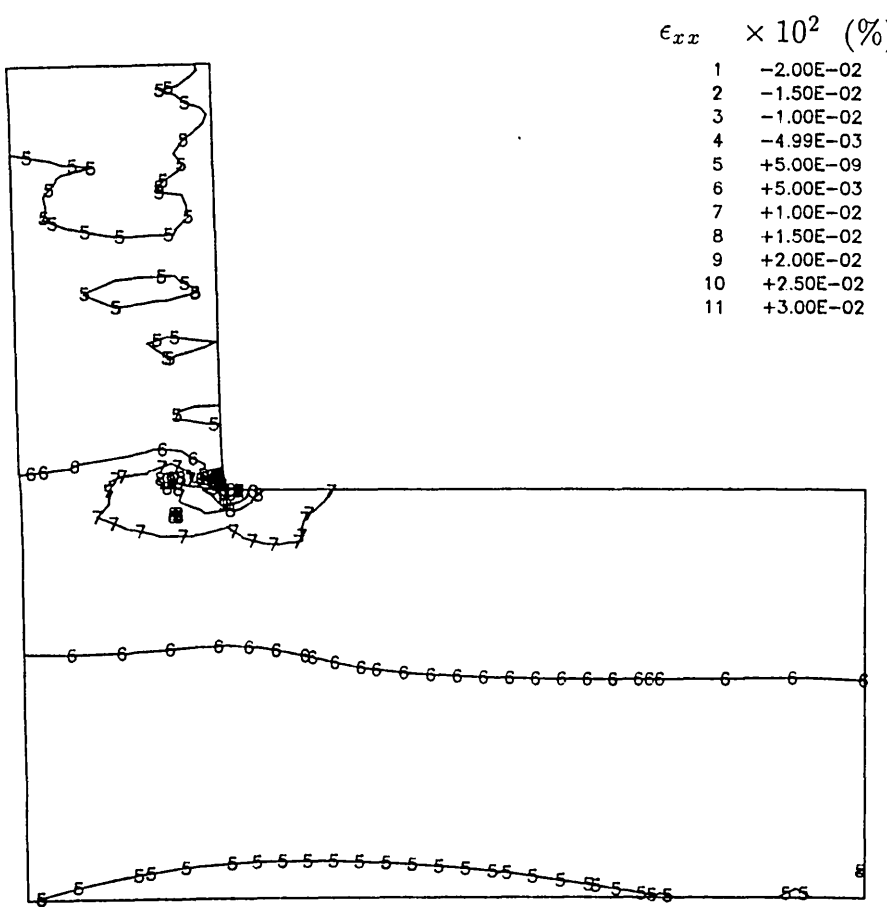


Fig. 7.15. Contours of von Mises stress σ_M in fillet. Stacking sequence K: $[\pm 45/0_3/\pm 45/0]_s$ at 362.5 N/mm^2 applied stress.

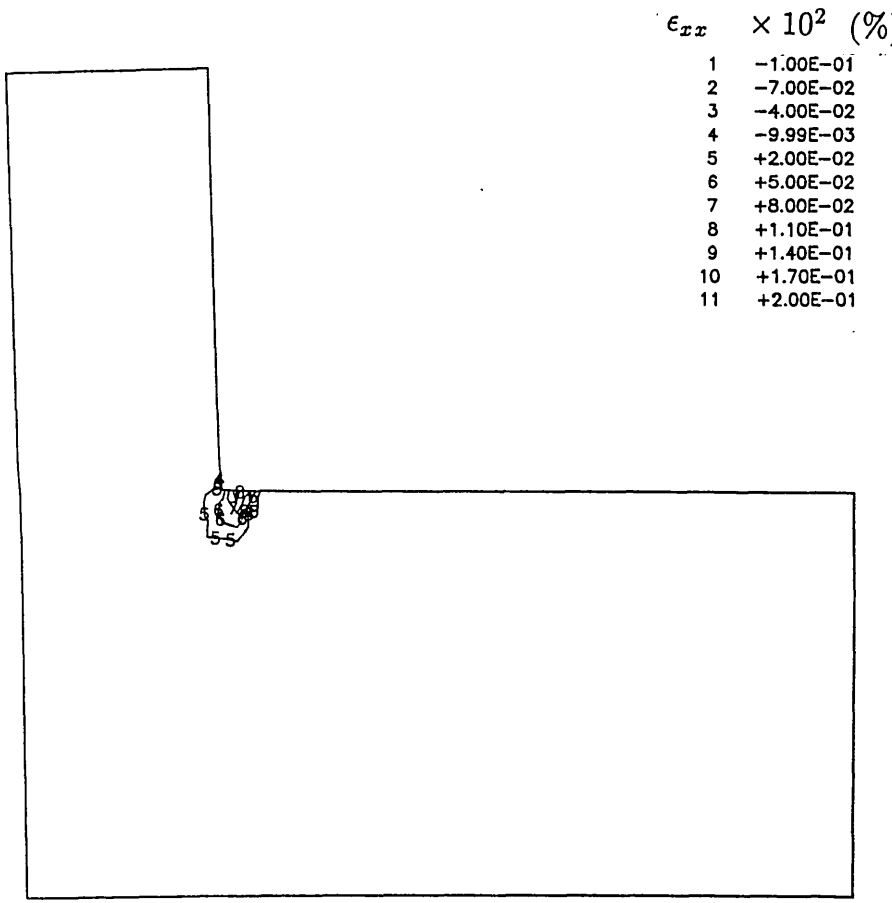


(a) Before fillet fracture.

Fig. 7.16. Contours of longitudinal direct strain ϵ_{xx} at end of lap. Stacking sequence K: $[\pm 45/0_3/\pm 45/0]_s$ at 362.5 N/mm^2 applied stress.

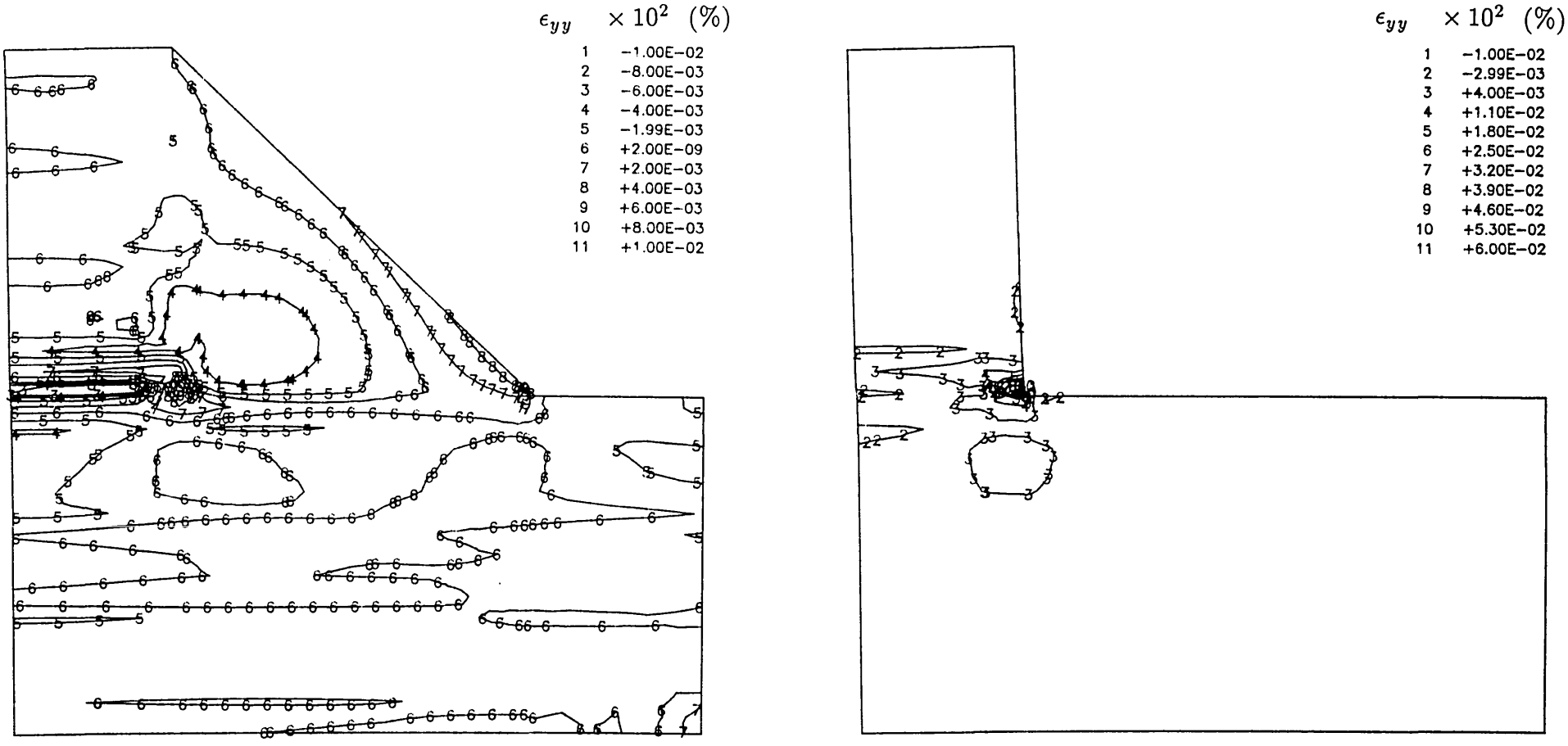


(b) After fillet fracture.



(c) After shear fracture of ±45° plies.

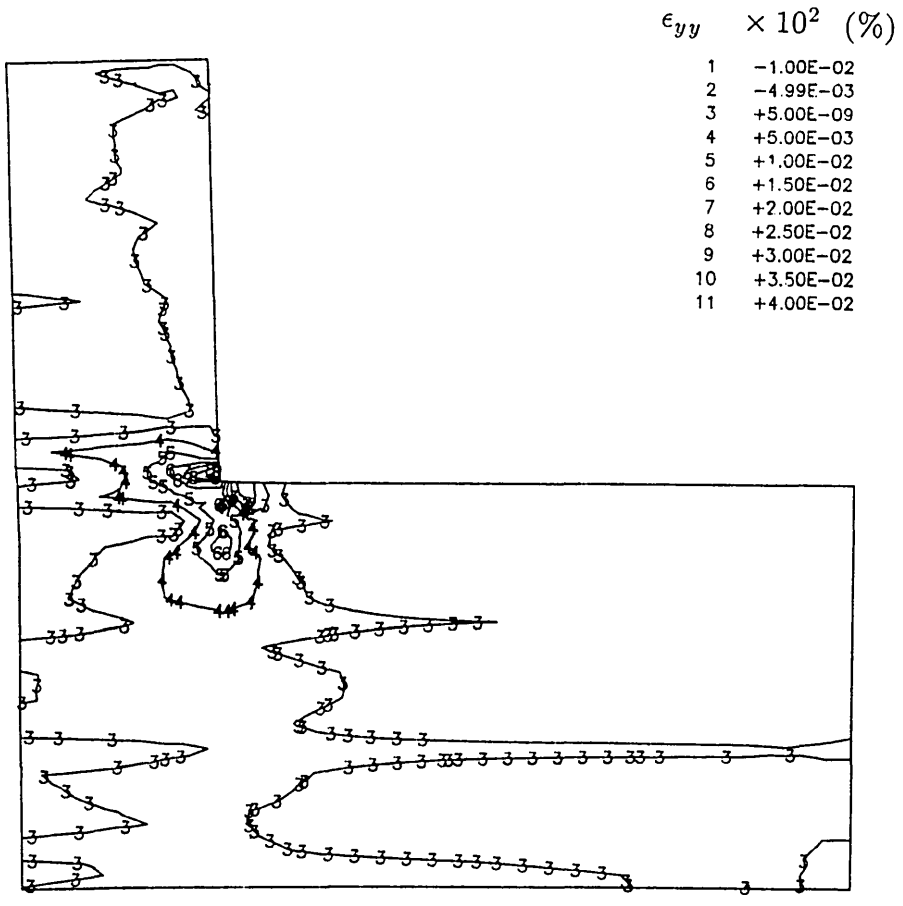
Fig. 7.16. (continued) Contours of longitudinal direct strain ϵ_{xx} at end of lap. Stacking sequence K: $[\pm 45/0_3/\pm 45/0]_s$ at 362.5 N/mm^2 applied stress.



(a) Before fillet fracture.

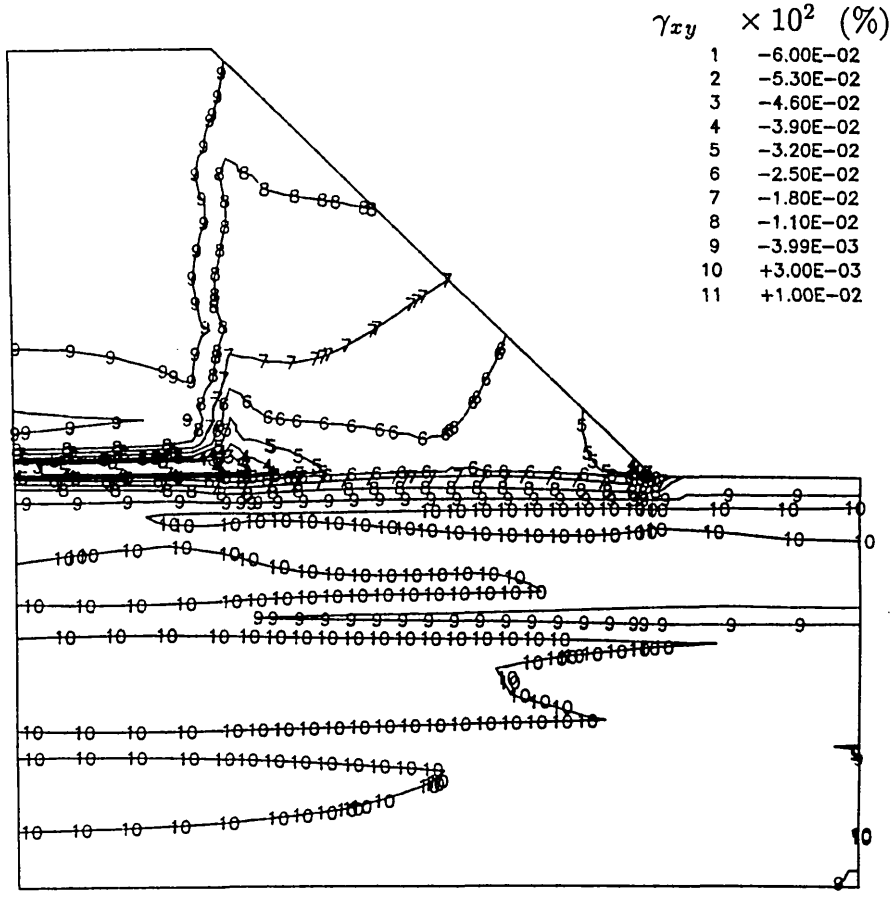
(b) After fillet fracture.

Fig. 7.17. Contours of transverse direct strain ϵ_{yy} at end of lap. Stacking sequence K: $[\pm 45/0_3/\pm 45/0]_s$ at 362.5 N/mm^2 applied stress.



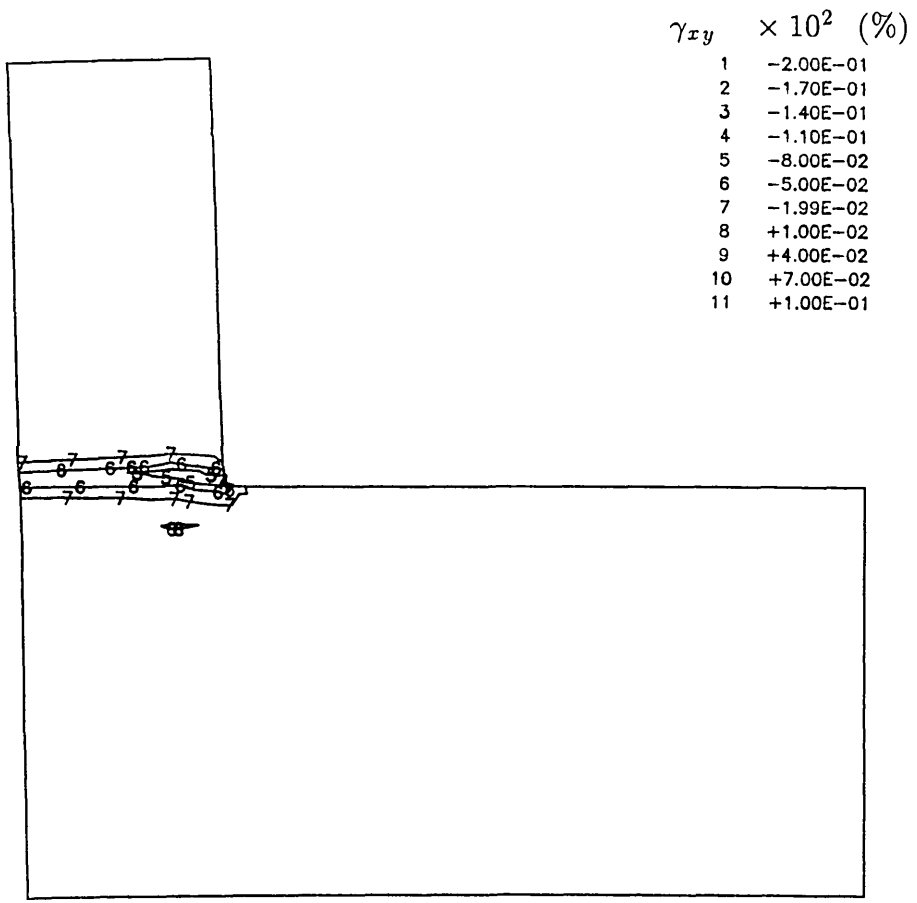
(c) After shear fracture of ±45° plies.

Fig. 7.17. (continued) Contours of transverse direct strain ϵ_{yy} at end of lap. Stacking sequence K: $[\pm 45/0_3/\pm 45/0]_s$ at 362.5 N/mm^2 applied stress.

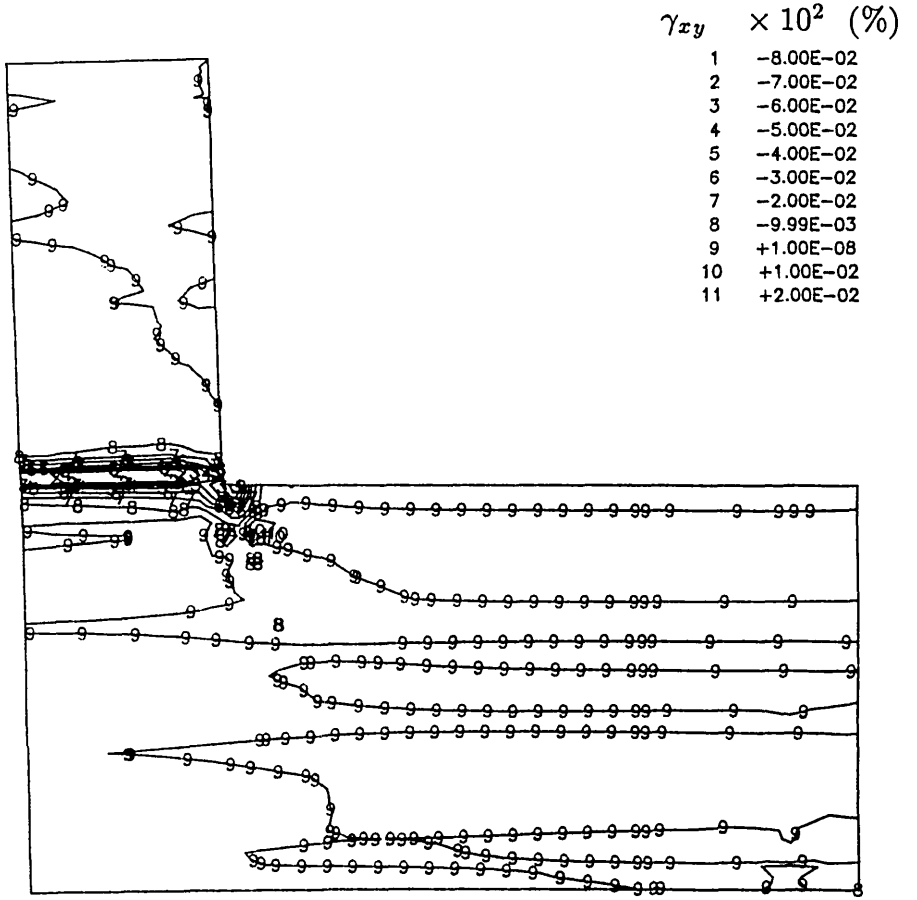


(a) Before fillet fracture.

Fig. 7.18. Contours of shear strain γ_{xy} at end of lap. Stacking sequence K: $[\pm 45/0_3/\pm 45/0]_s$ at 362.5 N/mm^2 applied stress.



(b) After fillet fracture.



(c) After shear fracture of ±45° plies.

Fig. 7.18. (continued) Contours of shear strain γ_{xy} at end of lap. Stacking sequence K: $[\pm 45/0_3/\pm 45/0]_s$ at 362.5 N/mm^2 applied stress.

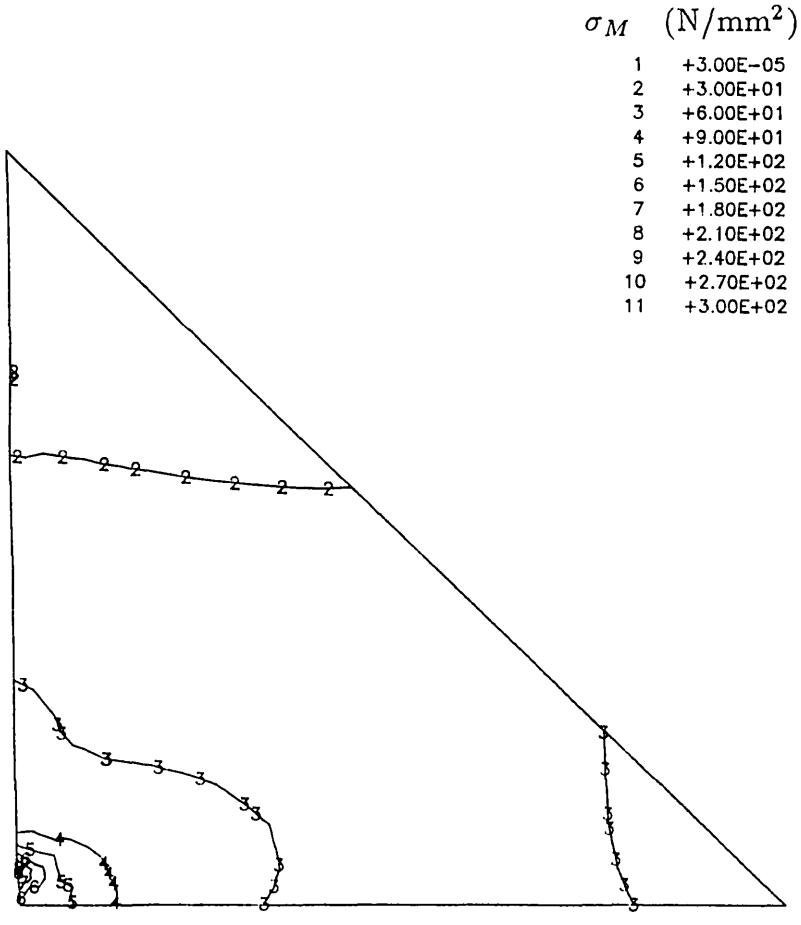
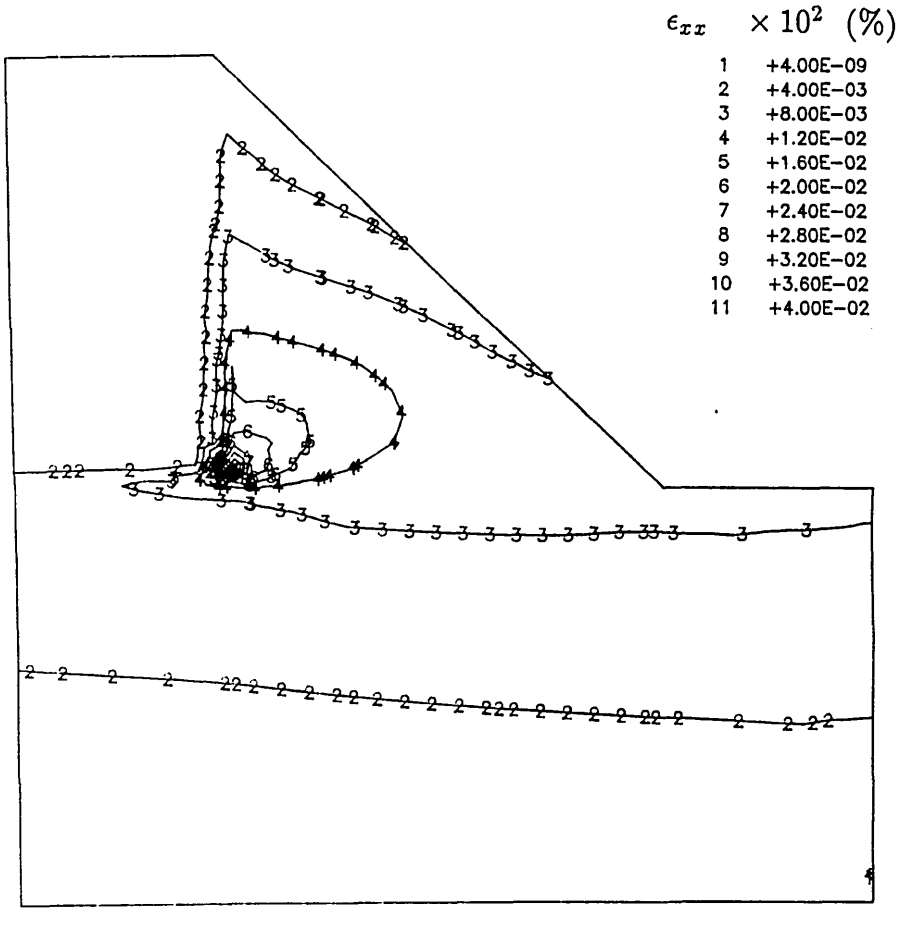
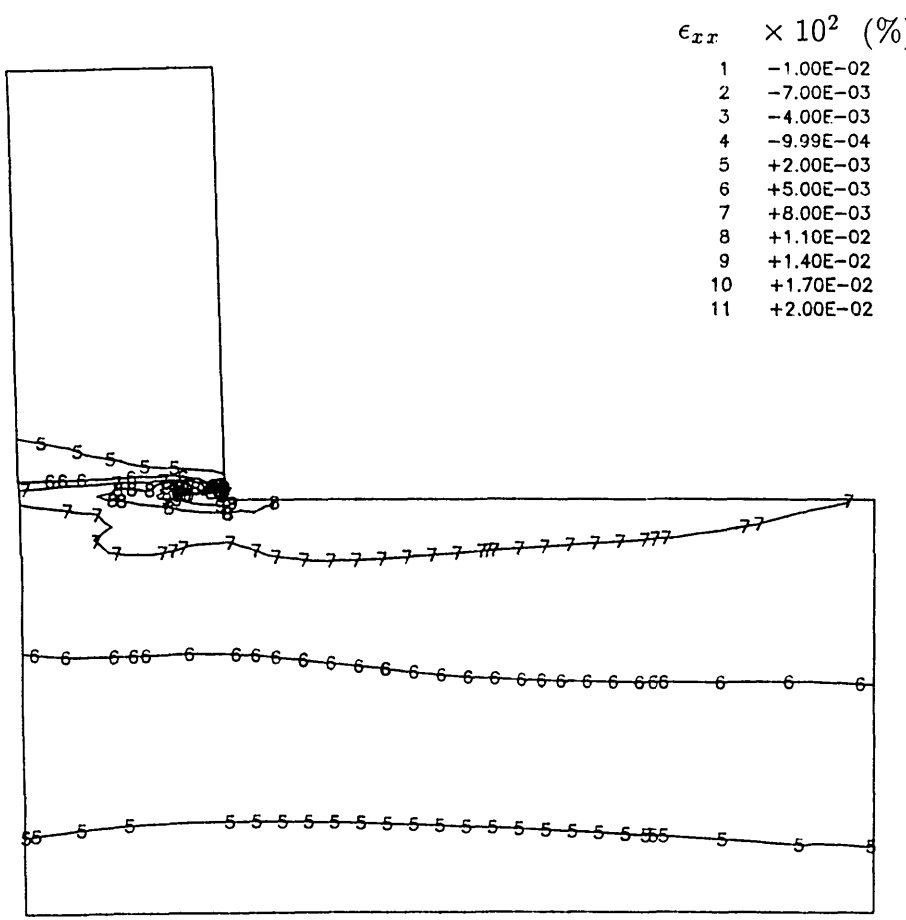


Fig. 7.19. Contours of von Mises stress σ_M in fillet. Stacking sequence L: $[0/\pm45/0_2/\pm45/0]_s$ at 354.2 N/mm^2 applied stress.

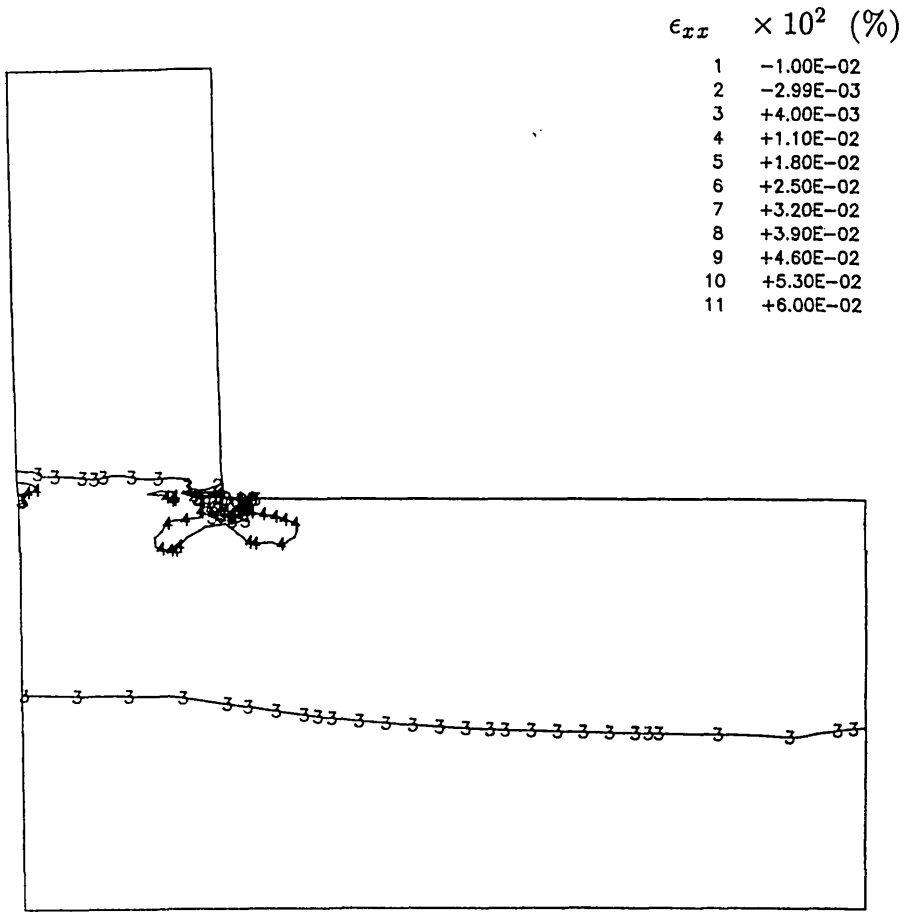


(a) Before fillet fracture.

Fig. 7.20. Contours of longitudinal direct strain ϵ_{xx} at end of lap. Stacking sequence L: $[0/\pm45/0_2/\pm45/0]_s$ at 354.2 N/mm^2 applied stress.

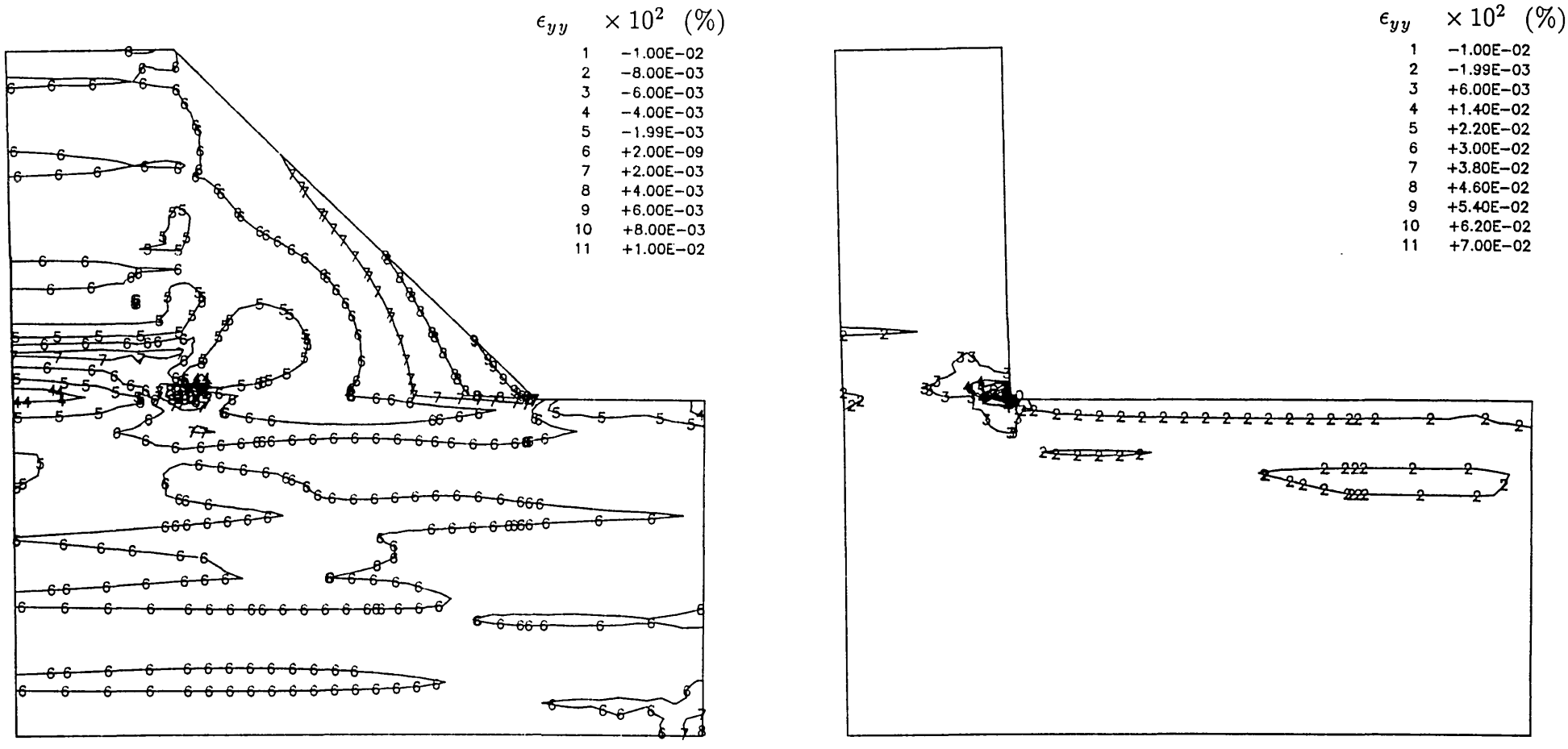


(b) After fillet fracture.



(c) After tensile fracture of 0° ply.

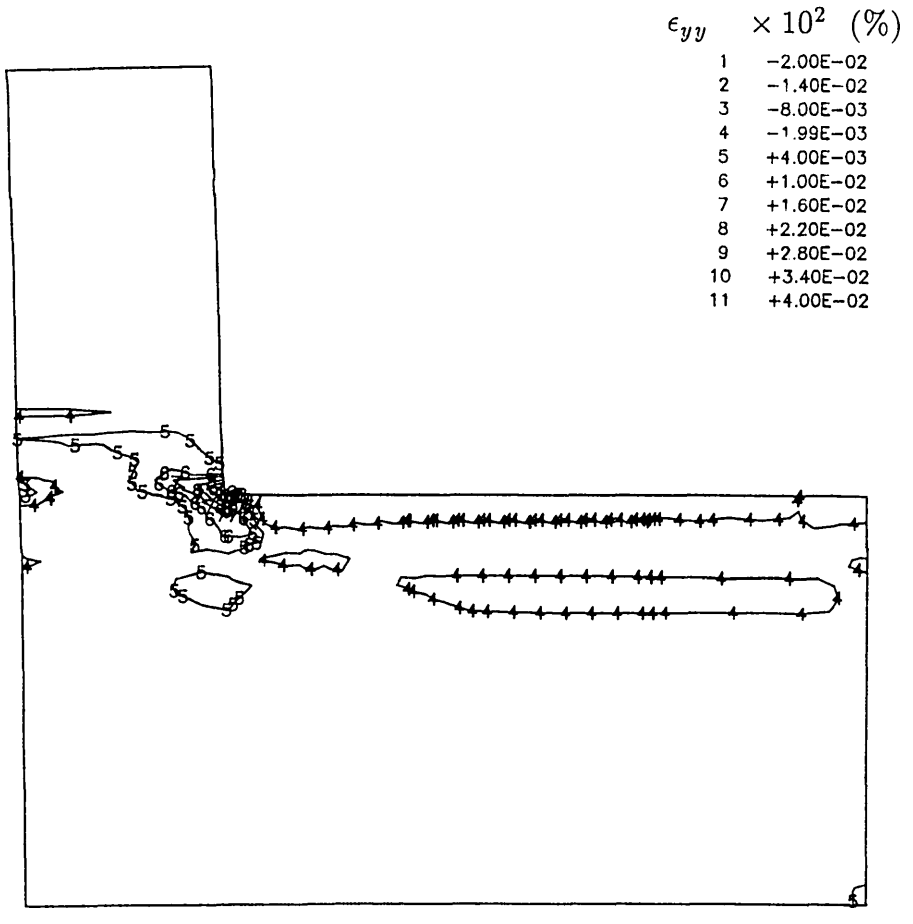
Fig. 7.20. (continued) Contours of longitudinal direct strain ϵ_{xx} at end of lap. Stacking sequence L: $[0/\pm 45/0_2/\pm 45/0]_s$ at 354.2 N/mm^2 applied stress.



(a) Before fillet fracture.

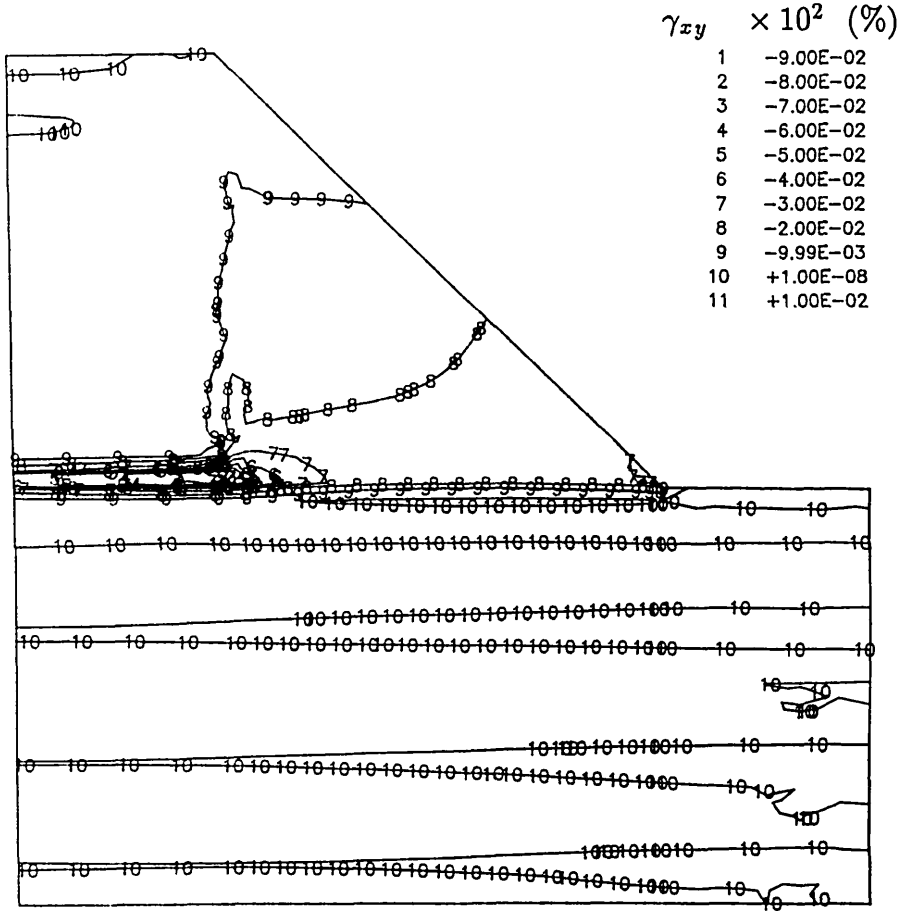
(b) After fillet fracture.

Fig. 7.21. Contours of transverse direct strain ϵ_{yy} at end of lap. Stacking sequence L: $[0/\pm 45/0_2/\pm 45/0]_s$ at 354.2 N/mm^2 applied stress.



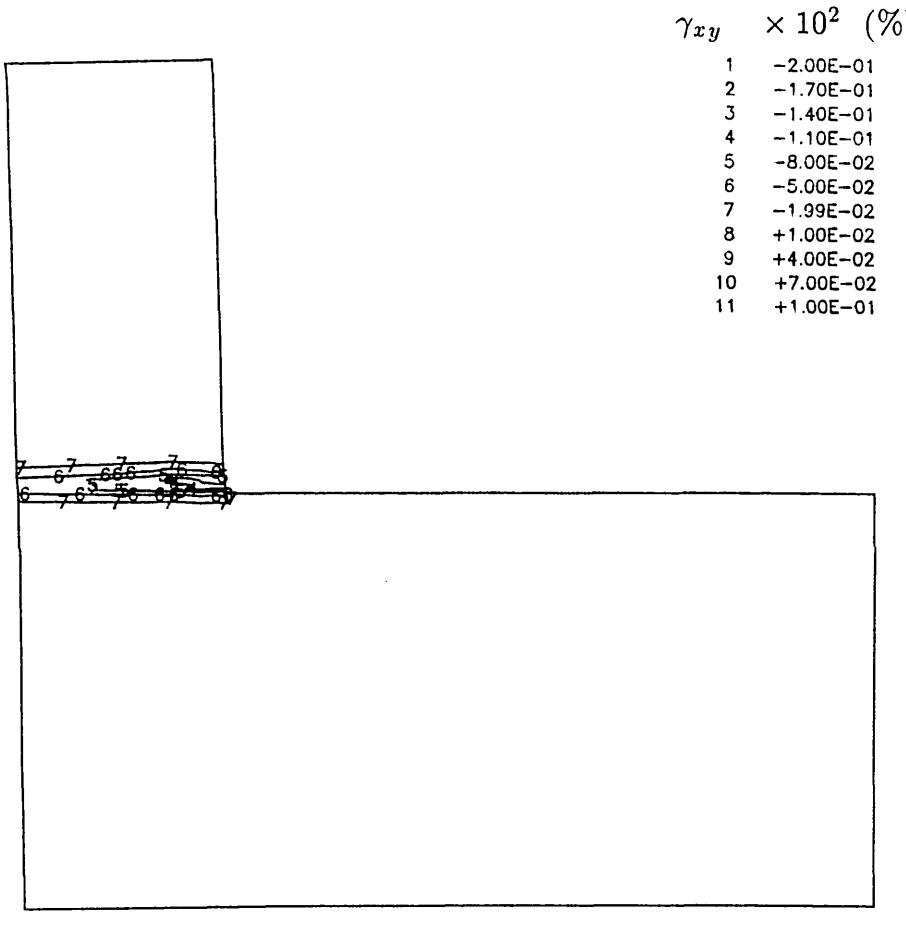
(c) After tensile fracture of 0° ply.

Fig. 7.21. (continued) Contours of transverse direct strain ϵ_{yy} at end of lap. Stacking sequence L: $[0/\pm 45/0_2/\pm 45/0]_s$ at 354.2 N/mm^2 applied stress.

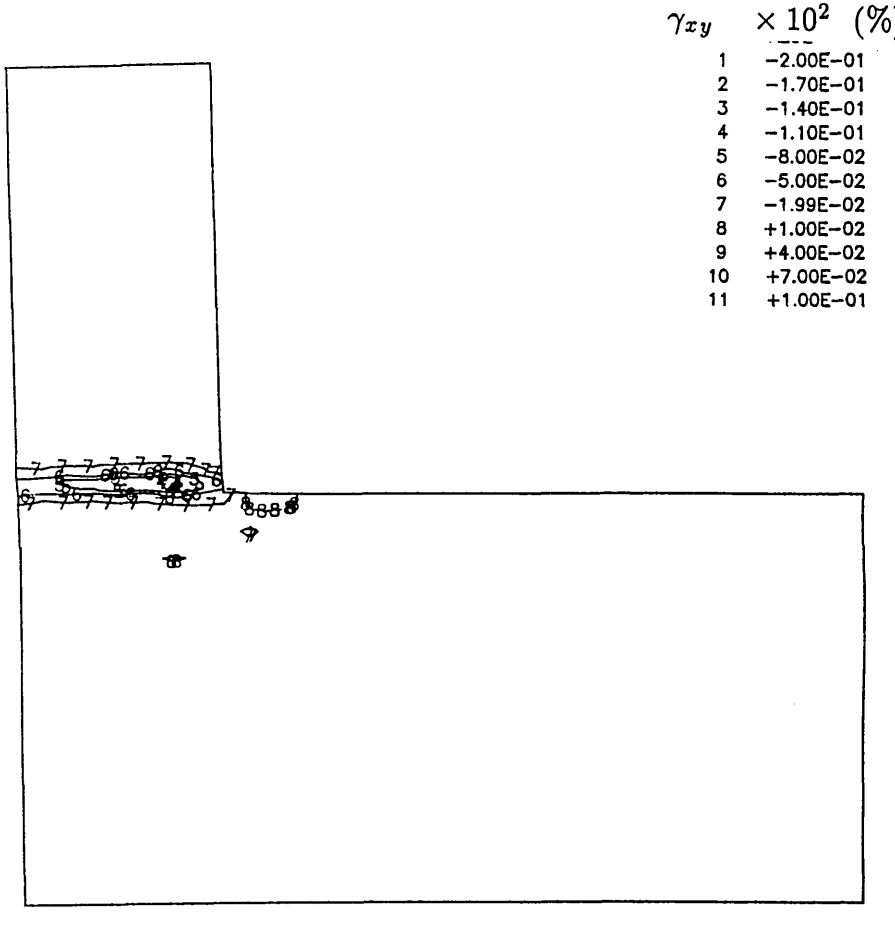


(a) Before fillet fracture.

Fig. 7.22. Contours of shear strain γ_{xy} at end of lap. Stacking sequence L: $[0/\pm 45/0_2/\pm 45/0]_s$ at 354.2 N/mm^2 applied stress.

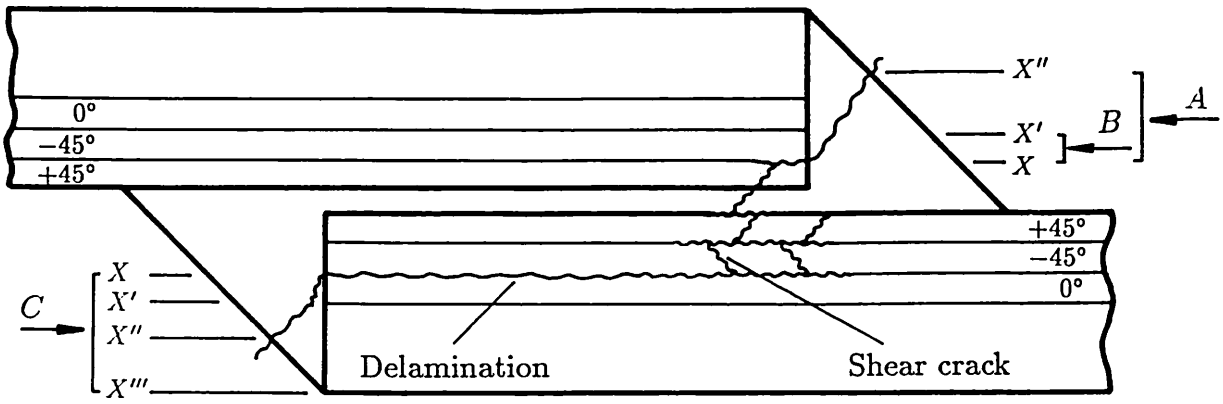


(b) After fillet fracture.

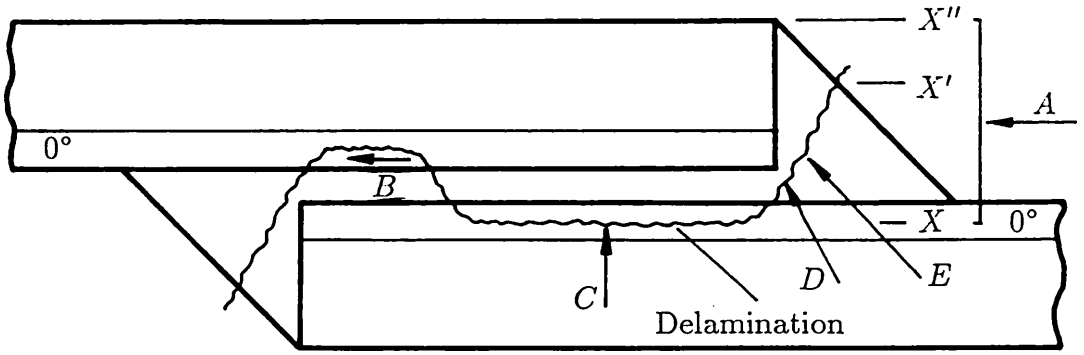


(c) After tensile fracture of 0° ply.

Fig. 7.22. (continued) Contours of shear strain γ_{xy} at end of lap. Stacking sequence L: $[0/\pm 45/0_2/\pm 45/0]_s$ at 354.2 N/mm^2 applied stress.



(a) Stacking sequence K.



(b) Stacking sequences L–N.

Fig. 7.23. Two-dimensional view of joint failure mode.

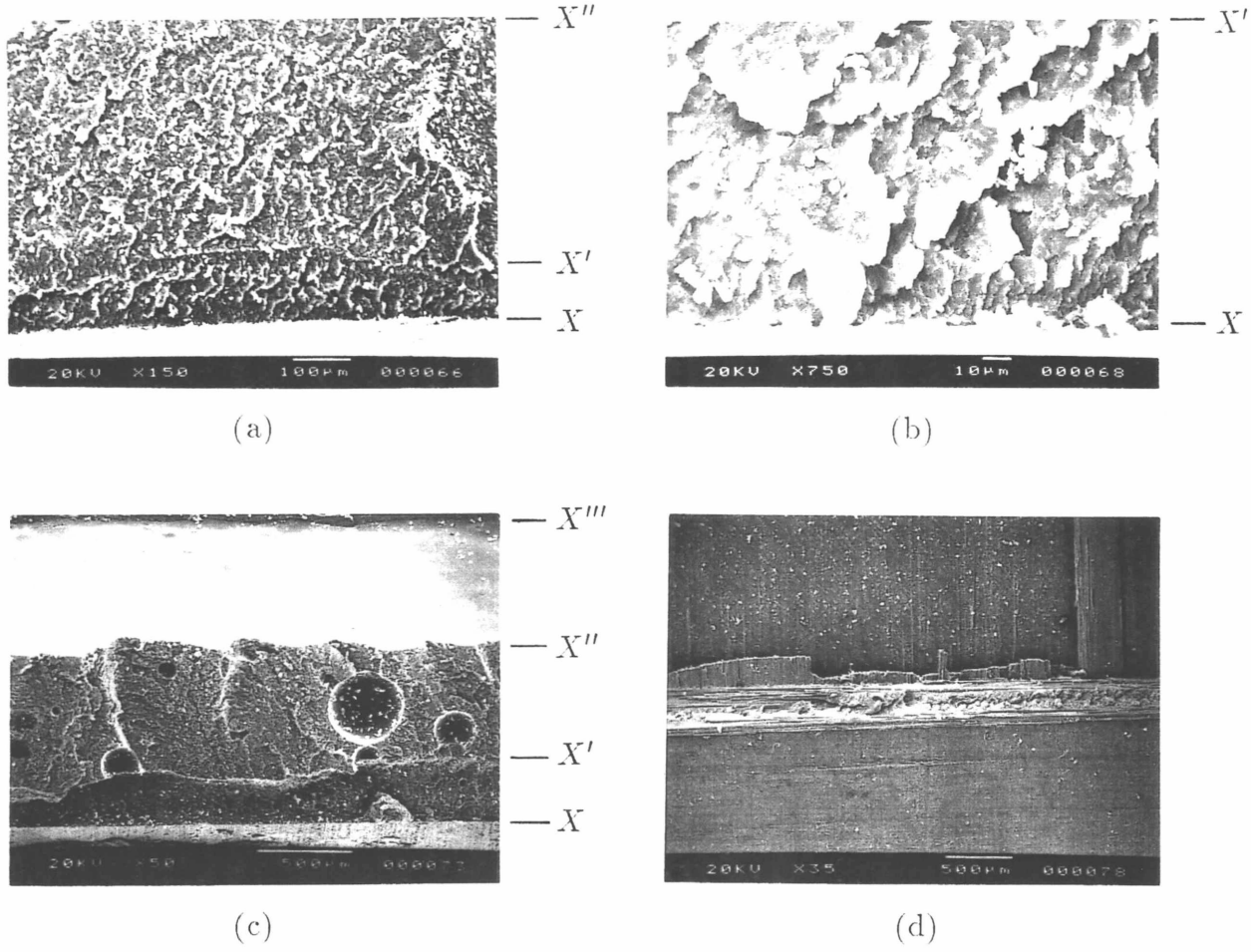


Fig. 7.24. SEM, taken from stacking sequence K: $[\pm 45/0_3/\pm 45/0]_s$, showing (refer to Fig. 7.23(a) for arrow direction):

(a) View arrow A—two fracture modes of adhesive fillet: X–X' and X'–X''.

(b) View arrow B—adhesive 'ductile' (flaky) failure.

(c) View arrow C—two fillet cracks meeting along X'.

(d) Fracture of $-45°$ fibres along $+45°$ line at ultimate failure.

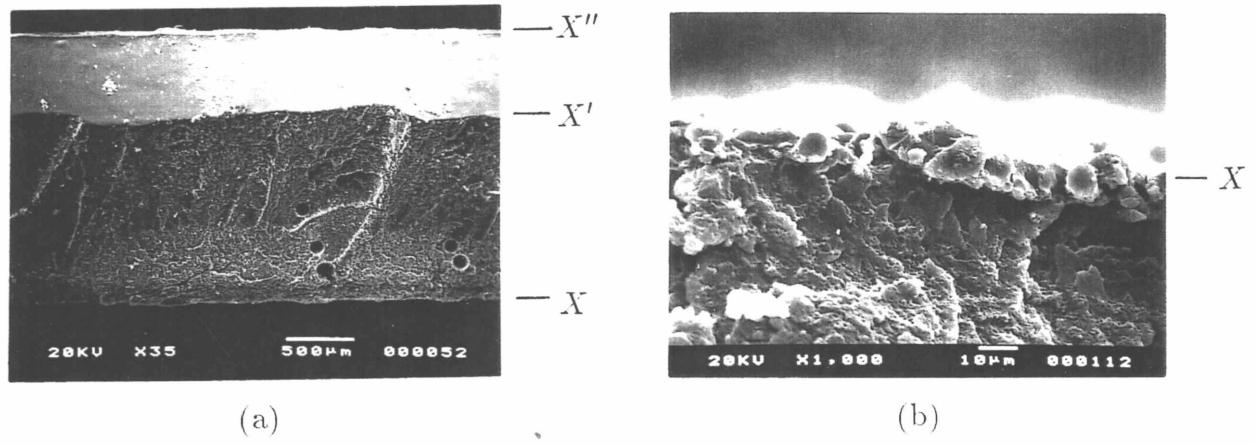
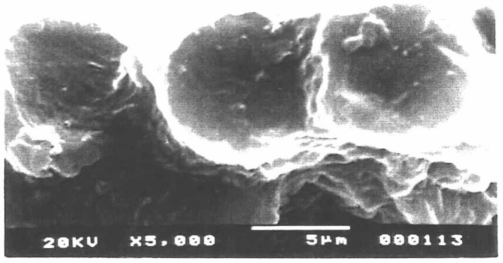


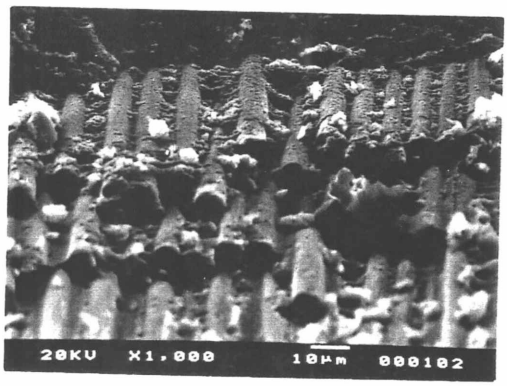
Fig. 7.25. SEM, taken from stacking sequence L: $[0/\pm 45/0_2/\pm 45/0]_s$, showing (refer to Fig. 7.23(b) for arrow direction):

(a) View arrow A—adhesive fillet brittle fracture.

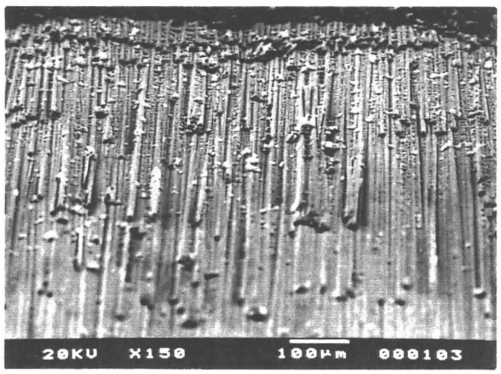
(b) View arrow A—fibre and associated adhesive (at the bond-line level) brittle fracture.

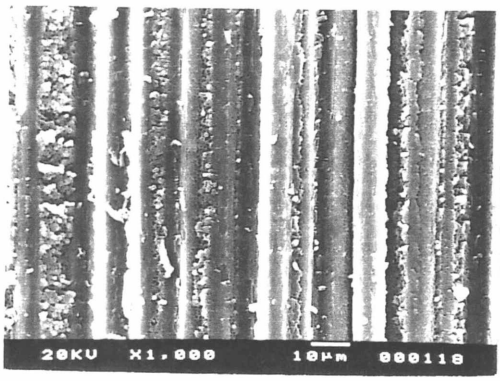


— X



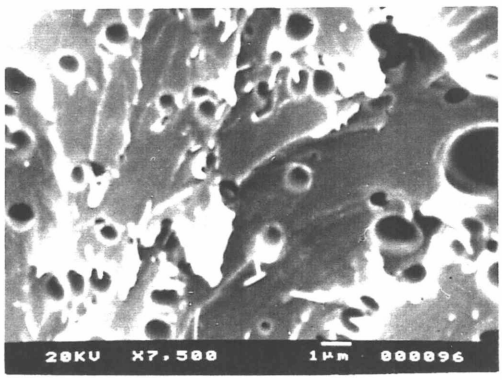
(c) (d)

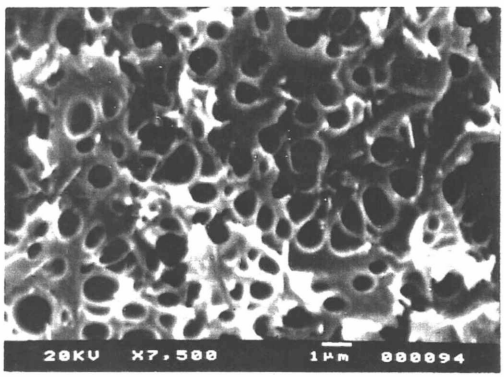




(e) (f)

Fig. 7.25. (continued) SEM, taken from stacking sequence L: $[0/\pm 45/0_2/\pm 45/0]_s$, showing (refer to Fig. 7.23(b) for arrow direction):
(c) View arrow A—fibre tensile fracture.
(d) & (e) View arrow B—the step-like fracture of surface fibres.
(f) View arrow C—intralaminar shear fracture of 0° surface ply.





(a) (b)

Fig. 7.26. SEM, taken from stacking sequence M: $[0_2/\pm 45/0/\pm 45/0]_s$, showing (refer to Fig. 7.23(b) for arrow direction):
(a) View arrow D—adhesive brittle fracture at the bondline level.
(b) View arrow E—high concentration of toughening phase particles.

Chapter 8

JOINTS WITH CROSS-PLY ADHERENDS

8.1 INTRODUCTION

In this chapter the performance is presented of joints with cross-ply adherends with the following lay-ups:

1. $[0/90]_{3s}$ and $[90/0]_{3s}$ at $l/t = 16.7$.
2. $[0/90]_{2s}$ and $[90/0]_{2s}$ at $l/t = 25.0$.
3. $[0/90]_{s}$ and $[90/0]_{s}$ at $l/t = 50.0$.

Numerical crack simulation has been undertaken to determine post initial failure strain distribution.

8.2 EXPERIMENTAL RESULTS

Test results are given in Table 8.1. Note the high scatter in the results. Joints with cross-ply adherends having 0° surface ply are stronger than those having 90° surface layer except for the four-ply laminates where the situation is reversed. The fractured joints are shown in Fig. 8.1.

8.3 CONTINUUM ANALYSIS

Adherend mechanical properties and stresses from Hart-Smith's analysis are given in Table 8.2. For adherends with 0° surface ply, joint strength is increased with the increase in both k_b and l/t. For adherends with 90° surface layer, joint strength is increased with the decrease in k_b and increase in l/t. The values of the membrane

and bending Poisson's ratios for 0°/90° lay-ups are relatively smaller than those for 0°/±45° lay-ups. With cross-ply adherends, there is no coupling between bending and twisting deformations, i.e. $m = 0$.

As the l/t ratio is increased, both the adherend bending and adhesive peel stresses are reduced.

8.4 FINITE ELEMENT ANALYSIS

The finite element model used is the same as that described in Chapter 6 (Fig. 6.3) but with $[90/0]_{2s}$ lay-up. With this type of lay-up, failure usually initiates in the 90° ply next to the fillet tip. Numerical crack simulation at the fillet tip has been undertaken to determine post initial failure strain distribution. The crack in the 90° layer has been modelled by the use of reduced stiffness elements as shown in Fig. 8.2. The results of nonlinear analysis are presented in Figs. 8.3–8.10 (the reference axes system (x, y) is shown in Fig. 8.2).

8.5 DISCUSSION

The mechanisms of failure of joints with cross-ply $[90/0]_{2s}$ adherends are presented. The discussion applies also to joints with $[90/0]_{3s}$ and $[90/0]_{s}$ adherends.

For cross-ply adherends having 0° surface layer, the failure mechanisms are the same as those described in the previous Chapter for adherends with 0° surface ply. The modes of failure, with cross-ply adherends having 0° or 90° surface layer, are not affected by changes in the l/t ratio.

8.5.1 Lay-up $[90/0]_{2s}$

Fig. 8.3(a) shows contours of von Mises stress in the adhesive fillet. It is interesting to note that, in this case, the maximum concentration of stress is at the fillet tip and not at the fillet root as shown in the previous Chapter. The maximum von Mises stress at the fillet tip (60 N/mm^2) does not exceed the ultimate tensile strength of the adhesive (68 N/mm^2). However, it does indicate that the fillet tip region is the potential site for the initiation of failure. This is consistent with experimental observations as the initial crack in the joint does not start at the fillet but in the 90° ply next to the fillet tip.

Failure is initiated by a transverse crack in the 90° ply next to the fillet tip as shown in Fig. 8.11. The initiation and progression of failure at the fillet tip is demonstrated in Fig. 8.12. Fig. 8.13 shows a three-dimensional view of the fractured surfaces.

It can be seen from Fig. 8.4(a) that the longitudinal direct strain in the 90° ply next to the fillet tip (approaching 0.88%) exceeds the corresponding ultimate value (0.77%) indicating ply failure in this site. The longitudinal direct strain concentration in the root of the fillet (1.1%) is below the adhesive ultimate tensile strain (3.5%). Both the peel and shear strains at the end of the lap region, in the composite and adhesive, are below their respective ultimate values—see Figs. 8.5(a) and 8.6(a). The composite ultimate in-plane shear strain is 1.61%; the adhesive ultimate shear strain is 4.28%.

Fig. 8.7 shows the variation of the longitudinal and transverse direct and shear stresses along the centreline of the 90° ply next to the bondline at the fillet tip region. Clearly, all stresses peak under the fillet tip, with the exception of the shear stress having its highest peak under the fillet root. Both the transverse and shear stresses are well below their respective ultimate values ($72\,N/mm^2$ and $108\,N/mm^2$ respectively). Figs. 8.8 and 8.9 show the variation of the longitudinal and transverse direct and shear stresses along the centreline of the 0° ply adjoining the surface 90° layer and along the centreline of the adhesive layer respectively. In both cases, all stresses are below their respective ultimate values. Fig. 8.10 shows the adherend longitudinal direct stress distribution at the fillet tip. Again it is clear that the outermost 90° ply has failed at about half the load bearing capacity of the neighbouring 0° layer.

The modes of transverse fracture in the 90° ply are shown in Fig. 8.14(a) and (b). This fracture is associated with some transverse microcracking in the 90° ply as seen in Fig. 8.14(c). Transverse microcracking in the 90° ply is extended to the resin rich interface between the 90° and 0° plies—see Fig. 8.12(a).

After the cracking of the 90° layer, the stress concentration at the fillet tip is relieved as shown in Fig. 8.3(b). Contours of longitudinal and transverse direct and shear strains at the end of the lap after the 90° ply fracture are shown in Figs. 8.4(b), 8.5(b) and 8.6(b) respectively. The longitudinal direct strain in the

0° ply next to the outermost 90° layer has increased from 0.55% (Fig. 8.4(a)) to 0.6% (Fig. 8.4(b)). The transverse direct strain at the crack tip has changed from compressive (−0.05%, Fig. 8.5(a)) to tensile (0.33%, Fig. 8.5(b)). The shear strain at the crack tip has increased from 0.2% (Fig. 8.6(a)) to 0.6% (Fig. 8.6(b)). The peel and shear strain concentrations at the crack tip are somewhat underestimated.

Cracking of the 90° ply causes shear strain concentration at the crack tip. This shear strain concentration coupled with peeling strain causes the development of cracks in the resin rich interface as seen in Fig. 8.12(b) and (c). A shear failure propagates from the crack tip with the formation of resin shear cusps as shown in Figs. 8.12(d) and 8.14(c) and (d).

It is argued, for the failure configuration presented in Fig. 8.11, that the 90° ply at the left hand fillet tip cracked first, followed by similar cracking at the right hand fillet tip. This is because the shear crack initiated at the left hand side has propagated further than that initiated at the right hand side. Further evidence of transverse microcracking in the 90° ply and shear cracking at the 90°/0° interface are shown in Fig. 8.14(e) and (f) and Fig. 8.14(g) and (h) respectively. Ultimate failure occurs when the left hand crack reaches the right hand fillet. Fillet crack starts at X and propagates towards X'' as seen in Fig. 8.14(i) and (j). Fillet fracture is associated with a 'brittle' failure at the centre of the lap—where the right hand shear crack has reached. Fig. 8.14(k) and (l) show the 90° ply and adhesive layer ultimate failures at the centre of the lap respectively.

8.6 CONCLUSIONS

1. For cross-ply adherends with 90° surface layer:
   a) Failure is initiated by a transverse crack in the 90° ply next to the fillet tip. This is followed by shear cracking along the 90°/0° interface.
   b) The failure initiation site has been predicted by numerical analysis.
   c) Joint strength is increased with the decrease in k_b and increase in l/t.
2. For cross-ply adherends having 0° surface ply:

a) There is no change in the mechanisms of failure to those described in the previous Chapter for adherends with 0° surface layer.

b) Joint strength is increased with the increase in both k_b and l/t.

Table 8.1. Test results.

	Stress at failure (N/mm^2)			
Lay-up	Min.	Max.	Mean	C_v (%)
$[0/90]_{3s}$	450.9	577.2	506.1	10.5
$[90/0]_{3s}$	159.3	241.4	187.7	19.9
$[0/90]_{2s}$	457.3	586.8	529.5	10.4
$[90/0]_{2s}$	220.4	245.9	237.8	5.0
$[0/90]_s$	482.5	610.7	529.1	11.1
$[90/0]_s$	572.1	729.9	628.8	11.2

C_v—Coefficient of variation

Table 8.2. Adherend mechanical properties and stresses from Hart-Smith's analysis.

Lay-up	E_m	E_b	ν_m	ν_b	D	k_b	l/t	P	σ_{av}	σ_b	σ_{max}	σ_p
$[0/90]_{3s}$	74.1	90.2	0.041	0.052	25.4	1.219	16.7	781.6	521.1	417.9	939.0	120.5
$[90/0]_{3s}$	74.1	57.9	0.041	0.033	16.3	0.781	16.7	290.8	193.9	198.0	391.9	71.3
$[0/90]_{2s}$	74.1	98.3	0.041	0.061	8.2	1.330	25.0	538.0	538.0	300.9	838.9	67.8
$[90/0]_{2s}$	74.1	49.8	0.041	0.031	4.2	0.672	25.0	246.8	246.8	145.6	392.4	46.2
$[0/90]_s$	74.1	122.4	0.041	0.118	1.3	1.673	50.0	275.2	550.4	161.0	711.4	22.9
$[90/0]_s$	74.1	25.6	0.041	0.025	0.03	0.345	50.0	325.6	651.2	50.3	701.5	15.7

E_m— effective membrane elastic modulus of adherends in direction of applied load ($\times 10^3$ N/mm^2).
E_b— effective bending elastic modulus of adherends corresponding to a bending moment about an in-plane axis normal to the direction of applied load ($\times 10^3$ N/mm^2).
ν_m— effective membrane Poisson's ratio of adherends associated with E_m.
ν_b— effective bending Poisson's ratio of adherends associated with E_b.
D— flexural rigidity of adherends ($\times 10^3$ Nmm).
k_b— bending stiffness parameter.
l/t— ratio of overlap length to adherend thickness.
P— experimental mean load at failure per unit joint width (N/mm).
σ_{av}— adherend average stress.
σ_b— adherend bending stress.
σ_{max}— adherend maximum stress.
σ_p— adhesive peel stress.

All stresses are given in N/mm^2.

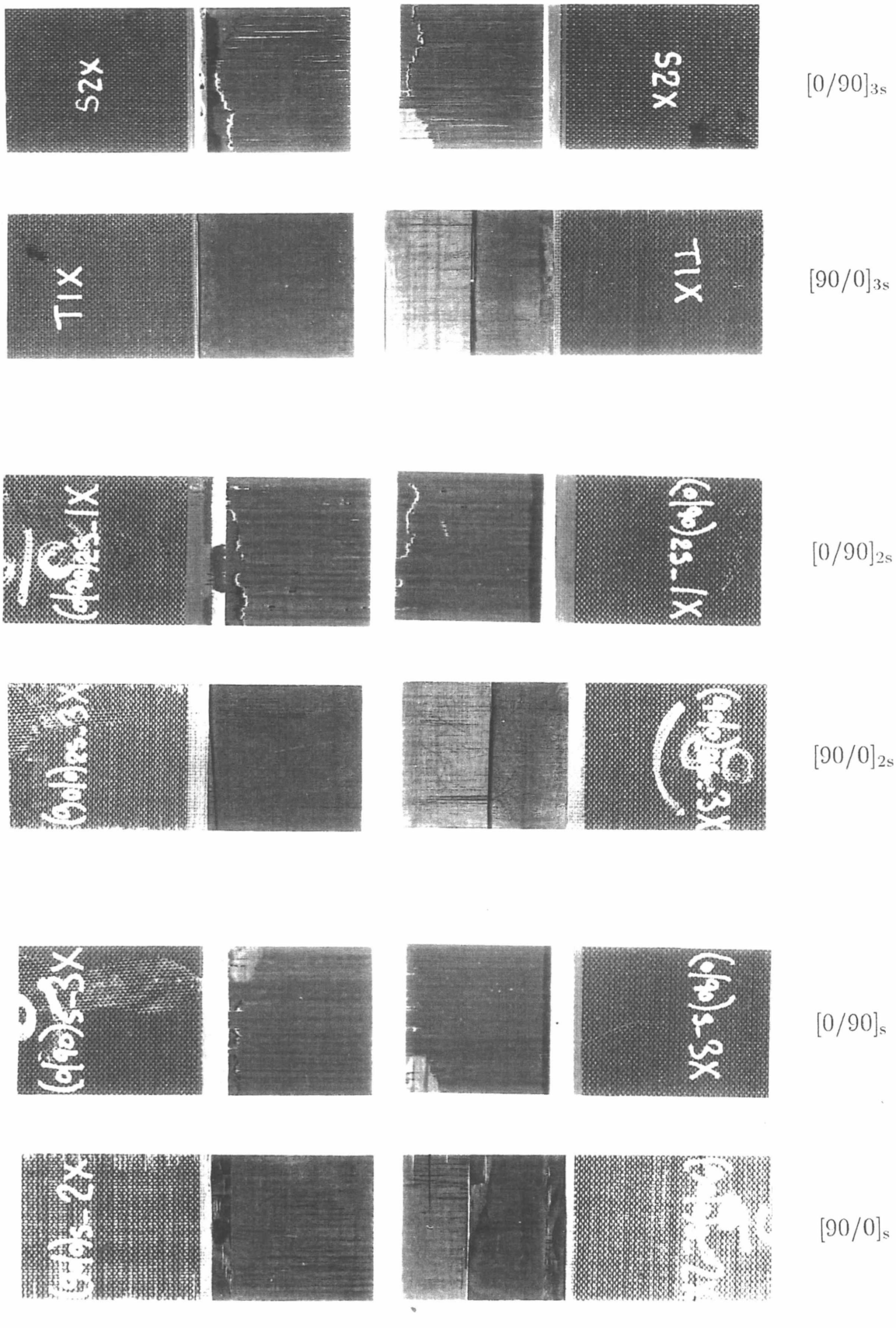


Fig. 8.1. The bonded specimens with cross-ply adherends after fracture (↔: direction of 0° fibres).

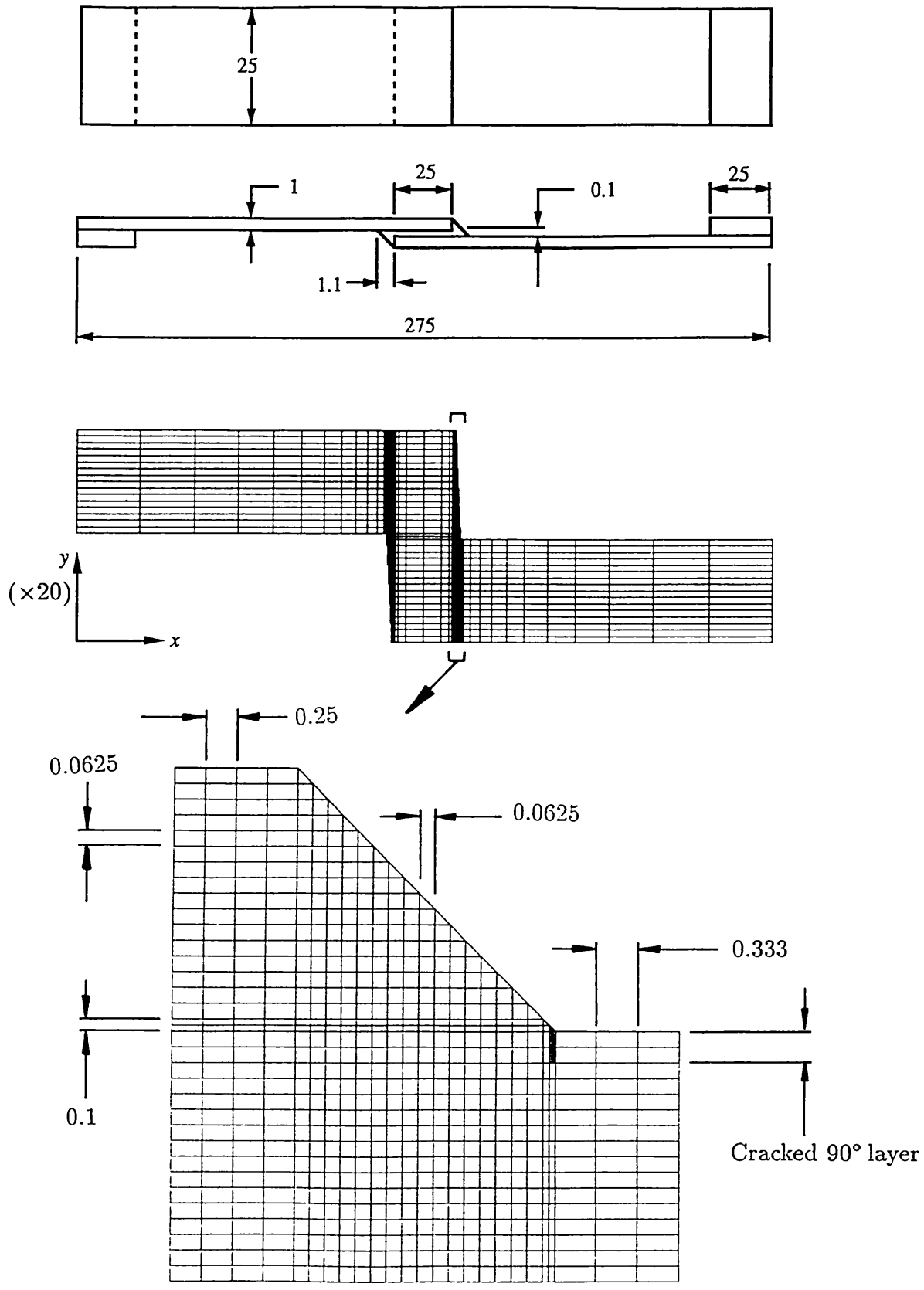
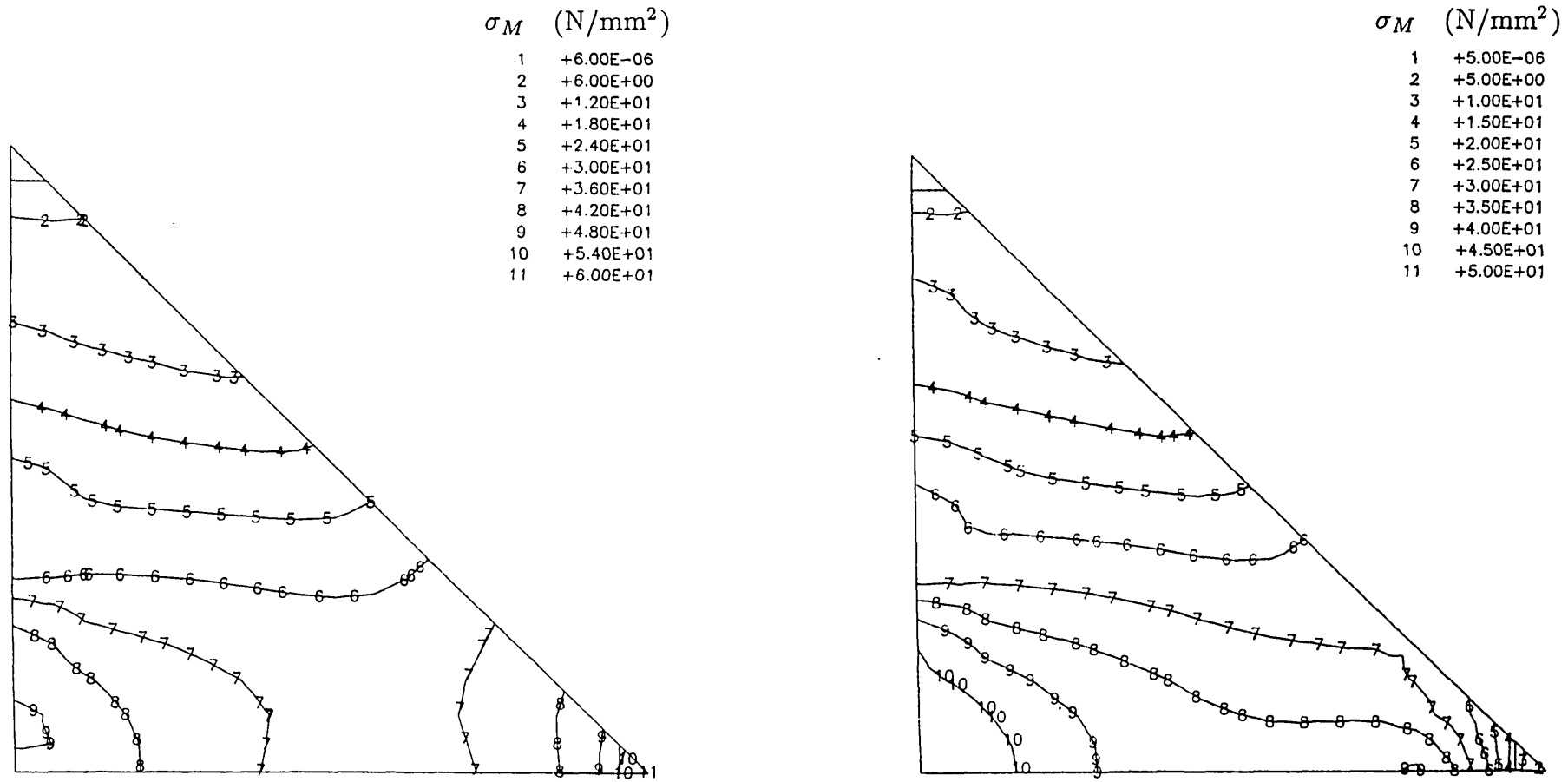


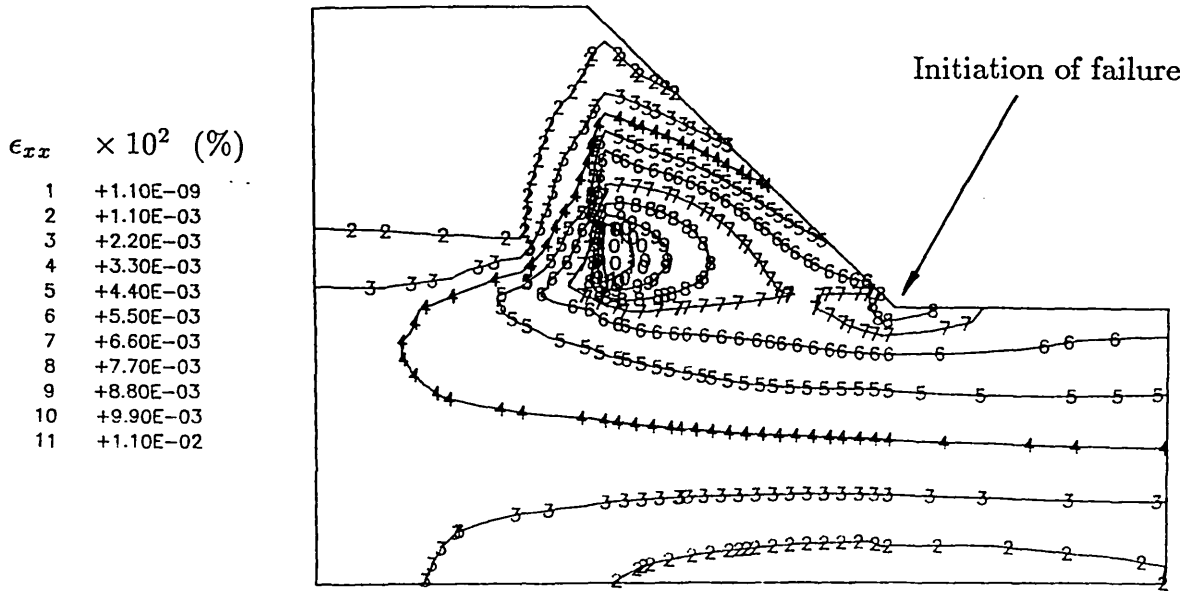
Fig. 8.2. Joint geometry and finite element model for the $[90/0]_{2s}$ lay-up. Dimensions are given in millimetres (not to scale). The cracked elements are shaded.



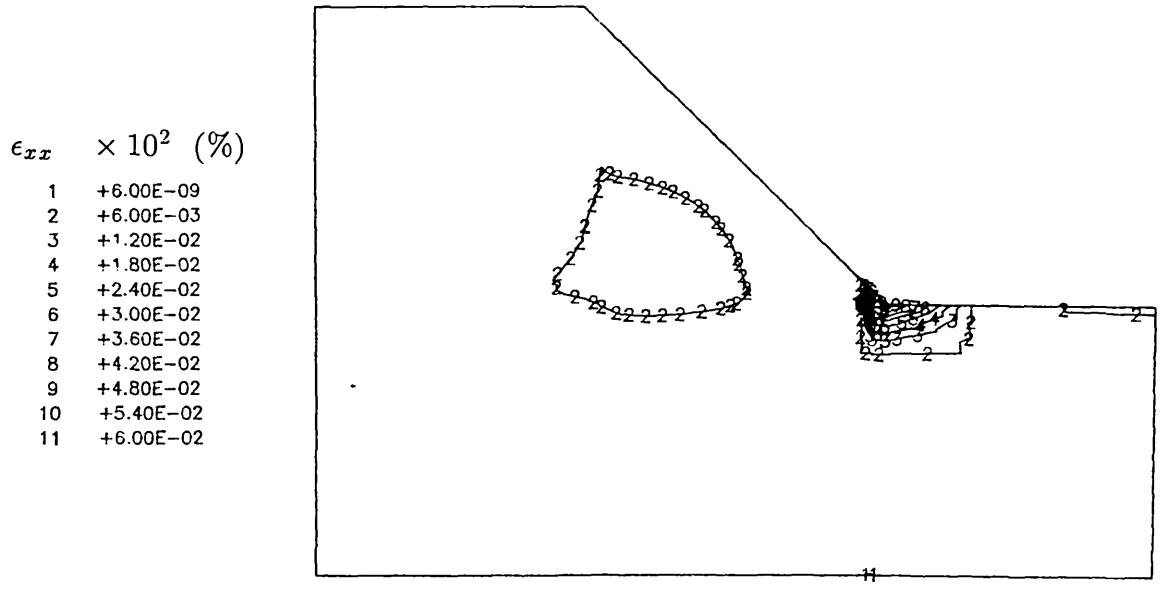
(a) Before 90° ply crack.

(b) After 90° ply crack.

Fig. 8.3. Contours of von Mises stress σ_M in the fillet. Lay-up $[90/0]_{2s}$ at 237.8 N/mm^2 applied stress.

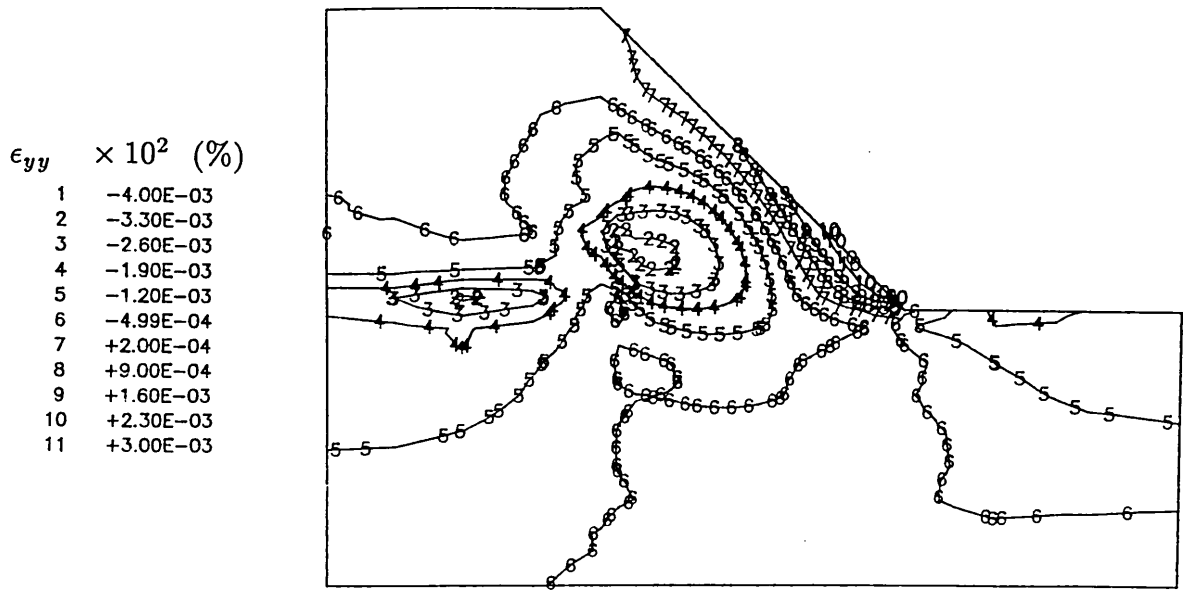


(a) Before 90° ply crack.

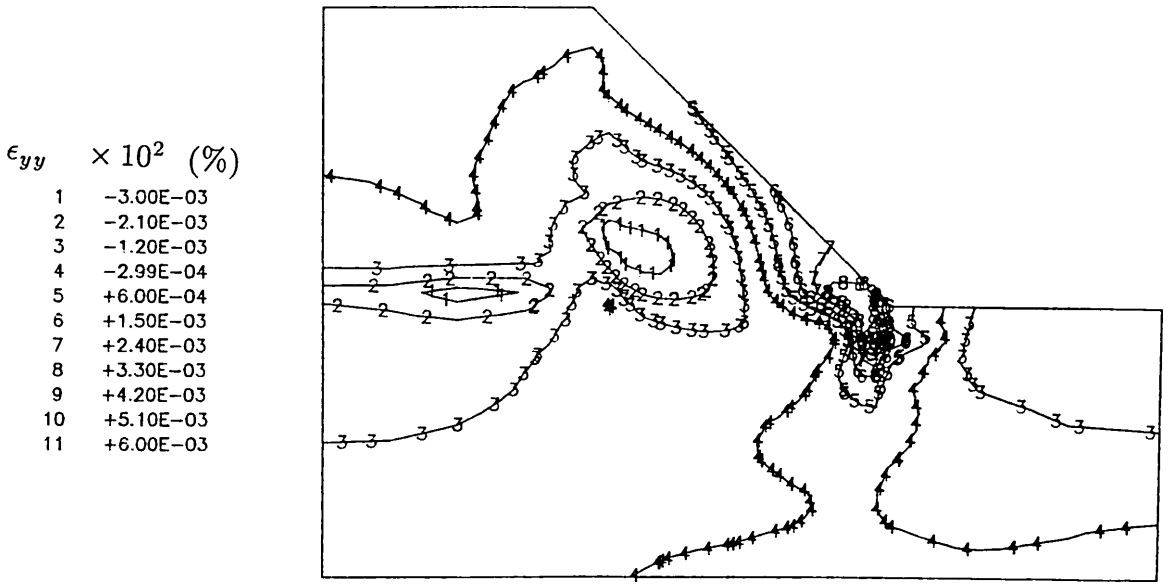


(b) After 90° ply crack.

Fig. 8.4. Contours of longitudinal direct strain ϵ_{xx} at end of lap. Lay-up $[90/0]_{2s}$ at 237.8 N/mm^2 applied stress.

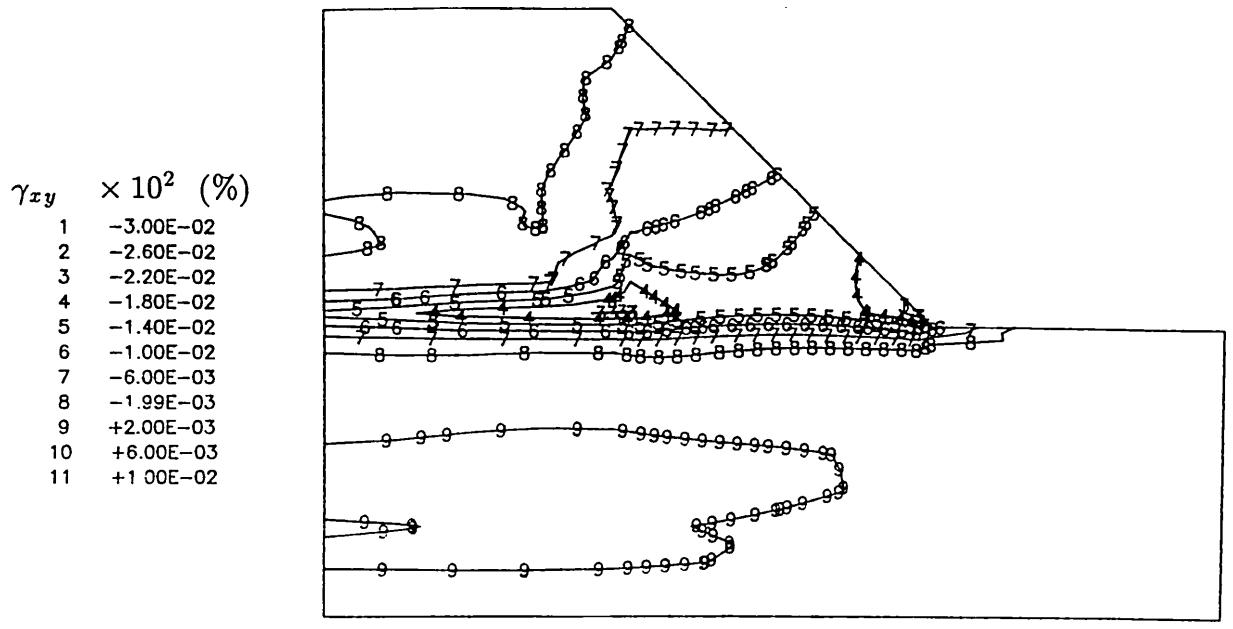


(a) Before 90° ply crack.

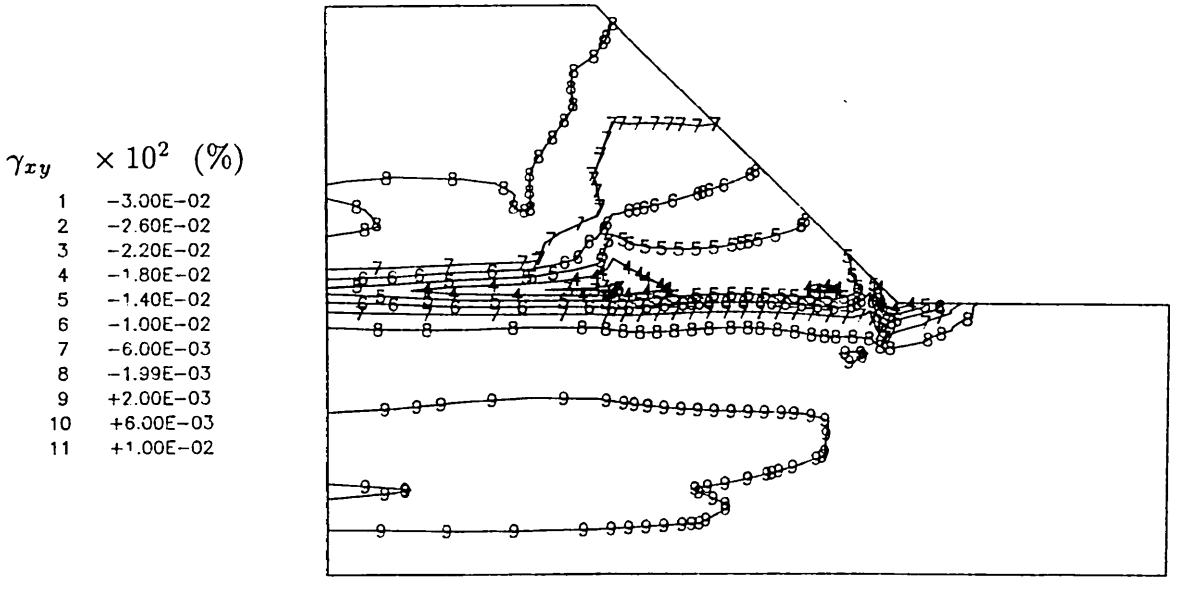


(b) After 90° ply crack.

Fig. 8.5. Contours of transverse direct strain ϵ_{yy} at end of lap. Lay-up $[90/0]_{2s}$ at 237.8 N/mm^2 applied stress.



(a) Before 90° ply crack.



(b) After 90° ply crack.

Fig. 8.6. Contours of shear strain γ_{xy} at end of lap. Lay-up $[90/0]_{2s}$ at 237.8 N/mm^2 applied stress.

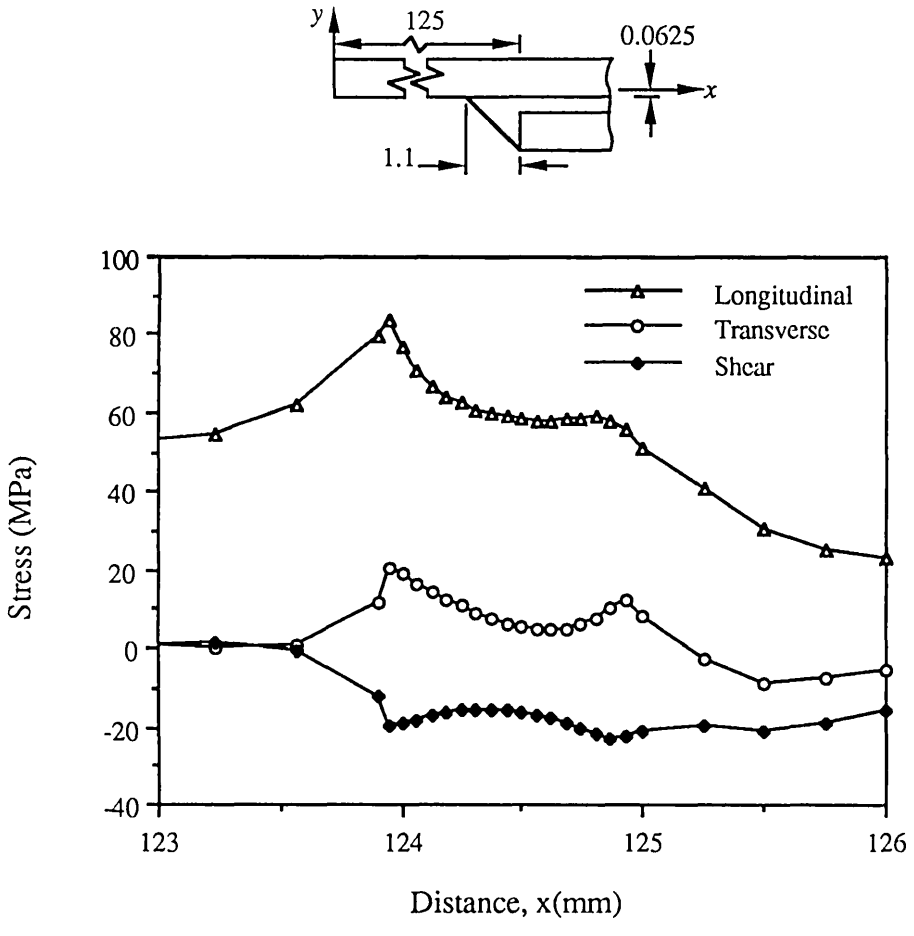


Fig. 8.7. Variation of longitudinal and transverse direct and shear stresses (σ_{xx}, σ_{yy} and τ_{xy} respectively) along the centreline of the 90° ply next to the bondline. Lay-up $[90/0]_{2s}$ at 237.8 N/mm^2 applied stress.

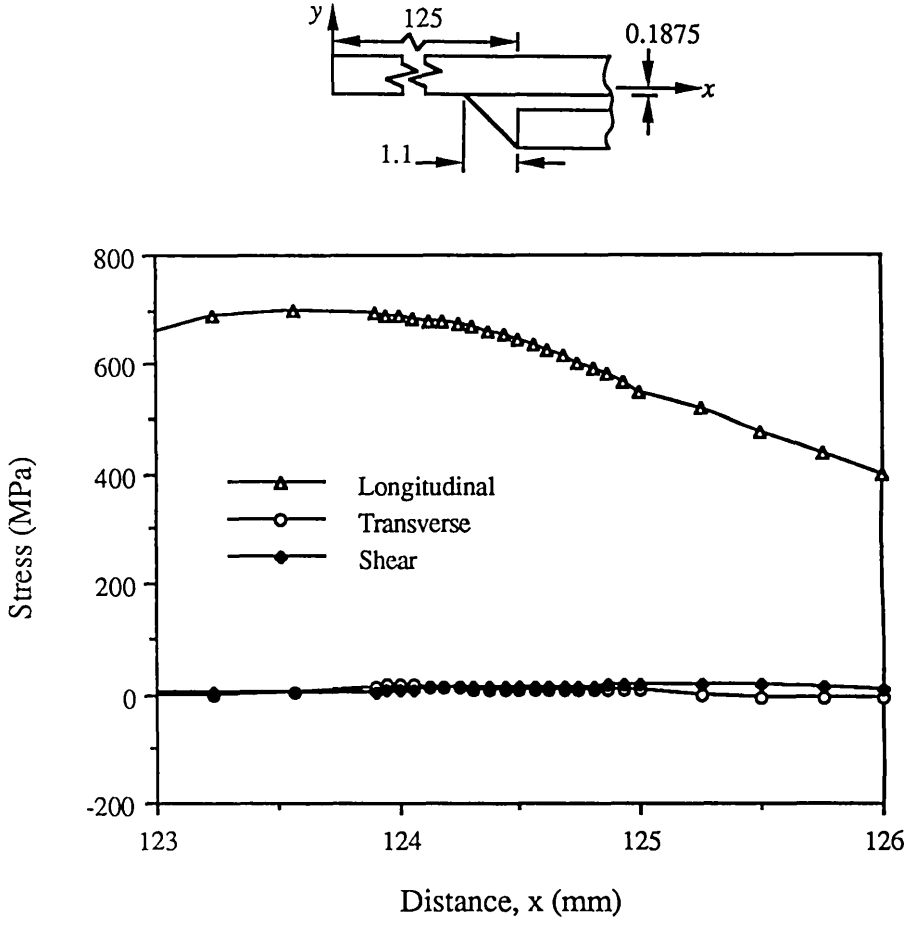


Fig. 8.8. Variation of longitudinal and transverse direct and shear stresses (σ_{xx}, σ_{yy} and τ_{xy} respectively) along the centreline of the outermost 0° ply. Lay-up $[90/0]_{2s}$ at 237.8 N/mm^2 applied stress.

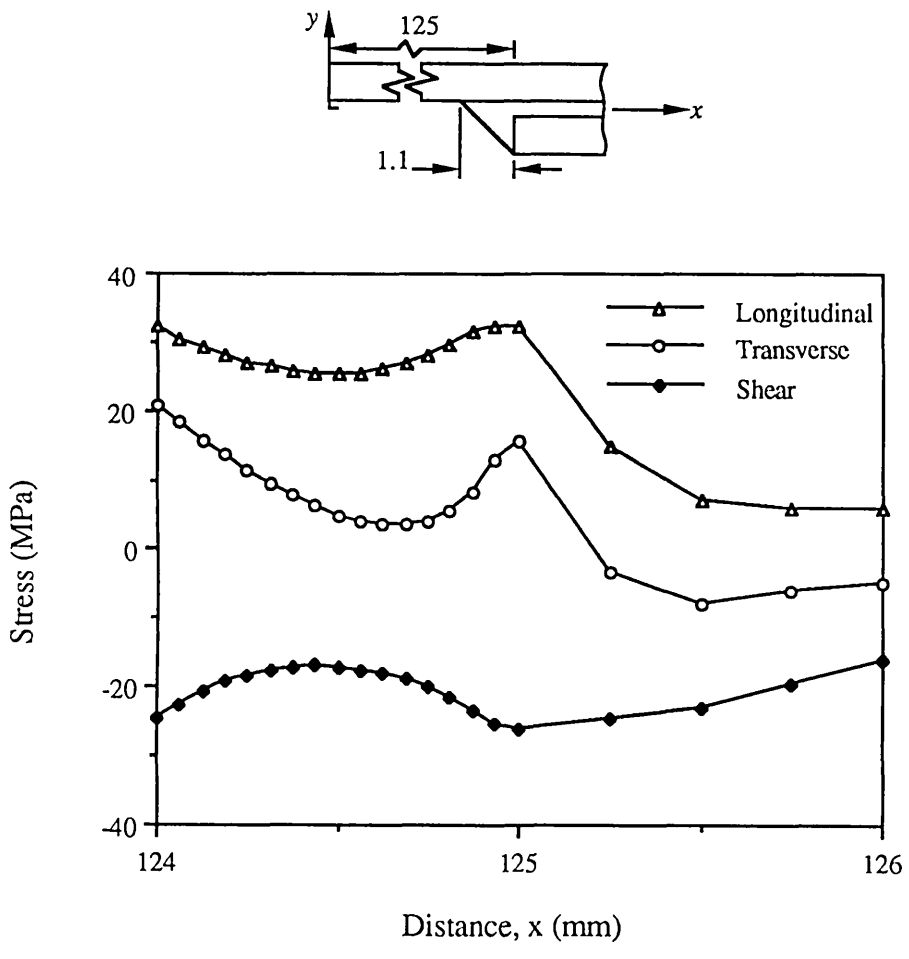


Fig. 8.9. Variation of longitudinal and transverse direct and shear stresses (σ_{xx}, σ_{yy} and τ_{xy} respectively) along the centreline of the adhesive layer. Lay-up $[90/0]_{2s}$ at 237.8 N/mm^2 applied stress.

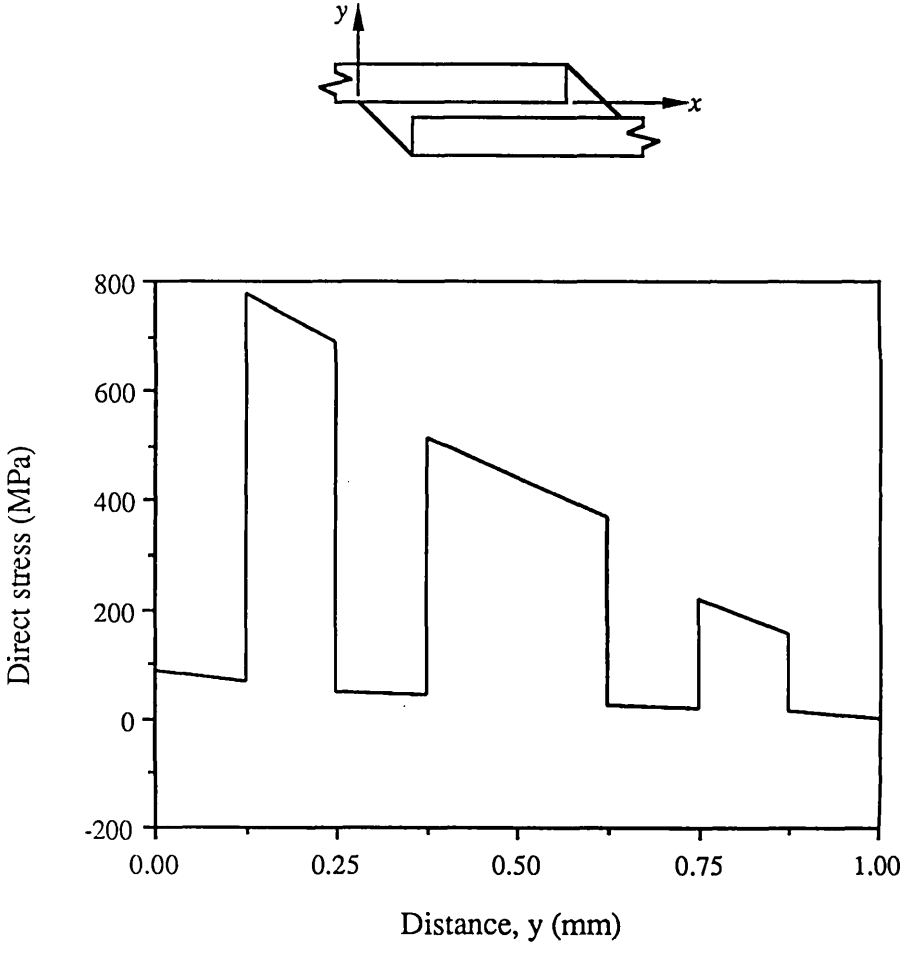


Fig. 8.10. Adherend longitudinal direct stress (σ_{xx}) distribution along the y-axis at the fillet tip. Lay-up $[90/0]_{2s}$ at 237.8 N/mm^2 applied stress.

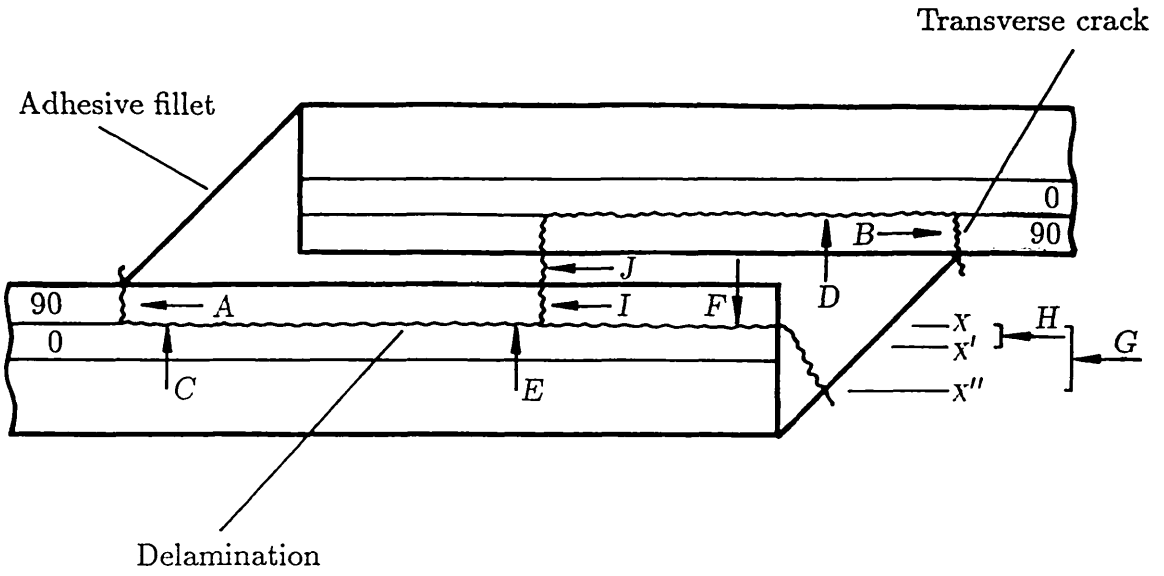


Fig. 8.11. Two-dimensional view of joint failure mode for adherends with 90° surface ply.

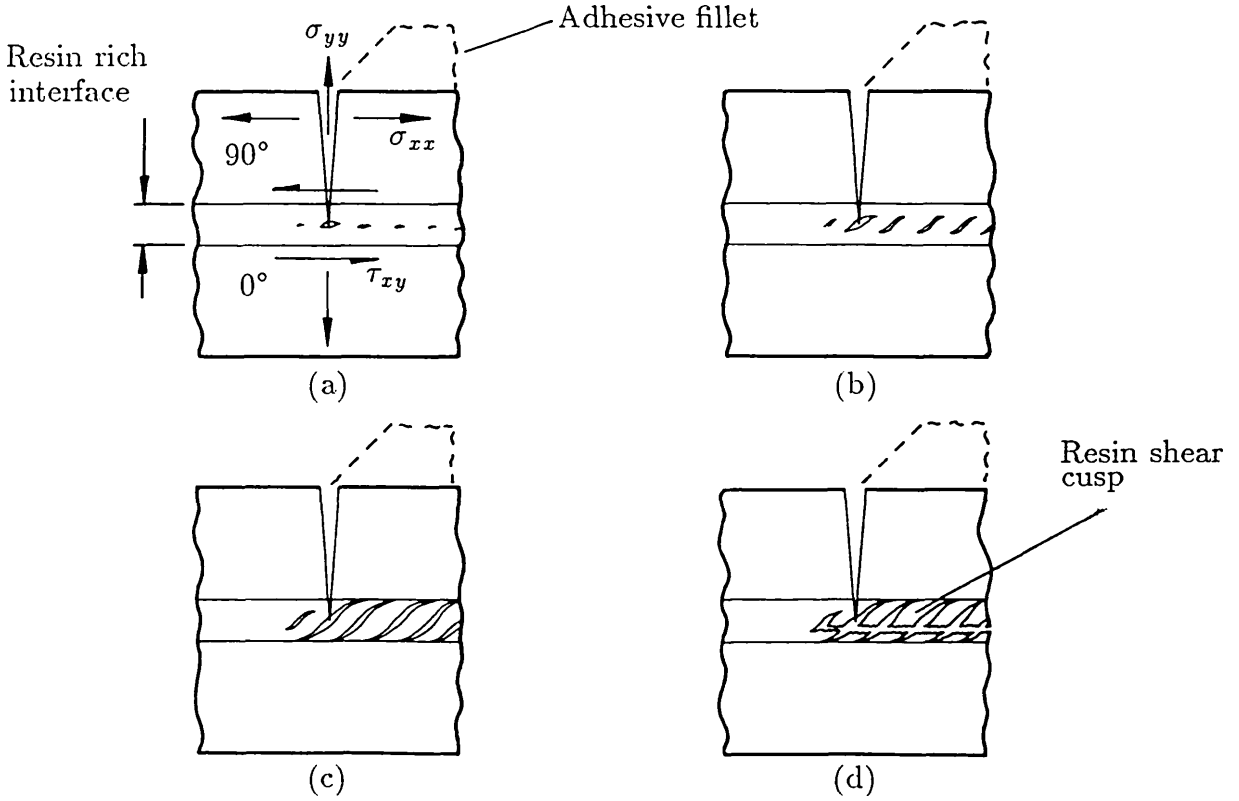


Fig. 8.12. Initiation and progression of failure at fillet tip.

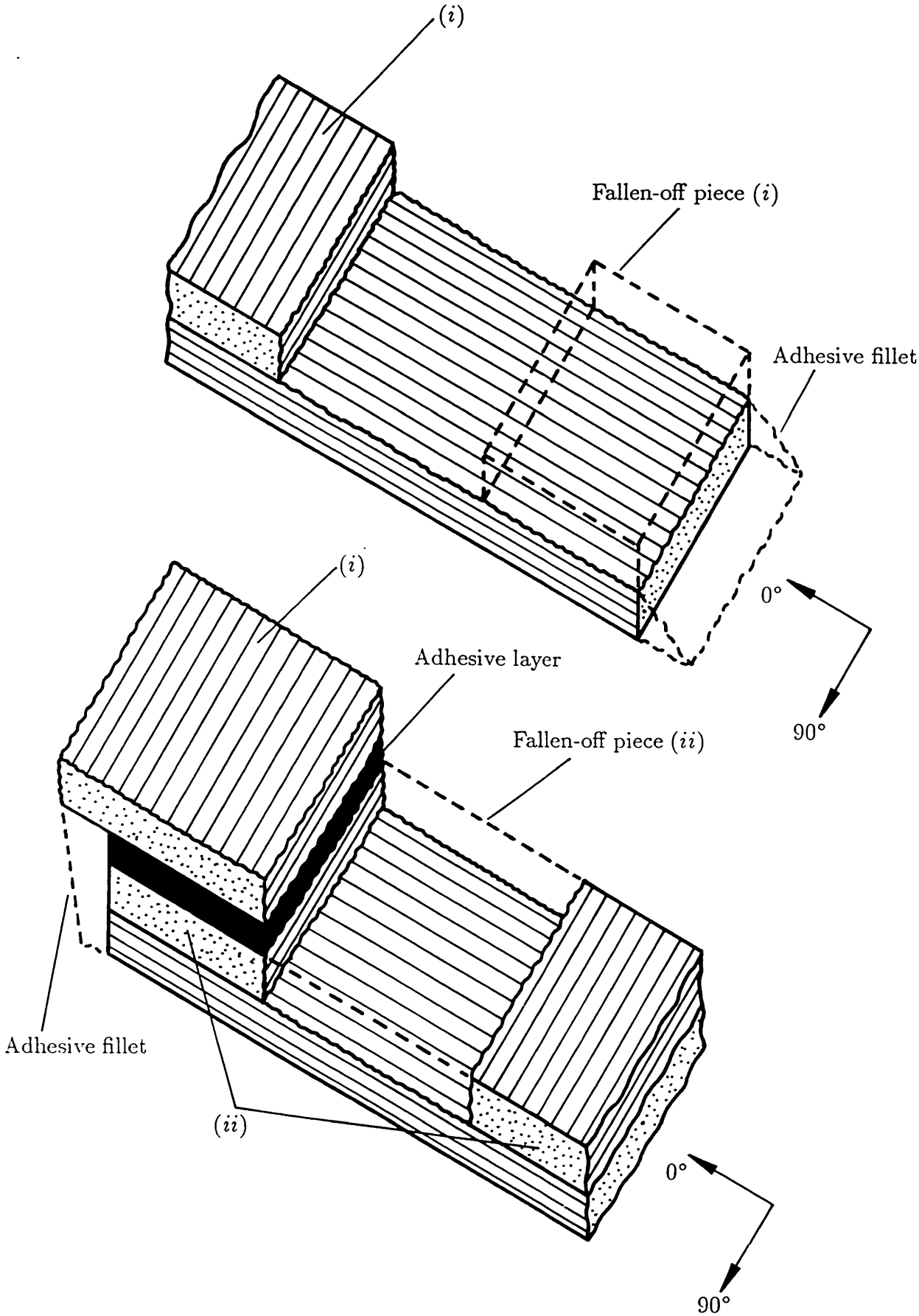
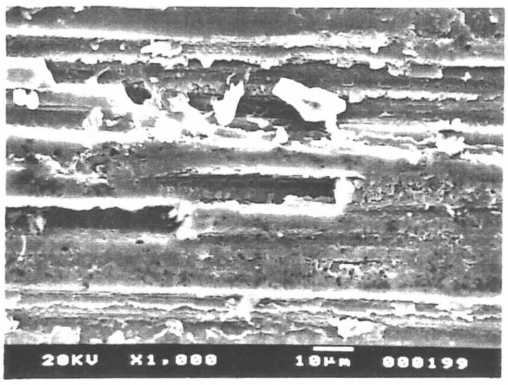
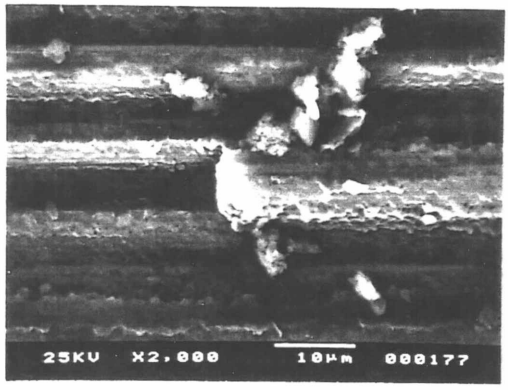


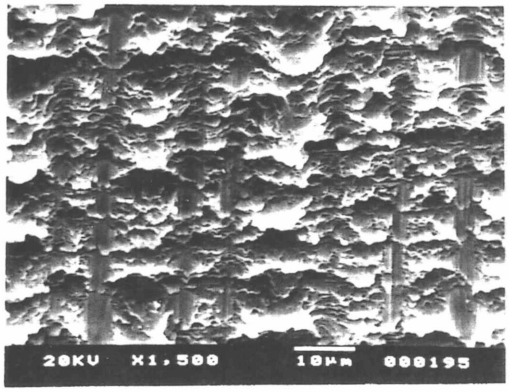
Fig. 8.13. Three-dimensional view of the fractured surfaces of cross-ply adherends with 90° surface layer. Only the first two plies are shown.



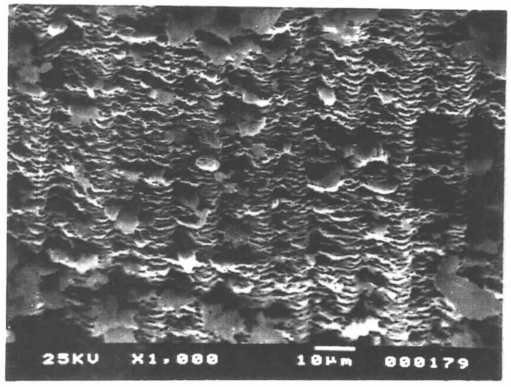
(a)



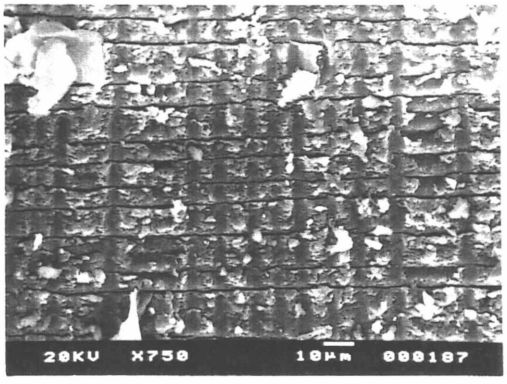
(b)



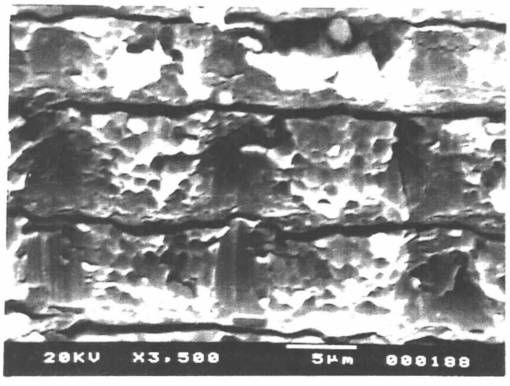
(c)



(d)



(e)



(f)

Fig. 8.14. SEM, taken from lay-up $[90/0]_{2s}$, showing (refer to Fig. 8.11 for arrow direction):

(a) View arrow *A*—matrix tensile fracture.

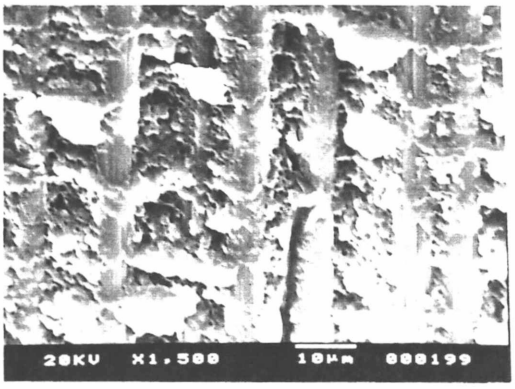
(b) View arrow *B*—fibre transverse tensile fracture.

(c) View arrow *C*—shear cusps on 90° ply surface. Note the transverse cracking in 90° ply and impressions of 0° fibres.

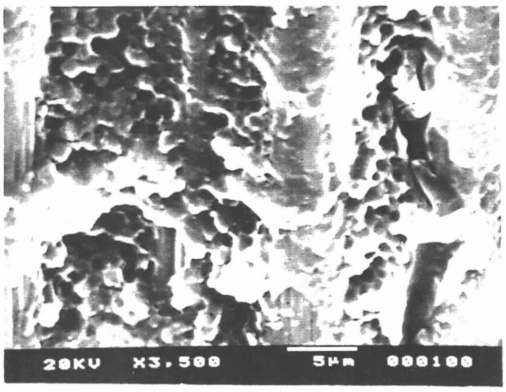
(d) View arrow *D*—shear cusps on 0° ply surface.

(e) & (f) View arrow *E*—transverse microcracks in 90° ply of about one fibre diameter spacing.

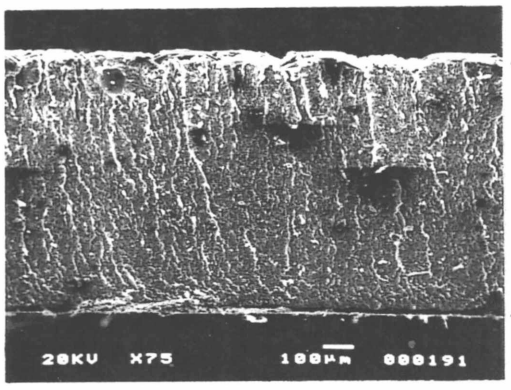
↕ : direction of 0° fibres.



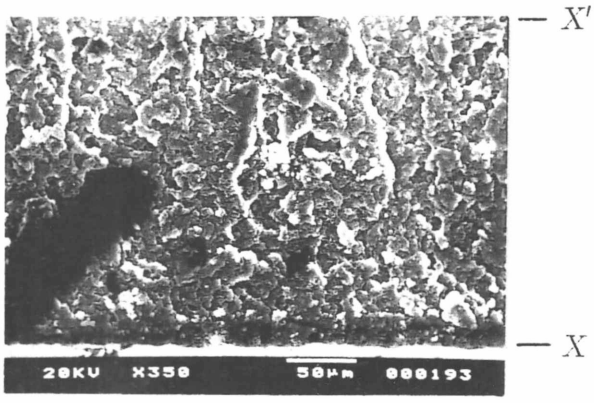
(g)



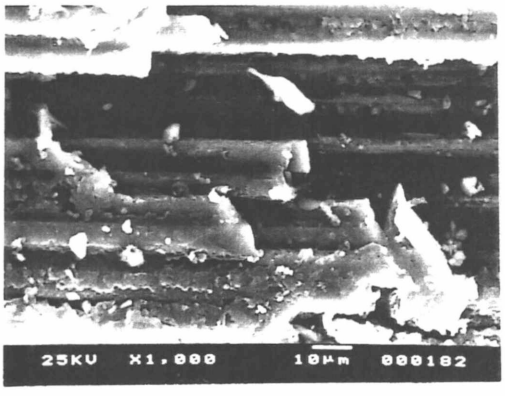
(h)



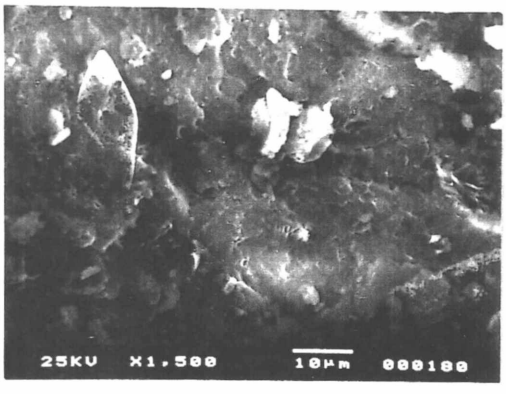
(i)



(j)



(k)



(l)

Fig. 8.14. (continued) SEM, taken from lay-up $[90/0]_{2s}$, showing (refer to Fig. 8.11 for arrow direction):

(g) & (h) View arrow *F*—shear cusps on 0° ply surface.
(i) View arrow *G*—fractured adhesive fillet.
(j) View arrow *H*—'brittle' fillet fracture.
(k) View arrow *I*—fibre transverse tensile fracture.
(l) View arrow *J*—adhesive layer 'brittle' fracture.

↕ : direction of 0° fibres.

Chapter 9

OTHER LAY-UPS

9.1 INTRODUCTION

The performance of joints with the following lay-ups is presented.

1. O: $[\pm 45/90/0/\pm 45/0]_s$ and P: $[0/90/(\pm 45)_2/0]_s$ at $l/t = 14.3$.
2. Q: $[\pm 45/90/0_2/\pm 45/0]_s$ and R: $[0_2/90/(\pm 45)_2/0]_s$ at $l/t = 12.5$.
3. $[0_4]_s$ at $l/t = 25$ and $[0_8]_s$ at $l/t = 12.5$.

9.2 EXPERIMENTAL RESULTS

The experimental results are given in Table 9.1. Some lay-ups resulted in higher experimental scatter than others. Joints with lay-up O are stronger than those with lay-up P. On the other hand, joints with lay-up R are stronger than those with lay-up Q. These results are similar to those of Chapter 7 in that having a single 0° layer on top of a 'soft' ply group does not necessarily increase joint strength. The fractured joints are shown in Fig. 9.1. Note the initiation of failure at a joint corner for adherends having 0° surface layer.

9.3 CONTINUUM ANALYSIS

Adherend mechanical properties and stresses from Hart-Smith's analysis are shown in Table 9.2. Comparing joints in laminates O and P and Q and R, it can be seen that both lay-up and overlap length are different. However, the following points may be made. Comparing lay-ups O and Q (±45° surface plies), joint strength is increased with the decrease in the k_b value. On the other hand, comparing lay-ups

P and R (0° surface ply), joint strength is increased with the increase in the k_b value.

As expected, increasing the l/t ratio for unidirectional adherends increased the joint strength.

9.4 FINITE ELEMENT ANALYSIS

The finite element model used is the same as that described in Chapter 7 (Fig. 7.7, with plane strain elements). Joints with lay-ups $[0_8]_s$ and Q have been analysed. The results of nonlinear analyses are shown in Figs. 9.2–9.13.

9.5 DISCUSSION

The mechanisms of failure of joints with lay-ups $[0_8]_s$ and Q are presented. For lay-ups $[0_4]_s$ and O, the failure modes are the same as those described for lay-ups $[0_8]_s$ and Q respectively.

The failure characteristics of joints with lay-ups P and R are the same as those described in Chapter 7 for adherends with 0° surface layer.

9.5.1 Unidirectional $[0_8]_s$ lay-up

The modes of failure of joints with unidirectional adherends are similar to those described in Chapter 7 for adherends with 0° surface layer. Fig. 9.2 shows contours of von Mises stress in the fillet. Again, the finite element analysis predicts failure at the root of the fillet while experiments show that failure starts at the fillet free surface.

Contours of longitudinal direct strain at the end of the lap are shown in Fig. 9.3. It can be seen that the maximum longitudinal direct strain in the 0° ply next to the bondline occurs near the fillet root having a value of 1.2%. This value approaches the ultimate tensile strain of the 0° ply (1.25%), indicating fibre tensile fracture as observed experimentally at this site. From Fig. 9.4, the maximum peel strain in the composite (0.6%) and adhesive (0.8%) are below their respective ultimate values (0.77% and 3.5% respectively). From Fig. 9.5, the maximum shear strain in the outermost 0° ply (5.6%) and adhesive layer (8.9%) have exceeded

their respective linear ultimate values (1.61% and 4.28% respectively), indicating shear failures. The prediction of the high shear strains is due to the linear shear stress-strain relationship used in the analysis. Thus, using a nonlinear shear stress-strain relationship for the composite and adhesive will reduce the predicted shear strains. Longitudinal and transverse direct and shear stress distributions along the centreline of the 0° ply next to the bondline are shown in Figs. 9.6 and 9.7.

Fracture of joints with unidirectional adherends is associated with longitudinal splitting due to Poisson's ratio effects and interface debonding of broken fibres due to stress concentrations created at the fibre ends—see Fig. 9.1.

9.5.2 Lay-up Q: $[\pm 45/90/0_2/\pm 45/0]_s$

Figs. 9.14–9.16 show the modes of failure. Contours of von Mises stress in the fillet are shown in Fig. 9.8. High stress concentrations occur at both the fillet root and tip ($120\,\mathrm{N/mm^2}$). Failure initiates at the left hand fillet, starting at X and proceeding towards X' as shown in Fig. 9.14. The fractured fillet is shown in Fig. 9.16(a). Fig. 9.16(b) shows the impressions of a 'brittle' type of failure. Note that there is no drawing of the rubber particle holes. Fig. 9.16(c) shows the 'ductile' fracture of that part of the adhesive fillet adjacent to the +45° ply next to the bondline. Note the adhesive ligaments associated with a 'ductile' failure and the drawing of the rubber particle holes.

Contours of longitudinal direct strain at the end of lap are shown in Fig. 9.9. The shear strain in the +45° layer next to the bondline is 1.4% at the fillet root and 1.8% at the fillet tip. The latter value exceeds the ultimate shear strain value of 1.61%, indicating shear cracking in this ply, as observed experimentally. From Fig. 9.10, the maximum peel strain in the composite and adhesive are below their respective ultimate values. From Fig. 9.11, the maximum shear strain in the adhesive layer (4.4%) has exceeded the linear ultimate shear strain of the adhesive. The same comments mentioned in Section 9.5.1 regarding the need for nonlinear material modelling apply. Longitudinal and transverse direct and shear stress distributions along the centreline of the +45° layer next to the bondline are shown in Figs. 9.12 and 9.13.

Resin shear cusps on the surface of a $-45°$ ply are shown in Fig. 9.16(d). These are due to interlaminar shear between the $\pm 45°$ plies. An intralaminar shear type of fracture is depicted in Fig. 9.16(e) and (f). The micrographs are taken from the edge of a shear cracked $-45°$ ply as shown in Fig. 9.14. Note the intralaminar shear cusps and constituent debonding.

Shear fracture of the $\pm 45°$ plies next to the bondline is associated with transverse cracking of the adjacent $90°$ layer as depicted in Fig. 9.16(g). Constituent debonding and fibre transverse tensile fracture are shown in Fig. 9.16(h). Fig. 9.16(i) shows matrix tensile fracture.

Cracking of the right hand fillet follows the fracture of the left hand fillet. Again failure of the fillet is initiated at the free surface and proceeds inwards. Fig. 9.16(j) and (k) shows the fractured right hand fillet. The crack from the left hand fillet side proceeds along the $90°/0°$ interface in a shear mode as depicted in Fig. 9.16(l). At ultimate failure, the left hand shear crack meets the right hand fillet crack at X' (see Fig. 9.14). This is associated with a 'dynamic' fracture of the $-45°$ layer as shown in Fig. 9.15.

9.6 CONCLUSIONS

1. For lay-ups O and Q ($\pm 45°/90°/0°$ surface plies), failure is characterised by shear cracking of the surface $\pm 45°$ layers associated with transverse cracking of the $90°$ ply. Failure then proceeds along the $90°/0°$ interface mainly in a shear mode.
2. For lay-ups P and R ($0°$ surface layer) and unidirectional adherends the mechanisms of failure are the same as those described in Chapter 7 for adherends with $0°$ surface ply. However, failure of unidirectional adherends is associated with longitudinal splitting due to Poisson's ratio effects and debonding of the interface of broken fibres due to stress concentrations created at the fibre ends.

Table 9.1. Test results.

	Stress at failure (N/mm^2)			
Lay-up	Min.	Max.	Mean	C_v (%)
O: $[\pm45/90/0/\pm45/0]_s$	346.6	380.2	369.2	4.2
P: $[0/90/(\pm45)_2/0]_s$	291.6	367.2	334.1	10.5
Q: $[\pm45/90/0_2/\pm45/0]_s$	252.7	313.5	282.8	10.1
R: $[0_2/90/(\pm45)_2/0]_s$	367.3	427.1	393.4	7.7
$[0_4]_s$	641.5	912.3	774.4	16.2
$[0_8]_s$	472.5	493.3	482.7	2.3

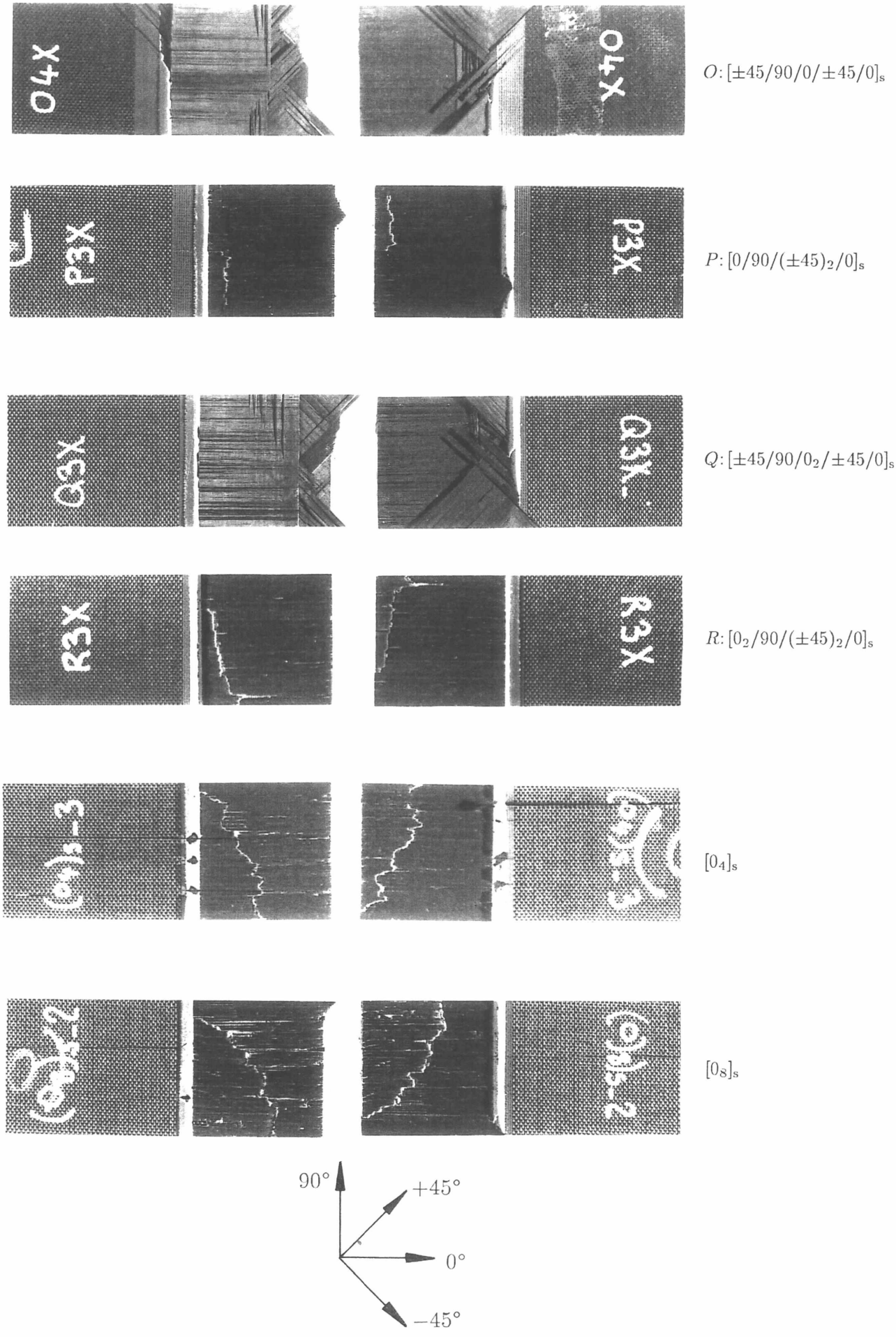
C_v—Coefficient of variation

Table 9.2. Adherend mechanical properties and stresses from Hart-Smith's analysis.

Lay-up	E_m	E_b	ν_m	ν_b	D	k_b	m	l/t	P	σ_{av}	σ_b	σ_{max}	σ_p
O: $[\pm45/90/0/\pm45/0]_s$	59.1	39.5	0.403	0.399	21.0	0.665	−0.100	14.3	683.2	390.4	301.5	691.9	153.4
P: $[0/90/(\pm45)_2/0]_s$	59.1	67.2	0.403	0.228	31.6	1.004	−0.153	14.3	619.2	353.8	344.4	698.2	142.6
Q: $[\pm45/90/0_2/\pm45/0]_s$	68.9	48.7	0.401	0.380	37.9	0.693	−0.085	12.5	592.8	296.4	314.5	610.9	155.0
R: $[0_2/90/(\pm45)_2/0]_s$	68.9	90.6	0.401	0.236	64.0	1.168	−0.127	12.5	835.2	417.6	475.2	892.8	180.4
$[0_4]_s$	138.0	138.0	0.320	0.320	12.8	1.000	0.000	25.0	795.6	795.6	458.0	1253.6	91.5
$[0_8]_s$	138.0	138.0	0.320	0.320	102.5	1.000	0.000	12.5	998.8	499.4	632.3	1131.7	178.7

E_m— effective membrane elastic modulus of adherends in direction of applied load ($\times10^3$ N/mm^2).
E_b— effective bending elastic modulus of adherends corresponding to a bending moment about an in-plane axis normal to the direction of applied load ($\times10^3$ N/mm^2).
ν_m— effective membrane Poisson's ratio of adherends associated with E_m.
ν_b— effective bending Poisson's ratio of adherends associated with E_b.
D— flexural rigidity of adherends ($\times10^3$ Nmm).
k_b— bending stiffness parameter.
m— coefficient of mutual bend-twist coupling corresponding to a bending moment about an in-plane axis normal to the direction of applied load.
l/t— ratio of overlap length to thickness of adherend.
P— experimental mean load at failure per unit joint width (N/mm).
σ_{av}— adherend average stress.
σ_b— adherend bending stress.
σ_{max}— adherend maximum stress.
σ_p— adhesive peel stress.

All stresses are given in N/mm^2.



O: $[\pm 45/90/0/\pm 45/0]_s$

P: $[0/90/(\pm 45)_2/0]_s$

Q: $[\pm 45/90/0_2/\pm 45/0]_s$

R: $[0_2/90/(\pm 45)_2/0]_s$

$[0_4]_s$

$[0_8]_s$

Fig. 9.1. The bonded specimens after fracture.

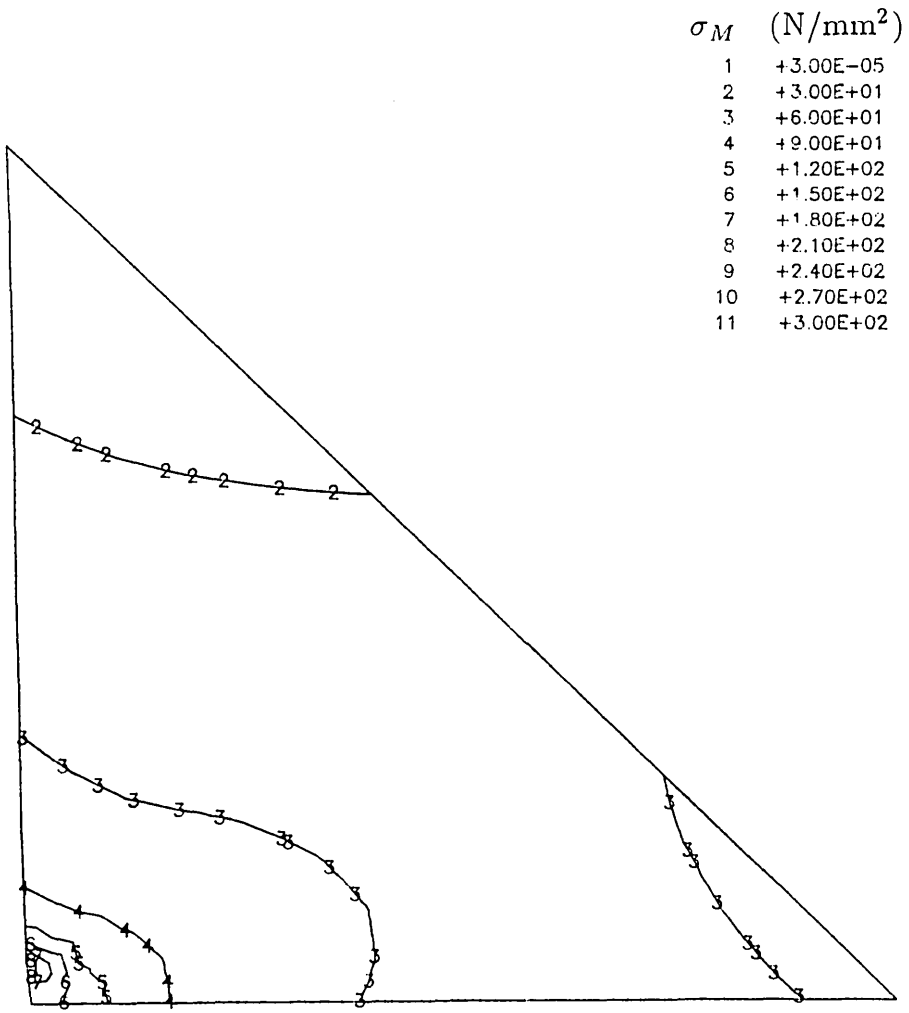


Fig. 9.2. Contours of von Mises stress σ_M in the fillet. Unidirectional $[0_8]_s$ lay-up at 482.7 N/mm^2 applied stress.

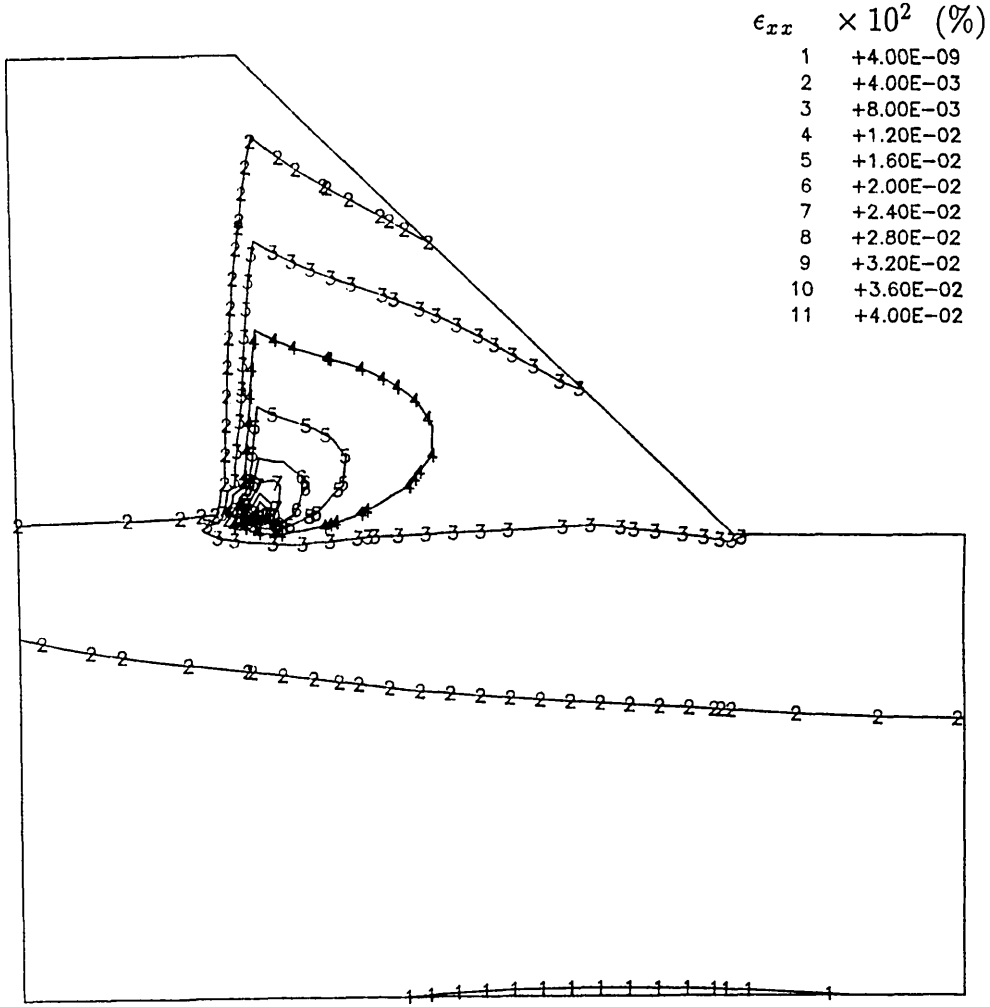


Fig. 9.3. Contours of longitudinal direct strain ϵ_{xx} at end of lap. Unidirectional $[0_8]_s$ lay-up at 482.7 N/mm^2 applied stress.

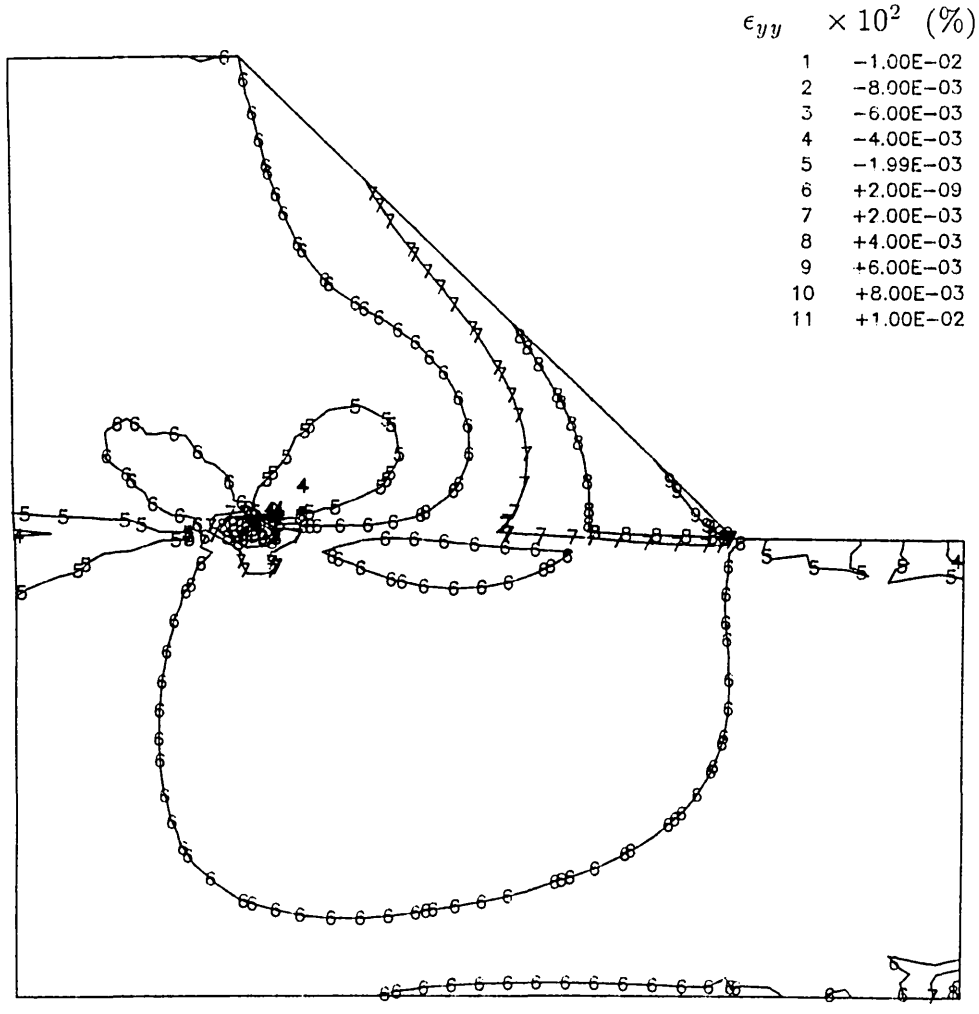


Fig. 9.4. Contours of transverse direct strain ϵ_{yy} at end of lap. Unidirectional $[0_8]_s$ lay-up at 482.7 N/mm^2 applied stress.

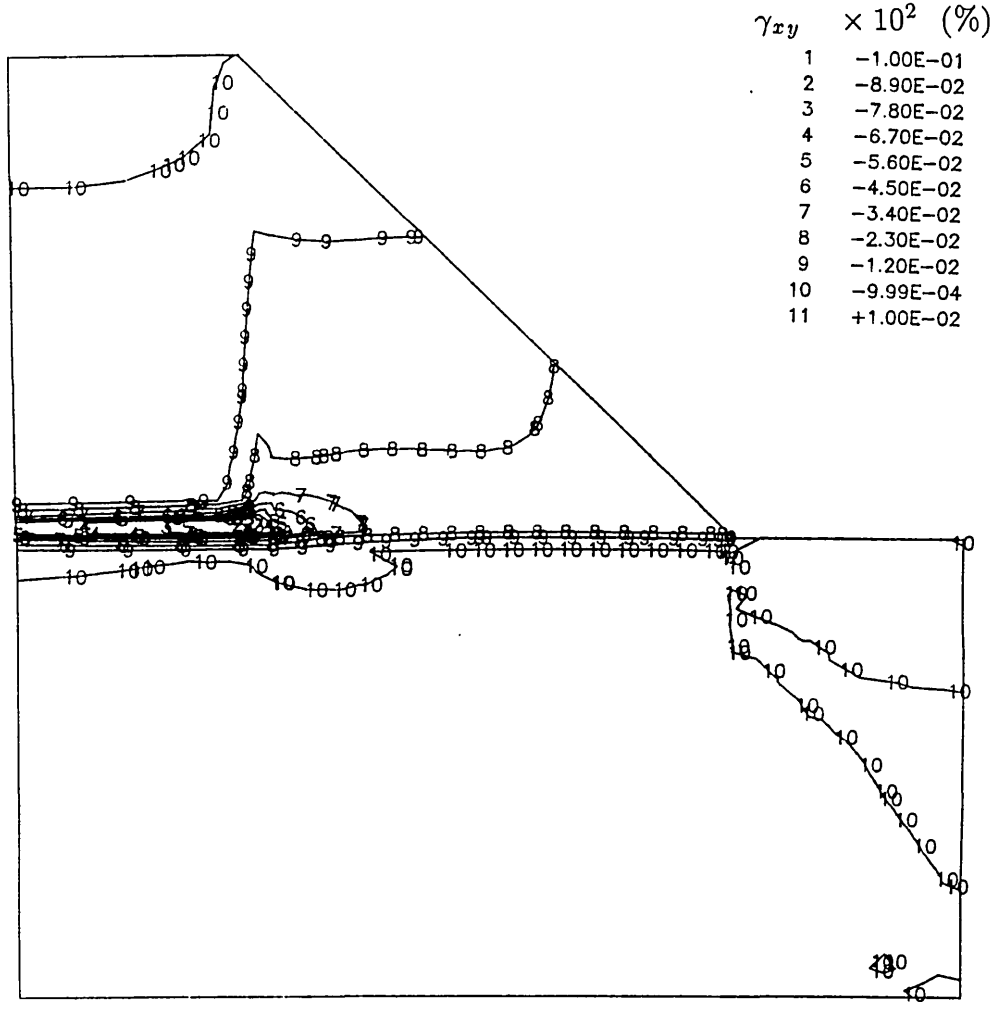


Fig. 9.5. Contours of shear strain γ_{xy} at end of lap. Unidirectional $[0_8]_s$ lay-up at 482.7 N/mm^2 applied stress.

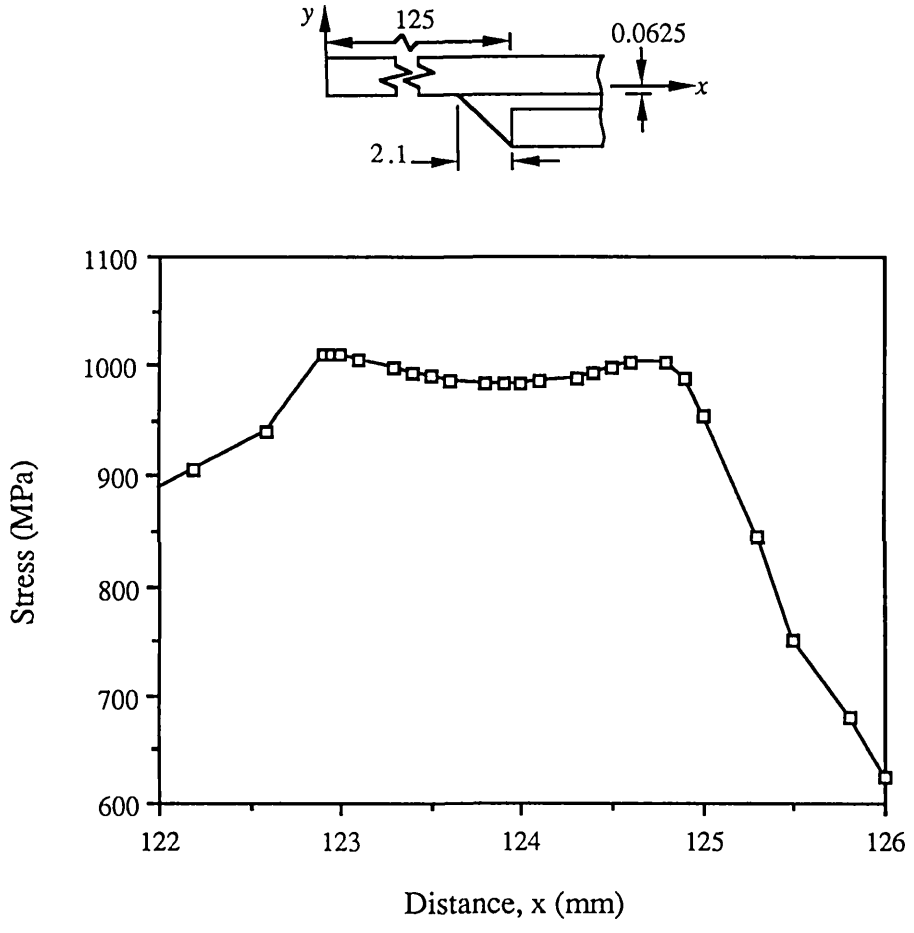


Fig. 9.6. Longitudinal direct stress (σ_{xx}) distribution along the centreline of the 0° ply next to the bondline. Unidirectional $[0_8]_s$ lay-up at 482.7 N/mm^2 applied stress.

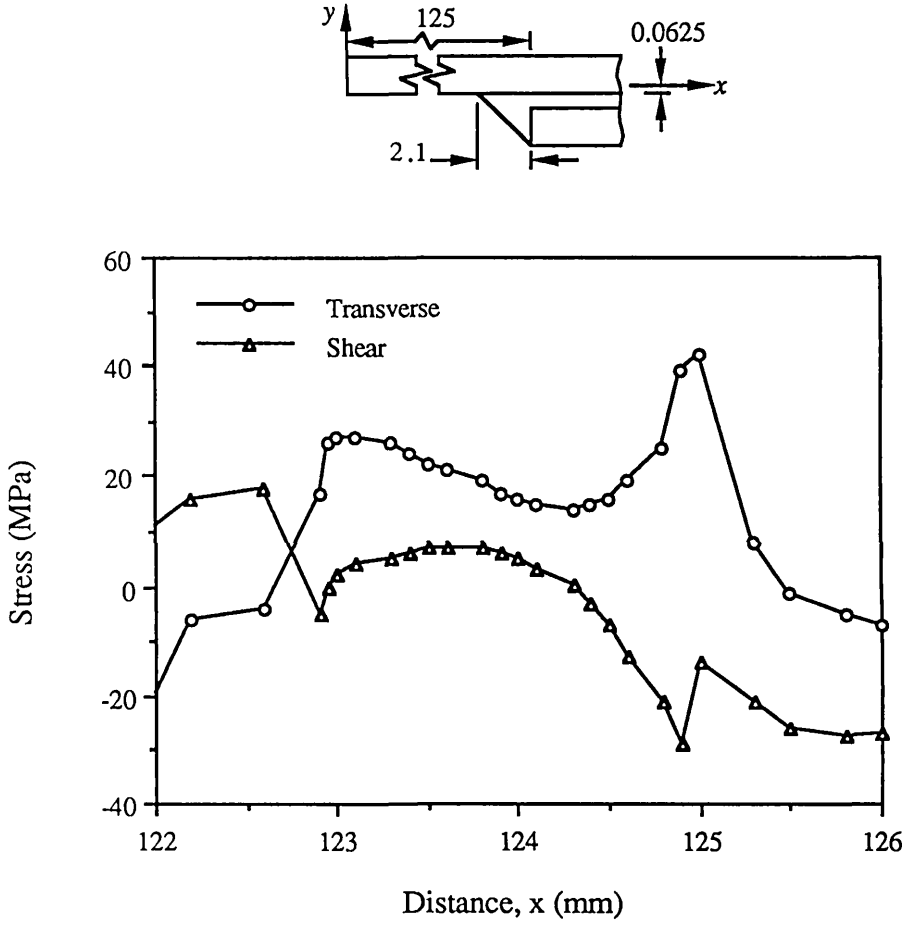


Fig. 9.7. Transverse direct and shear stress (σ_{yy} and τ_{xy} respectively) distributions along the centreline of the 0° ply next to the bondline. Unidirectional $[0_8]_s$ lay-up at 482.7 N/mm^2 applied stress.

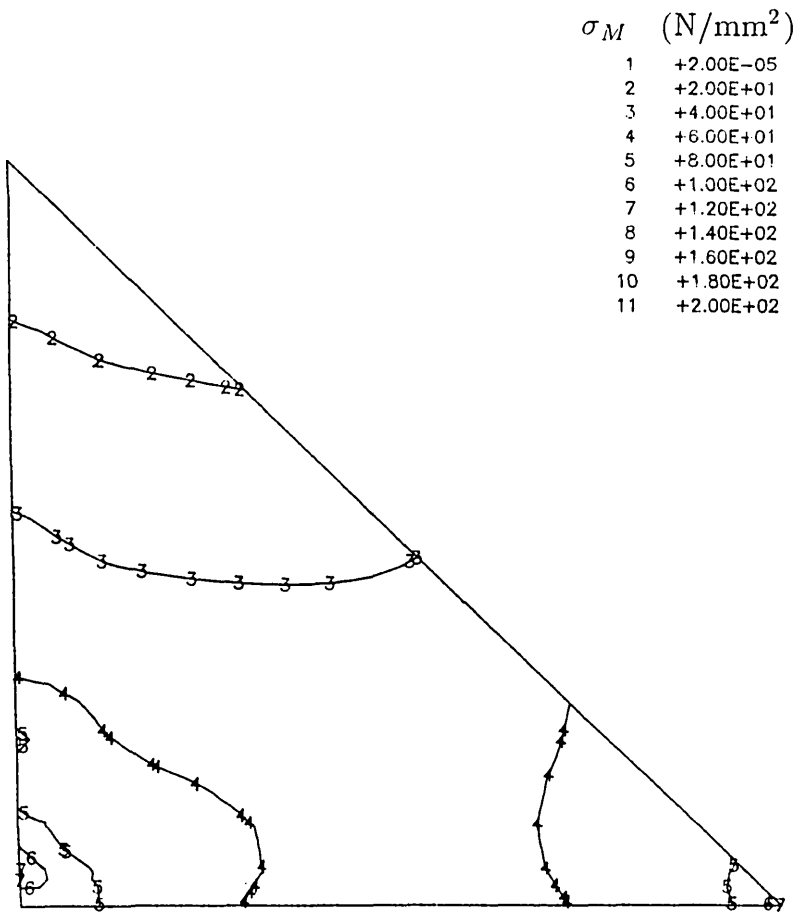


Fig. 9.8. Contours of von Mises stress σ_M in the fillet. Lay-up Q: $[\pm 45/90/0_2/\pm 45/0]_s$ at 282.8 N/mm^2 applied stress.

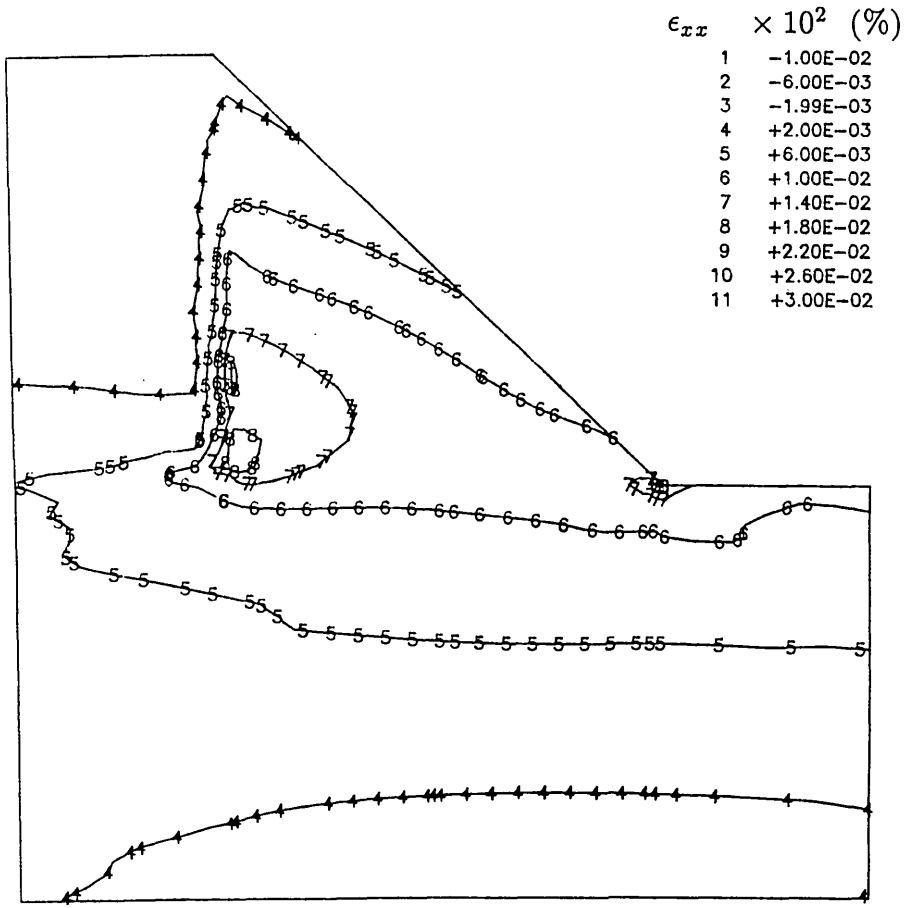


Fig. 9.9. Contours of longitudinal direct strain ϵ_{xx} at end of lap. Lay-up Q: $[\pm 45/90/0_2/\pm 45/0]_s$ at 282.8 N/mm^2 applied stress.

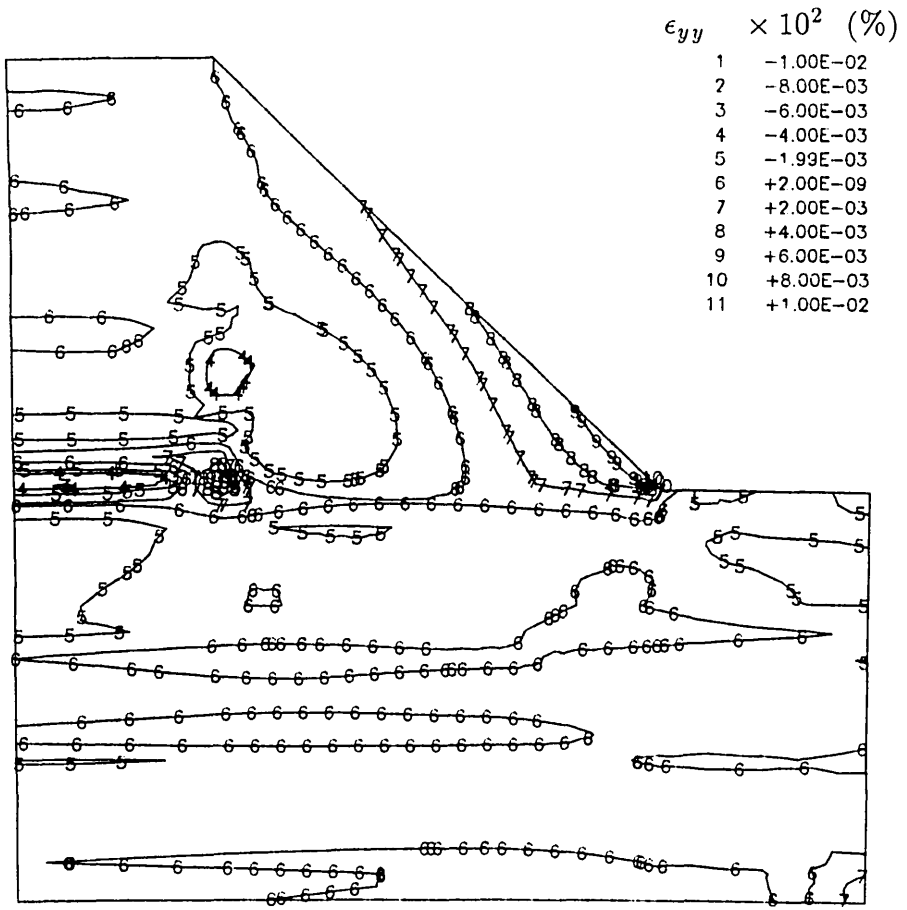


Fig. 9.10. Contours of transverse direct strain ϵ_{yy} at end of lap. Lay-up Q: $[\pm 45/90/0_2/\pm 45/0]_s$ at 282.8 N/mm^2 applied stress.

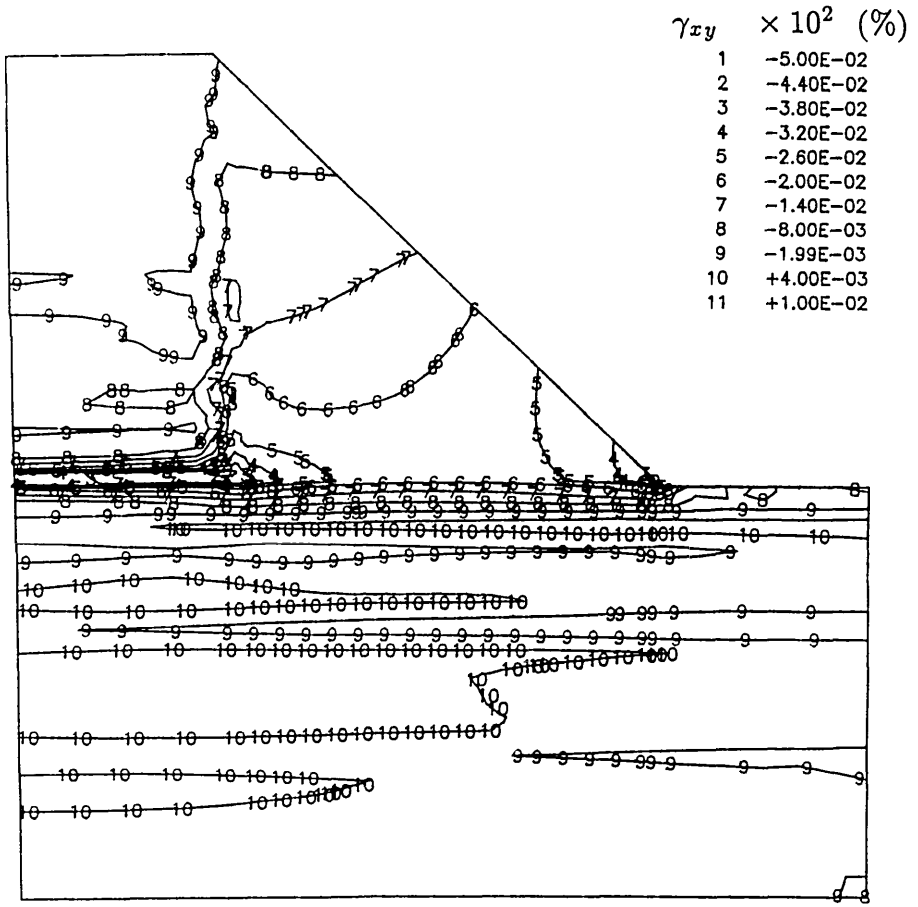


Fig. 9.11. Contours of shear strain γ_{xy} at end of lap. Lay-up Q: $[\pm 45/90/0_2/\pm 45/0]_s$ at 282.8 N/mm^2 applied stress.

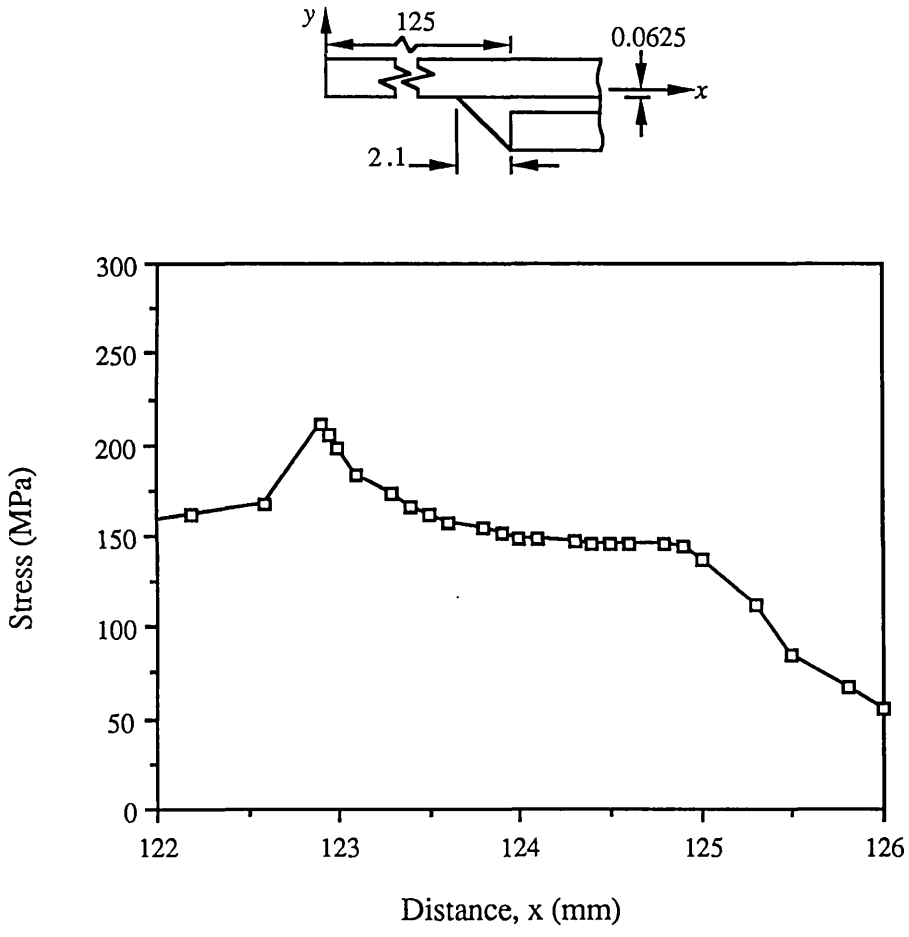


Fig. 9.12. Longitudinal direct stress (σ_{xx}) distribution along the centreline of the +45° ply next to the bondline. Lay-up Q: $[\pm 45/90/0_2/\pm 45/0]_s$ at 282.8 N/mm^2 applied stress.

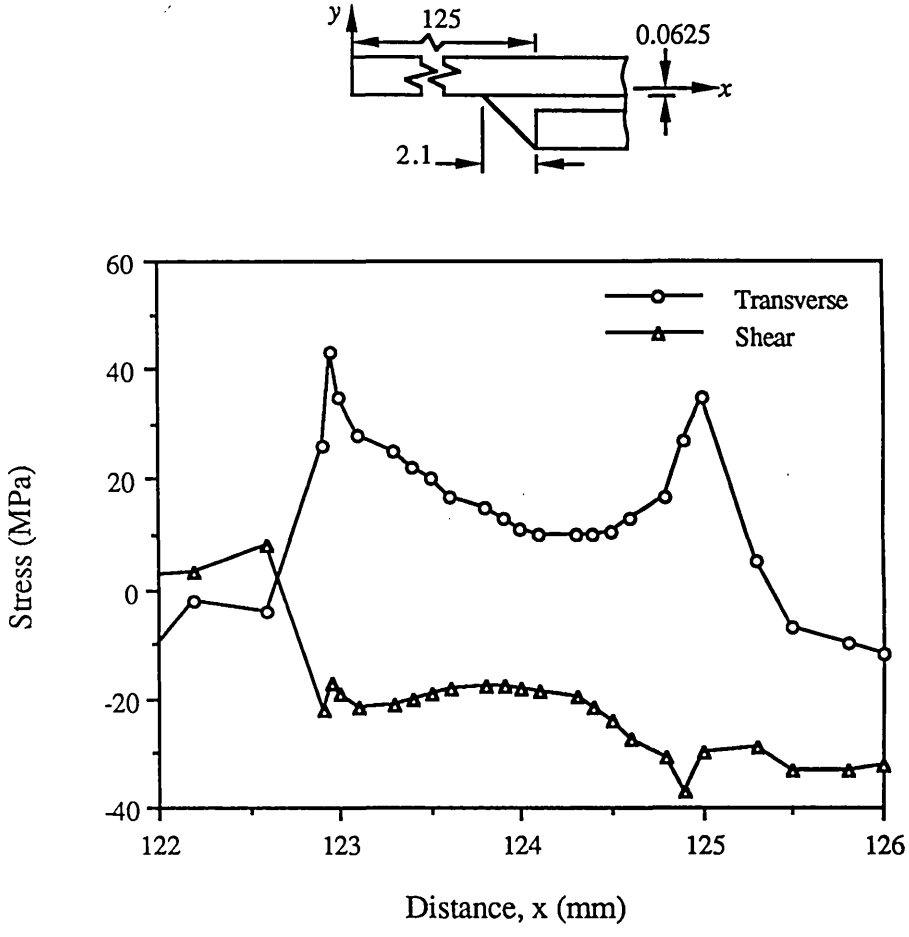


Fig. 9.13. Transverse direct and shear stress (σ_{yy} and τ_{xy} respectively) distributions along the centreline of the +45° ply next to the bondline. Lay-up Q: $[\pm 45/90/0_2/\pm 45/0]_s$ at 282.8 N/mm^2 applied stress.

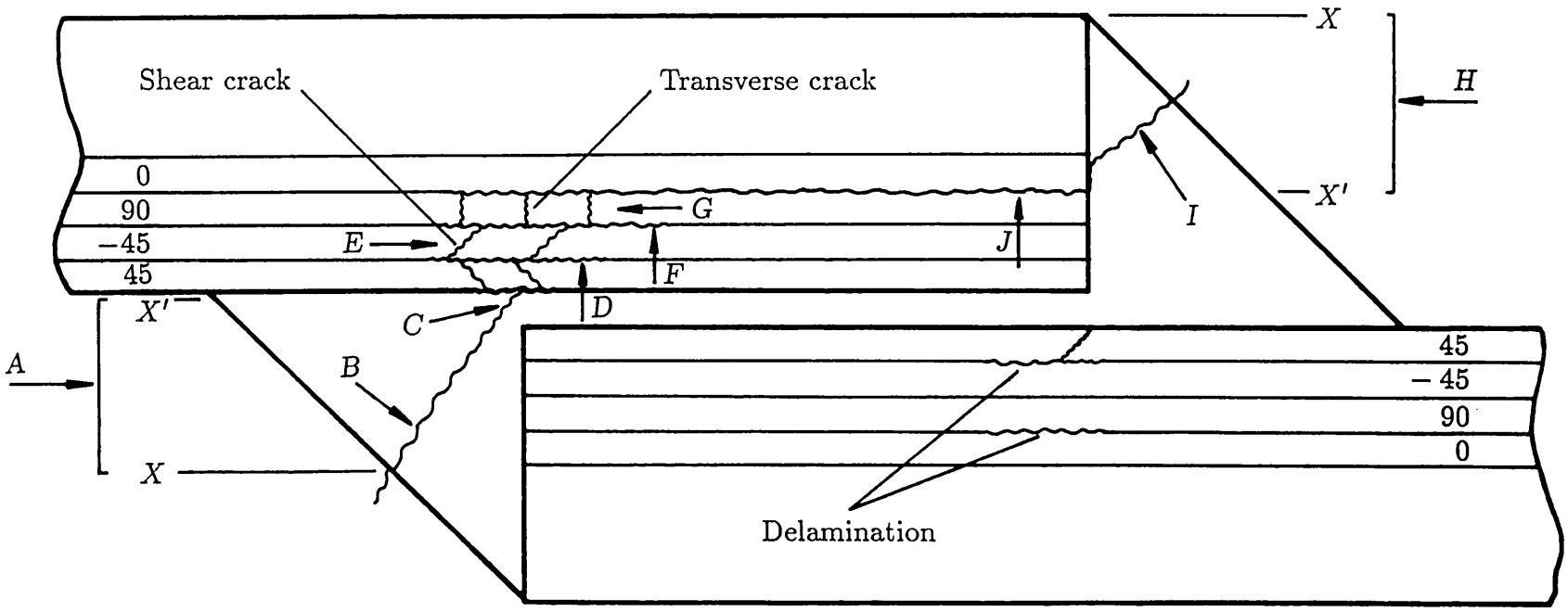


Fig. 9.14. Two-dimensional view of joint failure with lay-ups O: $[\pm 45/90/0/\pm 45/0]_s$ and Q: $[\pm 45/90/0_2/\pm 45/0]_s$.

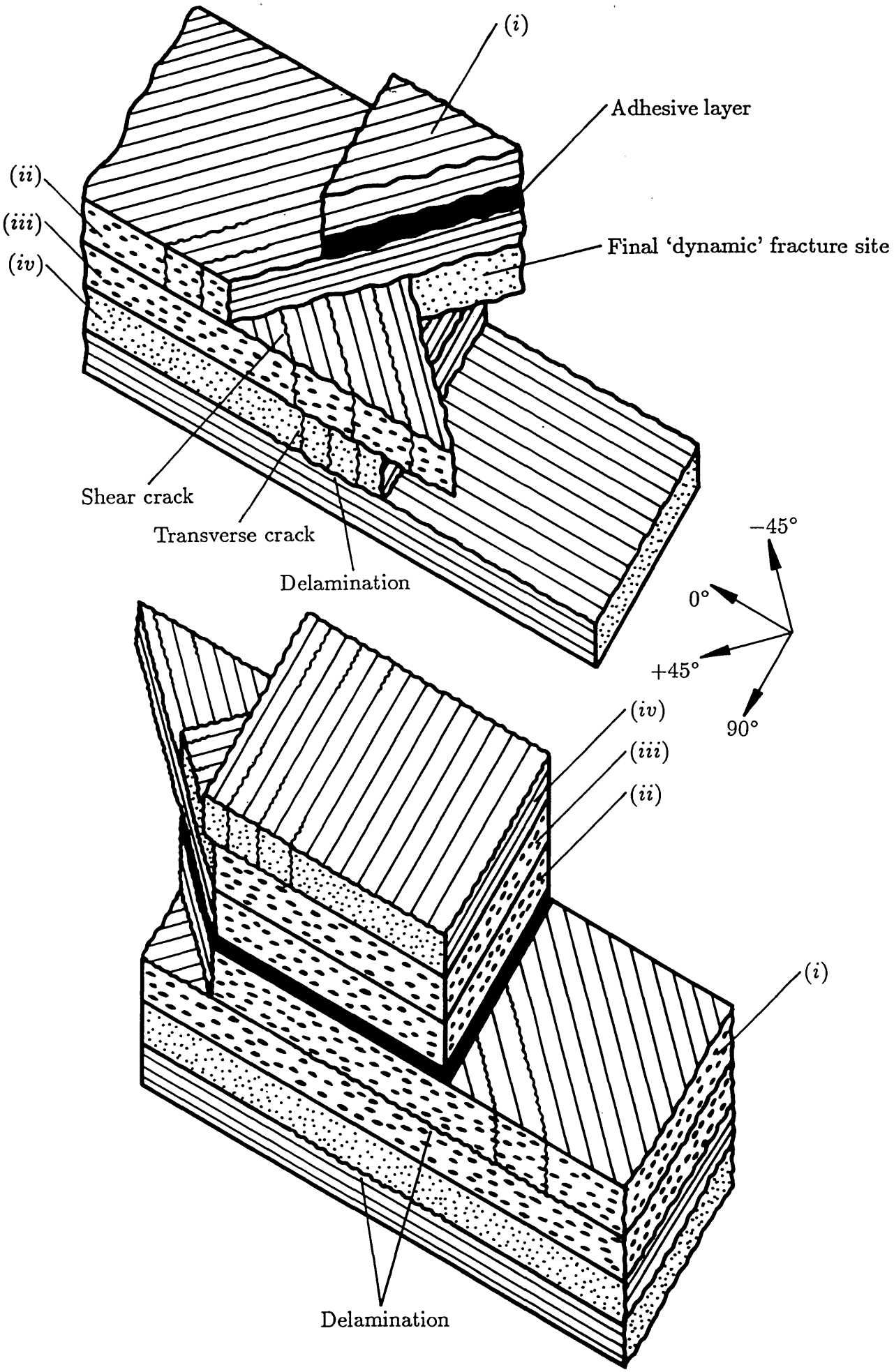
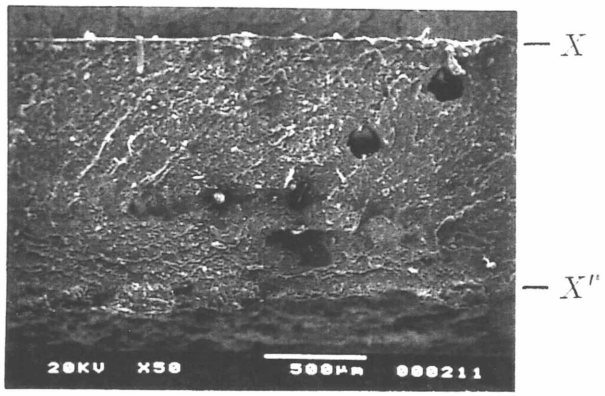
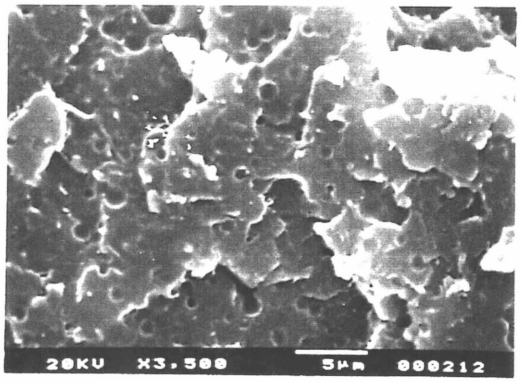


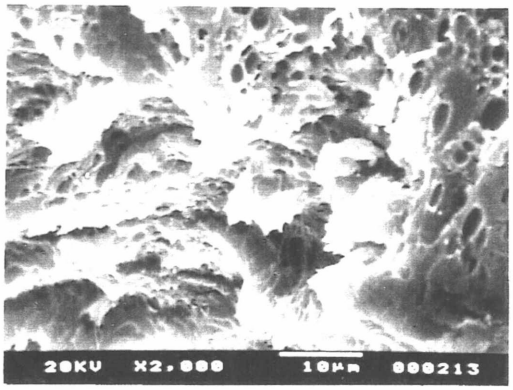
Fig. 9.15. Three-dimensional view of the fractured surfaces with lay-ups O: $[\pm 45/90/0/\pm 45/0]_s$ and Q: $[\pm 45/90/0_2/\pm 45/0]_s$. Only the first four plies are shown. For clarity, the adhesive fillet is not drawn.



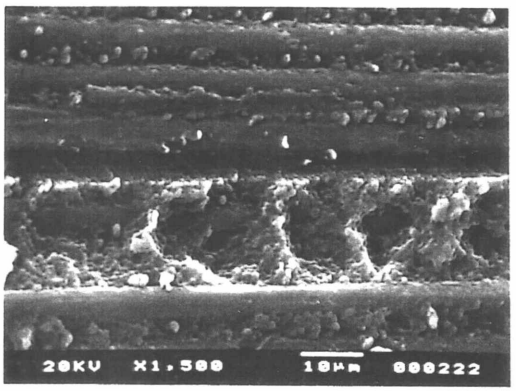
(a)



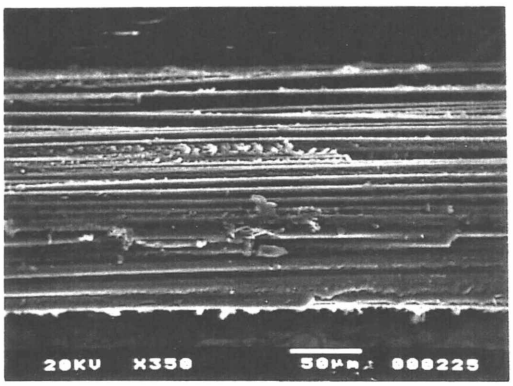
(b)



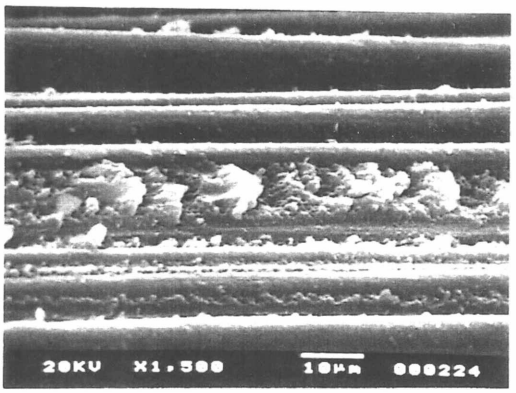
(c)



(d)



(e)



(f)

Fig. 9.16. SEM, taken from lay-up Q: $[\pm 45/90/0_2/\pm 45/0]_s$, showing (refer to Fig. 9.14 for arrow direction):

(a) View arrow A—the fractured fillet.

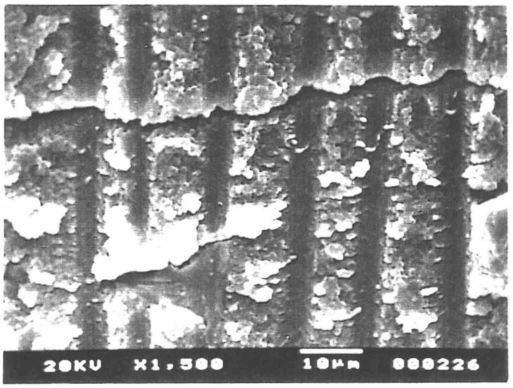
(b) View arrow B—'brittle' adhesive fracture.

(c) View arrow C—'ductile' adhesive fracture.

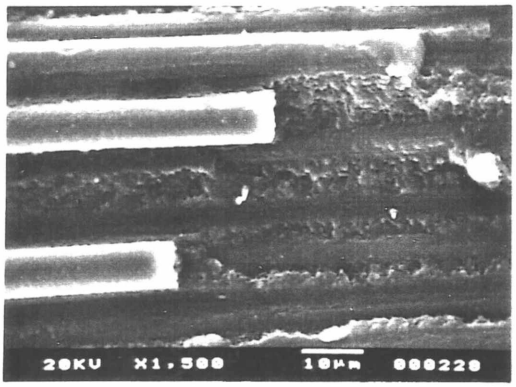
(d) View arrow D—resin cusps due to interlaminar shear on a $-45°$ layer's surface.

(e) View arrow E—a through-thickness view of a sheared $-45°$ ply.

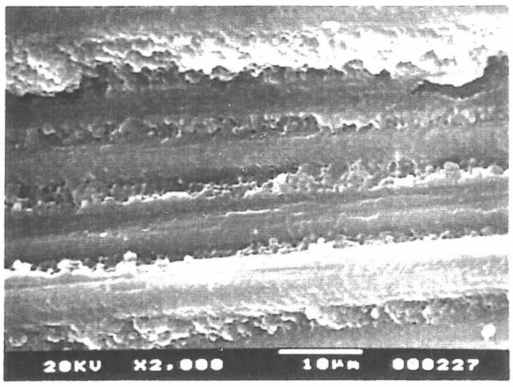
(f) View arrow E—an enlarged view showing resin cusps and constituent debonding due to intralaminar shear.



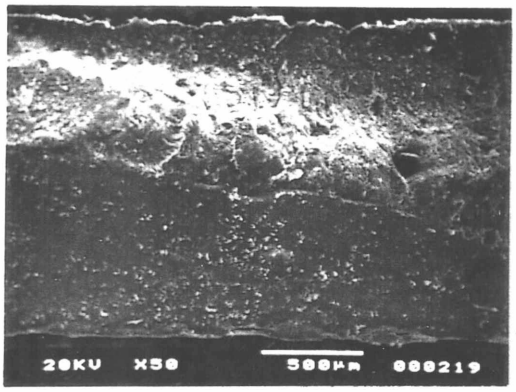
(g)



(h)



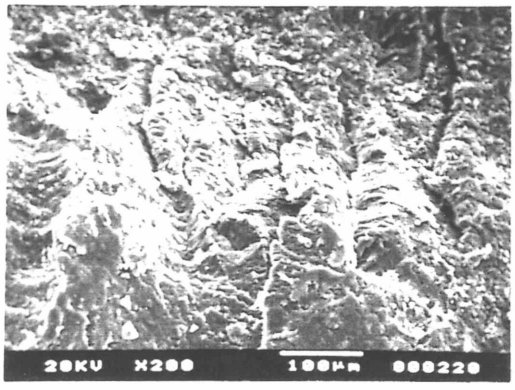
(i)



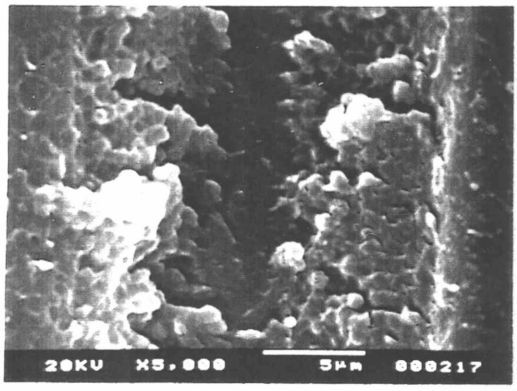
X'

X

(j)



(k)



(l)

Fig. 9.16. (continued) SEM, taken from lay-up Q: $[\pm 45/90/0_2/\pm 45/0]_s$, showing (refer to Fig. 9.14 for arrow direction):

(g) View arrow F—matrix cracking as seen on the surface of a 90° ply.

(h) & (i) View arrow G—transverse cracking in a 90° ply. Note the constituent debonding and fibre transverse tensile failure.

(j) View arrow H—fillet fracture.

(k) View arrow I—fillet fracture.

(l) View arrow J—resin shear cusps on 0° fibres.

$\updownarrow$: direction of 0° fibres

Chapter 10

DESIGN GUIDELINES

10.1 INTRODUCTION

A simple joint ranking factor is proposed which attempts to rank joint strength relative to stacking sequence changes. This factor is based on the effective mechanical properties of the adherends. The predicted and actual joint ranks are compared.

10.2 JOINT RANKING FACTOR

As mentioned in Chapter 3, because the bending stiffness parameter k_b does not address directly the influence of the surface layers, it can only be used as a joint ranking factor for adherends having the same surface plies. In addition, k_b does not incorporate the effect of the bend-twist coupling on the performance of a joint.

The previous Chapters offered some understanding of the effect of stacking sequence on the strength of bonded joints. As a result, an attempt is made to encompass in a single expression the effects of the different mechanical properties of the adherends on the performance of the joint.

The ratio of the bending to membrane elastic moduli of the adherends (E_b/E_m) governs the out-of-plane deformation of a joint. It should be noted that the ratio E_b/E_m is approximately equivalent to the k_b parameter. Thus, if:

1. $E_b/E_m > 1$, the bending modulus is higher than the membrane modulus, reducing joint rotation and hence increasing joint strength. It should be noted that the reduction in joint rotation is associated with a high bending moment and the eccentricity of the load path is not reduced.

$E_b = E_m$ (all 0°) — why not symmetric?

2. $E_b/E_m < 1$, by the same token above, reducing the bending modulus (by a 'soft' ply group) relives the bending moment at the end of the overlap which in turn contributes to enhanced joint strength. This is because the laminate surface failure strain is much higher than the above case.

3. $E_b/E_m = 1$, this is a critical ratio. Joint strength may be increased on either side of this ratio.

Thus, as the term $|(E_b/E_m) - 1|$ is increased, joint strength is increased.

The bending Poisson's ratio ν_b governs the transverse curvature of the adherends. It is thought that the difference between the bending and membrane Poisson's ratios $(\nu_b - \nu_m)$ contributes to the performance of a joint. Thus, if:

1. $\nu_b - \nu_m > 0$, the bending Poisson's ratio exceeds the membrane Poisson's ratio causing 'excessive' transverse deformations and contributing to joint degradation (e.g. resin cracking).

2. $\nu_b - \nu_m < 0$, although the transverse deformations are less severe than the above case, however, the enhancement of the bending stiffness of the laminate by the anti-clastic curvature is reduced, which in turn reduces joint strength.

3. $\nu_b - \nu_m = 0$, this seems to be a good compromise between the above two cases. It corresponds to unidirectional or isotropic adherends.

Thus, as the term $(1 - |\nu_b - \nu_m|)$ is increased, joint strength is increased.

As mentioned in Chapter 3, the effect of the coefficient of mutual bend-twist coupling m is to induce a shear system in the joint. Hence, as this coefficient is increased, joint strength is decreased. Thus, as the term $(m+1)$ is increased, joint strength is increased.

A simple joint ranking factor (JRF) is proposed which ranks joint strength relative to stacking sequence changes. JRF is defined as the product of the above three terms. Thus,

$$JRF = |(E_b/E_m) - 1| \times (1 - |\nu_b - \nu_m|) \times (m + 1). \qquad (10.1)$$

For a given set of stacking sequences, the highest JRF value corresponds to the strongest joint.

10.3 DISCUSSION

The predicted joint rank (PJR) is compared to the actual joint rank (AJR) corresponding to the adherend mean experimental stress at failure (σ_m) for a given l/t ratio. The results are shown in Table 10.1. Joints with unidirectional adherends are not included as they are influenced only by the l/t ratio.

10.3.1 Six-ply adherends

From Table 10.1(a), it can be seen that joints with stacking sequence B are predicted to be stronger than those with stacking sequence A, which agrees with experimental results. Although the value of the $|(E_b/E_m) - 1|$ term for stacking sequence A is higher than that for stacking sequence B, joints with the latter stacking sequence are stronger due to the following reasons:

a) The difference between ν_b and ν_m is less for stacking sequence B than that for stacking sequence A.

b) The surface $\pm 45°$ layers of stacking sequence B offer higher resistance to twisting deformations than the single $0°$ surface layer of stacking sequence A. Hence, the coefficient of mutual bend-twist coupling of stacking sequence B is lower than that for stacking sequence A.

10.3.2 Eight-ply adherends

Table 10.1(b) shows poor prediction of joint ranks. This could possibly be attributed to variability in material processing and bonding. Further testing of joints with stacking sequences D, E and F is suggested.

10.3.3 Sixteen-ply adherends

The predicted joint ranks matches the actual joint ranks as shown in Table 10.1(c). It can be seen that the relative ratio of the E_b/E_m term between stacking sequences K and L is such that it is more advantageous to have $\pm 45°$ surface plies than a single $0°$ surface layer due to the reasons outlined in Section 10.2.

10.3.4 Cross-ply adherends

Table 10.1(d) shows the joint ranking factors for cross-ply adherends. It can be seen that the joint ranking factor values for the twelve- and eight-ply adherends are very close. This indicates that a more accurate determination of the equivalent mechanical properties of the laminates is required for a better prediction of joint ranks in this case. It should be noted that Poisson's deformations with lay-ups containing 90° layers are of relatively lesser influence on joint performance than those with lay-ups without 90° plies.

For the four-ply adherends, joints with $[90/0]_s$ lay-up are predicted, with a more significant joint ranking factor margin, to be stronger than joints with $[0/90]_s$ lay-up, as obtained experimentally.

10.3.5 Other lay-ups

From Table 10.1(e), it can be seen that joints with lay-up O are predicted to be stronger than joints with lay-up P, which agrees with the experimental results. The difference between the joint ranking factor values of lay-ups O and P is 'large', indicating joint ranks clearly.

On the other hand, the difference between the joint ranking factor values of lay-ups Q and R is small indicating that these lay-ups require a more accurate determination of material properties. In addition, rounding off of figures will affect the results in this case.

10.3.6 Other groupings

Table 10.2 shows the joint ranking factor with groupings having the same lay-up and surface layer. For all groupings, the joint ranking factor values correlate with experimental results except for lay-ups E: $[0/\pm 45/0]_s$, F: $[0_2/\pm 45]_s$ and $[0/90]_s$. Further improvement to the joint ranking factor may be obtained by: (a) incorporating the effect of the l/t ratio and (b) considering the surface ply failure strain as a criterion.

10.4 CONCLUSIONS

1. A joint ranking factor which encompasses the different mechanical properties of the adherends is proposed. The JRF is better than the k_b parameter in predicting joint rank.
2. Generally, better agreement is obtained between the predicted and actual joint ranks for adherends with $0°/\pm 45°$ lay-up than $0°/90°$ and $0°/\pm 45°/90°$ lay-ups. Good correlation between the joint ranking factor values and experimental results has been obtained when the adherends are grouped according to their lay-up and surface layer.
3. Modifiers to the joint ranking factor are suggested to include the influence of the l/t ratio and the surface ply failure strain.

Table 10.1. Joint ranking factors.

(a) Six-ply adherends.

Stacking sequence	E_m	E_b	ν_m	ν_b	m	E_b/E_m	$\nu_b - \nu_m$	$\lvert(E_b/E_m) - 1\rvert$	$1 - \lvert\nu_b - \nu_m\rvert$	$m+1$	JRF	PJR	AJR	σ_m	l/t
A: $[0/\pm45]_s$	61.6	103.8	0.668	0.491	−0.240	1.685	−0.177	0.685	0.823	0.760	0.428	2	2	505.7	33.3
B: $[\pm45/0]_s$	61.6	26.5	0.668	0.654	−0.144	0.430	−0.014	0.570	0.986	0.856	0.481	1	1	652.1	33.3

(b) Eight-ply adherends.

Stacking sequence	E_m	E_b	ν_m	ν_b	m	E_b/E_m	$\nu_b - \nu_m$	$\lvert(E_b/E_m) - 1\rvert$	$1 - \lvert\nu_b - \nu_m\rvert$	$m+1$	JRF	PJR	AJR	σ_m	l/t
D: $[\pm45/0_2]_s$	81.0	37.1	0.638	0.672	−0.093	0.458	0.034	0.542	0.966	0.907	0.475	1	3	508.7	25.0
E: $[0/\pm45/0]_s$	81.0	91.5	0.638	0.580	−0.138	1.130	−0.058	0.130	0.942	0.862	0.106	3	1	571.0	25.0
F: $[0_2/\pm45]_s$	81.0	123.8	0.638	0.440	−0.165	1.528	−0.198	0.528	0.802	0.835	0.354	2	2	535.8	25.0

(c) Sixteen-ply adherends.

Stacking sequence	E_m	E_b	ν_m	ν_b	m	E_b/E_m	$\nu_b - \nu_m$	$\lvert(E_b/E_m) - 1\rvert$	$1 - \lvert\nu_b - \nu_m\rvert$	$m+1$	JRF	PJR	AJR	σ_m	l/t
K: $[\pm45/0_3/\pm45/0]_s$	81.0	66.0	0.638	0.657	−0.047	0.815	0.019	0.185	0.981	0.953	0.173	3	3	362.5	12.5
L: $[0/\pm45/0_2/\pm45/0]_s$	81.0	83.6	0.638	0.626	−0.055	1.032	−0.012	0.032	0.988	0.945	0.030	4	4	354.2	12.5
M: $[0_2/\pm45/0/\pm45/0]_s$	81.0	98.5	0.638	0.588	−0.065	1.216	−0.050	0.216	0.950	0.935	0.192	2	2	431.3	12.5
N: $[0_3/(\pm45)_2/0]_s$	81.0	110.7	0.638	0.543	−0.076	1.367	−0.095	0.367	0.905	0.924	0.307	1	1	461.5	12.5

Table 10.1. (continued) Joint ranking factors.

(d) Cross-ply adherends.

Lay-up	E_m	E_b	ν_m	ν_b	m	E_b/E_m	$\nu_b-\nu_m$	$\lvert(E_b/E_m)-1\rvert$	$1-\lvert\nu_b-\nu_m\rvert$	$m+1$	JRF	PJR	AJR	σ_m	l/t
$[0/90]_{3s}$	74.1	90.2	0.041	0.052	0.000	1.217	0.011	0.217	0.989	1.000	0.215	2	1	506.1	16.7
$[90/0]_{3s}$	74.1	57.9	0.041	0.033	0.000	0.781	−0.008	0.219	0.992	1.000	0.217	1	2	187.7	16.7
$[0/90]_{2s}$	74.1	98.3	0.041	0.061	0.000	1.327	0.020	0.327	0.980	1.000	0.320	2	1	529.5	25.0
$[90/0]_{2s}$	74.1	49.8	0.041	0.031	0.000	0.672	−0.010	0.328	0.990	1.000	0.325	1	2	237.8	25.0
$[0/90]_s$	74.1	122.4	0.041	0.118	0.000	1.652	0.077	0.652	0.923	1.000	0.602	2	2	529.1	50.0
$[90/0]_s$	74.1	25.6	0.041	0.025	0.000	0.345	−0.016	0.654	0.984	1.000	0.643	1	1	628.8	50.0

(e) Other lay-ups.

Lay-up	E_m	E_b	ν_m	ν_b	m	E_b/E_m	$\nu_b-\nu_m$	$\lvert(E_b/E_m)-1\rvert$	$1-\lvert\nu_b-\nu_m\rvert$	$m+1$	JRF	PJR	AJR	σ_m	l/t
O: $[\pm45/90/0/\pm45/0]_s$	59.1	39.5	0.403	0.399	−0.100	0.668	−0.004	0.332	0.996	0.900	0.298	1	1	369.2	14.3
P: $[0/90/(\pm45)_2/0]_s$	59.1	67.2	0.403	0.228	−0.153	1.137	−0.175	0.137	0.825	0.847	0.096	2	2	334.1	14.3
Q: $[\pm45/90/0_2/\pm45/0]_s$	68.9	48.7	0.401	0.380	−0.085	0.707	−0.021	0.293	0.979	0.915	0.262	1	2	282.8	12.5
R: $[0_2/90/(\pm45)_2/0]_s$	68.9	90.6	0.401	0.236	−0.127	1.315	−0.165	0.315	0.835	0.873	0.230	2	1	393.4	12.5

E_m— effective membrane elastic modulus of adherends in direction of applied load ($\times10^3$ N/mm^2).

E_b— effective bending elastic modulus of adherends corresponding to a bending moment about an in-plane axis normal to the direction of applied load ($\times10^3$ N/mm^2).

ν_m— effective membrane Poisson's ratio of adherends associated with E_m.

ν_b— effective bending Poisson's ratio of adherends associated with E_b.

m— coefficient of mutual bend-twist coupling corresponding to a bending moment about an in-plane axis normal to the direction of applied load.

JRF— joint ranking factor.

PJR— predicted joint rank.

AJR— actual joint rank.

σ_m— adherend mean experimental stress at failure (N/mm^2).

l/t— ratio of overlap length to thickness of adherend.

Table 10.2. JRF with other groupings.

(a) Lay-up 0°/±45° with ±45° surface layers.

Lay-up	l/t	σ_m	JRF
B: $[\pm 45/0]_s$	33.3	652.1	0.481
D: $[\pm 45/0_2]_s$	25.0	508.7	0.475
K: $[\pm 45/0_3/\pm 45/0]_s$	12.5	362.5	0.173

(b) Lay-up 0°/±45° with 0° surface layer.

Lay-up	l/t	σ_m	JRF
A: $[0/\pm 45]_s$	33.3	505.7	0.428
E: $[0/\pm 45/0]_s$	25.0	571.0	0.106
F: $[0_2/\pm 45]_s$	25.0	535.8	0.354
L: $[0/\pm 45/0_2/\pm 45/0]_s$	12.5	354.2	0.030
M: $[0_2/\pm 45/0/\pm 45/0]_s$	12.5	431.3	0.192
N: $[0_3/(\pm 45)_2/0]_s$	12.5	461.5	0.307

(c) Lay-up 0°/90° with 0° surface layer.

Lay-up	l/t	σ_m	JRF
$[0/90]_{3s}$	16.7	506.1	0.215
$[0/90]_{2s}$	25.0	529.5	0.320
$[0/90]_s$	50.0	529.1	0.602

(d) Lay-up 0°/90° with 90° surface layer.

Lay-up	l/t	σ_m	JRF
$[90/0]_{3s}$	16.7	187.7	0.217
$[90/0]_{2s}$	25.0	237.8	0.325
$[90/0]_s$	50.0	628.8	0.643

Table 10.2. (continued) JRF with other groupings.

(e) Lay-up 0°/±45°/90° with ±45° surface layers.

Lay-up	l/t	σ_m	JRF
O: $[\pm 45/90/0/\pm 45/0]_s$	14.3	369.2	0.298
Q: $[\pm 45/90/0_2/\pm 45/0]_s$	12.5	282.8	0.262

(f) Lay-up 0°/±45°/90° with 0° surface layer.

Lay-up	l/t	σ_m	JRF
P: $[0/90/(\pm 45)_2/0]_s$	14.3	334.1	0.096
R: $[0_2/90/(\pm 45)_2/0]_s$	12.5	393.4	0.230

l/t— ratio of overlap length to thickness of adherend.

σ_m— adherend mean experimental stress at failure (N/mm^2).

JRF— joint ranking factor.

Chapter 11

CONCLUSIONS AND RECOMMENDATIONS FOR FUTURE WORK

11.1 CONCLUSIONS

This work offers a more fundamental understanding than was previously available of the influence of stacking sequence on the performance of bonded joints. Detailed accounts of the mechanisms of failure of joints with various stacking sequences are given. These have been supported by fractographic and numerical analyses.

Generally, joints of a given lay-up with adherends having a single 0° surface layer are not necessarily stonger than those with adherends having ±45° surface plies. This is due to the bending moment relief offered by the ±45° surface layers. The resistance of the adherends to twisting deformations is enhanced by ±45° surface plies. In addition, there is some evidence that the basic tensile strength of the laminate is increased by the 'padding' effect offered by a 'soft' surface ply group. These findings correlate well with the requirement for a 'soft' ply group for enhanced fatigue and impact resistance.

Voids in the adhesive layer and fillet, due to the entrapment of vapours of water and other volatile materials in the adhesive and composite, have a detrimental effect on the performance of a joint. Drying the adhesive and composite prior to bonding, as described in Chapter 4, is necessary.

Moiré interferometry has been shown to be a useful technique in the determination of strain distributions in bonded joints. Good agreement has been obtained

between strains obtained using moiré interferometry and geometrically nonlinear finite element analysis.

The continuum method of Hart-Smith has been evaluated. The flexural rigidity and bending stiffness parameters (D and k_b respectively) have been modified to incorporate the effect of the bending Poisson's ratio. It is found that, because k_b does not address directly the influence of the surface layers, it can only be used as a joint ranking factor for adherends having the same surface plies.

Joint failure has been predicted using geometrically nonlinear finite element analysis. The results of the numerical crack simulation have correlated with the sequence of joint failure, with excellent agreement between predicted and measured failure strains.

A simple joint ranking factor, which ranks joint strength relative to stacking sequence changes, has been proposed. This factor encompasses the effects of the various mechanical properties of the adherends, but needs further modification to account for the influence of the l/t ratio and surface layer failure strain.

11.1.1 Six-ply adherends

1. Joints with stacking sequence A: $[0/\pm 45]_s$ are weaker than those with stacking sequence B: $[\pm 45/0]_s$ due to the following reasons:
   a) The bending moment relief offered by the 'soft' surface ply group of stacking sequence B outweighs the benefit of the unidirectional surface layer of stacking sequence A. This phenomenon is analogous to the yielding effect in metallic adherends.
   b) The coefficient of mutual bend-twist coupling and bending Poisson's ratio act together in favour of a stronger joint with stacking sequence B.
   c) The basic tensile strength of stacking sequence A is lower than that of stacking sequence B.
2. The bending stiffness parameter k_b does not act as a joint ranking factor as it does not address directly the influence of laminates' surface plies.
3. The poor prediction of the adherend and adhesive stresses by Hart-Smith's analysis is mainly due to the 'smeared' mechanical properties of the adherends.

4. The geometrically nonlinear finite element analysis predicts joint failure using either maximum strain or maximum stress failure criteria. However, the nonlinear shear stress-strain relationship of the adhesive needs to be modelled.
5. The linear finite element analysis grossly over-estimates joint strains and stresses.
6. The JRF predictions correlate with experimental results.

11.1.2 Eight-ply adherends

1. With all stacking sequences (D: $[\pm 45/0_2]_s$, E: $[0/\pm 45/0]_s$ and F: $[0_2/\pm 45]_s$), failure is usually initiated by fillet fracture followed by adherend failure. Fillet fracture initiates at the fillet free surface and propagates, almost parallel to the adherend edge, to the fillet root.
2. For adherends with $\pm 45°$ surface plies, failure proceeds inwards from the surface layer and is manifested by intralaminar and interlaminar shear cracking.
3. For adherends with $0°$ surface layer, failure initiates by fibre tensile fracture followed by delamination within the $0°$ ply.
4. The linear finite element analysis predicts higher stresses than the continuum method of Hart-Smith because it considers the discrete layered nature of the laminate and does not allow for geometric nonlinearity. Laminate failure load may be predicted using nonlinear finite element analysis.
5. For the 25 mm overlap, the order of the stacking sequence relative to mean joint strength is as follows: E, F and D. For the 12.5 mm overlap, joints with stacking sequences D and E are of equal mean strength followed by joints with stacking sequence F. However, the maximum strength values for the 12.5 mm overlap follow the same order as that for the 25 mm overlap.
6. The effect of the l/t ratio on joint strength is influenced by the adherend stacking sequence and by the surface plies. As the l/t ratio is increased, higher joint strengths may be attained with adherends having $0°$ surface layer than those with $\pm 45°$ surface plies.

7. The flexural rigidity and bending stiffness parameters for stacking sequence F are higher than those for stacking sequence E. However, contrary to expectations, joints with stacking sequence F are weaker than those with stacking sequence E.
8. The JRF predictions do not agree with experimental results.

11.1.3 Sixteen-ply adherends

1. There is no advantage in placing a single 0° layer next to the bondline as compared to ±45° plies (stacking sequences K: $[\pm 45/0_3/\pm 45/0]_s$ and L: $[0/\pm 45/0_2/\pm 45/0]_s$). Placing more than one longitudinal ply next to the bondline increases the bending stiffness of the laminate significantly so as to increase joint strength (stacking sequences M: $[0_2/\pm 45/0/\pm 45/0]_s$ and N: $[0_3/(\pm 45)_2/0]_s$).
2. With all stacking sequences, fillet fracture initiates at the fillet free surface and propagates at an angle to the adherend edge to the fillet root.
3. Strains obtained using moiré interferometry agree well with predicted strains using geometrically nonlinear finite element analysis. Hence, material nonlinearity seems to be of little influence.
4. The predicted strains using numerical crack simulation correlate with the sequence of joint failure.
5. For stacking sequences L, M and N, joint strength is increased as the flexural rigidity and bending stiffness parameters are increased.
6. Good agreement has been obtained between the JRF predictions and experimental results.

11.1.4 Cross-ply adherends

1. For cross-ply (0°/90°) adherends with 90° surface layer:
   a) Failure is initiated by a transverse crack in the 90° ply next to the fillet tip. This is followed by shear cracking along the 90°/0° interface.
   b) The failure initiation site has been predicted by numerical analysis.

c) Joint strength is increased with the decrease in k_b and increase in l/t.

d) Good agreement has been obtained between the JRF predictions and experimental results.

2. For cross-ply adherends having 0° surface ply:

a) There is no change in the mechanisms of failure to those described in Chapter 7 for adherends with 0° surface layer.

b) Joint strength is increased with the increase in both k_b and l/t.

c) The JRF predictions correlate with experimental results for all lay-ups except $[0/90]_s$.

11.1.5 Other lay-ups

1. For lay-ups O: $[\pm 45/90/0/\pm 45/0]_s$ and Q: $[\pm 45/90/0_2/\pm 45/0]_s$:

a) Failure is characterised by shear cracking of the surface ±45° layers associated with transverse cracking of the 90° ply. Failure then proceeds along the 90°/0° interface mainly in a shear mode.

b) Joint strength is increased with the decrease in the k_b value.

c) The JRF predictions agree with experimental results.

2. For lay-ups P: $[0/90/(\pm 45)_2/0]_s$ and R: $[0_2/90/(\pm 45)_2/0]_s$:

a) The failure mechanisms are the same as those described in Chapter 7 for adherends with 0° surface ply.

b) Joint strength is increased with the increase in the k_b value.

c) The JRF predictions correlate with experimental results.

3. The mechanisms of failure of joints with unidirectional adherends are the same as those described in Chapter 7 for adherends with 0° surface layer. However, failure is associated with longitudinal splitting due to Poisson's ratio effects and debonding of the interface of broken fibres due to stress concentrations created at the fibre ends. As expected, joint strength is increased with the increase in the l/t ratio.

11.2 RECOMMENDATIONS FOR FUTURE WORK

1. Testing of joints with $l/t > 50$ is recommended to confirm the mechanisms of failure presented.
2. The nonlinear shear stress-strain relationship of the adhesive and composite should be incorporated in the finite element analysis. With single lap joints, material nonlinearity is of secondary importance to the geometric nonlinearity used in this work. However, including material nonlinearity will further improve the prediction of joint strength.
3. Further assessment of the through-thickness and shear strains should be obtained from moiré interferometry. The author had enough time only to correlate the longitudinal direct strain obtained using moiré interferometry to numerical prediction. It is suggested that contour maps of the longitudinal and transverse direct and shear strains at the end of the lap are plotted from the U and V displacement fields. These maps may then be compared to the numerically predicted contour plots presented in this report.
4. Fractography has proved to be a powerful technique in the understanding of joint failure. Its use in any future work on bonded joints is encouraged.
5. Further evaluation of the proposed joint ranking factor by incorporating modifiers that account for l/t and failure strains.

Appendix A

MECHANICAL PROPERTIES OF THE COMPOSITE AND ADHESIVE

A.1 INTRODUCTION

Testing of composite materials is not simple due to their anisotropic nature. The states of stress within the composite when it is under load is complicated by the varied elastic constants of the constituent materials. This is complicated further by the directional strength and stiffness brought about by orientation of the reinforcement in the composite. The reinforcement itself may have anisotropic properties which further complicates composites testing. The CRAG test methods [90] have been used to determine the mechanical properties of the composite. Bulk specimens have been used to determine the mechanical properties of the adhesive.

A.2 MODES OF FAILURE

The modes of failure of unidirectional composite are presented.

A.2.1 Longitudinal tensile failure

Failure initiates as a tensile fracture of fibres at the weakest cross-section of the specimen. As the load increases, further fibres are fractured in a random manner. The interface of broken fibres may become debonded because of stress concentrations created at the fibre ends and this may contribute to the separation of the composite at a given cross-section. Cracks at different cross-sections of the composite may join up by debonding of the fibres along their length or by shear failure of the matrix.

Thus the characteristics of a longitudinal tensile failure are: (a) brittle composite fracture, (b) fibre pull-out, (c) interface-matrix shear failure and (d) fibre-matrix fracture (constituents debonding). Fibre pull-out depends on the bond strength and the load transfer mechanism from the matrix to the fibre. For a given failure path, a mixture of interface-matrix and fibre-matrix fractures may occur.

A.2.2 Transverse tensile failure

Failure is initiated by matrix or interface tensile fracture. Some fibre transverse tensile failures may also occur. The fibres act as stress raisers in the matrix and interface. Thus the characteristics of a transverse tensile failure are: (a) matrix tensile fracture, (b) fibre-matrix fracture (constituents debonding), (c) fibre transverse tensile fracture and (d) fibre splitting. Usually, a fractured surface exhibits a mixture of the above failure characteristics.

A.2.3 Longitudinal compression failure

Fibre microbuckling is usually preceded by matrix yielding, constituents' debonding and matrix microcrackling. Failure may initiate by transverse splitting by exceeding the ultimate transverse tensile strain due to Poisson's ratio effect. Microbuckling of the fibres may result in shear strains in the interfibre matrix which may exceed the ultimate shear strain of the matrix causing matrix shear failure. Thus the characteristics of longitudinal compression failure are: (a) matrix yielding, (b) constituents' debonding, (c) matrix microcracking, (d) fibre microbuckling and (f) matrix shear cracking.

The longitudinal compressive strength value usually reflects the quality of the test method rather than 'pure' composite compressive strength. In this case, the Celanese test fixture is used. Several test fixtures for compression testing are available with some fixtures yielding higher compressive strength values than others. This may occur at the expense of restricting certain modes of compressive failure.

A.2.4 Transverse compression failure

Failure is initiated by matrix shear failure with fibre-matrix bond failure (interface failure).

A.2.5 In-plane shear failure

This type of failure is characterised by matrix shear failure with constituent debonding.

A.3 UNIDIRECTIONAL PROPERTIES

The mechanical properties of the composite are presented in Table A.1. It is thought that the longitudinal tensile strength value reported is lower than that expected for this material. All the mechanical properties of the composite presented in Table A.1 have been determined experimentally, using the appropriate CRAG test method, with the exception of the ultimate in-plane shear strain S_ϵ. This value has been derived from the in-plane shear modulus G_{12} (secant modulus at 0.5% shear strain from $[(\pm 45)_4]_s$ specimen in tension) and the ultimate in-plane shear strength S (from short beam shear test) assuming the linear relationship

$$S_\epsilon = \frac{S}{G_{12}}. \tag{A.1}$$

Typical stress-strain curves are depicted in Figs. A.1–A.6. The longitudinal tensile stress-strain curve (Fig. A.1) is basically linear to failure. However, it can be seen that after about 0.8% strain there is an increase in stiffness. This may be due to improved fibre alignment in resisting the applied load. It can be argued that matrix microcracking and constituent debonding act to improve fibre alignment. Fig. A.2 shows a linear stress-strain relationship in the transverse tensile test up to about 0.5% strain, afterwhich some nonlinear matrix (and to some extent interface) behaviour is exhibited.

The stress-strain relationship in a longitudinal compression test is essentially linear as shown in Fig. A.3. However, macrobuckling of the specimen tends to introduce a nonlinear effect (after about 0.75% strain). As the transverse compression failure is dominated by shear fracture of the resin, the stress-strain curve is nonlinear as shown in Fig. A.4.

The shear stress-strain curve, obtained from $[(\pm 45)_4]_s$ specimen in tension, is highly nonlinear—see Fig. A.5. In Fig. A.6, the longitudinal stress-strain curve of $[(\pm 45)_4]_s$ material loaded to failure is depicted.

A.4 ADHESIVE MECHANICAL PROPERTIES

The adhesive mechanical properties are listed in Table A.2. Adhesive tensile elastic modulus and Poisson's ratio were obtained by applying strain gauges on adhesive specimens of $100 \times 12.8 \times 2.5\,\text{mm}$ dimensions. These specimens were prepared by laying-up several layers of the film adhesive and curing in an aluminium channel section placed in an oven. The specimens contained voids so the ultimate tensile strength of the adhesive was not attained. The shear modulus was established by using the relationship between the elastic constants

$$G = \frac{E}{2(1+\nu)}. \tag{A.2}$$

Tiu [69], by improved manufacturing techniques, obtained the ultimate tensile stress and strain of the adhesive. His adhesive tensile stress-strain curve is shown in Fig. A.7. The stress-strain curve is linear up to about 1% strain.

The ultimate shear stress and strain values, together with the shear stress-strain curve (Fig. A.8) are reported from reference [70]. From Fig. A.8, the initial shear modulus is $800\,\text{N/mm}^2$. Clearly this value does not agree with the calculated shear modulus of $1145\,\text{N/mm}^2$.

Table A.1. Mechanical properties of XAS/914C composite.

Longitudinal elastic modulus	E_1	$\times 10^3$ N/mm^2	138
Transverse elastic modulus	E_2	$\times 10^3$ N/mm^2	9.4
In-plane shear modulus	G_{12}	$\times 10^3$ N/mm^2	6.7
Major Poisson's ratio	ν_{12}		0.32
Ultimate longitudinal tensile strength	X_t	N/mm^2	1540
Ultimate longitudinal compressive strength	X_c	N/mm^2	1230
Ultimate transverse tensile strength	Y_t	N/mm^2	72
Ultimate transverse compressive strength	Y_c	N/mm^2	281
Ultimate in-plane shear strength	S	N/mm^2	108
Ultimate longitudinal tensile strain	$X_{\epsilon t}$	%	1.25
Ultimate longitudinal compressive strain	$X_{\epsilon c}$	%	1.16
Ultimate transverse tensile strain	$Y_{\epsilon t}$	%	0.77
Ultimate transverse compressive strain	$Y_{\epsilon c}$	%	3.77
Ultimate in-plane shear strain	S_ϵ	%	1.61

Note: The above mechanical properties are given for unidirectional prepreg, dry and at room temperature with nominal fibre volume fraction V_f of 0.60.

Table A.2. Mechanical properties of Redux 308A adhesive.

Elastic modulus	E	N/mm^2	3000
Shear modulus	G	N/mm^2	1145
Poisson's ratio	ν		0.31
Tensile strength		N/mm^2	68
Shear strength		N/mm^2	49
Ultimate tensile strain		%	3.5
Ultimate shear strain		%	35

$$\text{Linear ultimate shear strain} = \frac{\text{shear strength}}{\text{shear modulus}} = 4.28\%$$

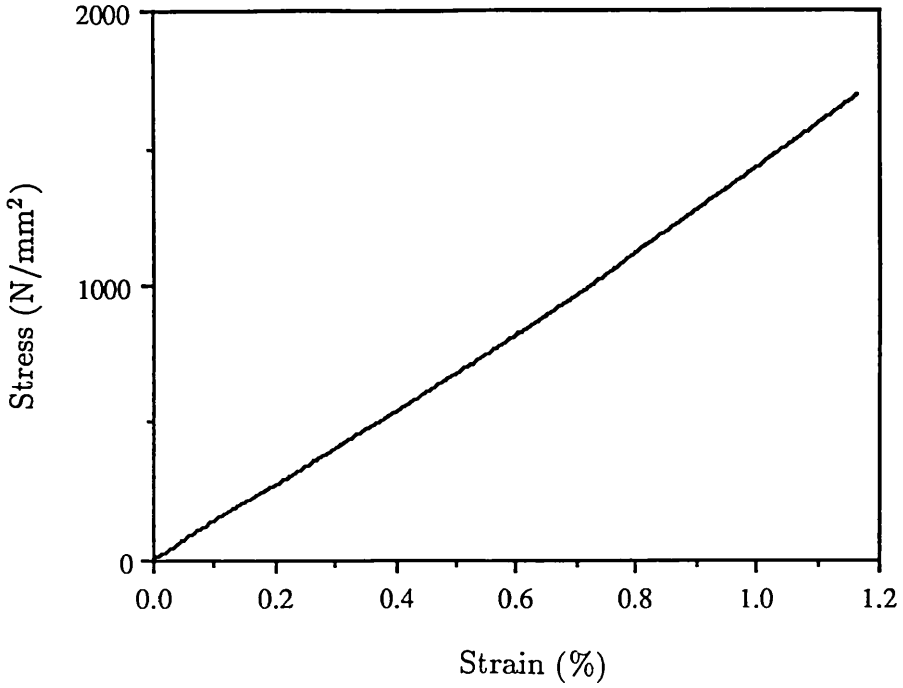


Fig. A.1. Longitudinal tensile stress-strain curve for XAS/914C.

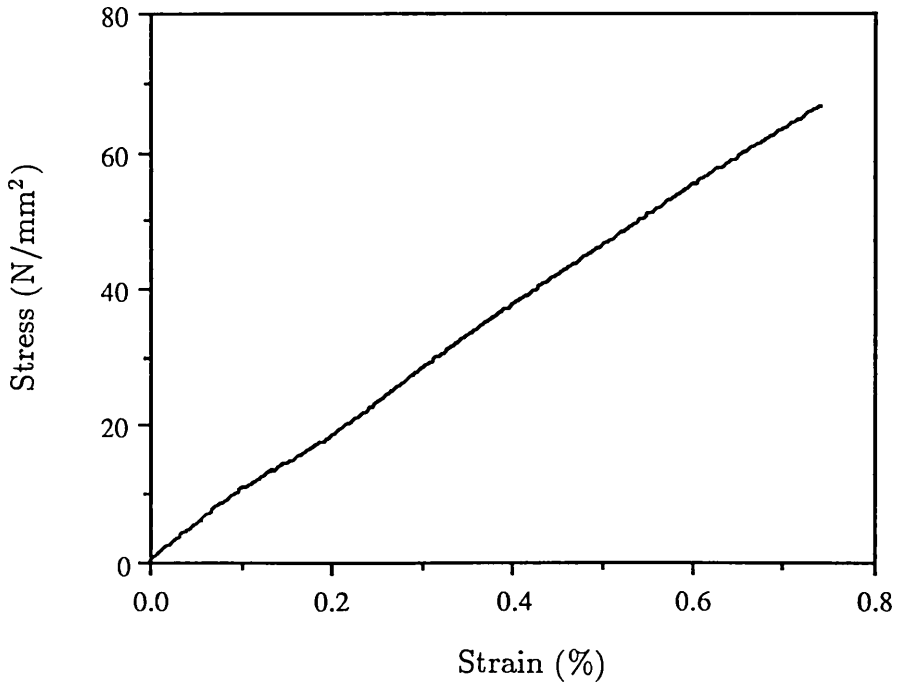


Fig. A.2. Transverse tensile stress-strain curve for XAS/914C.

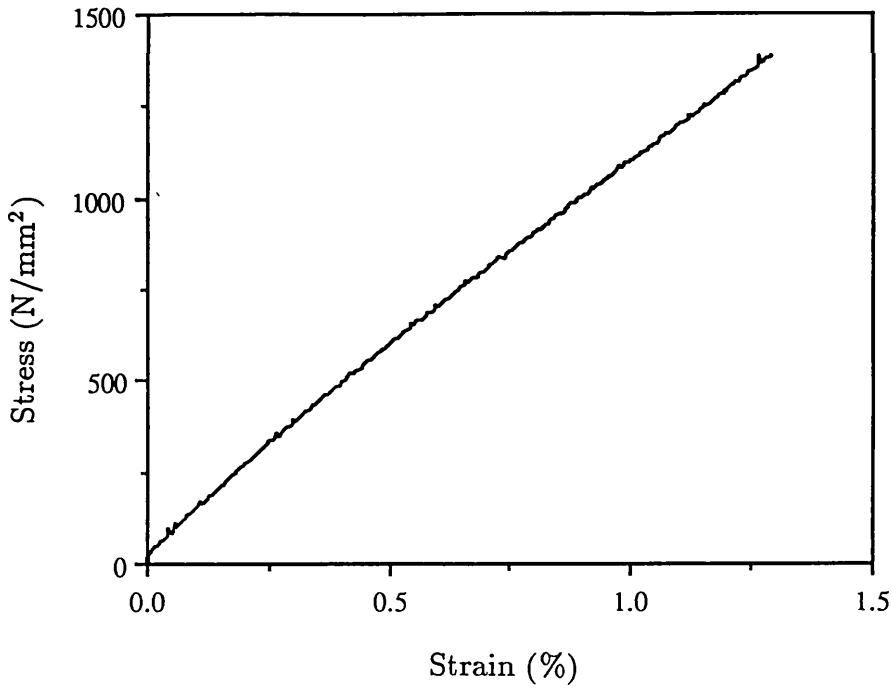


Fig. A.3. Longitudinal compression stress-strain curve for XAS/914C.

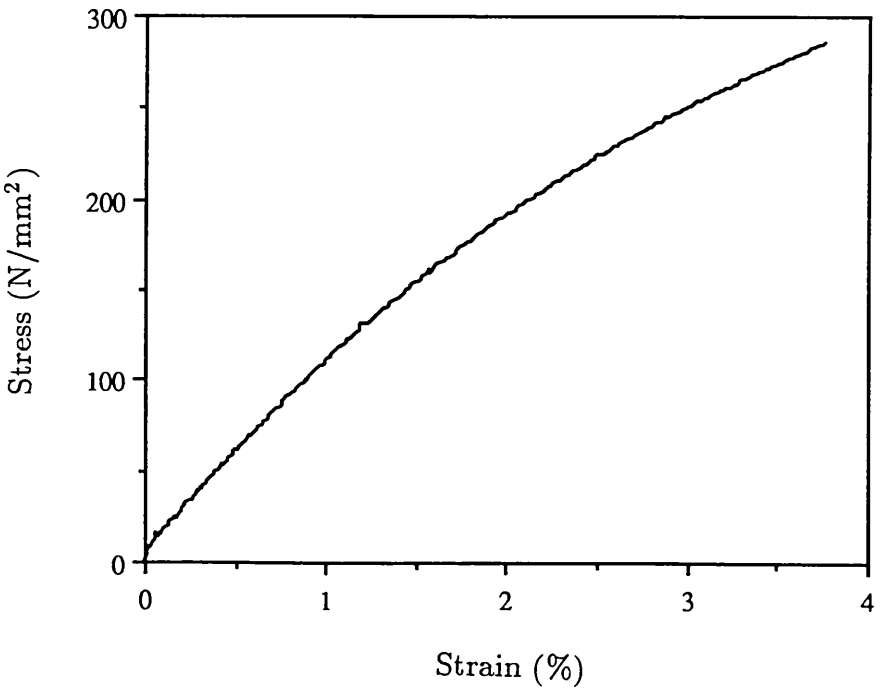


Fig. A.4. Transverse compression stress-strain curve for XAS/914C.

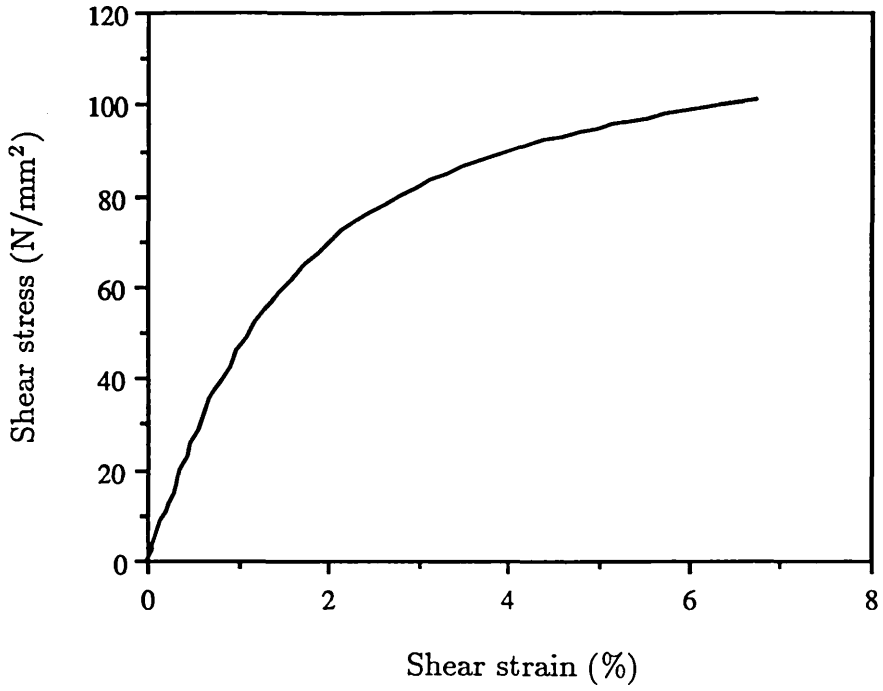


Fig. A.5. Shear stress-strain curve for XAS/914C.

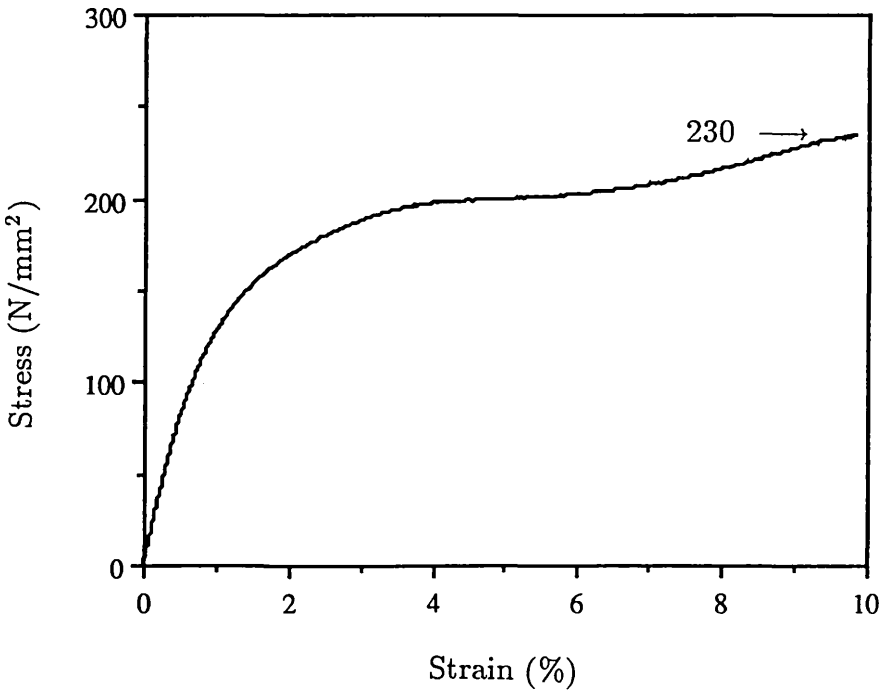


Fig. A.6. Longitudinal tensile stress-strain curve for $[(\pm 45)_4]_s$ XAS/914C laminate.

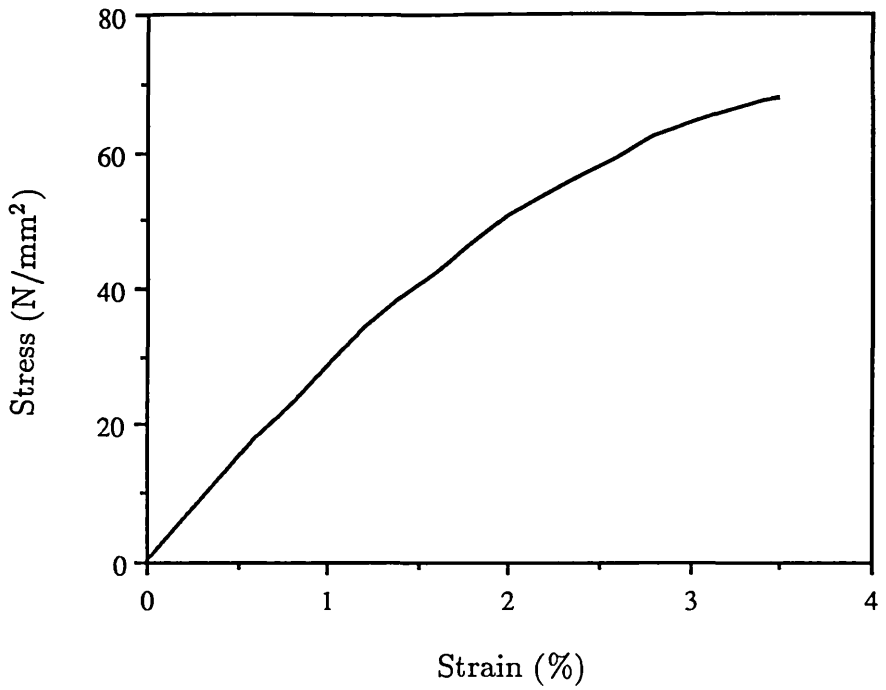


Fig. A.7. Tensile stress-strain curve for Redux 308A [69].

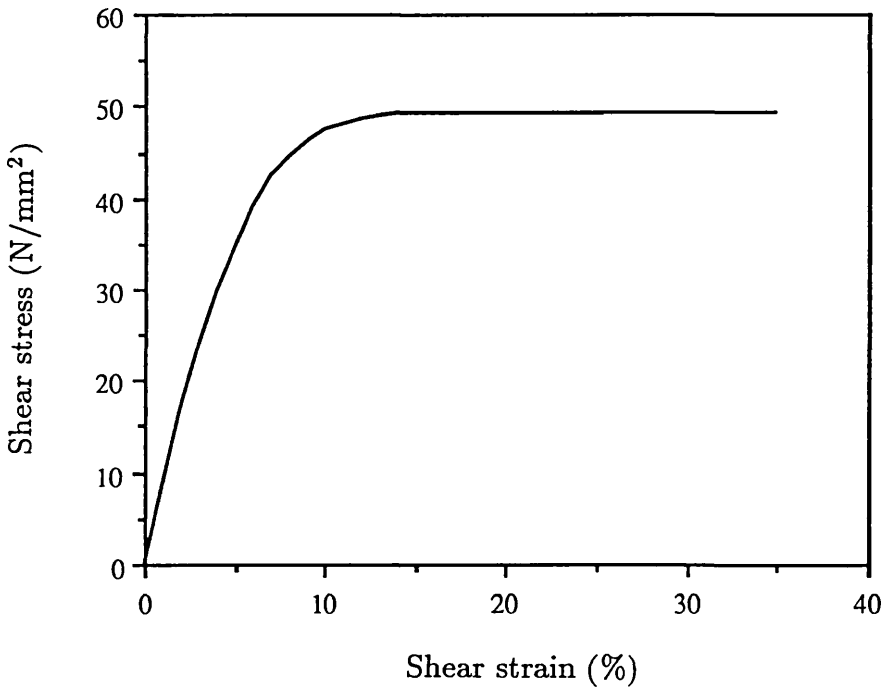


Fig. A.8. Shear stress-strain curve for Redux 308A [70].

Appendix B

TENSILE PROPERTIES OF LAMINATES

B.1 INTRODUCTION

Tensile tests on some laminates have been carried out. The results indicate a beneficial effect in having a 'soft' ply group on the laminate surfaces.

B.2 RESULTS AND DISCUSSION

The specimen size used is 200 × 25 mm. The gauge length is 100 mm, with 50 mm from either end of the specimen used for gripping. The jaws of the tensile testing machine (Zwick) allowed gripping without the need for end tabs. This is due to the fine serations of the grips which do not seriously damage the specimen.

Tensile strengths are presented in Table B.1. It can be seen that laminates with ±45° surface plies are stronger than those with a 0° surface ply. It is thought that having ±45° plies on the laminate surface is beneficial in tension. This may be due to the 'padding' effect for the load bearing 0° plies introduced by a 'soft' ply group on the laminate surafce. Fig. B.1 shows the specimens after tensile fracture. Laminate failure has not occurred at the end of the gripped region, so stress concentrations at the end of the gripped region are not the driving factor for this behaviour.

Table B.2 shows a comparison between experimental and theoretical (lamination theory) values of the elastic modulus and Poisson's ratio in tension. Good agreement between experiment and theory has been obtained. Figs. B.2 and B.3

show the stress-strain curves for stacking sequences A and B. The slopes (elastic moduli) of the two curves are the same. However, higher strains are attained with a 'soft' ply group on the laminate surfaces. Similar argument is applicable to Figs. B.4 and B.5.

Table B.1. Tensile strength of laminates.

	Tensile strength (N/mm^2)			
Stacking sequence	Min.	Max.	Mean	C_v (%)
A: $[0/\pm45]_s$	566.6	669.0	619.2	6.3
B: $[\pm45/0]_s$	635.2	761.6	711.9	7.9
D: $[\pm45/0_2]_s$	954.9	1132.4	1031.1	8.6
F: $[0_2/\pm45]_s$	811.1	992.8	901.5	9.1

C_v—Coefficient of variation

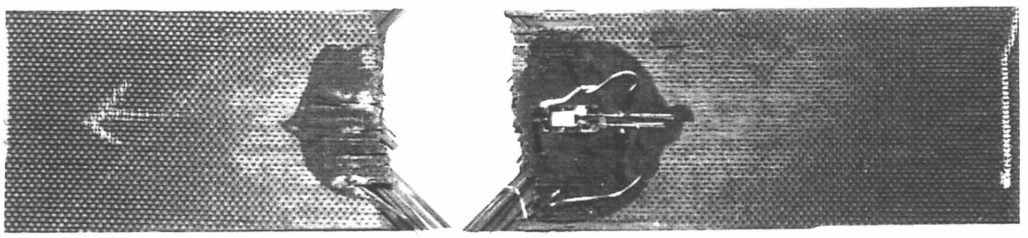
Table B.2. Mechanical properties of laminates.

	Experimental		Theoretical	
Stacking sequence	E_m	ν_m	E_m	ν_m
A: $[0/\pm45]_s$	59.0	0.757	61.6	0.668
B: $[\pm45/0]_s$	59.5	0.782	61.6	0.668
D: $[\pm45/0_2]_s$	79.2	0.763	81.0	0.638
F: $[0_2/\pm45]_s$	78.6	0.699	81.0	0.638

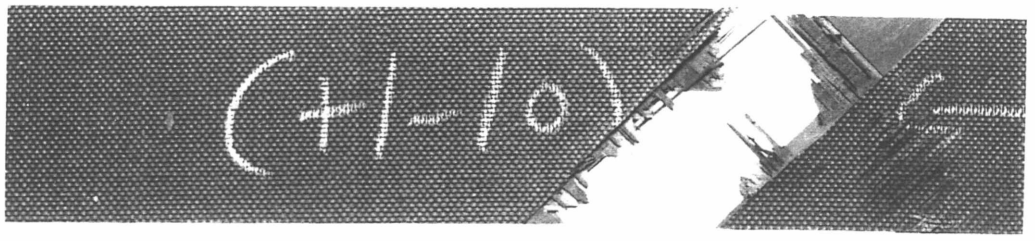
E_m— effective membrane elastic modulus of laminate in direction of applied load ($\times 10^3$ N/mm^2).

ν_m— effective membrane Poisson's ratio of laminate (associated with E_m).

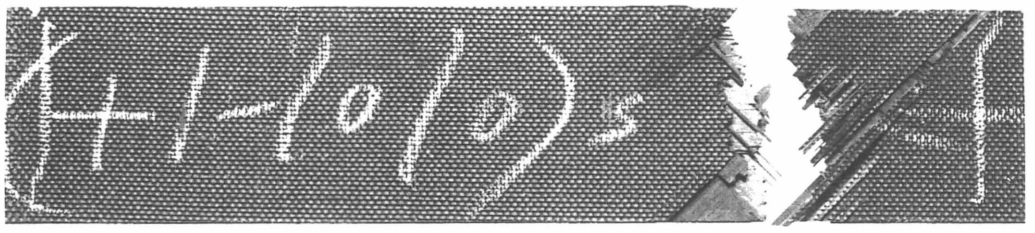
Theoretical properties are obtained using lamination theory with the material data given in Appendix A.



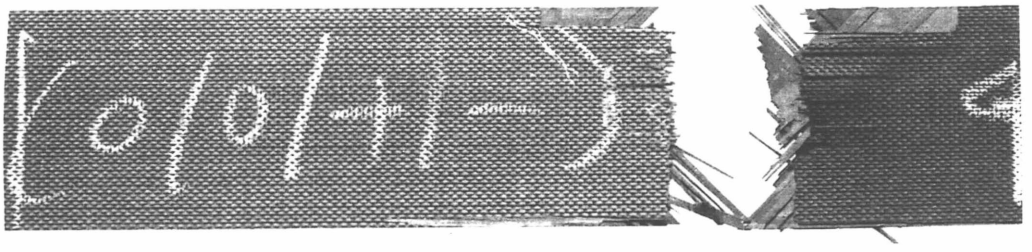
A: $[0/\pm 45]_s$



B: $[\pm 45/0]_s$



D: $[\pm 45/0_2]_s$



F: $[0_2/\pm 45]_s$

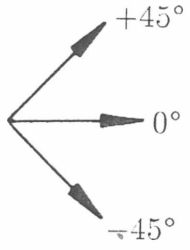


Fig. B.1. The specimens after tensile fracture (only the test section is shown).

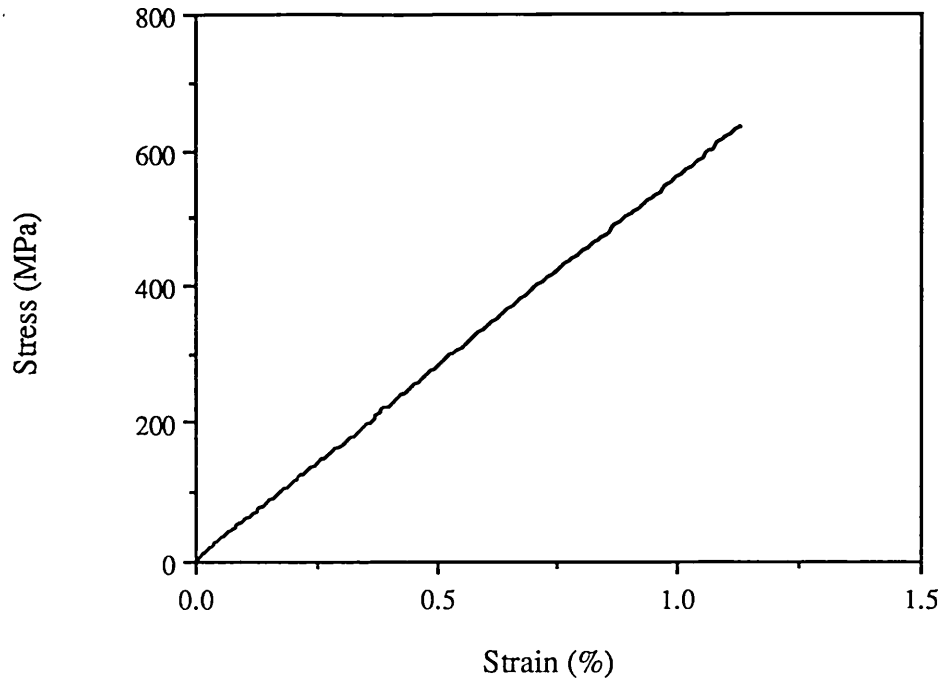


Fig. B.2. Stress-strain curve for stacking sequence A: $[0/\pm 45]_s$.

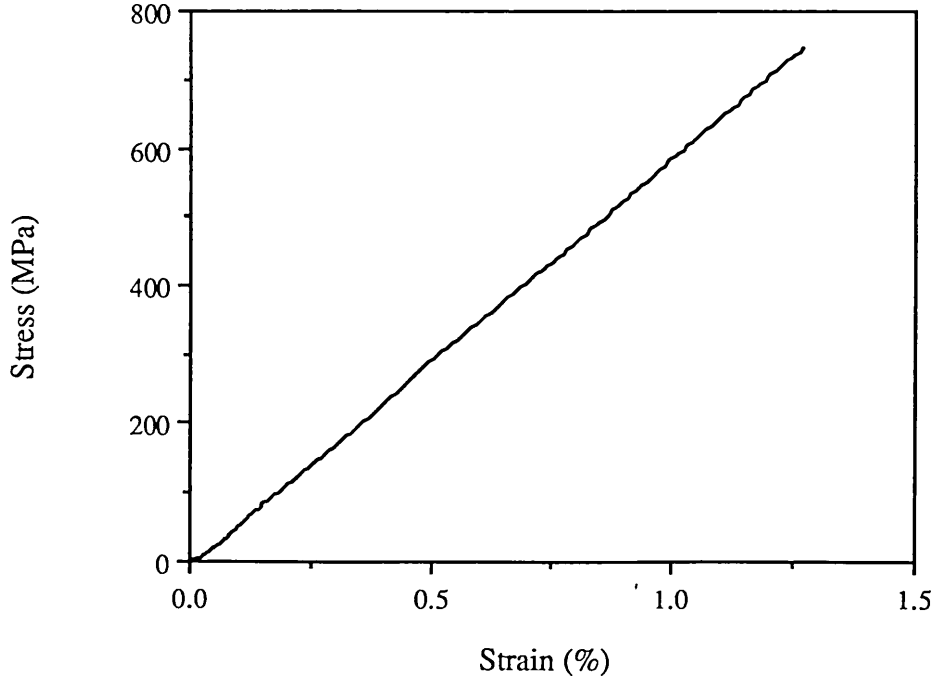


Fig. B.3. Stress-strain curve for stacking sequence B: $[\pm 45/0]_s$.

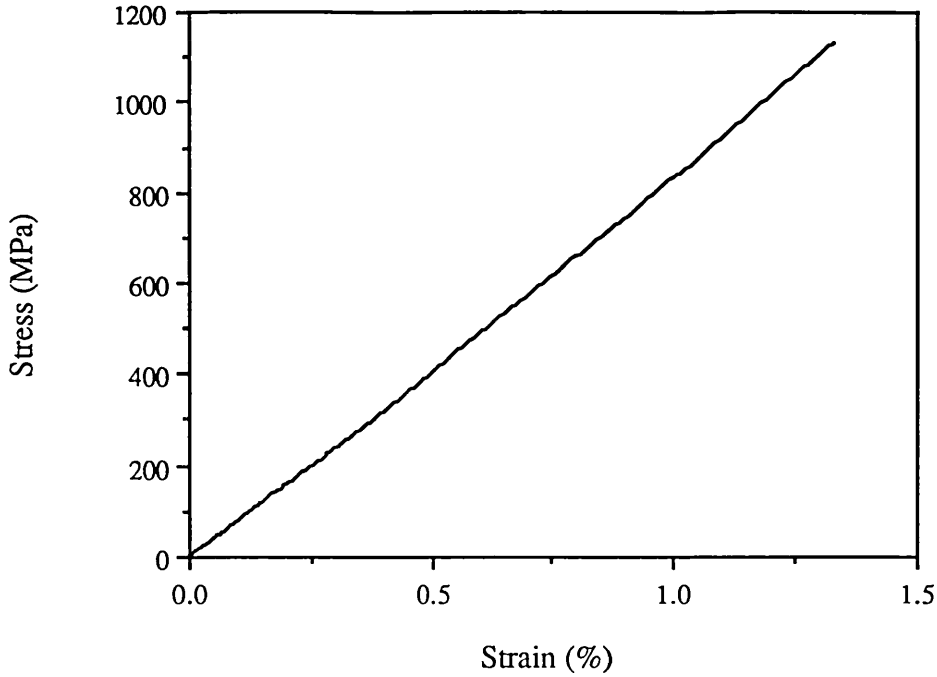


Fig. B.4. Stress-strain curve for stacking sequence D: $[\pm 45/0_2]_s$.

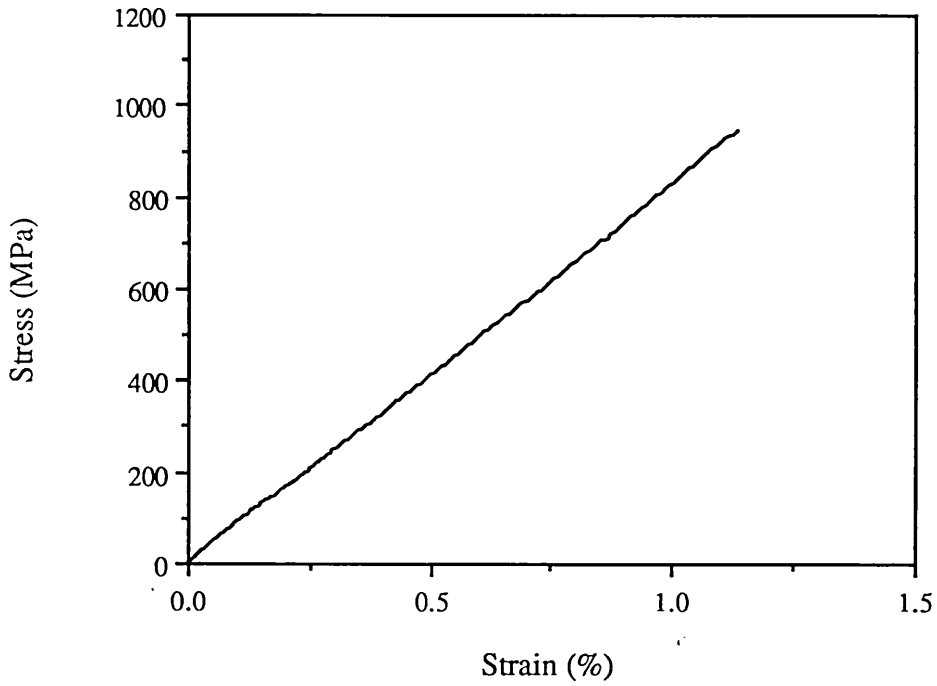


Fig. B.5. Stress-strain curve for stacking sequence F: $[0_2/\pm 45]_s$.

Appendix C

FLEXURAL PROPERTIES OF LAMINATES

C.1 INTRODUCTION

A three-point flexure test has been undertaken to determine the change of the adherend flexural properties with stacking sequence changes. Six- and eight-ply laminates have been examined. The presence of interlaminar shear stresses undermined the accurate determination of the bending properties. Laminates with 0° surface ply fail by fibre tensile fracture followed by delamination at the interface between the adjacent surface plies. Laminates with ±45° surface plies fail by intralaminar shear fracture associated with larger central deflections.

C.2 THREE-POINT FLEXURE TEST

The central load in three-point bending produces a bending moment on the beam that varies linearly from zero at the supports to a maximum value at the centre. A uniformly distributed interlaminar shear stress all along the beam's length is produced. This may cause premature failure. The formulae used are from the ASTM standards [91].

The flexural strength is the maximum stress in the outer fibres which occurs at mid-span. A linear stress-strain relation is assumed. The maximum bending stress in the outer fibres is given by

$$\sigma_b = \frac{3PS}{2wt^2} \tag{C.1}$$

where P = load at failure, S = span between supports, w = width of specimen and t = thickness of specimen. The maximum bending strain in the outer fibres is given by

$$\epsilon_b = \frac{6\delta t}{S^2} \tag{C.2}$$

where δ = maximum deflection of the centre of the beam. The bending elastic modulus is given by

$$E_b = \frac{S^3 m}{4wt^3} \tag{C.3}$$

where m = slope of the linear load-deflection curve.

Large span-to-depth ratios result in large central deflections which makes it necessary to account for the horizontal forces developed at the supports in the calculation of the bending moment. The bend-twist coupling effects in multi-directional laminates tend to lift-off the specimen at the supports. Narrow specimens and high span-to-depth ratios tend to minimise the lift-off effects.

In view of the above remarks, the following parameters were used. The span length used with all specimens tested was 25 mm. The loading roller diameter was 6.36 mm and the support rollers diameter was 7.14 mm. A larger loading roller size than the one used is usually recommended to avoid specimen damage. For the six-ply laminates (nominal thickness 0.75 mm), the following ratios were used: $\frac{w}{t} = 10$ and $\frac{S}{t} = 33.3$. The free overhang length was 12.5 mm on either side. For the eight-ply laminates (nominal thickness 1.0 mm), the following ratios were used: $\frac{w}{t} = 10$ and $\frac{S}{t} = 25$. The free overhang length was 17.5 mm on either side.

C.3 MODES OF FAILURE

The test was stopped as soon as the outermost ply cracked. In the case of laminates with 0° ply on the outer surface, the tensile fracture of the outermost 0° ply was followed immediately by shear cracking, on either side of the tensile crack, in the resin rich interface separating the outermost two plies. For lamintes with ±45° surface plies, the test was terminated on the appearance of the first intralaminar shear crack. As expected, larger central deformations were attained with laminates having a 'soft' ply group (±45°) on the outermost surfaces.

C.4 TEST RESULTS

Tables C.1 and C.2 show the flexural properties for the six- and eight-ply laminates. The lower values of the experimental bending elastic modulus as compared to the theoretical ones are due to shear deformations. A higher span-to-depth ratio may reduce the difference between the experimental and theoretical values. Figs. C.1 and C.2 show the stress-strain curves for the various laminates tested.

Table C.1. Flexural properties of six-ply adherends.

	Experimental			Theoretical
Stacking sequence	ϵ_b	σ_b	E_b	E_b
A: $[0/\pm 45]_s$	2.02	1610	82.1	103.8
B: $[\pm 45/0]_s$	3.04	666	22.0	26.5
$[0_3]_s$	2.01	2237	111.4	138.0

ϵ_b— maximum bending strain in the outer fibres (%).

σ_b— maximum bending stress in the outer fibres (N/mm^2).

E_b— effective bending elastic modulus of adherend ($\times 10^3$ N/mm^2).

The theoretical value of the bending elastic modulus E_b is obtained using lamination theory with the material data given in Appendix A.

Table C.2. Flexural properties of eight-ply adherends.

	Experimental			Theoretical
Stacking sequence	ϵ_b	σ_b	E_b	E_b
D: $[\pm 45/0_2]_s$	3.15	1091	33.9	37.1
E: $[0/\pm 45/0]_s$	1.92	1361	71.4	91.5
F: $[0_2/\pm 45]_s$	1.84	1746	91.9	123.8
$[0_4]_s$	1.98	2028	103.4	138.0

ϵ_b— maximum bending strain in the outer fibres (%).

σ_b— maximum bending stress in the outer fibres (N/mm^2).

E_b— effective bending elastic modulus of adherend ($\times 10^3$ N/mm^2).

The theoretical value of the bending elastic modulus E_b is obtained using lamination theory with the material data given in Appendix A.

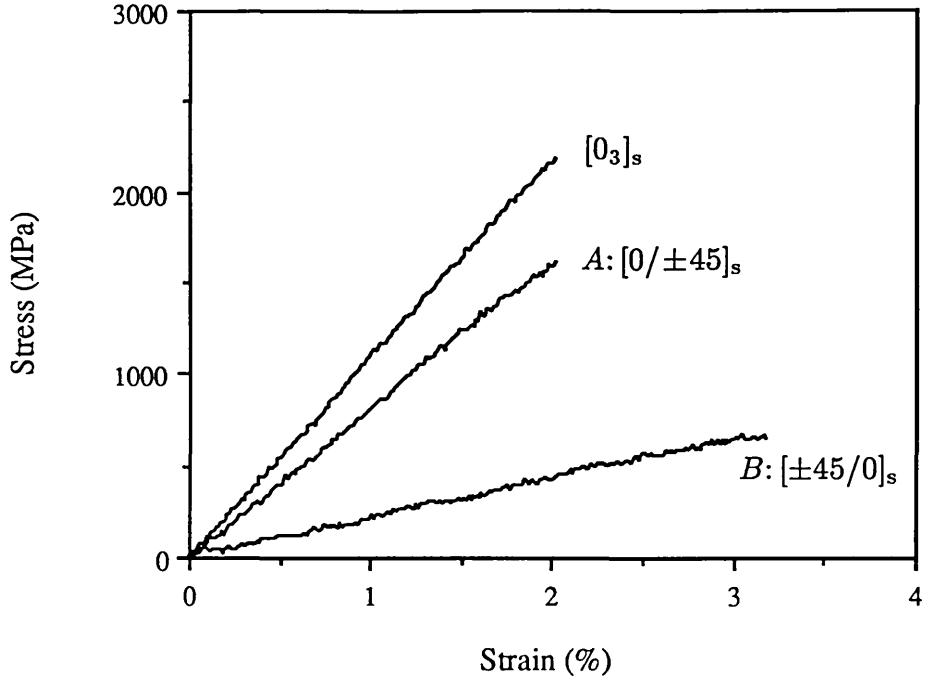


Fig. C.1. Stress-strain curves for six-ply laminates in bending.

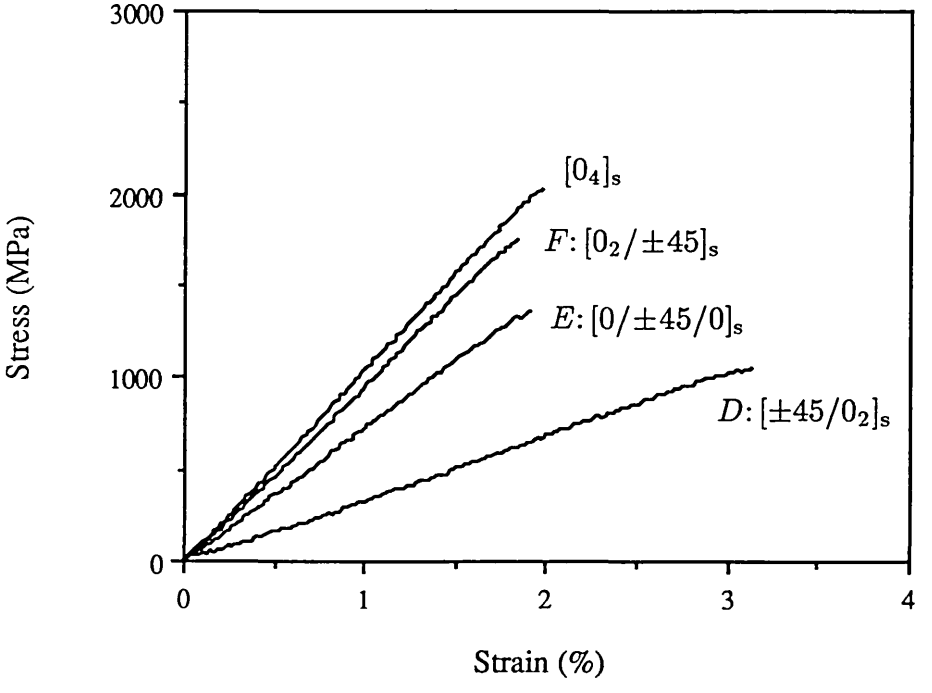


Fig. C.2. Stress-strain curves for eight-ply laminates in bending.

REFERENCES

[1] Hart-Smith, L.J.,"Adhesively bonded joints for fibrous composite structures," Douglas Aircraft Co., McDonnell Douglas Corp., *Paper 7740*, presented to Int. Symp. on Joining and Repair of FRP, Imperial College, London (1986).

[2] Vinson, J.R. and Sierakowski, R.L., *The behavior of structures composed of composite materials*, Martinus Nijhoff Pub., 239–262 (1986).

[3] Sneddon, I.N., "The distribution of stresses in adhesive joints," *Adhesion*, D.D. Eley, Ed., Chapter 9, OUP (1961).

[4] Mitra, P., "Literature survey on stress analysis of bonded joints," *Ciba-Geigy (UK) Ltd., Bonded Structures Divn.* (1973).

[5] Matthews, F.L., Kilty, P.F. and Godwin, E.W., "A review of the strength of joints in fibre-reinforced plastics. Part 2: adhesively bonded joints," *Composites* **13**, 29–37 (1982).

[6] Adams, R.D. and Wake, W.C., *Structural adhesive joints in engineering*, Elsevier Applied Science Pub. (1984).

[7] Shields, J., "Adhesive bonding," *Engineering Design Guides*, OUP.

[8] de Bruyne, N. A. and Houwink, R. (Eds.), *Adhesion and Adhesives*, Elsevier Publishing Co. (1951).

[9] Volkersen, O., "Die Nietkraftverteilung in zugbeanspruchten Nietverbindungen mit konstanten Laschenquerschnitten," *Luftfahrtforschung* **15**, 41–47 (1938).

[10] Goland, M. and Reissner, E., "The stresses in cemented joints," *J. Appl. Mech.* **11**, A17–A27 (1944).

[11] de Bruyne, N.A., "The strength of glued joints," *Aircraft Engineering* **16**, 115–118 (1944).

[12] Cornell, R.W., "Determination of stresses in cemented lap joints," *J. Applied Mechanics* **20**, 355–364 (1953).

[13] Cherry, B.W. and Harrison, N.L., "The optimum profile for a lap joint," *J. Adhesion* **2**, 125–128 (1970).

[14] Wooley, G.R. and Carver, D.R., "Stress concentration factors for bonded lap joints," *J. Aircraft* **8**, 817–820 (1971).

[15] Hart-Smith, L.J.,"Adhesive bonded single lap joints," *NASA CR-112236*, Douglas Aircraft Co., NASA Langley (1973).

[16] Barker, R.M. and Hatt, F.,"Analysis of bonded joints in vehicular structures," *AIAA J.* **11**, 1650–1654 (1973).

[17] Adams, R.D. and Peppiatt, N.A., "Effect of Poisson's ratio strains in adherends on stresses of an idealised lap joint," *J. Strain Anal.* **8**, 134–139 (1973).

[18] Adams, R.D. and Peppiatt, N.A., "Stress analysis of adhesive-bonded lap joints," *J. Strain Anal.* **9**, 185–196 (1974).

[19] Hart-Smith, L.J., "Analysis and design of advanced composite bonded joints," *NASA CR-2218*, Douglas Aircraft Co., NASA Langley (1974).

[20] Chang, D.J. and Muki, R., "Stress distribution in a lap joint under tension-shear, " *Int. J. Solids Structures* **10**, 503–517 (1974).

[21] Oplinger, D.W., "Stress analysis of composite joints," *Proc. Fourth Army Mat. Tech. Conf.—Advances in Joining Tech.*, 405–452 (1975).

[22] Renton, W.J. and Vinson, J.R., "On the behaviour of bonded joints in composite material structures," *Engng Fracture Mech.* **7**, 41–60 (1975).

[23] Renton, W.J. and Vinson, J.R., "Fatigue behavior of bonded joints in composite material structures," *J. Aircraft* **12**, 442–447 (1975).

[24] Renton, W.J. and Vinson, J.R., "The efficient design of adhesive bonded joints," *J. Adhesion* **7**, 175–193 (1975).

[25] Renton, W.J. and Vinson, J.R., "Analysis of adhesively bonded joints between panels of composite materials," *J. Appl. Mech.*, 101–106 (1977).

[26] Dootson, M. and Grant, P.J., "Bonded joints in aircraft structures," *Proc. Sixth Cranfield Conf.— Plastics Design Engng*, Cranfield Institute of Technology, Cranfield, Bedford, (1975).

[27] Srinivas, S., "Analysis of bonded joints," *NASA TN D-7855* (1975).

[28] Allman, D.J., "A theory of elastic stresses in adhesive bonded lap joints," *RAE TR-76024* (1976).

[29] Thamm, F., "Stress distribution in lap joints with partially thinned adherends," *J. Adhesion* **7**, 301–309 (1976).

[30] Ojalvo, I.U. and Eidinoff, H.L.,"Bond thickness effects upon stresses in single-lap adhesive joints," *AIAA J.* **16**, 204–211 (1978).

[31] Cooper, P.A. and Sawyer, J.W., "A critical examination of stresses in an elastic single lap joint," *NASA TP-1507* (1979).

[32] Chan, W.S. and Sun, C.T., "Interfacial stresses and strength of lap joints," *Proc. AIAA/ASME/ASCE/AHS 21st Structures, Structural Dynamics and Materials Conf.*, Seattle, Washington, 656–663 (1980).

[33] Pickett, A.K. and Hollaway, L., "The analysis of elastic adhesive stresses in bonded lap joints in FRP structures," *Composite Structures* **3**, 55–79 (1985).

[34] Kairouz, K.C., "Discrete flexible joints," *MSc thesis*, Cranfield Institute of Technology, Cranfield, Bedford (1986).

[35] Roy, S. and Reddy, J.N., "A finite element analysis of adhesively bonded composite joints with moisture diffusion and delayed failure," *Computers and Structures* **29**, 1011–1031 (1988).

[36] Mylonas, C.,"Experiments on composite models with applications to cemented joints," *Exp. Stress Anal.* **12**, 129–142 (1954).

[37] Demarkles, L.R., "Investigation of the use of a rubber analog in the study of stress distribution in riveted and cemented joints," *NACA TN-3413* (1955).

[38] Adams, R.D., Chambers, S.H., Del Strother, P.J.A. and Peppiatt, N.A., "Rubber model for adhesive lap joints," *J. Strain Anal.* **8**, 52–57 (1973).

[39] Tuttle, M.E., Barthelemy, B.M. and Brinson, H.F., "Strain measurement within a single lap joint using embedded strain gages," *Report No. VPI-E-84-1*, Virginia Polytechnic Institute and State University, Blacksburg, Virginia (1984).

[40] Post, D., Czarnek, R., Wood, J.D. and Joh, D., "Deformations and strains in a thick adherend lap joint," *Adhesively bonded joints: testing, analysis and design, ASTM STP 981*, W.S. Johnson, Ed., American Society for Testing and Materials, Philadelphia, 107–118 (1988).

[41] Wake, W.C., Ed., *Developments in adhesives-1*, Chapter 10, Preparing low-energy surfaces for bonding by Dukes, W.A. and Kinloch, A.J, Applied Science Pub. (1977).

[42] Stone, M.H., "Effects of degree of abrasion of carbon fibre composite surfaces on strengths of adhesive bonded joints," *RAE TM-327* (1979).

[43] Hart-Smith, L.J., "Design and analysis of bonded repairs for fibrous composite aircraft structures," *Douglas Aircraft Co. Paper 7133*, presented to International Workshop on Defence Applications of Advanced Repair Technology for Metal and Composite Structures, Naval Research Laboratory, Washington, D.C. (1981).

[44] Parker, B.M. and Waghorne, R.M., "Surface pretreatment of carbon fibre-reinforced composites for adhesive bonding," *Composites* **13**, 280–288 (1982).

[45] Hart-Smith, L.J., Ochsner, R.W. and Radecky, R.L., "Surface preparation of fibrous composites for adhesive bonding or painting," *Douglas Services Magazine* **41**, 12–22 (1984).

[46] Parker, B.M., "The use of primers in the adhesive bonding of carbon fibre reinforced composites" *RAE TR-88048* (1988).

[47] Parker, B.M., "Bondability of carbon fibre composites" *Proceedings of a Seminar on Bonding and Repair of Composites*, National Exhibition Centre, Birmingham, Butterworth & Co. Pub. (1989).

[48] Stone, M.H., "Weakening of adhesive bonded lap joints by cracking in fillets during testing," *RAE TM-341* (1980).

[49] Sage, G.N. and Tiu, W.P., "The effect of glue-line voids and inclusions on the fatigue strength of bonded joints in composites," *Composites* **13**, 228–232 (1982).

[50] Allen, K.W., "Bubbles in adhesive joints with CFRP adherends," *J. Adhesion* **17**, 45–50 (1984).

[51] Dallas, R.N., "Methods of joining advanced fibrous composites," *Composite Materials: Testing and Design, ASTM STP 460*, 381–392 (1969).

[52] Althof, W., "Strength properties of bonded joints of carbon fibre reinforced composites," *Deutsche Luft- und Raumfahrt, DLR FB 71-31*, RAE translation (1971).

[53] Yuceoglu, U. and Updike, D.P., "Stress concentrations in bonded multi-layer stiffening strips and base plates," *Proc. ASME Structures, Design, Structural Dynamics and Materials Conf.*, 99–110 (1980).

[54] Matthews, F.L. and Tester, T.T., "The influence of stacking sequence on the strength of bonded CFRP single lap joints," *Int. J. Adhesion and Adhesives* **5**, 13–18 (1985).

[55] Cushman, J.B., McCleskey, S.F. and Ward, S.H., "Test and analysis of Celion 3000/PMR-15, Graphite/Polyimide bonded composite joints," *NASA CR-3602* (1983).

[56] Martin, R.H. and Sage, G.N., "Prediction of the fatigue strength of bonded joints between multi-directional laminates of CFRP," *Composite Structures* **6**, 141–163 (1986).

[57] Grant, P. and Lewington, J.A., "Some important considerations in the design of composite bonded joints in aerospace structures," *Canadian Aeronautics and Space Journal* **33**, 91–98 (1987).

[58] Hart-Smith, L.J., "Further developments in the design and analysis of adhesive-bonded structural joints," *Joining of Composite Materials, ASTM*

STP 749, K.T. Kedward, Ed., American Society for Testing and Materials, 3–31 (1981).

[59] Bowditch, M.R. and Stannard, K.J., "Adhesive bonding of GRP" *Composites* **13**, 298–304 (1982).

[60] Parker, B.M., "The effect of extended hot-humid exposure of adhesive bonded carbon fibre composite joints. Part 1: 175°C cured matrix," *RAE TR-89001* (1989).

[61] Parker, B.M., "The effect of extended hot-humid exposure of adhesive bonded carbon fibre composite joints. Part 2: 120°C cured matrix," *RAE TR-89061* (1990).

[62] Weitsman, Y.,"Stresses in adhesive joints due to moisture and temperature," *J. Comp. Mat.* **11**, 378–394 (1977).

[63] Stone, M.H., "Effect of temperature and duration of cure on the heat distortion temperature, joint strength and durability of some structural adhesives bonded to aluminium," *RAE TM-318* (1979).

[64] Stone, M.H., "A comparison of the strengths of metal-metal and metal-CFRP adhesive bonded joints at various test temperatures," *RAE TR-82102* (1982).

[65] Myhre, S.H., Labor, J.D., and Aker, S.C., "Moisture problems in advanced composite structural repair," *Composites* **13**, 289–297 (1982).

[66] Parker, B.M., "The effect of composite prebond moisture on adhesive-bonded CFRP-CFRP joints," *Composites* **14**, 226–232 (1983).

[67] Megson, T.H., *Aircraft structures for engineering students*, Chapter 3, Torsion of solid sections, Edward Arnold Pub. (1980).

[68] Kairouz, K.C. and Matthews, F.L., "Influence of ply stacking sequence on the strength of bonded CFRP joints," *Progress Report No. 1*, MoD (PE) Agreement No. 2037/332 XR/MAT, Imperial College, London (1988).

[69] Tiu, W.P., "Fatigue strength prediction of adhesively bonded unidirectional carbon fibre reinforced composite joints," *PhD thesis*, Department of Aeronautics, City University, London (1987).

[70] ESDU Data Item No. 81022, "Guide to the use of data items in the design of bonded joints," Engineering Sciences Data Unit, London (1981).

[71] ICB-FINEL user manual, Babcock Power Ltd. and Imperial College, London (1983).

[72] Abaqus (version 4.8) user manual, Hibbitt, Karlsson and Sorensen Inc., Providence, R.I., U.S.A.

[73] Zienkiewicz, O.C., *The finite element method*, McGraw-Hill Pub. (1977).

[74] Hearn, E.J., *Mechanics of Materials*, Pergamon Press Pub. (1980).

[75] Robson, J.E., "A survey of failure criteria," *Review paper, Industrial Affiliates Programme*, Centre for Composite Materials, Imperial College, London (1989).

[76] Information Sheet No. FTA.49e, "Fibredux 914," Ciba-Geigy Plastics, Cambridge (1984).

[77] Instruction Sheet No. RTA.7d, "Redux 308A," Ciba-Geigy Plastics, Cambridge (1980).

[78] Bishopp, J., *Private communication*, Ciba-Geigy Plastics, Cambridge.

[79] Tuttle, M.E. and Pendleton, R.L., Eds., *Manual on experimental methods for mechanical testing of composites*, Chapter 4, Moiré interferometry for composites by Post, D., Society for Experimental Mechanics.

[80] Daniel, I.M. and Rowlands, R.E., "Determination of strain concentration in composites by moiré techniques," *J. Comp. Mat.* **5**, 250–254 (1971).

[81] Byron Pipes, R. and Daniel, I.M., "Moiré analysis of the interlaminar shear edge effect in laminated composites," *J. Comp. Mat.* **5**, 255–259 (1971).

[82] Post, D., "Moiré interferometry at VPI and SU," *Exp. Mech.* **23**, 203–210 (1983).

[83] Post, D., "The analysis of deformations and strains in composites by moiré interferometry," *Proc. Sixth Int. Conf. Comp. Mat.*, F.L. Matthews et al., Eds., Imperial College, London, Elsevier Applied Science Pub., 5.251–5.261 (1987).

[84] Purslow, D., "Some fundamental aspects of composites fractography," *RAE TR-81127* (1981).

[85] Purslow, D., "The application of composites fractography to the investigation of the failure of a wind tunnel model," *RAE TR-83020* (1983).

[86] Purslow, D., "Fractography of fibre-reinforced thermoplastics, Part 3. Tensile, compressive and flexural failures," *Composites* **19**, 358–366 (1988).

[87] Greenhalgh, E.S., "On defect growth and failure in carbon fibre composite structures," *RAE TR-89045* (1989).

[88] Parvizi, A., Garrett, K.W. and Bailey, J.E., "Constrained cracking in glass fibre-reinforced epoxy cross-ply laminates," *J. Mater. Sci.* **13**, 195–201 (1978).

[89] Kairouz, K.C. and Matthews, F.L., "Influence of ply stacking sequence on the strength of bonded CFRP joints," *Progress Report No. 5*, MoD (PE) Agreement No. 2037/332 XR/MAT, Imperial College, London (1989).

[90] Curtis, P.T., Ed., "CRAG test methods for the measurement of the engineering properties of fibre reinforced plastics," *RAE TR-85099* (1985).

[91] ASTM Standard Test Method No. D790-84a, "Flexural properties of unreinforced and reinforced plastics and electrical insulating materials," *ASTM standards and literature references for composite materials*, American Society for Testing and Materials, Philadelphia (1987).